Advanced Structured Materials

Konstantin Naumenko
Manja Krüger *Editors*

Advances in Mechanics of High-Temperature Materials

Springer

Advanced Structured Materials

Volume 117

Common engineering materials reach in many applications their limits and new developments are required to fulfil increasing demands on engineering materials. The performance of materials can be increased by combining different materials to achieve better properties than a single constituent or by shaping the material or constituents in a specific structure. The interaction between material and structure may arise on different length scales, such as micro-, meso- or macroscale, and offers possible applications in quite diverse fields.

This book series addresses the fundamental relationship between materials and their structure on the overall properties (e.g. mechanical, thermal, chemical or magnetic etc) and applications.

The topics of *Advanced Structured Materials* include but are not limited to

- classical fibre-reinforced composites (e.g. glass, carbon or Aramid reinforced plastics)
- metal matrix composites (MMCs)
- micro porous composites
- micro channel materials
- multilayered materials
- cellular materials (e.g., metallic or polymer foams, sponges, hollow sphere structures)
- porous materials
- truss structures
- nanocomposite materials
- biomaterials
- nanoporous metals
- concrete
- coated materials
- smart materials

Advanced Structured Materials is indexed in Google Scholar and Scopus.

More information about this series at http://www.springer.com/series/8611

Konstantin Naumenko · Manja Krüger
Editors

Advances in Mechanics of High-Temperature Materials

Springer

Editors
Konstantin Naumenko
Institut für Mechanik
Otto-von-Guericke-Universität Magdeburg
Magdeburg, Sachsen-Anhalt, Germany

Manja Krüger
Institut für Energie- und Klimaforschung
Forschungszentrum Jülich GmbH
Jülich, Nordrhein-Westfalen, Germany

ISSN 1869-8433 ISSN 1869-8441 (electronic)
Advanced Structured Materials
ISBN 978-3-030-23868-1 ISBN 978-3-030-23869-8 (eBook)
https://doi.org/10.1007/978-3-030-23869-8

© Springer Nature Switzerland AG 2020
This work is subject to copyright. All rights are reserved by the Publisher, whether the whole or part of the material is concerned, specifically the rights of translation, reprinting, reuse of illustrations, recitation, broadcasting, reproduction on microfilms or in any other physical way, and transmission or information storage and retrieval, electronic adaptation, computer software, or by similar or dissimilar methodology now known or hereafter developed.
The use of general descriptive names, registered names, trademarks, service marks, etc. in this publication does not imply, even in the absence of a specific statement, that such names are exempt from the relevant protective laws and regulations and therefore free for general use.
The publisher, the authors and the editors are safe to assume that the advice and information in this book are believed to be true and accurate at the date of publication. Neither the publisher nor the authors or the editors give a warranty, expressed or implied, with respect to the material contained herein or for any errors or omissions that may have been made. The publisher remains neutral with regard to jurisdictional claims in published maps and institutional affiliations.

This Springer imprint is published by the registered company Springer Nature Switzerland AG
The registered company address is: Gewerbestrasse 11, 6330 Cham, Switzerland

Preface

Many structures operate in high-temperature environment and must be able to withstand complex mechanical loadings over a long period of time. Examples include components of power plants, chemical refineries, heat engines and microelectronics. Design procedures and residual life assessments for pipework systems, rotors, turbine blades, etc., are required to take inelastic deformation, creep and fatigue damage processes into account. The aim of "Mechanics of High-Temperature Materials" is the development of theoretical and experimental methods to analyze time-dependent changes of stress and strain states in engineering structures up to the critical stage of rupture.

During the last decades, many advances and new results in the field of high-temperature materials behavior were presented in conference proceedings and scientific papers. Examples include: the development and analysis of new alloys for (ultra)high-temperature applications; interlinks of mechanics with materials science in multi-scale analysis of deformation and damage mechanisms over a wide range of stresses and temperature; the development and calibration of advanced constitutive models for the analysis of inelastic behavior under transient loading conditions; the development of procedures for a stable identification of material parameters in advanced constitutive equations; the introduction of gradient-enhanced state variables to account localized deformation and damage processes; the development and verification of material subroutines for the use in general-purpose finite element codes; the application of the finite element method to the inelastic analysis of engineering structures under complex thermo-mechanical loading profiles; and application of new experimental methods, such as digital image correlation, for analysis of inelastic deformation under multi-axial stress state.

This volume of the *Advanced Structured Materials* Series contains a collection of contributions on advanced approaches of mechanics of high-temperature materials. Most of them were presented in the Session on High-Temperature Materials and Structures at the 28th International Workshop on Computational Mechanics of Materials (IWCMM) in Glasgow, UK, September 10–12, 2018. We thank Conference Chairs Dr. Selda Oterkus, Dr. Erkan Oterkus and Prof. Siegfried Schmauder for inviting us to organize this session and for a big support during the workshop.

We would like to acknowledge Series Editors Profs. Holm Altenbach and Andreas Öchsner for giving us the opportunity to publish this volume. We would like to acknowledge Dr. Christoph Baumann from Springer Publisher for the assistance and support during the preparation of this book.

Magdeburg, Germany Konstantin Naumenko
Jülich, Germany Manja Krüger
May 2019

Contents

Analysis of a Power Plant Rotor Made of Tempered Martensitic Steel Based on a Composite Model of Inelastic Deformation

Johanna Eisenträger, Konstantin Naumenko, Yevgen Kostenko and Holm Altenbach

Abstract Power plant components are subjected to high temperatures up to 903 K, which induce creep deformations. Furthermore, power plants are frequently started and shut-down, thus resulting in cyclic loads on the components. Since they provide adequate mechanical and thermal properties, tempered martensitic steels are ideal candidates to withstand these conditions. The contribution at hand presents a phase mixture model for simulating the mechanical behavior of tempered martensitic steels at high temperatures. To provide a unified description of the rate-dependent deformation including hardening and softening, the model makes use of an iso-strain approach including a hard and a soft constituent. The model is implemented into the finite element method, using the implicit Euler method for time integration of the evolution equations. In addition, the consistent tangent operator is derived. As a final step, the behavior of an idealized steam turbine rotor during a cold start and a subsequent hot start is simulated by means of a thermo-mechanical finite element analysis. First, the heat transfer analysis is conducted, while prescribing the instationary steam temperature and the heat transfer coefficients. The resulting temperature fields serve as input for the subsequent structural analysis, which yields the stress and strain fields in the rotor.

J. Eisenträger (✉) · K. Naumenko · H. Altenbach
Otto von Guericke University Magdeburg, Universitätsplatz 2,
39106 Magdeburg, Germany
e-mail: johanna.eisentraeger@ovgu.de

K. Naumenko
e-mail: konstantin.naumenko@ovgu.de

H. Altenbach ·
e-mail: holm.altenbach@ovgu.de

Y. Kostenko
Siemens AG, Power and Gas Division, Rheinstr. 100,
45478 Mülheim an der Ruhr, Germany
e-mail: yevgen.kostenko@siemens.com

K. Naumenko and M. Krüger (eds.), *Advances in Mechanics of High-Temperature Materials*, Advanced Structured Materials 117,
https://doi.org/10.1007/978-3-030-23869-8_1

1 Introduction

In service, power plant components are subjected to challenging conditions, such as high temperatures and intermittent loads. Steam temperatures should be as high as possible to increase the efficiency of power plants, such that temperatures up to 903 K are common [1–4]. In addition, frequent start-ups and shut-downs induce cyclic loads, which is due to the increasing popularity of renewable energy sources such as solar and wind energies. Since this type of energy production strongly depends on the ambient conditions, conventional power plants are started and shut-down in order to compensate gaps or surpluses in energy production. These cyclic loads feature long holding times (typically several hours up to one month) [3, 5–8], as depicted schematically in Fig. 1.

Tempered martensitic steels with high chromium content (9–12%) are commonly used materials for power plant components [9–13], cf. Fig. 1. Due to their outstanding thermo-mechanical properties, such as high tensile and creep strength, a low coefficient of thermal expansion, and high corrosion resistance [5, 11, 13–17], tempered martensitic steels are ideal candidates for operations in power plants. The contribution at hand presents a constitutive model, which is calibrated with material tests on the alloy X20CrMoV12-1, a typical representative of tempered martensitic steels. From the 1950s, this steel has been utilized for forged components of turbine shafts for high-pressure applications as well as tubes and pressure vessels [18].

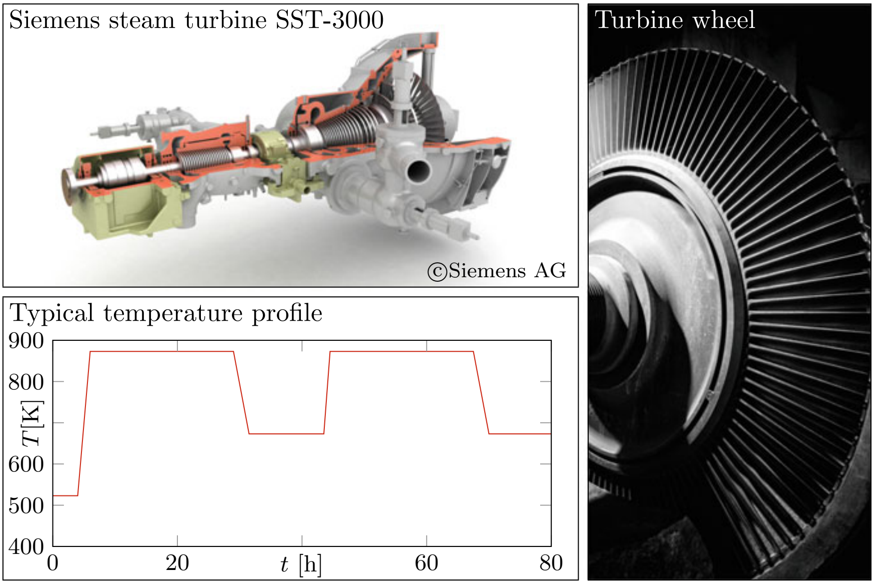

Fig. 1 Power plant components and a typical temperature profile with day–night cycles, cf. [19]. Picture of turbine wheel according to [20]

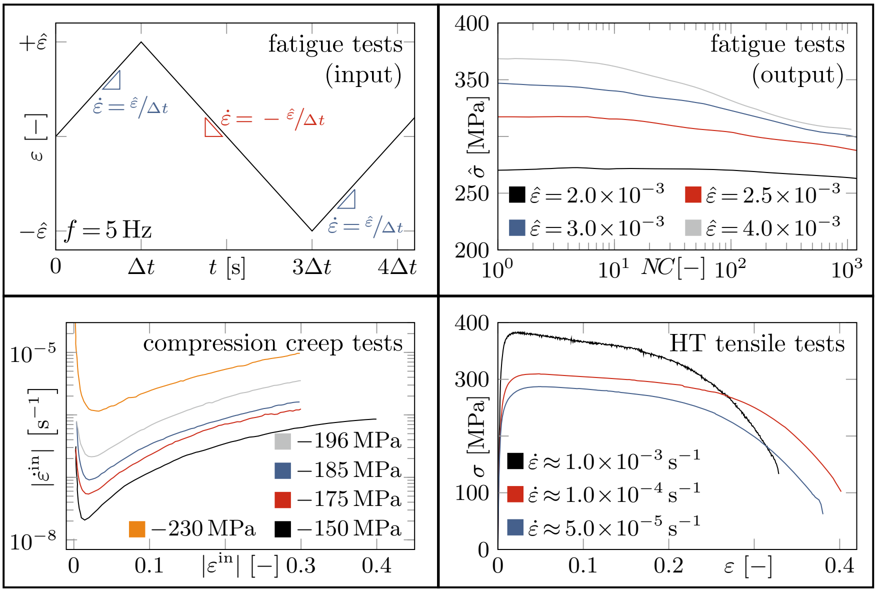

Fig. 2 Material tests on X20CrMoV12-1 at 873 K. Strain ε versus time t for one cycle during fatigue tests with prescribed strain amplitudes $\hat{\varepsilon}$ (top left), stress amplitude $\hat{\sigma}$ versus number of cycles NC as result of fatigue tests [8] (top right), absolute inelastic strain rate $|\dot{\varepsilon}^{\mathrm{in}}|$ versus absolute inelastic strain $|\varepsilon^{\mathrm{in}}|$ for creep tests under constant compressive stress σ [9] (bottom left), stress σ versus strain ε for high temperature (HT) tensile tests at constant strain rates $\dot{\varepsilon}$ (bottom right), cf. [19, 21]

Nevertheless, tempered martensitic steels suffer from softening under creep and fatigue loads [3, 6–10, 22–25]. Under creep conditions, the softening effect results in an increase of the strain rate with time and deformation [26], as it can be observed in the bottom left diagram of Fig. 2, where the results of creep tests under constant compressive stress levels are presented. It has been found that softening is based on the coarsening of microstructural elements, such as subgrains and carbides [9, 22–24]. This softening effect occurs also under cyclic loads [8], as it is shown in the top diagrams of Fig. 2. Here, the input and the results of strain-controlled fatigue tests at 873 K are presented. Note that the total strain ε is prescribed as a triangular function of time with a frequency of $f = 5$ Hz. The top right diagram depicts the stress amplitude $\hat{\sigma}$ with respect to the number of cycles NC for different prescribed amplitudes of total strain $\hat{\varepsilon}$. It becomes obvious that the stress amplitude reduces over time, which is due to cyclic softening [8]. Several papers confirm the cyclic softening effect for tempered martensitic steels, and this phenomenon is attributed to the coarsening of subgrains [3, 6, 7, 10, 25, 27]. In addition, softening can also be observed during high temperature (HT) tensile tests [14–16, 28]. At elevated temperatures and low strain rates, the stress decreases steadily as the strain increases, as it is also shown in the bottom right diagram of Fig. 2, where stress-strain curves are shown for HT tensile tests under constant strain rates and temperature. According to [14], this effect is based on the annihilation of subgrain boundaries and mobile dislocations.

During the last years, several models have been developed to simulate the mechanical behavior of tempered martensitic steels and to account for the softening effect. In general, these approaches can be divided into two categories: macromechanical and micromechanical approaches. The first category provides a macroscopic description of the mechanical behavior. Usually, the results of classical tests, such as HT tensile, creep, or fatigue tests, are required for the calibration. Based on the definition of strains, these models are classified into unified and nonunified approaches. Unified models introduce only one time-dependent inelastic strain [29], whereas nonunified models define separate variables for instantaneous plastic strains and time-dependent inelastic deformation. Typical examples of nonunified viscoplastic models for tempered martensitic steels are presented in [30–33]. Often, as for example in [30], the Chaboche model with several backstresses is used to model nonlinear kinematic hardening. One of the first attempts to account for this phenomenon goes back to the backstress concept introduced by Armstrong and Frederick [34]. Afterwards, Chaboche suggested to superpose several Armstrong–Frederick-type backstresses to obtain a more accurate description of the cyclic behavior [35].

However, nonunified models exhibit several drawbacks, such as a vague definition of “instantaneous” strains, numerical difficulties while implementing different flow rules for instantaneous plastic strains and time-dependent inelastic strains, and the disregard of interactions between instantaneous plasticity and time-dependent creep [29]. As an alternative, unified models have been suggested to model rate-dependent inelasticity in combination with nonlinear kinematic hardening of Chaboche type, e.g. [36–42]. These contributions often employ the Chaboche model in conjunction with several backstresses, which results in a large number of parameters, i.e. usually more than 10 temperature-dependent material parameters. One should bear in mind that during the calibration, additional parameters need to be determined in order to account for the temperature dependence of the primary parameters such that the actual number of required material parameters is at least twice as much. Consequently, making use of the Chaboche model with several backstresses increases the number of parameters, especially if wide temperature ranges should be taken into account. Additionally, physical interpretations should be provided for all quantities, which is a difficult task, if several backstresses have been introduced.

Contrarily to the macromechanical approaches, micromechanical models make use of parameters which are explicitly related to microstructural properties, e.g. grain sizes or dislocation densities [31]. Several models for tempered martensitic steels incorporating microstructural quantities like subgrain widths or dislocation densities are available in literature [10, 28, 43–47]. Note that the calibration of these models is usually a complex procedure because it is based on microscopic observations.

Furthermore, material scientists have established so-called phase mixture models [9, 18, 48]. In their original formulations, these models are related to the microstructure since hardening and softening effects are incorporated based on an iso-strain composite [49] with soft and hard constituents [9, 18]. The alloy under considera-

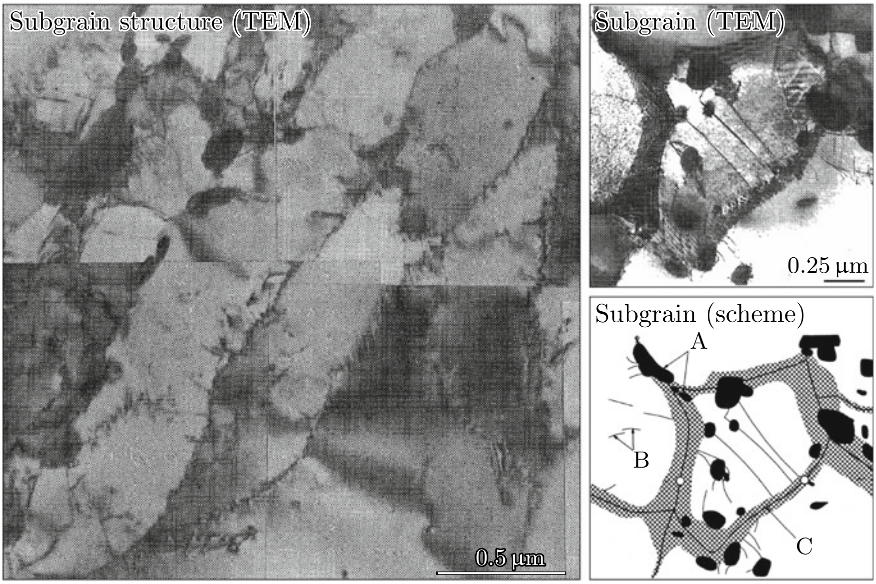

Fig. 3 Microstructure of martensitic steels (A carbides, B dislocations, C boundary), cf. [9, 18]

tion is assumed to consist of soft subgrains separated from each other by relatively hard boundaries [26]. Note that the volume fraction of the hard constituent is related to microstructural quantities such as the mean subgrain size. In order to account for softening based on the coarsening of subgrains, the volume fraction of the hard constituent is assumed to decrease towards a saturation value [50]. Usually, results from microstructural observations are required to calibrate this class of constitutive models [9, 18, 48], cf. Fig. 3.

Nevertheless, using microscopy such as transmission electron microscopy (TEM) or scanning electron microscopy (SEM) to calibrate micromechanical models often demands for significant effort, time, and financial resources. On the other hand, material tests like creep or HT tensile tests are straightforward and less time-consuming to conduct. Because of this, Naumenko et al. transform a micromechanical phase mixture model into a macroscopic mixture model and introduce a softening variable and a backstress of Armstrong–Frederick-type as internal variables [50, 51]. Furthermore, the model is calibrated with respect to a relatively narrow temperature range ($773\,\mathrm{K} \leq T \leq 873\,\mathrm{K}$). The simulation of a creep test with intermittent loads reveals the good performance of the model although only 11 material parameters (of which only 2 are temperature-dependent) are required.

To sum up, the introduced phase mixture model exhibits two principal benefits compared to other approaches. Firstly, a small number of material parameters is involved since only two internal variables—a backstress and a softening variable—are introduced. Secondly, macroscopic tests are used for the calibration of the model such that time-consuming microscopy is not required for parameter identification.

Therefore, the contribution at hand uses the phase mixture model to describe the mechanical behavior of the tempered martensitic steel X20CrMoV12-1, which provides the basis for the analysis of power plant components. Based on the well-known alloy X20CrMoV12-1, which has been examined in detail such that an elaborated experimental database is available, the applicability and performance of the phase mixture model are demonstrated. The extension of the presented approach to newly developed alloys is straightforward.

In the following, let us outline the structure of the contribution at hand. Section 2 presents the governing equations of the phase mixture model. In a first step, this is done in close connection to the microstructure of the material, and in a second step, the model is referred to the macroscale by introduction of internal variables. Since the overall aim of this contribution is the analysis of power plant components with complex geometries under realistic boundary conditions, the constitutive model is implemented into the finite element method, which is based on implicit time integration. Therefore, Sect. 3 provides a description of the stress update algorithm as well as the derivation of the consistent tangent operator. Finally, the thermo-mechanical finite element analysis of a steam turbine rotor is presented in Sect. 4. The first part of the section discusses the heat transfer analysis, where the steam temperature and heat transfer coefficients serve as input. Afterwards, the second part presents the results of the structural analysis with the phase mixture model, whereas the instationary temperature field is provided as input. Note that the analysis accounts for the influence of the different starting procedures. The final section of this contribution gives a brief summary, and areas for further research are identified, cf. Sect. 5.

2 Phase Mixture Model

This section presents the governing equations for the phase mixture model, which serves as basis for simulating the mechanical behavior of the tempered martensitic steel X20CrMoV12-1. In a first step, the microscopic model is introduced, cf. Sect. 2.1. Next, the microscopic approach is transformed into a macroscopic model by introduction of internal variables, cf. Sect. 2.2.

2.1 Microscopic Model

Within the microscopic phase mixture model, the material is represented by a mixture, composed of two distinct constituents. We presume that the constituents exhibit an identical elastic behavior, whereas their inelastic behavior differs. Note that the identical elastic behavior of the constituents is a significant, but realistic assumption, which substantially simplifies the governing equations [52]. In order to distinguish both constituents with respect to their inelastic behavior, one should actually make

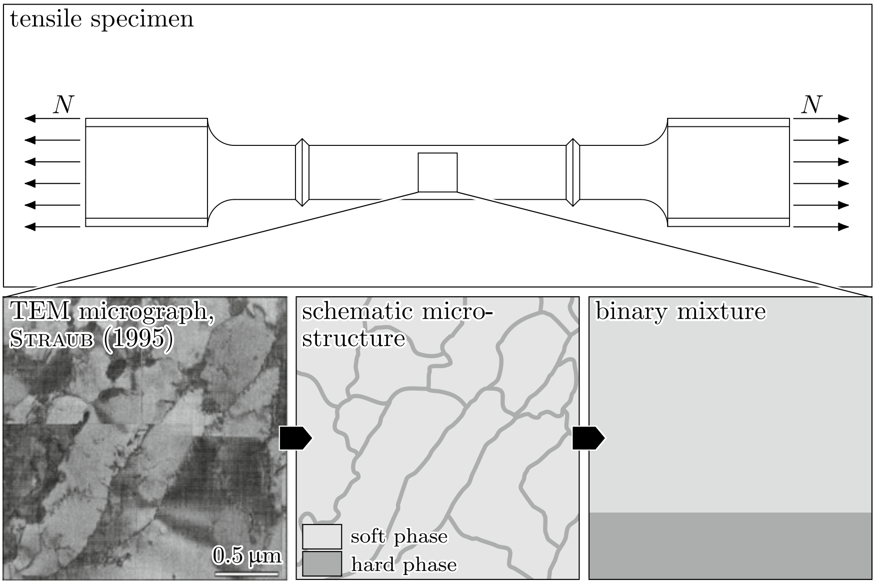

Fig. 4 Representation of the microstructure by means of the binary phase mixture model, cf. [19]

use of the terms “inelastic-soft” and “inelastic-hard”. Nevertheless, in the following, we only utilize the terms “soft” and “hard” to refer to both constituents; usually we will indicate this by employing the index $\square_k \forall\, k \in \{\mathrm{s}, \mathrm{h}\}$. The following derivation of the governing equations is based on [19, 50, 53], where further information can be found. Note that the hard phase refers to the subgrain or grain boundaries, i.e. regions with a high dislocation density and a large number of carbides, while the soft phase is related to the subgrain interior, i.e. regions with a low dislocation density and a small number of carbides. Figure 4 illustrates this division of the real microstructure into the two phases.

Since the model will be used to simulate the mechanical behavior of real power plant components, we only consider geometrically linear processes. This restriction reduces the computational effort significantly compared to geometrically nonlinear models. Nevertheless, if the model is used for large-strain applications, alternative approaches to model rate-dependent inelasticity with kinematic hardening and softening are available in literature, e.g. [54, 55].

Because of the limitation to geometrically linear processes, the linear strain tensor $\boldsymbol{\varepsilon}$ is used in the remainder of the current treatise. Applying the iso-strain assumption, we assume equal strain states in both constituents:

$$\boldsymbol{\varepsilon} = \boldsymbol{\varepsilon}_{\mathrm{h}} = \boldsymbol{\varepsilon}_{\mathrm{s}} \tag{1}$$

with the strain tensor $\boldsymbol{\varepsilon}$. Within the framework of the applied unified description of the material behavior, the inelastic strain tensor $\boldsymbol{\varepsilon}_k^{\mathrm{in}}$ comprises both instantaneous plastic strains and time-dependent creep strains [29]. The strains are splitted additively into elastic and inelastic parts, which are marked with the superscripts $\square^{\mathrm{el}}$ and $\square^{\mathrm{in}}$, respectively:

$$\boldsymbol{\varepsilon} = \boldsymbol{\varepsilon}_k^{\mathrm{el}} + \boldsymbol{\varepsilon}_k^{\mathrm{in}}. \tag{2}$$

Hooke's law is applied to describe the identical linear elastic behavior of both constituents:

$$\boldsymbol{\varepsilon}_k^{\mathrm{el}} = \frac{\sigma_{\mathrm{m}_k}}{3K}\boldsymbol{I} + \frac{\boldsymbol{\sigma}'_k}{2G} \tag{3}$$

or:

$$\boldsymbol{\sigma}_k = K\varepsilon_{\mathrm{V}_k}^{\mathrm{el}}\boldsymbol{I} + 2G\boldsymbol{\varepsilon}_k^{\mathrm{el}'} \tag{4}$$

with the stress tensor $\boldsymbol{\sigma}$, the bulk modulus K, and the shear modulus G. Note that the volumetric strain $\varepsilon_{\mathrm{V}} = \mathrm{tr}\,(\boldsymbol{\varepsilon})$ is determined as the trace of the strain tensor, and $\sigma_{\mathrm{m}} = \frac{1}{3}\mathrm{tr}\,(\boldsymbol{\sigma})$ is the mean stress. The prime $\square' = \square - \frac{1}{3}\mathrm{tr}\,(\square)\,\boldsymbol{I}$ represents the deviatoric part of a second-order tensor, and $\boldsymbol{I} = \boldsymbol{e}_i \otimes \boldsymbol{e}_i$ is the second-order identity tensor.

A mixture rule is applied to compute the overall stress $\boldsymbol{\sigma}$ based on the stress tensors of the individual constituents:

$$\boldsymbol{\sigma} = \eta_{\mathrm{s}}\boldsymbol{\sigma}_{\mathrm{s}} + \eta_{\mathrm{h}}\boldsymbol{\sigma}_{\mathrm{h}}, \tag{5}$$

while the following restriction holds for the volume fractions η_k of the constituents:

$$\eta_{\mathrm{s}} + \eta_{\mathrm{h}} = 1 \qquad \forall\, 0 \leq \eta_k \leq 1. \tag{6}$$

After applying the trace operator to Eqs. (1), (2), and (3), one obtains:

$$\varepsilon_{\mathrm{V}} = \varepsilon_{\mathrm{V}_{\mathrm{h}}} = \varepsilon_{\mathrm{V}_{\mathrm{s}}}, \tag{7}$$

$$\varepsilon_{\mathrm{V}} = \varepsilon_{\mathrm{V}_k}^{\mathrm{el}} + \varepsilon_{\mathrm{V}_k}^{\mathrm{in}}, \tag{8}$$

$$\varepsilon_{\mathrm{V}_k}^{\mathrm{el}} = \frac{\sigma_{\mathrm{m}_k}}{K}. \tag{9}$$

Within the framework of classical plasticity, one presumes that the inelastic strains are not influenced by the spherical part of the stress tensor, i.e. $\varepsilon_{\mathrm{V}_k}^{\mathrm{in}} = 0 \Rightarrow \boldsymbol{\varepsilon}_k^{\mathrm{in}} = \boldsymbol{\varepsilon}_k^{\mathrm{in}'}$. Taking this assumption into account and inserting Eqs. (8) and (9) into Eq. (7) yield:

$$\sigma_{\mathrm{m}} = \sigma_{\mathrm{m}_{\mathrm{h}}} = \sigma_{\mathrm{m}_{\mathrm{s}}} = K\varepsilon_{\mathrm{V}}. \tag{10}$$

Because of identical elastic properties of both constituents, the mean stresses do not differ in the whole mixture such that Eqs. (1) and (5) can be applied to the deviatoric parts of the tensors only:

$$\boldsymbol{\varepsilon}' = \boldsymbol{\varepsilon}'_{\mathrm{h}} = \boldsymbol{\varepsilon}'_{\mathrm{s}}, \tag{11}$$

$$\boldsymbol{\sigma}' = \eta_{\mathrm{s}} \boldsymbol{\sigma}'_{\mathrm{s}} + \eta_{\mathrm{h}} \boldsymbol{\sigma}'_{\mathrm{h}}. \tag{12}$$

In order to formulate constitutive equations for the entire mixture, we transform Eq. (3) such that the deviatoric stresses $\boldsymbol{\sigma}'_k$ for the constituents can be determined. The resulting expressions are inserted into Eq. (12), which yields the constitutive law for the mixture after some transformations:

$$\boldsymbol{\varepsilon} = \frac{\sigma_{\mathrm{m}}}{3K} \boldsymbol{I} + \frac{\boldsymbol{\sigma}'}{2G} + \boldsymbol{\varepsilon}^{\mathrm{in}}, \tag{13}$$

where $\boldsymbol{\varepsilon}^{\mathrm{in}}$ denotes the inelastic strain of the mixture:

$$\boldsymbol{\varepsilon}^{\mathrm{in}} = (1 - \eta_{\mathrm{h}})\, \boldsymbol{\varepsilon}^{\mathrm{in}}_{\mathrm{s}} + \eta_{\mathrm{h}} \boldsymbol{\varepsilon}^{\mathrm{in}}_{\mathrm{h}}. \tag{14}$$

In the following, we specify evolution equations for the inelastic strain rates $\dot{\boldsymbol{\varepsilon}}^{\mathrm{in}}_k$ based on the suggestions in [50, 56]:

$$\dot{\boldsymbol{\varepsilon}}^{\mathrm{in}}_{\mathrm{s}} = \frac{3}{2} \dot{\varepsilon}^{\mathrm{in}}_{\mathrm{vM_s}} \frac{\boldsymbol{\sigma}'_{\mathrm{s}}}{\sigma_{\mathrm{vM_s}}}, \tag{15}$$

$$\dot{\boldsymbol{\varepsilon}}^{\mathrm{in}}_{\mathrm{h}} = \frac{3}{2} \dot{\varepsilon}^{\mathrm{in}}_{\mathrm{vM}} \frac{\boldsymbol{\sigma}'_{\mathrm{h}} - \boldsymbol{\sigma}'}{\sigma_{\mathrm{vM_\star}}} \tag{16}$$

with the von Mises equivalent inelastic strain rate in the soft constituent $\dot{\varepsilon}^{\mathrm{in}}_{\mathrm{vM_s}}$ and in the mixture $\dot{\varepsilon}^{\mathrm{in}}_{\mathrm{vM}}$ as well as the von Mises equivalent stress in the soft constituent $\sigma_{\mathrm{vM_s}}$ and the von Mises equivalent saturation stress $\sigma_{\mathrm{vM_\star}}$:

$$\dot{\varepsilon}^{\mathrm{in}}_{\mathrm{vM_s}} = \sqrt{\frac{2}{3} \dot{\boldsymbol{\varepsilon}}^{\mathrm{in}}_{\mathrm{s}} : \dot{\boldsymbol{\varepsilon}}^{\mathrm{in}}_{\mathrm{s}}}, \tag{17}$$

$$\dot{\varepsilon}^{\mathrm{in}}_{\mathrm{vM}} = \sqrt{\frac{2}{3} \dot{\boldsymbol{\varepsilon}}^{\mathrm{in}} : \dot{\boldsymbol{\varepsilon}}^{\mathrm{in}}}, \tag{18}$$

$$\sigma_{\mathrm{vM_s}} = \sqrt{\frac{3}{2} \boldsymbol{\sigma}'_{\mathrm{s}} : \boldsymbol{\sigma}'_{\mathrm{s}}}, \tag{19}$$

$$\sigma_{\mathrm{vM_\star}} = \sqrt{\frac{3}{2} \left(\boldsymbol{\sigma}'_{\mathrm{h_\star}} - \boldsymbol{\sigma}'\right) : \left(\boldsymbol{\sigma}'_{\mathrm{h_\star}} - \boldsymbol{\sigma}'\right)}. \tag{20}$$

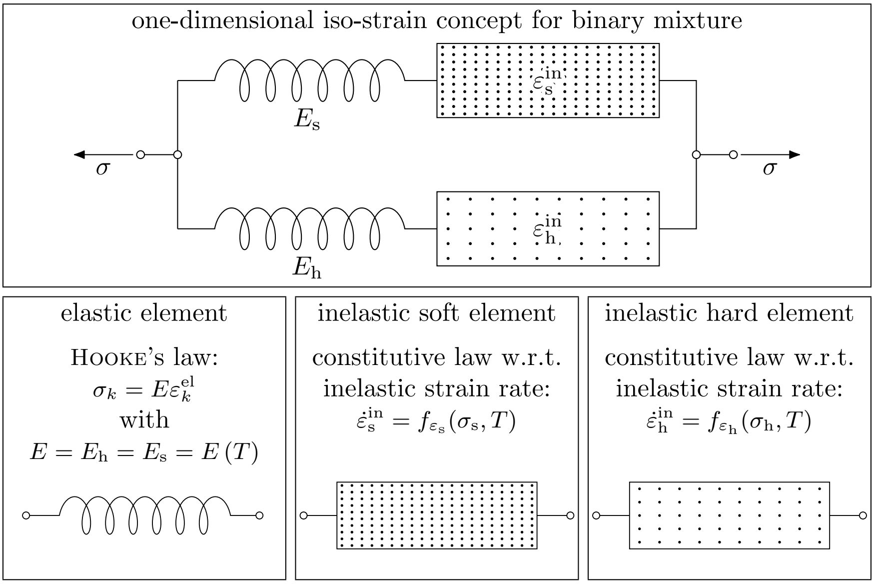

Fig. 5 Iso-strain concept for binary mixture with constant volume fractions of constituents, cf. [21]

The tensor $\boldsymbol{\sigma}'_{h_\star}$ represents the saturation stress deviator of the hard constituent. We make use of the following evolution equation for the equivalent inelastic strain rate in the soft constituent $\dot{\varepsilon}^{in}_{vM_s}$:

$$\dot{\varepsilon}^{in}_{vM_s} = f_\sigma\left(\sigma_{vM_s}\right) f_T(T)\,. \tag{21}$$

Additionally, an evolution equation for the volume fraction of one constituent should be formulated, cf. Eq. (6):

$$\dot{\eta}_h = f_\eta\left(\boldsymbol{\sigma}_h, \dot{\boldsymbol{\varepsilon}}^{in}_h, T\right). \tag{22}$$

The one-dimensional phase mixture model is illustrated in Fig. 5, whereas the volume fractions of the constituents are assumed as constant.

2.2 Macroscopic Model

The model presented in the previous section is closely connected to microstructural processes such that results from microscopic observations would be required for the calibration. But since in this case only results from macroscopic tests, such as HT tensile tests or creep tests, are available, the model is referred to the macroscale by introducing two internal variables: the backstress $\boldsymbol{\beta}$ and the softening variable Γ.

The following definitions hold for the backstress tensor $\boldsymbol{\beta}$ and the corresponding equivalent von Mises variable β_{vM}:

$$\boldsymbol{\beta} = \frac{\eta_{\mathrm{h}_0}}{1-\eta_{\mathrm{h}_0}}\left(\boldsymbol{\sigma}'_{\mathrm{h}} - \boldsymbol{\sigma}'\right) \qquad \forall \quad 0 < \eta_{\mathrm{h}_0} < 1, \tag{23}$$

$$\beta_{\mathrm{vM}} = \sqrt{\frac{3}{2}\boldsymbol{\beta} : \boldsymbol{\beta}} \forall \quad 0 \le \beta_{\mathrm{vM}} \le \beta_{\mathrm{vM}_\star} \tag{24}$$

with the saturation values:

$$\boldsymbol{\beta}_\star = \frac{\eta_{\mathrm{h}_0}}{1-\eta_{\mathrm{h}_0}}\left(\boldsymbol{\sigma}'_{\mathrm{h}_\star} - \boldsymbol{\sigma}'\right), \tag{25}$$

$$\beta_{\mathrm{vM}_\star} = \sqrt{\frac{3}{2}\boldsymbol{\beta}_\star : \boldsymbol{\beta}_\star}. \tag{26}$$

The variable $\eta_{\mathrm{h}_0} = \eta_{\mathrm{h}}\,(t=0)$ denotes the volume fraction of the hard constituent in initial state. Furthermore, the tensor $\boldsymbol{\beta}$ can be interpreted as a backstress similar to the backstress introduced by Armstrong and Frederick [34], which is shown in [50]. In addition, we define the softening variable Γ and the corresponding saturation value $\Gamma_\star$ based on the volume fractions of the hard constituent:

$$\Gamma = \frac{\eta_{\mathrm{h}}}{1-\eta_{\mathrm{h}}}\frac{1-\eta_{\mathrm{h}_0}}{\eta_{\mathrm{h}_0}} \qquad \forall \quad \Gamma_\star \le \Gamma \le 1, \tag{27}$$

$$\Gamma_\star = \frac{\eta_{\mathrm{h}\star}}{1-\eta_{\mathrm{h}\star}}\frac{1-\eta_{\mathrm{h}_0}}{\eta_{\mathrm{h}_0}} \qquad \forall \quad 0 < \eta_{\mathrm{h}\star} < 1. \tag{28}$$

Note that the parameter $\eta_{\mathrm{h}\star}$ represents the saturation value for the volume fraction of the hard constituent. In order to obtain expressions for the stresses and inelastic strain rates of the constituents based on the new internal variables, we make use of the definitions (23)–(28), Eqs. (12), (15), (16), and (21):

$$\boldsymbol{\sigma}'_{\mathrm{h}} = \boldsymbol{\sigma}' + \frac{1-\eta_{\mathrm{h}_0}}{\eta_{\mathrm{h}_0}}\boldsymbol{\beta}, \tag{29}$$

$$\boldsymbol{\sigma}'_{\mathrm{s}} = \tilde{\boldsymbol{\sigma}}', \tag{30}$$

$$\dot{\boldsymbol{\varepsilon}}^{\mathrm{in}}_{\mathrm{h}} = \frac{3}{2}\dot{\varepsilon}^{\mathrm{in}}_{\mathrm{vM}}\frac{\boldsymbol{\beta}}{\beta_{\mathrm{vM}_\star}}, \tag{31}$$

$$\dot{\boldsymbol{\varepsilon}}_{\mathrm{s}}^{\mathrm{in}} = \frac{3}{2} f_{\sigma}\left(\tilde{\sigma}_{\mathrm{vM}}\right) f_{T}\left(T\right) \frac{\tilde{\boldsymbol{\sigma}}'}{\tilde{\sigma}_{\mathrm{vM}}}, \tag{32}$$

whereas the effective stress $\tilde{\boldsymbol{\sigma}}'$ as well as the corresponding von Mises stress $\tilde{\sigma}_{\mathrm{vM}}$ are introduced:

$$\tilde{\boldsymbol{\sigma}}' = \boldsymbol{\sigma}' - \Gamma \boldsymbol{\beta}, \tag{33}$$

$$\tilde{\sigma}_{\mathrm{vM}} = \sqrt{\frac{3}{2} \tilde{\boldsymbol{\sigma}}' : \tilde{\boldsymbol{\sigma}}'}. \tag{34}$$

Next, Eq. (13) is differentiated with respect to the time t:

$$\dot{\boldsymbol{\varepsilon}}^{\mathrm{in}} = \dot{\boldsymbol{\varepsilon}} - \frac{\partial}{\partial t} \left(\frac{\sigma_{\mathrm{m}}}{3K} \boldsymbol{I} + \frac{\boldsymbol{\sigma}'}{2G} \right). \tag{35}$$

Equation (2) with respect to the individual constituents is processed similarly, while Eq. (3) is taken into account:

$$\dot{\boldsymbol{\varepsilon}} = \frac{\partial}{\partial t} \left(\frac{\sigma_{\mathrm{m}}}{3K} \boldsymbol{I} + \frac{\boldsymbol{\sigma}'_k}{2G} \right) + \dot{\boldsymbol{\varepsilon}}_k^{\mathrm{in}}. \tag{36}$$

We evaluate above equation with respect to the soft constituent and insert it into Eq. (35). Additionally, the stress deviator $\boldsymbol{\sigma}'_{\mathrm{s}}$ and the inelastic strain rate $\dot{\boldsymbol{\varepsilon}}_{\mathrm{s}}^{\mathrm{in}}$ are substituted based on Eqs. (30) and (32). Further transformations yield an evolution equation for the inelastic strain $\boldsymbol{\varepsilon}^{\mathrm{in}}$:

$$\dot{\boldsymbol{\varepsilon}}^{\mathrm{in}} = \frac{3}{2} f_{\sigma}\left(\tilde{\sigma}_{\mathrm{vM}}\right) f_{T}\left(T\right) \frac{\tilde{\boldsymbol{\sigma}}'}{\tilde{\sigma}_{\mathrm{vM}}} - \frac{\partial}{\partial t} \left(\frac{\Gamma \boldsymbol{\beta}}{2G} \right). \tag{37}$$

Since it is discussed in [50, 57] that the last term affects the inelastic strain rate only at the very beginning of inelastic deformation, this term is neglected in the remainder such that the evolution equation for the inelastic strain is simplified as follows:

$$\dot{\boldsymbol{\varepsilon}}^{\mathrm{in}} = \frac{3}{2} f_{\sigma}\left(\tilde{\sigma}_{\mathrm{vM}}\right) f_{T}\left(T\right) \frac{\tilde{\boldsymbol{\sigma}}'}{\tilde{\sigma}_{\mathrm{vM}}}. \tag{38}$$

In the following, a similar procedure is applied to the hard constituent: Equation (36) is formulated with respect to the hard constituent and inserted into Eq. (35). We replace the stress deviator $\boldsymbol{\sigma}'_{\mathrm{h}}$ and the inelastic strain rate $\dot{\boldsymbol{\varepsilon}}_{\mathrm{h}}^{\mathrm{in}}$ using Eqs. (29) and (31), such that one obtains an evolution equation for the backstress $\boldsymbol{\beta}$:

$$\dot{\boldsymbol{\beta}} = \frac{1}{G} \frac{\mathrm{d}G}{\mathrm{d}T} \dot{T} \boldsymbol{\beta} + 2G \frac{\eta_{\mathrm{h}_0}}{1 - \eta_{\mathrm{h}_0}} \left(\dot{\boldsymbol{\varepsilon}}^{\mathrm{in}} - \frac{3}{2} \dot{\varepsilon}_{\mathrm{vM}}^{\mathrm{in}} \frac{\boldsymbol{\beta}}{\beta_{\mathrm{vM}_{\star}}} \right). \tag{39}$$

Furthermore, we make use of the following evolution equation for the softening variable, since it is suggested in [50]:

$$\dot{\Gamma} = C_\Gamma \left[\Gamma_\star\left(\sigma_{\mathrm{vM}}\right) - \Gamma\right] \dot{\varepsilon}^{\mathrm{in}}_{\mathrm{vM}}. \tag{40}$$

The softening variable Γ replaces the volume fraction of the hard constituent, cf. Eq. (27), such that Eq. (40) describes the decrease of the softening variable towards its saturation value $\Gamma_\star$ with increasing inelastic deformation. Thus, softening based on the coarsening of subgrains can be accounted for. Note that the evolution equation is restricted to proportional loading. For highly nonproportional loading, one can resort to refined approaches, e.g. [58].

The calibration of the phase mixture model with respect to the alloy X20CrMoV12-1 is discussed extensively in [19, 57]. Based on this, the following stress and temperature response functions have been determined:

$$E\left(T\right) = C_1 + C_2 T^3, \tag{41}$$

$$G\left(T\right) = C_3 + C_4 T^3, \tag{42}$$

$$f_T\left(T\right) = \exp\left(-\frac{Q}{\mathrm{R}T}\right), \tag{43}$$

$$f_\sigma\left(\tilde{\sigma}_{\mathrm{vM}}\right) = a_\sigma \sinh\left(\frac{\tilde{\sigma}_{\mathrm{vM}}}{b_\sigma}\right)\left[1 + \left(\frac{\tilde{\sigma}_{\mathrm{vM}}}{c_\sigma}\right)^{m_\sigma}\right], \tag{44}$$

$$\beta_{\mathrm{vM}_\star}\left(\sigma_{\mathrm{vM}}\right) = \frac{2a_\beta}{1 + \exp\left(-b_\beta \sigma_{\mathrm{vM}}\right)} - a_\beta, \tag{45}$$

$$\Gamma_\star\left(\sigma_{\mathrm{vM}}\right) = \frac{a_\Gamma}{1 + \exp\left[-b_\Gamma\left(\sigma_{\mathrm{vM}} - c_\Gamma\right)\right]} \tag{46}$$

with the Young's modulus E of the mixture. Note that the bulk modulus K can be easily determined based on the Young's modulus and the shear modulus:

$$K = \frac{GE}{3\left(3G - E\right)}. \tag{47}$$

All constants and identified parameters are listed in Table 1. The applicability and precision of the calibrated phase mixture model have been carefully examined based on experimental results for HT tensile and creep tests, cf. [19, 57]. It was found that the model adequately described rate-dependent inelasticity, hardening, and softening over large temperature and stress ranges, i.e. $673\,\mathrm{K} \le T \le 923\,\mathrm{K}$ and $100\,\mathrm{MPa} \le \sigma_{\mathrm{vM}} \le 700\,\mathrm{MPa}$, whereas the calibration is restricted to relatively high strain rates $\dot{\varepsilon}_{\mathrm{vM}} \ge 10^{-7}\,\mathrm{s}^{-1}$. To sum up, the presented approach is based on five governing equations:

- Hooke's law for linear isotropic elastic behavior of the mixture

$$\boldsymbol{\sigma} = K \varepsilon^{\mathrm{el}}_{\mathrm{V}} \boldsymbol{I} + 2G \boldsymbol{\varepsilon}^{\mathrm{el}'}, \tag{48}$$

Table 1 Used constants and identified material parameters for the phase mixture model, cf. [57]

Variable	Value	Unit	Meaning	Equation
C_1 C_2	2.23×10^{5} -1.64×10^{-4}	MPa MPa K^{-3}	Parameters in the temperature response function for the Young's modulus	(41)
C_3 C_4	82.6×10^{3} -2.87×10^{-5}	MPa MPa K^{-3}	Parameters in the temperature response function for the shear modulus	(42)
Q	540.6×10^{3}	J mol^{-1}	Activation energy in the temperature response functions for the inelastic strain rate	(43)
R	8.317	J (mol K)$^{-1}$	Universal gas constant in the temperature response functions for the inelastic strain rate	(43)
a_σ b_σ c_σ m_σ	1.54×10^{24} 25.8 483.6 35.7	s^{-1} MPa MPa –	Parameters in the stress response function for the inelastic strain rate	(44)
η_{h_0}	0.17	–	Reference value for the volume fraction of the hard constituent	(39)
a_β	80.0	MPa	Maximum value for the saturation backstress	(45)
b_β	2.70×10^{-2}	MPa^{-1}	Parameter in the evolution function for the saturation backstress	(45)
C_Γ	5.0	–	Parameter in the evolution equation for the softening variable	(40)
a_Γ b_Γ c_Γ	1.0 1.30×10^{-2} 520.0	– MPa^{-1} MPa	Parameters in the stress response function for the saturation softening variable	(46)

- the additive split of strains

$$\boldsymbol{\varepsilon} = \boldsymbol{\varepsilon}^{\mathrm{el}} + \boldsymbol{\varepsilon}^{\mathrm{in}}, \tag{49}$$

- the evolution equation for the inelastic strain, cf. Eq. (38),
- the evolution equation for the backstress, cf. Eq. (39),
- the evolution equation for the softening variable, cf. Eq. (40).

In addition, initial conditions (ICs) must be taken into account. For the simulation of the mechanical behavior of a virgin material, the following ICs hold:

$$\boldsymbol{\sigma}\,(t=0) = \mathbf{0}, \qquad \boldsymbol{\beta}\,(t=0) = \mathbf{0}, \qquad \Gamma\,(t=0) = 1. \tag{50}$$

3 Implementation into the Finite Element Method

Since this contribution aims at analyzing the mechanical behavior of real power plant components, the current section focuses on the implementation of the calibrated phase mixture model into the finite element method (FEM). For this purpose, Sect. 3.1 presents the stress update algorithm, in analogy to the derivations presented in [53]. Additionally, the derivation of the consistent tangent operator (CTO) is discussed in Sect. 3.2.

3.1 Stress Update Algorithm

As has been shown in Sect. 2.2, the phase mixture model requires the solution of three evolution equations with respect to the inelastic strain $\boldsymbol{\varepsilon}^{\text{in}}$, the backstress $\boldsymbol{\beta}$, and the softening variable Γ, cf. Eqs. (38)–(40). Usually, displacement increments are prescribed in finite element analyses, such that the strains are easily obtained based on the first derivatives of the displacements, whereas the stress and internal variables are determined based on the employed constitutive model. This process is often referred to as the stress update algorithm, cf. [59]. Thus, we formulate an evolution equation with respect to the stress $\boldsymbol{\sigma}$ by differentiating Eq. (13) once with respect to time and rearranging the resulting expression with respect to the time derivative of the stress tensor:

$$\dot{\boldsymbol{\sigma}} = K\dot{\varepsilon}_{\text{V}}\boldsymbol{I} + 2G\left(\dot{\boldsymbol{\varepsilon}} - \dot{\boldsymbol{\varepsilon}}^{\text{in}}\right) + \left(\frac{\mathrm{d}K}{\mathrm{d}T} + \frac{2}{3}\frac{\mathrm{d}G}{\mathrm{d}T}\right)\dot{T}\frac{\sigma_{\text{m}}}{K}\boldsymbol{I} + \frac{1}{G}\frac{\mathrm{d}G}{\mathrm{d}T}\dot{T}\boldsymbol{\sigma}'. \tag{51}$$

Note that the inelastic strain rate $\dot{\boldsymbol{\varepsilon}}^{\text{in}}$ is determined based on Eq. (38). The resulting system of evolution equations, i.e. Eqs. (39), (40), and (51) must be integrated with respect to time for prescribed displacement or strain increments, respectively. For this purpose, two general classes of numerical methods are available: explicit and implicit methods. Explicit methods determine an unknown equilibrium state at the time step t_{n+1} only by using quantities with respect to the previous time step t_n [60], such that these methods are straightforward to implement. Though explicit methods are only conditionally stable, i.e. their stability depends on the selected time step size [61]. Deploying the Courant–Friedrichs–Lewy condition, one can compute a critical time step size for an explicit time integration method [62].

As a remedy, one can make use of implicit methods. In this case, quantities with respect to a new equilibrium state t_{n+1} are computed not only based on the previous time steps, but also taking the current and future time steps into account. Therefore, a nonlinear system of equations must be solved at every time step [60]. Implicit methods feature unconditional stability, i.e. their stability is independent from the increment size. For these reasons, the backward Euler method as an implicit method is used in the contribution at hand for the numerical integration. Because of its straightforward formulation, this implicit method is commonly employed for the implementation of nonlinear material models, cf. for example [42, 63–65]. Suppose that one searches a solution for the ordinary differential equation $\dot{\boldsymbol{Z}} = \mathcal{F}(\boldsymbol{Z}, t)$ with respect to the unknown variable $\boldsymbol{Z}$. We prescribe the time increment Δt and assume that the variable $\boldsymbol{Z}_n$ at the time step t_n is known. Then, the backward Euler method approximates the solution at the time step $t_{n+1} = t_n + \Delta t$ in the following way [60]:

$$\boldsymbol{Z}_{n+1} = \boldsymbol{Z}_n + \Delta t\, \mathcal{F}(\boldsymbol{Z}_{n+1}, t_{n+1})\,. \tag{52}$$

Let us apply the approximation according to Eq. (52) to the governing equations of the phase mixture model. Assume that all quantities, i.e. the stress, the backstress, the softening variable, and the strains, are known with respect to an equilibrium state at the time step t_n. Next, temperature, strain, and time increments ΔT_{n+1}, $\Delta \boldsymbol{\varepsilon}_{n+1}$, and Δt_{n+1} are prescribed and all other quantities with respect to the unknown equilibrium state at the time step t_{n+1} must be computed. With the backward Euler method, the strains, the temperature, the stress, and the internal variables can be updated as follows [59]:

$$\Box_{n+1} = \Box_n + \Delta\, \Box_{n+1} \quad \forall \quad \Box = \left\{ \boldsymbol{\varepsilon}, \boldsymbol{\varepsilon}^{\mathrm{in}}, T, \boldsymbol{\sigma}, \boldsymbol{\beta}, \Gamma \right\}. \tag{53}$$

In the following, all variables refer to the time step $t_{\mathrm{n+1}}$, if not indicated otherwise. We apply the backward Euler method to the evolution Eqs. (38)–(40):

$$\Delta \boldsymbol{\varepsilon}^{\mathrm{in}}_{n+1} = \frac{3}{2} \Delta t f_\sigma\left(\tilde{\sigma}_{\mathrm{vM}}\right) f_T\left(T\right) \frac{\tilde{\boldsymbol{\sigma}}'}{\tilde{\sigma}_{\mathrm{vM}}}, \tag{54}$$

$$\Delta \boldsymbol{\beta}_{n+1} = \frac{1}{G} \frac{\mathrm{d}G}{\mathrm{d}T} \Delta T \boldsymbol{\beta} + 2G \frac{\eta_{\mathrm{h}_0}}{1 - \eta_{\mathrm{h}_0}} \left(\Delta \boldsymbol{\varepsilon}^{\mathrm{in}} - \frac{3}{2} \Delta \varepsilon^{\mathrm{in}}_{\mathrm{vM}} \frac{\boldsymbol{\beta}}{\beta_{\mathrm{vM}_\star}} \right), \tag{55}$$

$$\Delta \Gamma_{n+1} = C_\Gamma \left[\Gamma_\star \left(\sigma_{\mathrm{vM}}\right) - \Gamma \right] \Delta \varepsilon^{\mathrm{in}}_{\mathrm{vM}}. \tag{56}$$

In order to update the stress based on the strains and internal variables, we exploit Hooke's law and reformulate Eq. (48):

$$\boldsymbol{\sigma}_{n+1} = \boldsymbol{\mathcal{C}}_{n+1} : \boldsymbol{\varepsilon}^{\mathrm{el}}_{n+1} \tag{57}$$

with the elastic stiffness tensor $\boldsymbol{\mathcal{C}}$ and the fourth-order identity tensor:

$$\boldsymbol{\mathcal{C}} = \frac{1}{3} \left(3K - 2G\right) \boldsymbol{I} \otimes \boldsymbol{I} + 2G \boldsymbol{\mathcal{I}}, \tag{58}$$

$$\mathcal{I} = \frac{1}{2}\left(\boldsymbol{e}_i \otimes \boldsymbol{e}_j \otimes \boldsymbol{e}_j \otimes \boldsymbol{e}_i + \boldsymbol{e}_i \otimes \boldsymbol{e}_j \otimes \boldsymbol{e}_i \otimes \boldsymbol{e}_j\right). \tag{59}$$

Furthermore, one can replace the elastic strain in Eq. (57) based on the additive split of strains, cf. Eq. (49), considering Eq. (53):

$$\boldsymbol{\sigma}_{n+1} = \boldsymbol{\mathcal{C}}_{n+1} : \left(\boldsymbol{\varepsilon}_n + \Delta\boldsymbol{\varepsilon}_{n+1} - \boldsymbol{\varepsilon}_n^{\text{in}} - \Delta\boldsymbol{\varepsilon}_{n+1}^{\text{in}}\right). \tag{60}$$

To conclude, Eqs. (60) and (53)–(56) constitute a nonlinear system of equations which has to be solved. In order to implement the solution of this system of equations into a finite element code, we utilize matrix notation according to Voigt. Based on the introduced symmetric second-order tensors $\boldsymbol{\sigma} = \sigma_{ij}\boldsymbol{e}_i \otimes \boldsymbol{e}_j$, $\tilde{\boldsymbol{\sigma}} = \tilde{\sigma}_{ij}\boldsymbol{e}_i \otimes \boldsymbol{e}_j$, $\boldsymbol{\beta} = \beta_{ij}\boldsymbol{e}_i \otimes \boldsymbol{e}_j$, and $\boldsymbol{\varepsilon} = \varepsilon_{ij}\boldsymbol{e}_i \otimes \boldsymbol{e}_j$, the corresponding vectors $\mathbf{s}$, $\tilde{\mathbf{s}}$, $\mathbf{b}$, and $\mathbf{e}$ are defined as follows:

$$\mathbf{s} = \left[\sigma_{11}\ \sigma_{22}\ \sigma_{33}\ \sigma_{12}\ \sigma_{13}\ \sigma_{23}\right]^\top, \tag{61}$$

$$\tilde{\mathbf{s}} = \left[\tilde{\sigma}_{11}\ \tilde{\sigma}_{22}\ \tilde{\sigma}_{33}\ \tilde{\sigma}_{12}\ \tilde{\sigma}_{13}\ \tilde{\sigma}_{23}\right]^\top, \tag{62}$$

$$\mathbf{b} = \left[\beta_{11}\ \beta_{22}\ \beta_{33}\ \beta_{12}\ \beta_{13}\ \beta_{23}\right]^\top, \tag{63}$$

$$\mathbf{e} = \left[\varepsilon_{11}\ \varepsilon_{22}\ \varepsilon_{33}\ 2\varepsilon_{12}\ 2\varepsilon_{13}\ 2\varepsilon_{23}\right]^\top. \tag{64}$$

Note that the vectors of the deviatoric stresses, inelastic or elastic strains, and other incremental entities are formulated and labeled analogously. For the solution of the nonlinear system of equations using the Newton–Raphson method, we reformulate the system:

$$\mathbf{r}_\sigma^i = \mathbf{0}, \tag{65}$$

$$\mathbf{r}_\beta^i = \mathbf{0}, \tag{66}$$

$$r_\Gamma^i = 0 \tag{67}$$

with the residual quantities $\mathbf{r}_\sigma^i$, $\mathbf{r}_\beta^i$, and r_Γ^i

$$\mathbf{r}_\sigma^i = -\mathbf{e}_{n+1} + \mathbf{e}_n^{\text{in}} + \mathbf{C}_{n+1}^{-1}\mathbf{s}_{n+1}^i + \Delta\mathbf{e}_{n+1}^{\text{in}^i}, \tag{68}$$

$$\mathbf{r}_\beta^i = -\mathbf{b}_n + \mathbf{b}_{n+1}^i - \Delta\mathbf{b}_{n+1}^i, \tag{69}$$

$$r_\Gamma^i = -\Gamma_n + \Gamma_{n+1}^i - \Delta\Gamma_{n+1}^i \tag{70}$$

as well as the iteration index $\square^i$. Based on Eq. (58), the stiffness matrix $\mathbf{C}$ and its inverse $\mathbf{C}^{-1}$ are determined:

$$\mathbf{C} = \frac{1}{3}\begin{bmatrix} 3K+4G & 3K-2G & 3K-2G & 0 & 0 & 0 \\ 3K-2G & 3K+4G & 3K-2G & 0 & 0 & 0 \\ 3K-2G & 3K-2G & 3K+4G & 0 & 0 & 0 \\ 0 & 0 & 0 & 3G & 0 & 0 \\ 0 & 0 & 0 & 0 & 3G & 0 \\ 0 & 0 & 0 & 0 & 0 & 3G \end{bmatrix}, \tag{71}$$

$$\mathbf{C}^{-1} = \frac{1}{18KG}\begin{bmatrix} 2\,(3K+G) & 2G-3K & 2G-3K & 0 & 0 & 0 \\ 2G-3K & 2\,(3K+G) & 2G-3K & 0 & 0 & 0 \\ 2G-3K & 2G-3K & 2\,(3K+G) & 0 & 0 & 0 \\ 0 & 0 & 0 & 18K & 0 & 0 \\ 0 & 0 & 0 & 0 & 18K & 0 \\ 0 & 0 & 0 & 0 & 0 & 18K \end{bmatrix}. \tag{72}$$

Since we make use of the Newton–Raphson method, Eqs. (65)–(67) are linearized, cf. [60]:

$$\mathbf{A}^{i}_{n+1}\Delta\mathbf{p}^{i+1}_{n+1} = -\mathbf{r}^{i}_{n+1} \tag{73}$$

with the vector $\mathbf{p}^{i+1}_{n+1}$ and the residual vector $\mathbf{r}^{i}_{n+1}$:

$$\mathbf{p}^{i+1}_{n+1} = \left[\mathbf{s}^{i+1}_{n+1}\ \mathbf{b}^{i+1}_{n+1}\ \Gamma^{i+1}_{n+1}\right]^{\top}, \tag{74}$$

$$\mathbf{r}^{i}_{n+1} = \left[\mathbf{r}^{i}_{\sigma}\ \mathbf{r}^{i}_{\beta}\ r^{i}_{\Gamma}\right]^{\top}. \tag{75}$$

By solving Eq. (73), one obtains the vector of increments $\Delta\mathbf{p}^{i+1}_{n+1}$, such that the stress, the backstress, and softening variable are updated:

$$\mathbf{p}^{i+1}_{n+1} = \mathbf{p}^{i}_{n+1} + \Delta\mathbf{p}^{i+1}_{n+1}. \tag{76}$$

The derivatives of the residuals are summarized in the matrix $\mathbf{A}^{i}_{n+1}$:

$$\mathbf{A}^{i}_{n+1} = \begin{bmatrix} \dfrac{\partial\mathbf{r}^{i}_{\sigma}}{\partial\mathbf{s}} & \dfrac{\partial\mathbf{r}^{i}_{\sigma}}{\partial\mathbf{b}} & \dfrac{\partial\mathbf{r}^{i}_{\sigma}}{\partial\Gamma} \\ \dfrac{\partial\mathbf{r}^{i}_{\beta}}{\partial\mathbf{s}} & \dfrac{\partial\mathbf{r}^{i}_{\beta}}{\partial\mathbf{b}} & \dfrac{\partial\mathbf{r}^{i}_{\beta}}{\partial\Gamma} \\ \dfrac{\partial r^{i}_{\Gamma}}{\partial\mathbf{s}} & \dfrac{\partial r^{i}_{\Gamma}}{\partial\mathbf{b}} & \dfrac{\partial r^{i}_{\Gamma}}{\partial\Gamma} \end{bmatrix}. \tag{77}$$

We introduce the following abbreviations to shorten the expressions for the derivatives of the residuals:

$$c_1 = \frac{3}{2}\Delta t f_T\left(T\right), \quad c_2 = \frac{f_\sigma\left(\tilde{\sigma}_{\mathrm{vM}}\right)}{\tilde{\sigma}_{\mathrm{vM}}}, \quad c_3 = \frac{\partial f_\sigma\left(\tilde{\sigma}_{\mathrm{vM}}\right)}{\partial\tilde{\sigma}_{\mathrm{vM}}}, \tag{78}$$

$$c_4 = \tilde{\boldsymbol{\sigma}}' : \boldsymbol{\beta} = \tilde{\sigma}'_{ij}\,\beta_{ji}, \quad c_5 = \frac{\eta_{\mathrm{h}_0}}{1-\eta_{\mathrm{h}_0}}. \tag{79}$$

In addition, the auxiliary matrices $\mathbf{A}_1$ and $\mathbf{A}_2$ are defined:

$$\mathbf{A}_1 = \begin{bmatrix} 1&0&0&0&0&0\\ 0&1&0&0&0&0\\ 0&0&1&0&0&0\\ 0&0&0&1&0&0\\ 0&0&0&0&1&0\\ 0&0&0&0&0&1 \end{bmatrix}, \quad \mathbf{A}_2 = \begin{bmatrix} 1&1&1&0&0&0\\ 1&1&1&0&0&0\\ 1&1&1&0&0&0\\ 0&0&0&0&0&0\\ 0&0&0&0&0&0\\ 0&0&0&0&0&0 \end{bmatrix}. \tag{80}$$

Based on above abbreviations, one obtains the following expressions for the derivatives of the residuals:

$$\frac{\partial \mathbf{r}^i_\sigma}{\partial \mathbf{s}} = \mathbf{C}^{-1} + c_1\left[-\frac{3}{2}\frac{c_2-c_3}{\tilde{\sigma}^2_{\mathrm{vM}}}\tilde{\mathbf{s}}'\tilde{\mathbf{s}}'^\top + c_2\left(\mathbf{A}_1 - \frac{1}{3}\mathbf{A}_2\right)\right], \tag{81}$$

$$\frac{\partial \mathbf{r}^i_\sigma}{\partial \mathbf{b}} = c_1\left[\frac{3}{2}\left(c_2-c_3\right)\frac{\Gamma}{\tilde{\sigma}^2_{\mathrm{vM}}}\tilde{\mathbf{s}}'\tilde{\mathbf{s}}'^\top - c_2\Gamma\mathbf{A}_1\right], \tag{82}$$

$$\frac{\partial \mathbf{r}^i_\sigma}{\partial \Gamma} = c_1\left[\frac{3}{2}\frac{\left(c_2-c_3\right)c_4}{\tilde{\sigma}^2_{\mathrm{vM}}}\tilde{\mathbf{s}}' - c_2\mathbf{b}\right], \tag{83}$$

$$\begin{aligned}\frac{\partial \mathbf{r}^i_\beta}{\partial \mathbf{s}} = {}& 3Gc_1c_5\Bigg[\frac{c_2-c_3}{\tilde{\sigma}^2_{\mathrm{vM}}}\tilde{\mathbf{s}}'\tilde{\mathbf{s}}'^\top - \frac{2}{3}c_2\left(\mathbf{A}_1 - \frac{1}{3}\mathbf{A}_2\right) + \frac{c_3}{\tilde{\sigma}_{\mathrm{vM}}\,\beta_{\mathrm{vM}_\star}(\sigma_{\mathrm{vM}})}\tilde{\mathbf{s}}'\mathbf{b}^\top \\ & - \frac{f_\sigma\left(\tilde{\sigma}_{\mathrm{vM}}\right)}{\sigma_{\mathrm{vM}}\,\beta^2_{\mathrm{vM}_\star}(\sigma_{\mathrm{vM}})}\frac{\partial\beta_{\mathrm{vM}_\star}\left(\sigma_{\mathrm{vM}}\right)}{\partial\sigma_{\mathrm{vM}}}\mathbf{s}'\mathbf{b}^\top\Bigg],\end{aligned} \tag{84}$$

$$\begin{aligned}\frac{\partial \mathbf{r}^i_\beta}{\partial \mathbf{b}} = {}& \left[1 - \frac{1}{G}\frac{\mathrm{d}G}{\mathrm{d}T}\Delta T + 2Gc_1c_5\left(\frac{f_\sigma\left(\tilde{\sigma}_{\mathrm{vM}}\right)}{\beta_{\mathrm{vM}_\star}(\sigma_{\mathrm{vM}})} + c_2\Gamma\right)\right]\mathbf{A}_1 \\ & - 2Gc_1c_5\left[\frac{3}{2}\left(c_2-c_3\right)\frac{\Gamma}{\tilde{\sigma}^2_{\mathrm{vM}}}\tilde{\mathbf{s}}'\tilde{\mathbf{s}}'^\top + \frac{3}{2}\frac{c_3\Gamma}{\tilde{\sigma}_{\mathrm{vM}}\,\beta_{\mathrm{vM}_\star}(\sigma_{\mathrm{vM}})}\tilde{\mathbf{s}}'\mathbf{b}^\top\right],\end{aligned} \tag{85}$$

$$\frac{\partial \mathbf{r}^i_\beta}{\partial \Gamma} = -3Gc_1c_5\left[\frac{\left(c_2-c_3\right)c_4}{\tilde{\sigma}^2_{\mathrm{vM}}}\tilde{\mathbf{s}}' + \left(\frac{c_3c_4}{\tilde{\sigma}_{\mathrm{vM}}\,\beta_{\mathrm{vM}_\star}\left(\sigma_{\mathrm{vM}}\right)} - \frac{2}{3}c_2\right)\mathbf{b}\right], \tag{86}$$

$$\frac{\partial r^i_\Gamma}{\partial \mathbf{s}} = c_1C_\Gamma\left[\frac{c_3\left[\Gamma - \Gamma_\star(\sigma_{\mathrm{vM}})\right]}{\tilde{\sigma}_{\mathrm{vM}}}\tilde{\mathbf{s}}'^\top - c_2\frac{\partial\Gamma_\star(\sigma_{\mathrm{vM}})}{\partial\sigma_{\mathrm{vM}}}\mathbf{s}'^\top\right], \tag{87}$$

$$\frac{\partial r^i_\Gamma}{\partial \mathbf{b}} = c_1C_\Gamma\left[\Gamma_\star\left(\sigma_{\mathrm{vM}}\right) - \Gamma\right]\frac{c_3\Gamma}{\tilde{\sigma}_{\mathrm{vM}}}\tilde{\mathbf{s}}'^\top, \tag{88}$$

$$\frac{\partial r^i_\Gamma}{\partial \Gamma} = 1 + c_1C_\Gamma\left[\frac{2}{3}f_\sigma\left(\tilde{\sigma}_{\mathrm{vM}}\right) + \frac{c_3c_4\left[\Gamma_\star\left(\sigma_{\mathrm{vM}}\right) - \Gamma\right]}{\tilde{\sigma}_{\mathrm{vM}}}\right]. \tag{89}$$

Based on Eqs. (81)–(89), the matrix $\mathbf{A}^i_{n+1}$ in Eq. (77) can be computed. We solve the system of equations (73) using the Newton–Raphson method, cf. [60], within the following iteration loop, cf. [53]:

1. set initial values ($i = 0$):

$$\mathbf{s}^0_{n+1} = \mathbf{s}_n \qquad \mathbf{b}^0_{n+1} = \mathbf{b}_n \qquad \Gamma^0_{n+1} = \Gamma_n \tag{90}$$

2. iterate $i = 0, 1, \ldots, i_{\max}$
    a. compute residual vector $\mathbf{r}^i_{n+1}$ based on Eqs. (75) and (68)–(70)
    b. calculate matrix $\mathbf{A}^i_{n+1}$ and its inverse $\left(\mathbf{A}^i_{n+1}\right)^{-1}$ based on Eq. (77)
    c. determine the incremental change in the residual vector:

$$\Delta\mathbf{p}^{i+1}_{n+1} = -\left(\mathbf{A}^i_{n+1}\right)^{-1} \mathbf{r}^i_{n+1} \tag{91}$$

    d. update all variables:

$$\Box^{i+1}_{n+1} = \Box^i_{n+1} + \Delta\,\Box^{i+1}_{n+1} \qquad \forall\,\Box = \{\mathbf{p}, \mathbf{s}, \mathbf{b}, \Gamma\} \tag{92}$$

2. check for convergence: $\|\mathbf{r}^i_{n+1}\| \overset{?}{<} 10^{-6}$
    - criterion fulfilled ➧ exit loop
    - criterion not fulfilled ➧ $i \mapsto i + 1$, go to Step 2

where the symbol $\|\Box\|$ stands for the Euclidean norm of a vector. Note that the inversion in Step 2b is performed analytically based on the inversion rules for partitioned matrices, cf. [66]. If the iteration is converged, the current values of the stress $\mathbf{s}_{n+1}$, the backstress $\mathbf{b}_{n+1}$, and the softening variable Γ_{n+1} at time t_{n+1} are known.

3.2 Consistent Tangent Operator

In addition to the update of the stress and internal variables, the consistent tangent operator (CTO) needs to be computed [60, 64]. For the derivation of the mathematical expression, we make use of tensor notation in a first step and switch to matrix notation afterwards. Applying tensor notation, the CTO is represented by the fourth-order tensor $\boldsymbol{\mathcal{D}}$:

$$\boldsymbol{\mathcal{D}} = \left.\frac{\partial\boldsymbol{\sigma}}{\partial\boldsymbol{\varepsilon}}\right|_{n+1}. \tag{93}$$

In order to compute the derivative of the stress with respect to the strain, we exploit the implicit function theorem [67]. Thus, Eq. (60) is transformed in the following way:

$$\mathcal{F}\big(\boldsymbol{\sigma}_{n+1}, \boldsymbol{\beta}_{n+1}, \Gamma_{n+1}, \boldsymbol{\varepsilon}_{n+1}\big) = \mathbf{0} \tag{94}$$

with the implicit function $\mathcal{F}$:

$$\mathcal{F}\big(\boldsymbol{\sigma}_{n+1}, \boldsymbol{\beta}_{n+1}, \Gamma_{n+1}, \boldsymbol{\varepsilon}_{n+1}\big) = \boldsymbol{\sigma}_{n+1} - \boldsymbol{\mathcal{C}}_{n+1} : \big(\boldsymbol{\varepsilon}_{n+1} - \boldsymbol{\varepsilon}_n^{\text{in}} - \Delta\boldsymbol{\varepsilon}_{n+1}^{\text{in}}\big)\,. \tag{95}$$

The inelastic strain increment $\Delta\boldsymbol{\varepsilon}_{n+1}^{\text{in}}$ is computed based on Eq. (54), taking Eqs. (53), (55), and (56) into account. Exploiting the implicit function theorem [67], the CTO, i.e. the derivative of the stress with respect to the strains, is determined as follows:

$$\boldsymbol{\mathcal{D}} = \left.\frac{\partial\boldsymbol{\sigma}}{\partial\boldsymbol{\varepsilon}}\right|_{n+1} = -\left(\frac{\partial\mathcal{F}}{\partial\boldsymbol{\sigma}_{n+1}}\right)^{-1} : \frac{\partial\mathcal{F}}{\partial\boldsymbol{\varepsilon}_{n+1}}. \tag{96}$$

Note that the arguments of the implicit function $\mathcal{F}$ have been dropped for the sake of brevity. Based on Eq. (95), the implicit function $\mathcal{F}$ is derived with respect to the stress tensor:

$$\frac{\partial\mathcal{F}}{\partial\boldsymbol{\sigma}_{n+1}} = \boldsymbol{\mathcal{I}} + \boldsymbol{\mathcal{C}}_{n+1} : \frac{\partial\Delta\boldsymbol{\varepsilon}_{n+1}^{\text{in}}}{\partial\boldsymbol{\sigma}_{n+1}}, \tag{97}$$

while the derivative of the inelastic strain increment with respect to the stress is determined using Eq. (54):

$$\begin{aligned}\frac{\partial\Delta\boldsymbol{\varepsilon}_{n+1}^{\text{in}}}{\partial\boldsymbol{\sigma}_{n+1}} =& \frac{3}{2}\frac{\Delta t f_T(T)}{\tilde{\sigma}_{\text{vM}}}\left[\frac{3}{2}\left(\frac{1}{\tilde{\sigma}_{\text{vM}}}\frac{\partial f_\sigma(\tilde{\sigma}_{\text{vM}})}{\partial\tilde{\sigma}_{\text{vM}}} - \frac{f_\sigma(\tilde{\sigma}_{\text{vM}})}{\tilde{\sigma}_{\text{vM}}^2}\right)\tilde{\boldsymbol{\sigma}}' \otimes \tilde{\boldsymbol{\sigma}}'\right.\\ &\left. + f_\sigma(\tilde{\sigma}_{\text{vM}})\left(\boldsymbol{\mathcal{I}} - \frac{1}{3}\boldsymbol{I}\otimes\boldsymbol{I}\right)\right].\end{aligned} \tag{98}$$

Deriving Eq. (95) with respect to the strain results in a significantly shorter expression:

$$\frac{\partial\mathcal{F}}{\partial\boldsymbol{\varepsilon}_{n+1}} = -\boldsymbol{\mathcal{C}}_{n+1}. \tag{99}$$

Next, we insert Eqs. (97) and (99) into Eq. (96) to obtain the final expression for the CTO in tensor notation:

$$\boldsymbol{\mathcal{D}} = \left(\boldsymbol{\mathcal{I}} + \boldsymbol{\mathcal{C}}_{n+1} : \frac{\partial\Delta\boldsymbol{\varepsilon}_{n+1}^{\text{in}}}{\partial\boldsymbol{\sigma}_{n+1}}\right)^{-1} : \boldsymbol{\mathcal{C}}_{n+1}. \tag{100}$$

Above expression is transferred to matrix notation:

$$\mathbf{D} = \left(\mathbf{A}_1 + \mathbf{C}_{n+1}\frac{\partial\Delta\mathbf{e}_{n+1}^{\text{in}}}{\partial\mathbf{s}_{n+1}}\right)^{-1} : \mathbf{C}_{n+1} \tag{101}$$

with the corresponding derivative of the inelastic strain increment with respect to the stress, cf. Eq. (98):

$$\frac{\partial \Delta \mathbf{e}^{\text{in}}_{n+1}}{\partial \mathbf{s}_{n+1}} = \frac{3}{2} \frac{\Delta t f_T(T)}{\tilde{\sigma}_{\text{vM}}} \left[\frac{3}{2} \left(\frac{1}{\tilde{\sigma}_{\text{vM}}} \frac{\partial f_\sigma(\tilde{\sigma}_{\text{vM}})}{\partial \tilde{\sigma}_{\text{vM}}} - \frac{f_\sigma(\tilde{\sigma}_{\text{vM}})}{\tilde{\sigma}^2_{\text{vM}}} \right) \tilde{\mathbf{s}}' \left(\tilde{\mathbf{s}}'\right)^\top + f_\sigma(\tilde{\sigma}_{\text{vM}}) \left(\mathbf{A}_1 - \frac{1}{3}\mathbf{A}_2 \right) \right]. \tag{102}$$

The presented stress update algorithm as well as the CTO have been implemented into the commercial FE code ABAQUS via a user material subroutine (UMAT). In [19, 53], the performance and accuracy of this implementation are examined based on several benchmark problems considering uniaxial as well as multiaxial stress and deformation states.

4 Analysis of an Idealized Rotor

The phase mixture model has been implemented into the FEM since this contribution aims at analyzing complex power plant components under realistic boundary conditions (BCs). Therefore, this section discusses the simulation of the mechanical behavior of a steam turbine rotor. Similar analyses have been conducted before, cf. [42, 68]. In [42], the cyclic thermo-mechanical behavior of an industrial gas turbine rotor is simulated with a viscoplastic constitutive model using an axisymmetric finite element mesh. Thereby, the thermo-mechanical analysis is divided into two steps. As a starting point, the temperature distribution in the rotor is computed during a heat transfer analysis. For this purpose, the gas temperatures are prescribed as thermal BCs, and the corresponding heat transfer coefficients are provided as input. In a second step, the temperature field serves as input for the structural analysis. Additionally, Zhu et al. present the results of a similar thermo-mechanical analysis based on a three-dimensional finite element model.

Nevertheless, both publications provide insufficient or normalized information with respect to the precise geometry of the rotors or the applied BCs. Therefore, this contribution makes use of a different model, i.e. we analyze an idealized steam turbine rotor with an inlet groove. This procedure is based on [12], where the authors examine the behavior of the rotor subjected to a hot start, a subsequent holding stage, as well as a cool-down. Though, the consideration of *cold* starts is of crucial importance since the temperature gradients are expected to exceed the thermal loads during a hot start significantly, thus resulting in a higher impact on the rotor. In contrast to previous calibrations of the phase mixture model, e.g. [50], which are restricted to relatively narrow temperature ranges, i.e. $773\,\text{K} \leq T \leq 873\,\text{K}$, the current model is applicable to a wider temperature range ($673\,\text{K} \leq T \leq 923\,\text{K}$), which allows for the consideration of cold starts. Thus, we examine the influence of a cold start and a subsequent hot start on the mechanical behavior of the rotor. In analogy to the approaches suggested in

[42, 68], the thermo-mechanical analysis is only partly coupled since the influence of the thermal loads on the mechanical behavior is taken into account, whereas the inverse phenomenon, i.e. the influence of the mechanical deformations on the temperature field, is neglected. This procedure results in a significant reduction of the computational effort compared to a fully coupled thermo-mechanical analysis. In summary, the thermal analysis (described in Sect. 4.1) will yield the temperature distribution, which will serve as input for the subsequent structural analysis, cf. Sect. 4.2.

4.1 Heat Transfer Analysis

In the following, the model, the BCs, as well as the results of the heat transfer analysis are presented. The upper pictures of Fig. 6 illustrate the idealized geometry and the employed axisymmetric finite element mesh. Note that we make use of the heat transfer element DCAX8, which is an axisymmetric quadrilateral element with 8 nodes and quadratic shape functions. The notch induces stress and strain gradients, which are accounted for by refining the mesh near the notch root. Furthermore, several partitions have been used in order to obtain a structured regular mesh. The

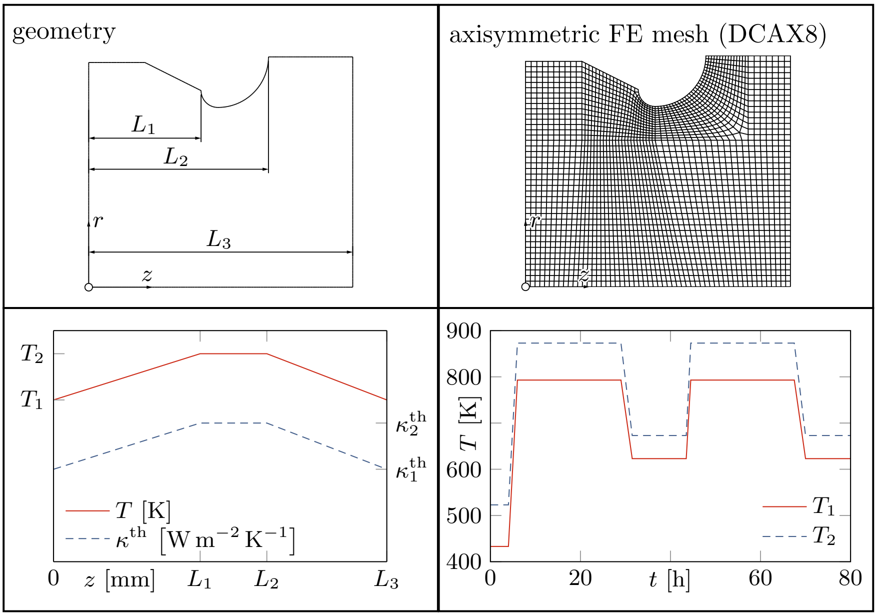

Fig. 6 Geometry, mesh, and loads for the heat transfer analysis of a steam turbine rotor with an inlet groove based on [12, 19]

bottom left diagram in Fig. 6 presents the dependence of the steam temperature on the longitudinal coordinate z. As can be seen, the steam temperature is assumed to depend linearly on the longitudinal coordinate, and it is constant near the notch, i.e. $T(L_1 \leq z \leq L_2) = T_2$. Furthermore, the rotor is equally heated from the left and the right side, i.e. $T(z=0) = T(z=L_3) = T_1$. Changes in the steam parameters are taken into account by different heat transfer coefficients κ_1^{th} and κ_2^{th}, which depend on the steam temperatures. Note that the heat transfer coefficients are reasonable experience values and have been derived according to [69].

The temporal change in the steam temperatures T_1 and T_2 is depicted in the bottom right diagram of Fig. 6. Since the complex thermo-mechanical loads in power plants are instationary and difficult to measure, it is a challenging task to obtain specific information on the temperature fields during the start-ups and shut-downs. Leyzerovich classified start-ups into three categories, i.e. cold, warm, and hot starts [70]. Considering a cold start, the previous shut-down must have taken place at least three days ago or the maximum pre-start temperature of the components must be lower than 393–433 K. In [71], similar limits are given for the steam temperatures. The outage before a hot start should not exceed 8–10 h, and all intermediate start-ups are denominated as warm starts [70]. Bearing these limits in mind, we define the pre-start steam temperatures $T_1(t=0\,\text{h}) = 433\,\text{K}$ and $T_2(t=0\,\text{h}) = 523\,\text{K}$ for the heat transfer analysis. In a first step, the rotor is heated up to a maximum temperature of 873 K. Then, the steam temperature is held constant over 23 h, which is followed by a decrease in temperature to 623–673 K. Finally, the rotor is restarted after a holding time of 12 h and the constant maximum temperature of 873 K is prescribed during 23 h before the final cool-down. A wide artificial temperature range for the loading profile has been chosen to demonstrate the characteristics of the model.

The results of the transient thermal analysis are summarized in Fig. 7. Note that the temperatures are evaluated at two specific points: point A at the notch root and point B on the axis of rotation. The temporal evolution of both temperatures is shown in Fig. 7, while the results with respect to the cold start are located at the left-hand side and the corresponding data for the hot start is shown at the right-hand side. Additionally, vertical lines indicate the points in time with respect to the maximum absolute temperature differences $|T_\text{A} - T_\text{B}|$ during the warm-up and the cool-down, respectively. Contour plots visualize the corresponding temperature fields. In agreement to the findings in [42], one observes the absolutely highest temperature differences during the start-ups. As one would expect, the maximum temperature difference ($\approx$227 K) occurs during the cold start, thus significantly exceeding the highest temperature difference during the hot start ($\approx$166 K). Because the rotor is heated externally by the steam, the temperature T_A at the surface is higher than the internal temperature T_B during heating-up. In contrast, while cooling down, the temperature in point B decreases more slowly than the surface temperatures, e.g. in point A. Consequently, the internal temperatures are higher than the temperatures at the surface. Furthermore, it is worth noticing that the maximum temperature difference during cool-down is relatively low ($\approx$72 K). The temperature difference is even lower during the holding stage and accounts for only $\approx$27 K.

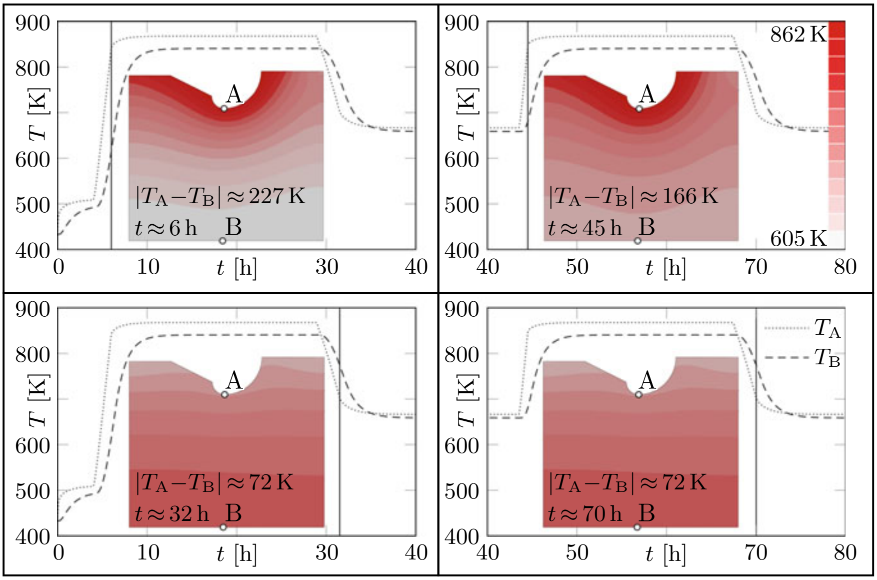

Fig. 7 Temperature distributions within the rotor and the temperatures T_A and T_B in points A and B versus time. Cold start (left) and hot start (right), cf. [19]

4.2 Structural Analysis

This section presents the structural analysis with the phase mixture model, starting with the obtained temperature fields as input. For this purpose, we make use of the continuum element CAX8, which is also an axisymmetric quadrilateral finite element with 8 nodes and quadratic shape functions. As can be seen in the upper pictures of Fig. 8, the finite element mesh from the heat transfer analysis is reused, which is due to the fact that the elements DCAX8 and CAX8 are both 8-node quadrilateral finite elements with quadratic shape functions, thus providing an identical description of the geometry and the field of unknowns in both cases. In addition, the applied mechanical BCs are depicted in the bottom left diagram in Fig. 8. Since the model is axisymmetric and rigid body motions must be prohibited, we set the displacements normal to the edges $r = 0$ and $z = 0$ to zero. The steam pressure $p(t)$ acts on the upper edge of the rotor (marked in red), and the time-dependent frequency $f(t)$ is prescribed such that the body rotates along the z axis (indicated in blue). Since the start-up and shut-down procedures are simulated, both the steam pressure as well as the frequency are time-dependent, cf. the bottom right diagram in Fig. 8.

In the following, selected results of the structural analysis are presented. The mechanical strains and stresses in point A are depicted over the time scale in Fig. 9. Thereby, a vector basis has been introduced, including the unit orthogonal vectors $\boldsymbol{n}$, $\boldsymbol{e}_t$, and $\boldsymbol{e}_\varphi$, cf. the bottom right diagram in Fig. 9. Note that these vectors also represent the principal directions of both the mechanical strain tensor and the stress

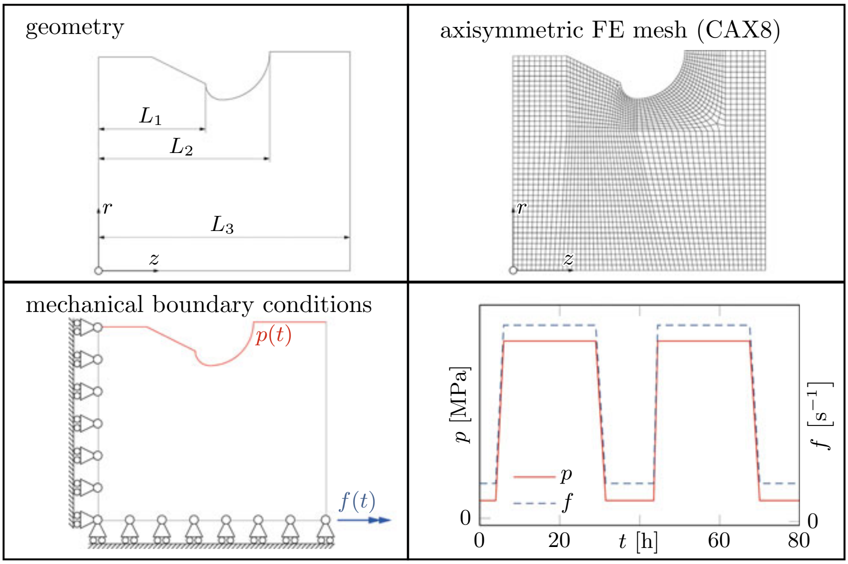

Fig. 8 Geometry, mesh, and loads for the structural analysis of a steam turbine rotor with an inlet groove based on [12, 19]

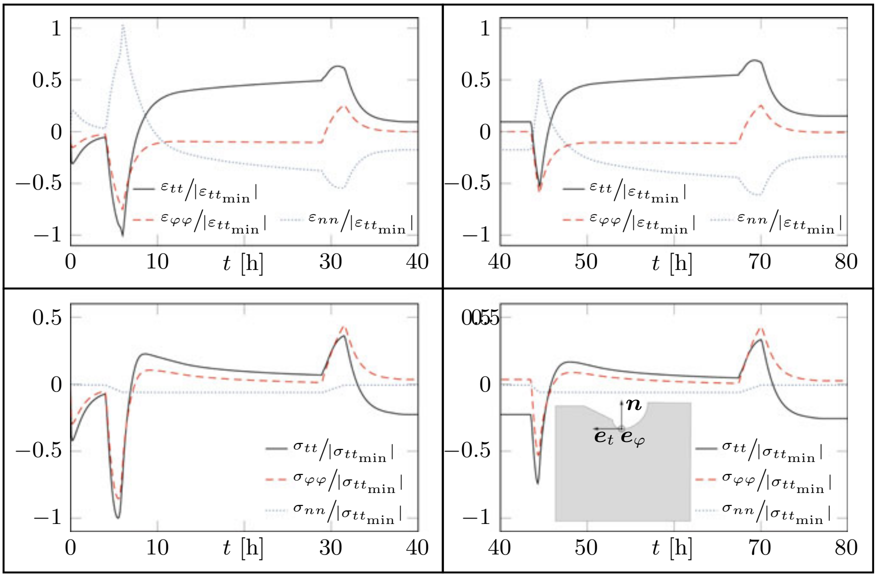

Fig. 9 Normalized mechanical strains (top) and stresses (bottom) in point A versus time. Cold start (left) and hot start (right), cf. [19]

tensor [12]. The absolute minimum tangential strain $|\varepsilon_{tt_{\min}}|$ is used to normalize the strains, which are shown over time in the upper diagrams of Fig. 9. The corresponding stress components are normalized with respect to the absolute minimum tangential stress $|\sigma_{tt_{\min}}|$, and these results are summarized depending on time in the lower diagrams of the same figure. As in the previous figures, we locate the results of the cold and hot start at the left and right-hand side, respectively.

Due to the BCs, the normal stress equals the negative steam pressure, i.e. $\sigma_{nn} = -p$. When the rotor is heated up, i.e. at $t \approx 6$ h and $t \approx 45$ h, compression occurs and the circumferential and tangential stresses and strains are minimized. It becomes obvious that the tangential and circumferential stresses and strains attain their absolute maximum values during the *cold* start. In addition, the tangential strain increases continuously, which is due to creep during the holding stages. Contrarily, the circumferential and tangential stresses decrease over time, thus stress relaxation can be observed. The rotor is subjected to tension during the cool-down since the tangential and circumferential stresses and strains are positive.

As it is shown in Fig. 9, the tangential stress and strain feature the highest absolute values throughout both cycles. For this reason, we focus on these two components in the following, cf. Fig. 10. The upper diagrams of this figure show both components, i.e. the normalized tangential strain and the corresponding stress, in point A depending on the time. In addition, the lower diagrams illustrate the dependence of the normalized tangential stress on the normalized tangential strain. We mark distinct points in red and assign numbers to each point to highlight the different stages during the temperature cycle, cf. Fig. 7 and 10. Between points 1 and 3, the rotor is heated up, whereas two stages can be distinguished: a warm-up with increasing temperature difference $T_{\mathrm{A}} - T_{\mathrm{B}}$ (1–2 during the cold start and 6–7 during the hot start) and a phase with decreasing temperature difference (2–3 and 7–8 for cold and hot start, respectively). With increasing temperature difference, the tangential stress and strain decrease, i.e. the rotor is compressed. In analogy, if the temperature difference decreases in the second stage, the lower temperature differences result in a reduction of the absolute strain and stress values. Afterwards, the holding stage follows between points 3–4 and 8–9, respectively. Here, creep and relaxation processes take place such that the strain increases continuously, whereas the stress is reduced at the same time. Applying a similar procedure as for the warm-up, the cool-down (4–6 and 9–11) can be divided into two different stages. Between the points 4–5 and 9–10, one can observe the decrease in the temperature difference up to $T_{\mathrm{A}} - T_{\mathrm{B}} \approx -72$ K. Here, tensile stresses and strains occur. Within the last range, i.e. 5–6 and 10–11, the cool-down is completed and followed by a short holding stage. Due to the low absolute temperature difference $|T_{\mathrm{A}} - T_{\mathrm{B}}|$, both the tangential stress and strain are reduced.

In what follows, let us examine the behavior of the normal and circumferential stresses and strains in detail. In the upper diagrams of Fig. 11, the normalized circumferential and normal strains are depicted depending on the normalized tangential strain in point A. Note that as before the diagrams on the left-hand side refer to the cold start, while the diagrams on the right-hand side show the results with respect to the hot start. The diagrams at the top reveal that the ratios of the principal

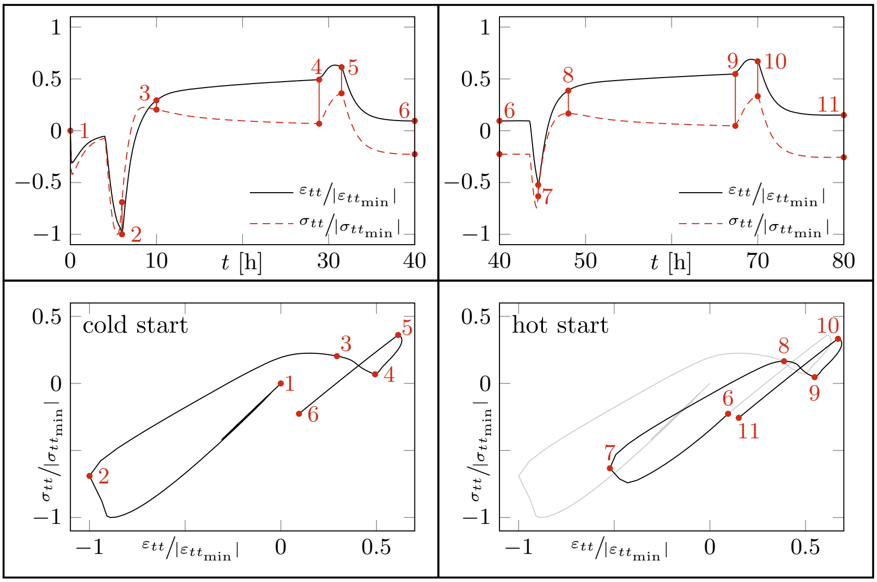

Fig. 10 Normalized tangential strain and stress in point A versus time (top). Normalized tangential stress versus normalized tangential strain in point A (bottom), cf. [19]

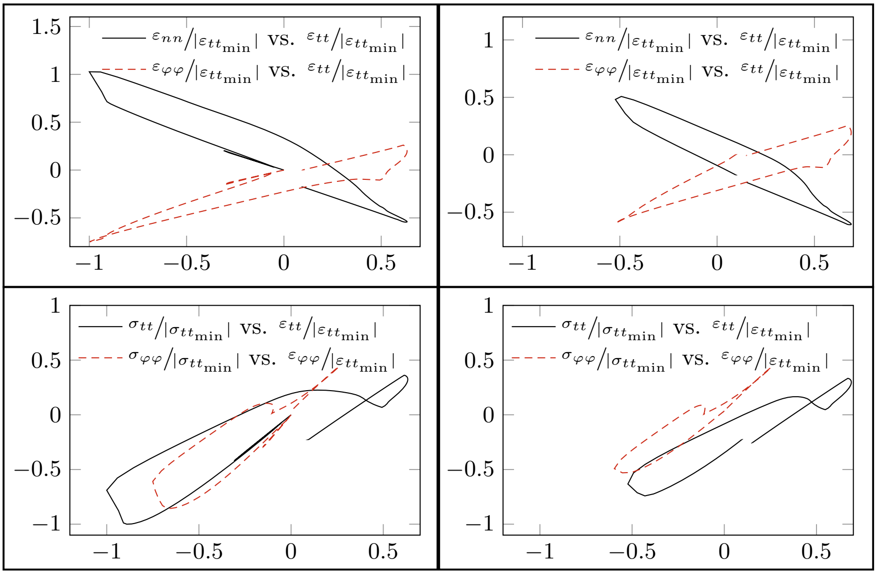

Fig. 11 Normalized circumferential and normal strains versus tangential strain (top). Normalized tangential and circumferential stresses versus corresponding strains (bottom) for cold (left) and hot start (right), cf. [19]

strains change during the cycles, i.e. one can observe nonproportional loading in point A [72]. Nevertheless, the principal directions $\boldsymbol{n}$, $\boldsymbol{e}_t$, and $\boldsymbol{e}_\varphi$ are still fixed. Additionally, the lower diagrams of Fig. 11 present the hysteresis loops with respect to the tangential and circumferential components. It becomes obvious that the hysteresis loops of the circumferential components are of a similar size as the corresponding loops of the tangential components, such that the influence of the circumferential components should definitely be taken into account when evaluating the mechanical work dissipated during the cycles [12].

The presented simulation results in this section agree well with published results for a hot start, cf. [12]. Note that cold starts have been simulated as well, which is possible due to the applicability of the current calibration to wide temperature ranges, i.e. $673\,\mathrm{K} \leq T \leq 923\,\mathrm{K}$. The simulation of a cold start followed by a hot start highlights the differences between the two starting procedures and the influence of the inhomogeneous temperature field on the stresses and strains.

5 Summary and Outlook

The contribution at hand presents a phase mixture model, the implementation of this model into the FEM, and the final analysis of a steam turbine rotor. Thereby, we focus on the tempered martensitic steel X20CrMoV12-1, whose mechanical behavior at elevated temperatures is modeled via the phase mixture approach.

The first part of the contribution, cf. Sect. 2, introduces the governing equations of the phase mixture model, which accounts for inelastic deformations as well as softening and hardening processes by modeling the material as an iso-strain composite consisting of a soft and a hard constituent. While the soft constituent refers to the subgrain interior, i.e. regions with low dislocation density, the hard constituent comprises the subgrain boundaries, i.e. regions with higher dislocation density. After introducing two internal variables—a backstress and a softening variable—one obtains a coupled system of three evolution equations with respect to the inelastic strain of the mixture and the two internal variables.

In a previous paper, this model is calibrated based on creep and HT tensile tests on the alloy X20CrMoV12-1. It has been demonstrated that the model accurately predicts the experimental data for wide ranges of temperature and stress, i.e. $673\,\mathrm{K} \leq T \leq 923\,\mathrm{K}$ and $100\,\mathrm{MPa} \leq \sigma \leq 700\,\mathrm{MPa}$, respectively. As can be seen, the applicability of the phase mixture model has been significantly extended compared to previous attempts, cf. [50], which are applicable to smaller ranges of stress and temperature ($150\,\mathrm{MPa} \leq \sigma \leq 200\,\mathrm{MPa}$, $773\,\mathrm{K} \leq T \leq 873\,\mathrm{K}$). Note that the model should only be applied to relatively high strain rates $\dot{\varepsilon}_{\mathrm{vM}} \geq 10^{-7}\,\mathrm{s}^{-1}$. After all, the presented constitutive model requires only 16 material parameters for robust simulations of hardening and softening behavior over wide ranges of stress and temperature, which constitutes a major advantage of the present approach. Note that the majority of the proposed models for tempered martensitic steels demands for 20 parameters and more, as already discussed in Sect. 1.

The next part of this contribution focuses on the implementation of the constitutive model into the FEM. For this purpose, the resulting system of evolution equations is implicitly integrated with respect to time based on the backward Euler method. Note that this procedure results in a nonlinear system of equations, which is solved by means of the Newton–Raphson method. In addition, the consistent tangent operator is derived analytically based on the system of evolution equations, while exploiting the implicit function theorem. To implement this model into the commercial finite element code ABAQUS, a UMAT subroutine has been written.

Finally, the implemented phase mixture model is used to simulate the mechanical behavior of a steam turbine rotor. Although similar analyses have already been conducted, cf. [12, 42, 68], the influence of the different starting procedures has not been examined yet. Therefore, a thermo-mechanical analysis for a cold start and a subsequent hot start is conducted using an axisymmetric model. In a first step, we prescribe the instationary steam temperature and heat transfer coefficients for a heat transfer analysis, which yields the resulting temperature field in the rotor. One observes that the largest temperature difference of 227 K occurs during the cold start. In contrast, the maximum temperature difference during cool-down is relatively low and accounts for only 72 K. Next, the computed temperature field is used as input for the subsequent structural analysis with the phase mixture model. It is worth noticing that the highest absolute stresses and strains occur during the cold start. In addition, the holding stages of both cycles exhibit creep and stress relaxation, such that the strains increase steadily while the stresses decrease over time. Generally speaking, these results highlight the differences in the temperature, stress, and strain fields depending on the start-up procedure under consideration, i.e. a cold or a hot start. The results clearly show that it is of crucial importance to consider cold starts as well during the simulation of power plant components. In a subsequent analysis, one could use these obtained stress and strain tensors to evaluate creep and fatigue damage, cf. [73], and to predict the lifetime of power plant components.

As a starting point, this contribution investigates a rotor with relatively simple geometry subjected to idealized thermo-mechanical loads. These simplifications and assumptions are due to the lack of precise data with respect to the geometry and the loads of real parts in literature. For this reason, power plant components under service-type loads should be analyzed with the phase mixture model in future studies. These analyses demand for the publication of additional experimental data concerning the thermo-mechanical loads on the components, such as the resulting temperature distribution on the surface of steam turbine rotors. Furthermore, the set-up of an axisymmetric finite element model, as it is also done in [42], is an acceptable simplification, but it would be beneficial to employ a three-dimensional model to account for the influence of the rotor blades, cf. Fig. 1.

In order to precisely predict the lifetime of power plant components, one should focus on simulating the effect of cyclic loads, i.e. the analysis should account for a large number of cycles. Then, a fine resolution of the temporal scale is required, such that the computational effort increases exponentially, considering also complex geometries and realistic BCs. Therefore, the numerical performance and efficiency of the current numerical implementation should be examined in detail. In case of high computational costs, one could replace the full Newton–Raphson method by less expensive approaches, such as the discretized or modified Newton–Raphson methods, cf. [60]. Nevertheless, the rate of convergence often deteriorates applying these methods, which should be checked carefully.

If the integration of other iteration approaches does not reduce the computational costs adequately, one can resort to explicit integration methods since the discrete constitutive equations are considerably easier to derive compared to implicit methods and a nonlinear system of equations must not be solved. However, explicit methods are only conditionally stable, such that automatic time stepping should be implemented including a critical time step size, cf. for example [74]. In this way, one could examine if the computational costs can be reduced by using explicit integration methods with automatic time stepping. Note that these possible improvements of the implementation of the phase mixture model are proposed in order to enable an efficient in-service assessment of power plant components, such that one can deduce measures to improve their design and extend their lifetime.

Acknowledgements The financial support rendered by the German Research Foundation (DFG) in context of the research training group "Micro-Macro-Interactions in Structured Media and Particle Systems" (GRK 1554) is gratefully acknowledged.

References

1. Masuyama, F.: Advances in physical metallurgy and processing of steels. History of power plants and progress in heat resistant steels. Iron Steel Inst. Jpn. Int. **41**(6), 612–625 (2001)
2. Breeze, P.A.: Power Generation Technologies. Newnes (2014)
3. Fournier, B., Dalle, F., Sauzay, M., Longour, J., Salvi, M., Caës, C., Tournié, I., Giroux, P.-F., Kim, S.-H.: Comparison of various 9–12%Cr steels under fatigue and creep-fatigue loadings at high temperature. Mater. Sci. Eng. A **528**(22–23), 6934–6945 (2011)
4. Hosseini, E., Kalyanasundaram, V., Li, X., Holdsworth, S.R.: Effect of prior deformation on the subsequent creep and anelastic recovery behaviour of an advanced martensitic steel. Mater. Sci. Eng. A **717**, 68–77 (2018)
5. Fournier, B., Sauzay, M., Mottot, M., Brillet, H., Monnet, I., Pineau, A.: Experimentally based modelling of cyclically induced softening in a martensitic steel at high temperature. In: Shibli, I.A., Holdsworth, S.R., Merckling, G. (eds.) ECCC Creep Conference, pp. 649–661. DEStech Publications, Lancaster, PA, USA (2005)
6. Fournier, B., Sauzay, M., Renault, A., Barcelo, F., Pineau, A.: Microstructural evolutions and cyclic softening of 9%Cr martensitic steels. J. Nucl. Mater. **386–388**, 71–74 (2009)
7. Fournier, B., Salvi, M., Dalle, F., de Carlan, Y., Caës, C., Sauzay, M., Pineau, A.: Lifetime prediction of 9–12% Cr martensitic steels subjected to creep-fatigue at high temperature. Int. J. Fatigue **32**(6), 971–978 (2010)
8. Röttger, D.R.: Untersuchungen zum Wechselverformungs- und Zeitstandverhalten der Stähle X20CrMoV121 und X10CrMoVNb91. Ph.D. Thesis, Universität GH Essen, Essen (1997)
9. Straub, S.: Verformungsverhalten und Mikrostruktur warmfester martensitischer 12%-Chromstähle. Ph.D. Thesis, Friedrich-Alexander-Universität, Erlangen-Nürnberg (1995)
10. Fournier, B., Sauzay, M., Pineau, A.: Micromechanical model of the high temperature cyclic behavior of 9–12%Cr martensitic steels. Int. J. Plast. **27**(11), 1803–1816 (2011)
11. Pétry, C., Lindet, G.: Modelling creep behaviour and failure of 9Cr–0.5Mo–1.8W–VNb steel. Int. J. Press. Vessel. Pip. **86**(8), 486–494 (2009)

12. Naumenko, K., Kutschke, A., Kostenko, Y., Rudolf, T.: Multi-axial thermo-mechanical analysis of power plant components from 9–12%Cr steels at high temperature. Eng. Fract. Mech. **78**(8), 1657–1668 (2011)
13. Götz, G.: Langzeitentwicklung der Mikrostruktur neuer 9–12% Chromstähle für den Einsatz in Kraftwerken. Ph.D. Thesis, Friedrich-Alexander-Universität, Erlangen-Nürnberg (2004)
14. Giroux, P.F., Dalle, F., Sauzay, M., Malaplate, J., Fournier, B., Gourgues-Lorenzon, A.F.: Mechanical and microstructural stability of P92 steel under uniaxial tension at high temperature. Mater. Sci. Eng. A **527**(16–17), 3984–3993 (2010)
15. Wang, L., Li, M., Almer, J.: In situ characterization of grade 92 steel during tensile deformation using concurrent high energy x-ray diffraction and small angle x-ray scattering. J. Nucl. Mater. **440**(1–3), 81–90 (2013)
16. Alsagabi, S., Shrestha, T., Charit, I.: High temperature tensile deformation behavior of grade 92 steel. J. Nucl. Mater. **453**(1–3), 151–157 (2014)
17. Kostenko, Y., Almstedt, H., Naumenko, K., Linn, S., Scholz, A.: Robust methods for creep fatigue analysis of power plant components under cyclic transient thermal loading. In: ASME Turbo Expo 2013: Turbine Technical Conference and Exposition, pp. V05BT25A040. American Society of Mechanical Engineers, New York (2013)
18. Polcik, P.: Modellierung des Verformungsverhaltens der warmfesten 9–12% Chromstähle im Temperaturbereich von 550–650°C. Ph.D. Thesis, Friedrich-Alexander-Universität, Erlangen-Nürnberg (1998)
19. Eisenträger, J.: A framework for modeling the mechanical behavior of tempered martensitic steels at high temperatures. Ph.D. Thesis, Otto von Guericke University Magdeburg (2018)
20. stern.de. Turbine - Technik VIEW Fotocommunity (2016)
21. Eisenträger, J., Naumenko, K., Altenbach, H., Gariboldi, E.: Analysis of temperature and strain rate dependencies of softening regime for tempered martensitic steel. J. Strain Anal. Eng. Des. **52**, 226–238 (2017)
22. Chilukuru, H., Durst, K., Wadekar, S., Schwienheer, M., Scholz, A., Berger, C., Mayer, K.H., Blum, W.: Coarsening of precipitates and degradation of creep resistance in tempered martensite steels. Mater. Sci. Eng. A **510–511**, 81–87 (2009)
23. Agamennone, R., Blum, W., Gupta, C., Chakravartty, J.K.: Evolution of microstructure and deformation resistance in creep of tempered martensitic 9–12%Cr-2%W-5%Co steels. Acta Mater. **54**(11), 3003–3014 (2006)
24. Orlová, A., Buršík, J., Kuchřoavá, K., Sklenička, V.: Microstructural development during high temperature creep of 9% Cr steel. Mater. Sci. Eng. A **245**, 39–48 (1998)
25. Fournier, B., Sauzay, M., Barcelo, F., Rauch, E., Renault, A., Cozzika, T., Dupuy, L., Pineau, A.: Creep-fatigue interactions in a 9 Pct Cr-1 Pct mo martensitic steel: Part II. Microstructural evolutions. Metall. Mater. Trans. A **40**(2), 330–341 (2009)
26. Blum, W.: Mechanisms of creep deformation in steel. In: Abe, F., Kern, T.-U., Viswanathan, R. (eds.) Creep-Resistant Steels, pp. 365–402. Woodhead Publishing Limited, Sawston (2008)
27. Verma, P., Srinivasa, N.S.C., Singha, V.: Low cycle fatigue behavior of modified 9Cr-1Mo steel at 300 °C. Mater. Sci. Eng. A **715**, 17–24 (2018)
28. Giroux, P.-F.: Experimental study and simulation of cyclic softening of tempered martensite ferritic steels. Ph.D. Thesis, École Nationale Supérieure des Mines de Paris (2011)
29. Chaboche, J.L., Rousselier, G.: On the plastic and viscoplastic constitutive equations: Part II: application of internal variable concepts to the 316 stainless steel. J. Press. Vessel. Technol. **105**(2), 159 (1983)
30. Wang, J., Steinmann, P., Rudolph, J., Willuweit, A.: Simulation of creep and cyclic viscoplastic strains in high-Cr steel components based on a modified Becker–Hackenberg model. Int. J. Press. Vessel. Pip. **128**, 36–47 (2015)
31. Velay, V., Bernhart, G., Penazzi, L.: Cyclic behavior modeling of a tempered martensitic hot work tool steel. Int. J. Plast. **22**(3), 459–496 (2006)
32. Farragher, T.P., Scully, S., O'Dowd, N.P., Leen, S.B.: Thermomechanical analysis of a pressurized pipe under plant conditions. J. Press. Vessel. Technol. **135**, 011204–1–011204–9 (2013)

33. Farragher, T.P., Scully, S., O'Dowd, N.P., Hyde, C.J., Leen, S.B.: High temperature, low cycle fatigue characterization of P91 weld and heat affected zone material. J. Press. Vessel. Technol. **136**(2), 021403–1–021403–10 (2014)
34. Armstrong, P.J., Frederick, C.O.: A mathematical representation of the multiaxial bauschinger effect. Technical report, Berkeley Nuclear Laboratories (1966)
35. Chaboche, J.L.: Constitutive equations for cyclic plasticity and cyclic viscoplasticity. Int. J. Plast. **5**(3), 247–302 (1989)
36. Koo, G.-H., Kwon, J.-H.: Identification of inelastic material parameters for modified 9Cr-1Mo steel applicable to the plastic and viscoplastic constitutive equations. Int. J. Press. Vessel. Pip. **88**, 26–33 (2011)
37. Wang, P., Cui, L., Lyschik, M., Scholz, A., Berger, C., Oechsner, M.: A local extrapolation based calculation reduction method for the application of constitutive material models for creep fatigue assessment. Int. J. Fatigue **44**, 253–259 (2012)
38. Saad, A.A., Sun, W., Hyde, T.H., Tanner, D.W.J.: Cyclic softening behaviour of a P91 steel under low cycle fatigue at high temperature. Procedia Eng. **10**, 1103–1108 (2011)
39. Saad, A.A.: Cyclic plasticity and creep of power plant materials. Ph.D. Thesis, University of Nottingham, Nottingham (2012)
40. Barrett, R.A., O'Donoghue, P.E., Leen, S.B.: An improved unified viscoplastic constitutive model for strain-rate sensitivity in high temperature fatigue. Int. J. Fatigue **48**, 192–204 (2013)
41. Zhang, S.-L., Xuan, F.-Z.: Interaction of cyclic softening and stress relaxation of 9–12% Cr steel under strain-controlled fatigue-creep condition: experimental and modeling. Int. J. Plast. 1–20 (2017)
42. Benaarbia, A., Rae, Y., Sun, W.: Unified viscoplasticity modelling and its application to fatigue-creep behaviour of gas turbine rotor. Int. J. Mech. Sci. **136**, 36–49 (2018)
43. Estrin, Y., Braasch, H., Brechet, Y.: A dislocation density based constitutive model for cyclic deformation. J. Eng. Mater. Technol. **118**(4), 441–447 (1996)
44. Sauzay, M., Brillet, H., Monneta, I., Mottot, M., Barcelo, F., Fournier, B., Pineau, A.: Cyclically induced softening due to low-angle boundary annihilation in a martensitic steel. Mater. Sci. Eng. A **400–401**, 241–244 (2005)
45. Sauzay, M., Fournier, B., Mottot, M., Pineau, A., Monnet, I.: Cyclic softening of martensitic steels at high temperature: experiments and physically based modelling. Mater. Sci. Eng. A **483–484**, 410–414 (2008)
46. Barrett, R.A., O'Donoghue, P.E., Leen, S.B.: A dislocation-based model for high temperature cyclic viscoplasticity of 9–12Cr steels. Comput. Mater. Sci. **92**, 286–297 (2014)
47. Barrett, R.A., O'Donoghue, P.E., Leen, S.B.: A physically-based constitutive model for high temperature microstructural degradation under cyclic deformation. Int. J. Fatigue **100**, 388–406 (2017)
48. Barkar, T., Ågren, J.: Creep simulation of 9–12% Cr steels using the composite model with thermodynamically calculated input. Mater. Sci. Eng. A **395**(1–2), 110–115 (2005)
49. Voigt, W.: Ueber die Beziehung zwischen den beiden Elasticitätsconstanten isotroper Körper. Ann. Phys. **274**(12), 573–587 (1889)
50. Naumenko, K., Altenbach, H., Kutschke, A.: A combined model for hardening, softening, and damage processes in advanced heat resistant steels at elevated temperature. Int. J. Damage Mech. **20**(4), 578–597 (2011)
51. Naumenko, K., Gariboldi, E.: A phase mixture model for anisotropic creep of forged Al–Cu–Mg–Si alloy. Mater. Sci. Eng. A **618**, 368–376 (2014)
52. Raj, S.V., Iskovitz, I.S., Freed, A.D.: Modeling the role of dislocation substructure during class M and exponential creep. In: Krausz, A.S., Krausz, K. (eds.) Unified Constitutive Laws of Plastic Deformation, pp. 343–439. Academic Press Inc., Cambridge (1996)
53. Eisenträger, J., Naumenko, K., Altenbach, H.: Numerical implementation of a phase mixture model for rate-dependent inelasticity of tempered martensitic steels. Acta Mech. **229**, 3051–3068 (2018)
54. Zhu, Y., Kang, G., Kan, Q., Bruhns, O.T.: Logarithmic stress rate based constitutive model for cyclic loading in finite plasticity. Int. J. Plast. **54**, 34–55 (2014)

55. Shutov, A.V., Kreißig, R.: Finite strain viscoplasticity with nonlinear kinematic hardening: phenomenological modeling and time integration. Comput. Methods Appl. Mech. Eng. **197**(21–24), 2015–2029 (2008)
56. Naumenko, K., Altenbach, H.: Modeling High Temperature Materials Behavior for Structural Analysis. Part I: Continuum Mechanics Foundations and Constitutive Models. Advanced Structured Materials, vol. 28. Springer International Publishing, Berlin (2016)
57. Eisenträger, J., Naumenko, K., Altenbach, H.: Calibration of a phase mixture model for hardening and softening regimes in tempered martensitic steel over wide stress and temperature ranges. J. Strain Anal. Eng. Des. **53**, 156–177 (2018)
58. Silbermann, C.B., Shutov, A.V., Ihlemann, J.: Modeling the evolution of dislocation populations under non-proportional loading. Int. J. Plast. **55**, 58–79 (2014)
59. Belytschko, T., Liu, W.K., Moran, B.: Nonlinear Finite Elements for Continua and Structures. Wiley, New York (2000)
60. Wriggers, P.: Nonlinear Finite Element Methods. Springer, Berlin (2008)
61. Luccioni, L.X., Pestana, J.M., Taylor, R.L.: Finite element implementation of non-linear elastoplastic constitutive laws using local and global explicit algorithms with automatic error control. Int. J. Numer. Methods Eng. **50**(5), 1191–1212 (2001)
62. Courant, R., Friedrichs, K., Lewy, H.: Über die partiellen Differenzengleichungen der mathematischen Physik. Math. Ann. **100**, 32–74 (1928)
63. Hartmann, S., Haupt, P.: Stress computation and consistent tangent operator using non-linear kinematic hardening models. Int. J. Numer. Methods Eng. **36**(22), 3801–3814 (1993)
64. Hartmann, S., Lührs, G., Haupt, P.: An efficient stress algorithm with applications in viscoplasticity and plasticity. Int. J. Numer. Methods Eng. **40**(6), 991–1013 (1997)
65. Kobayashi, M., Mukai, M., Takahashi, H., Ohno, N., Kawakami, T., Ishikawa, T.: Implicit integration and consistent tangent modulus of a time-dependent non-unified constitutive model. Int. J. Numer. Methods Eng. **58**(10), 1523–1543 (2003)
66. Harville, D.A.: Matrix Algebra From a Statistician's Perspective. Springer, New York (1997)
67. Ghorpade, S.R., Limaye, B.V.: A Course in Multivariable Calculus and Analysis. Springer, New York (2010)
68. Zhu, X., Chen, H., Xuan, F., Chen, X.: Cyclic plasticity behaviors of steam turbine rotor subjected to cyclic thermal and mechanical loads. Eur. J. Mech. A/Solids **66**, 243–255 (2017)
69. Stephan, P., Kabelac, S., Kind, M., Martin, H., Mewes, D., Schaber, K.: VDI Heat Atlas. Springer, Berlin (2010)
70. Leyzerovich, A.S.: Steam Turbines for Modern Fossil-fuel Power Plants. Fairmont Press, Lilburn, GA, USA (2008)
71. Strauß, K.: Kraftwerkstechnik zur Nutzung fossiler, nuklearer und regenerativer Energiequellen. Springer, Berlin (2009)
72. Suresh, S.: Fatigue of Materials. Cambridge University Press, Cambridge (2006)
73. Meng, Q., Wang, Z.: Creep damage models and their applications for crack growth analysis in pipes: a review. Eng. Fract. Mech. **205**, 547–576 (2019)
74. Sloan, S.W.: Substepping schemes for the numerical integration of elastoplastic stress-strain relations. Int. J. Numer. Methods Eng. **24**(5), 893–911 (1987)

Computational Assessment of the Microstructure-Dependent Thermomechanical Behaviour of AlSi12CuNiMg-T7—Methods and Microstructure-Based Finite Element Analyses

Carl Fischer, Axel Reichenbacher, Mario Metzger and Christoph Schweizer

Abstract In this paper, the influence of the microstructure of a cast aluminium alloy used for pistons in combustion engines on the local and global deformation behavior is investigated by means of microstructure-based cell models and the finite element method. Therefore, a representative microstructure is digitized using nano computer tomography. In the digitized and segmented data, the aluminium matrix, silicon particles, pores and two intermetallic phases are distinguished. Microstructure-based cell models are created and linear-elastic, thermal and viscoplastic material properties are assigned for the finite element simulation in ABAQUS/Standard. The elastic, macroscopic nearly isotropic material behavior is shown for 64 different microstructure-based cell models with 200 × 200 × 200 elements with microstructure-dependent material properties at room temperature. A microstructure cell is subjected to a thermal cycle with zero macroscopic loading in order to examine the influence of the thermal mismatch between the individual microstructure phases on the resulting stresses and strains on the micro level. High stresses at interfaces of silicon particles and the aluminium matrix occur in the linear-elastic simulation, whereas an elastic-viscoplastic material behavior of the aluminium matrix leads to a overall stress relief in the microstructure cell.

Keywords Cast aluminium alloy · Thermal fatigue · Microstructure-based cell models · Finite element analysis

---

C. Fischer (✉) · A. Reichenbacher · M. Metzger · C. Schweizer
Fraunhofer Institute for Mechanics of Materials IWM Freiburg,
Freiburg im Breisgau, Germany
e-mail: carl.fischer@iwm.fraunhofer.de

K. Naumenko and M. Krüger (eds.), *Advances in Mechanics of High-Temperature Materials*, Advanced Structured Materials 117,
https://doi.org/10.1007/978-3-030-23869-8_2

1 Introduction

In the current discussion regarding the emission of vehicles with combustion engines, the focus lies on the reduction of carbon dioxides and nitrogen oxides. The reduction of mileage is achieved by more efficient and highly loaded engines as well as by those of lighter vehicle design. However, severe emission standards and safety aspects must be maintained. Simply reducing the weight of the passenger cab or the car body is insufficient, meaning that other components, i.e. the combustion engine must also be designed with a lightweight construction. Preferably aluminium materials are used in many parts of the combustion engine that exhibit low density, high thermal conductivity, very good castability and high corrosion resistance.

Eutectic cast aluminium alloys (e.g. AlSi12) are currently used for pistons and hypo-eutectic cast aluminium alloys (e.g. AlSi7Mg or AlSi10Mg) for cylinder heads in diesel and gasoline engines. These components are exposed to severe temperature cycles during service, leading to low-cycle fatigue (LCF). Because the stresses are mainly caused by the temperature cycles, one speaks of thermomechanical fatigue (TMF). Since extreme thermal and mechanical loads involve time-dependent plastic deformation, short fatigue cracks are formed after relatively few thermal cycles and the fatigue crack growth limits the lifetime expectancy of the components. Due to the piston stroke, high-cycle fatigue (HCF) is superimposed to the thermal cycles, so that TMF/HCF loadings act on these components. Additionally, thermal fatigue interacts due to the combustion process and the impact of cold fuel on top of the piston bowl. In engine bench tests, a given design is investigated for its TMF/HCF behavior usually under more severe conditions than the engine is exposed to in service. However, these tests are still expensive and time consuming and uncertainties in the given design remain due to the fact that the test results must be extrapolated to typical service conditions.

The finite element method is a powerful tool to computationally analyze and optimize a component at low financial burden and thus reduce the overall development costs. Therefore, suitable material models for cyclic plasticity and mechanism-based lifetime models must be applied in a finite element (FE) simulation in order to predict reliable stresses and (in)elastic strains as well as lifetime. Downsizing concepts combined with new combustion processes, new supercharging concepts and advanced injection and ignition systems increase thermal and mechanical loads in the components. Because the materials are brought even closer to their load capacity under TMF/HCF, the quality of the underlying models for plasticity and lifetime must be even improved in the FE analysis.

In this paper, detailed microstructure-based FE analyses of an aluminium material are presented in order to determine the influence of the microstructure on local plasticity and possible (initial) fatigue cracking behavior. Based on these first FE analyses it is intended to develop a new mechanism- and microstructure-based lifetime model for the reliable lifetime prediction of aluminium materials. The paper is structured as follows: In Sect. 2, the materials microstructure and its mechanical properties are characterised. Section 3 describes the reconstruction of the FE model and the assign-

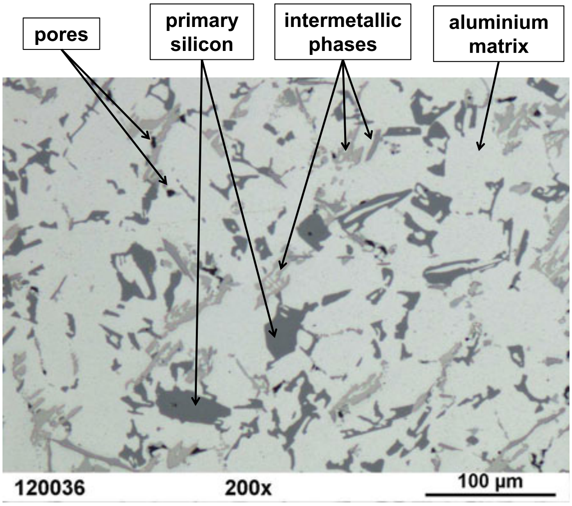

Fig. 1 Microstructure of the cast aluminium alloy AlSi12CuNiMg-T7

ment of microstructure-based material properties. Macroscopic anisotropic material behavior for a microstructure-dependent linear-elastic material law is investigated in Sect. 4. In Sect. 5 a microstructure-dependent plasticity model is applied and the resulting stress distribution in the FE model is analyzed under thermal loading. The paper is summarised in Sect. 6.

2 Microstructure and Material Characterization

In this paper, the cast aluminium alloy AlSi12CuNiMg-T7 is investigated, which is used for pistons in diesel combustion engines. The alloy is eutectic with 12% silicon, which ensures high-temperature strength at operating temperatures up to 420 °C. Before service, pistons are usually tempered to a strength enhancing T6 heat treatment by solution annealing, water quenching and artificial ageing. Due to the high service temperatures, the piston becomes overaged at near-surface areas already after a few hours of operation. The alloy is therefore additionally overaged to a T7 state for 100 h at 350 °C after the T6 heat treatment.

A typical section of the materials microstructure is shown in Fig. 1. The microstructure consists of α-aluminium matrix, large primary silicon particles up to a size of 100 µm, several intermetallic phases and isolated pores. The microstructure morphology of pistons is determined due to local very different solidification conditions. According to Gao et al. [1] the porosity, the secondary dendrite arm spacing, the aluminium matrix, silicon particles and rich iron-containing intermetallic phases have a major influence on the lifetime of cast aluminium alloys. The lifetime of the investigated AlSi12CuNiMg-T7 alloy depends, besides on the applied mechanical

Fig. 2 LCF and TMF lifetime behavior of the cast aluminium alloy AlSi12CuNiMg-T7

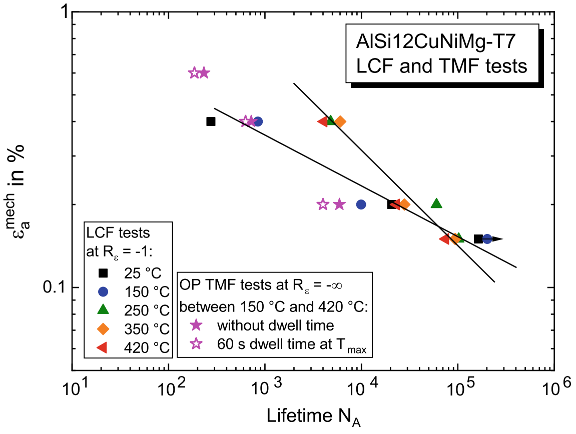

load, on the applied temperature, which is shown in the Wöhler diagram in Fig. 2 for strain-controlled LCF tests under fully reversed cyclic loading.

The LCF tests with a mechanical strain amplitude of $\varepsilon_a^{mech} = 0.4\%$ exhibit a shorter lifetime at low temperatures (i.e. at room temperature and 150 °C) than at temperatures above 250 °C. This inverse temperature dependency is also existent, but less pronounced, at a strain amplitude of $\varepsilon_a^{mech} = 0.2\%$. For many metallic materials, i.e. nickel-based superalloys, the lifetime reduces with increasing temperature due to a drop of the mechanical properties, i.e. Young's modulus E or cyclic yield stress σ_{CY}, that is also observed for the aluminium alloy at a strain amplitude of $\varepsilon_a^{mech} = 0.15\%$. In addition, anisothermal out-of-phase (OP) TMF tests between 150 and 420 °C are investigated without and with a dwell time of 60 s at maximum temperature. The TMF lifetimes are found to lie at the lower scatter band, whereas the applied dwell time in the TMF tests slightly reduces the lifetimes. Since the isothermal lifetime behavior can not be explained solely by means of the mechanical material properties, it can be assumed that the material's specific microstructure influences the mechanism of crack initiation and growth and thus the lifetime in dependence of the temperature.

Under HCF loading at room temperature, cracks are initiated by the partial debonding of the silicon particles from the aluminium matrix, while under LCF conditions crack initiation and crack growth is determined by the brittle fracture of the silicon particles [2]. At low temperatures, the mechanical stress is carried by the hard phases, that exhibit a higher strength than the aluminium matrix [2]. Due to high stress concentrations and the brittle fracture behavior of the silicon particles, small micro cracks are formed in the material [3], whereas the fracture surface is mostly perpendicular to the loading direction [4]. At elevated temperatures, the strength of the aluminium matrix is decreased significantly and the silicon particles detach from the aluminium matrix [3–5]. The fatigue crack growth is now determined mainly by the properties of the matrix, the shape of the crack tip front [2] and the circumjacent microstructure morphology [6]. The cracks preferably grow along cavities between of debonded particles, while with appropriate crack length or sufficient crack tip driving force, a crack might also cut particles and intermetallic phases [5–7].

The crack growth behavior was assessed with fracture mechanics parameters, i.e the cyclic crack-tip opening displacement $\Delta CTOD$ in [7, 8] for a dual Al-Si alloys or the J-integral in [9] for a ductile, porous solid material. The interaction between the material matrix and microstructural features such as hard phases or pores in terms of deformation, crack initiation and fatigue crack growth has often been studied for various metallic materials with two- or three-dimensional microstructure-based models by means of the finite element method. For particle reinforced metal matrix composites the reader is referred to [10–12], materials with metallographic structures, e.g. sintered steels to [13], lamellar cast iron to [14] and cast aluminium alloys, i.e. A356 to [2, 7, 15] and AlSi12 to [3, 16].

For the numerical analyses of stresses and strains of heterogeneous materials, e.g. by means of the finite element method, the microstructure must be digitized first, which is usually done by serial sectioning [10, 11] and X-ray computer tomography [2, 15, 17], single scanning electron [12, 13] or light microscopy [3, 16]. The digitized microstructure must then be prepared to establish microstructure-based cell models for the finite element analyses. The cell models can either be discretized with tetrahedron elements or voxel-based with hexahedron elements. With these two methods, the transfer of the digitized data into a robust finite element mesh is quite simple. However, a large number of finite elements are generated and hence long calculation times and also large computing capacities are required. Approaches to reduce the number of finite elements are i.e. the octree-based meshing method proposed in [18] or an overlay grid procedure as presented in [19]. In voxel-based meshes the interfaces between different microstructures are zig-zag shaped and especially in linear-elastic analyses, high local stresses and strains can occur at points with complex geometry shapes [2]. The interface between different microstructures can be modelled more precisely using a tetrahedron mesh, however the discretization might becomes very fine for an automatized meshing.

For hypo-eutectic cast aluminium alloys, the influence of pores as the origin for fatigue cracks is often studied in literature. In [15], crack initiation spots from experimental observations at pores with complex shaped geometries are reproduced in a microstructure-based FE model. The crack path is determined by a three-dimensional stress state and the respective plastic strain fields around the crack tip [15]. Furthermore, damage in silicon particles at the advancing crack tip front is considered [15]. According to Teranishi et al. [2], the stress concentration and the three-dimensional stress state of the silicon particles are the main reasons for the damage of particles of the investigated A356 alloy. Fan et al. [20] figured out, that fatigue cracks in a cast A356-T6 alloy develop preferentially from silicon particle clusters, pores, oxide films and locations with damaged or detached particles due to plastic shear strain and strongly activated slip bands. The influence of the particle or pore size and distance, the aspect ratio and particle clusters, as well as the distance of a pore to the surface is investigated in [20] with two-dimensional FE simulations.

The cast AlSi12CuNiMg alloy is analyzed in [3, 16] by means of temperature-dependent two-dimensional FE simulations. In both publications, the metallic matrix is modelled with an elastic-plastic material law, whereas the hard phase (in particular silicon particles) is assumed to behave linear-elastic. In [16], the inhomogeneous distribution of plastic strain is mentioned as the significant damage factor for the aluminium matrix, which is oriented in slip bands at 45° to the uniaxial loading direction. The comparison of finite element simulations with real shaped particles and with a simplified ellipsoidal shape shows almost no influence in the macroscopic material behavior, but the local stress concentration at the simplified shaped silicon particles is significantly diminished [16]. The local stresses in the metallic matrix depend hardly on the particle geometry [16]. At low temperatures, the stress is mainly received by the hard phase, while at high temperatures plastic yielding occurs in the metallic matrix around the particles [3].

Because of the complex microstructure morphology of cast aluminium alloys, two-dimensional FE simulations are limited to examine local stresses and plastic strains accurately. Therefore, a three-dimensional microstructure-based cell model is created for the FE simulation in ABAQUS for the AlSi12CuNiMg-T7 cast aluminium alloy. The focus lies on the thermal mismatch between the primary silicon particles and the aluminium matrix, that is responsible for thermal fatigue (TF). The influence of the microstructure and thermal fluctuations on the TF life can be experimentally analyzed. However, the experimental test set-up is rather complex and challenging, so that numerical simulations can be used instead to understand TF for the considered material. Therefore, microstructure-based cell models are created and elastic, viscoplastic and thermal material properties are assigned in the following sections.

3 Microstructure-Based Cell Model for FE Analysis

In this section, the numerical homogenization method for the computation of macroscopic quantities is described in Sect. 3.1. The digitization of the microstructure follows in Sect. 3.2, the reconstruction of the microstructure-based cell model in Sect. 3.3 and the assignment of the material properties in Sect. 3.4.

3.1 Numerical Homogenization Method for the Computation of Macroscopic Quantities

For the evaluation of the macroscopic quantities, i.e. of stresses and strains, it is necessary to homogenize the local results of the microstructure cells. According to Hill [21], the macroscopic quantity Ψ can be calculated by the volume average of the local varying quantities ψ:

$$\Psi = \langle \psi \rangle = \frac{1}{V} \int \psi \mathrm{d}V. \tag{1}$$

The integrated work-rate over the micro level $\dot{w}$ has to be equal to the work-rate calculated on the macro level $\dot{W}$:

$$\langle \dot{w} \rangle = \langle \sigma : \dot{\varepsilon} \rangle = \dot{W} = \Sigma : \dot{E}. \tag{2}$$

Therefore, one of the following boundary conditions from Hill [21] has to be fulfilled on the outer free surfaces of the volume element:

1. the fields of velocity are linear: $\underline{\dot{u}} = \dot{E} \cdot \underline{x}$,
2. the vectors for the force are linear: $\underline{t} = \sigma \cdot \underline{n} = \Sigma \cdot \underline{n}$,
3. a combination of these two boundary conditions: $(\underline{\dot{u}} - \dot{E} \cdot \underline{x}) \cdot ((\sigma - \Sigma) \cdot \underline{n}) = 0$,

where $\underline{\dot{u}}$ is the velocity vector, $\underline{t}$ the force vector, $\underline{x}$ the position vector, and $\underline{n}$ the normal vector of the surface. σ and ϵ is the stress, respectively strain tensor on the microscale and Σ and E on the macroscale. In the following different macroscopic uniaxial stress states are applied to the cells. Therefore, two opposite surfaces of the microstructure cell are loaded displacement controlled perpendicularly to the respective surface whereas the other four surfaces remain without force. Admissible periodic boundary conditions, i.e. according to Suquet [22], are not applied in this work.

3.2 *Digitization of the Microstructure*

A sample of the aluminium alloy's microstructure was digitized using nano computer tomography (nano-CT) technology. This technology is non-destructive and comparatively fast, but the subsequent segmentation of the microstructure features is time consuming and sometimes difficult, especially between silicon and aluminium. The digitized microstructure volume has a diameter of approximately 870 µm and a length of 1410 µm with a respective voxel edge length of 0.67 µm. A masked grey scale image of the digitized microstructure is shown in Fig. 3.

The grey scale value contains the information about the microstructure phase: Pores (0, black), silicon (1, dark grey), aluminium (2, grey) and two intermetallic phases (3/4) subdivided by weaker (3, light grey) and stronger (4, white) X-ray absorption. However, the investigated cast aluminium alloy includes more than two intermetallic phases (see in [3]). Since the composition of the intermetallic phases is not specified more precisely, the phases are named as intermetallic phase 1 and intermetallic phase 2. In a first step, the volume fractions of the microstructure features are analyzed for a volume of 800 × 800 × 2000 voxels. In this volume, the microstructure consists of 0.17% pores, 79.63% aluminium, 13.58% silicon, 5.59% intermetallic phase 1 and 1.03% intermetallic phase 2.

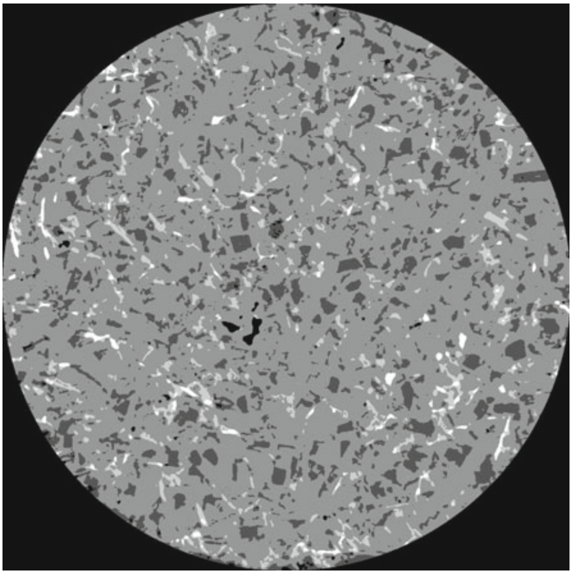

Fig. 3 With nano-CT technology digitized microstructure of the cast aluminium alloy AlSi12CuNiMg-T7

3.3 Reconstruction of the FE Model

For an automatized reconstruction of different microstructure-based cell models the Python [23] interface of ABAQUS/Standard [24] is used. Therefore, the cell size and its position in the overall digitized volume is defined first (see Fig. 4). The FE mesh is generated using the voxel-based meshing technique. Each voxel is converted to a hexahedron finite element with linear interpolation functions and reduced integration scheme (element type C3D8R according to the ABAQUS/Standard manual [24]).

Thus, the discretized cell size corresponds directly to the number of voxels of the digitized data. To generate a three-dimensional cell model, a whole stack of images is processed. A three-dimensional microstructure cell with a cell size of 200 × 200 × 200 finite elements is shown in Fig. 5.

3.4 Determination and Validation of Microstructure-Dependent Linear-Elastic, Viscoplastic and Thermal Material Properties

For the FE analysis of the cell models, reliable, temperature-dependent material properties must be assigned to the individual microstructural phases.

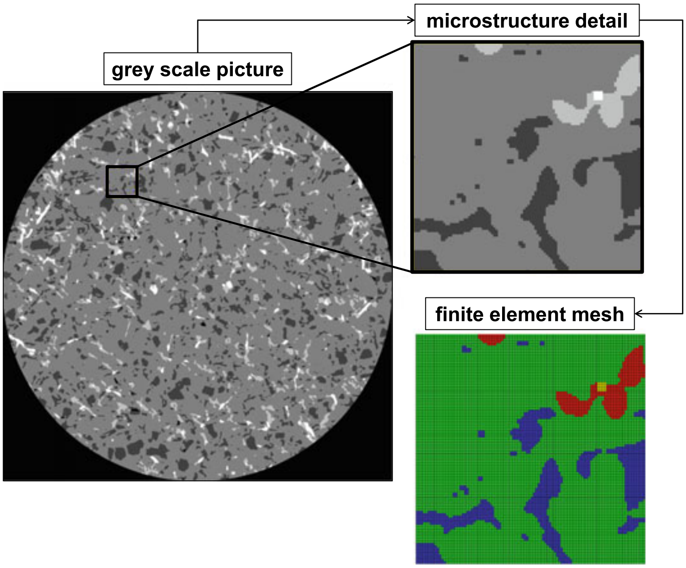

Fig. 4 Reconstruction of a FE mesh based on grey scale pictures. Left: Grey scale picture from nano-CT scan, right top: detail of selected area, right bottom: FE mesh with microstructure information

Fig. 5 Discretized three-dimensional cell model with microstructure information

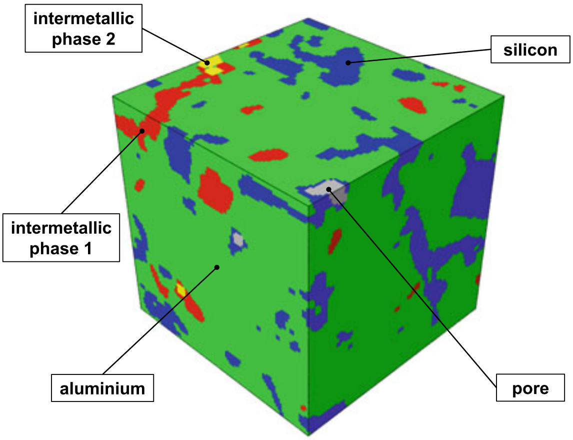

3.4.1 Linear-Elastic Properties

Material properties from the literature are used to describe the linear-elastic material behavior of the respective phases. The Young's modulus E for the AlSi12CuNiMg-T7 alloy is 80 GPa at room temperature, which was determined from the LCF tests in Fig. 2 at half lifetime. Values for aluminium of 69 GPa [1], 70.3 GPa [25] and

84.6 GPa [26] are given in the literature. Based on the literature values, $E = 71.7$ GPa is assigned to the aluminium matrix at room temperature.

For single crystal silicon, the Young's modulus according to Hopcroft et al. [27] is 169 GPa for the $\langle 110\rangle$-direction and 130 GPa for the $\langle 100\rangle$-direction. The value for the $\langle 110\rangle$-direction is almost confirmed by Ang et al. [28] with 163 GPa. According to Ang et al. [28], the modulus of elasticity decreases slightly with temperature, which is also reported in [29–31]. Chen [26] determined a Young's modulus of 148 GPa using nano indentation, which approximately corresponds to the value of 140.3 GPa given in [25]. In [3], literature data in a range between 120 and 165 GPa are reported. Based on the data found in the literature, a value of 148 GPa is applied for silicon at room temperature according to Chen [26]. A slight temperature dependence is taken into account as described in [28].

A list of potential intermetallic phases of the Al–Cu–Fe–Mg–Ni–Si system is given in [32]. The intermetallic phases for comparable AlSi12 alloys are investigated in [6, 26]. According to thermodynamic simulations by Chen [26], three stable intermetallic phases, namely Al_3Ni_2, Al_9FeNi and $Al_5Cu_2Mg_8Si_6$ are formed at a temperature of approximately 540 °C and the Al_7Cu_4Ni phase at approximately 370 °C. In [26], seven intermetallic phases were observed by differential scanning calorimetry tests, which are, in addition to the already mentioned phases, α-AlFeMnSi, the strengthening phase Mg_2Si and Al_2Cu. Moffat [6] traced AlCuNi phases, Mg_2Si and Al_2Cu. Based on energy-dispersive X-ray spectroscopy analyses, the aluminides $Al_3(CuNi)_2$, Al_9FeNi, $Al_{15}(CuFeMn)_3Si_2$, Al_7Cu_4 and Al_2Cu and the magnesium compound Mg_2Si are detected in [3].

Since only two intermetallic phases are separated in the digitized data, the intermetallic phases detected by Chen [26] are split into two groups with different Young's modulus: In the group of "soft" intermetallic phases, the phases Al_2Cu (0.3 wt%) and $Al_5Cu_2Mg_8Si_6$ (1.6 wt%) are described with a modulus of elasticity of 114 GPa. In the group of "hard" intermetallic phases, Al_9FeNi (6.4 wt%), Al_7Cu_4Ni (5.8 wt%) and AlFeMnSi (0.2 wt%) are described with a Young's modulus of 170 GPa. The determined volume fractions of the two phases according to Chen [26] are very similar to what is found in this work.

In order to capture the temperature-dependent material properties of the cast AlSi12CuNiMg-T7 alloy by means of the macroscopic response of the cell model, the microstructure-dependent material properties need to be temperature-dependent too. The slight temperature dependence of silicon is taken into account with the formula given in [28]. The Young's modulus of the aluminium matrix is scaled for elevated temperatures according to the experimentally found relation of the aluminium alloy: i.e. $E(T)/E_{20\,^\circ\mathrm{C}}$. For simplicity reasons, the intermetallic phases are assumed to behave temperature-independent.

For the microstructure-based analysis of the macroscopic elastic response, a voxel based cell of size 200 × 200 × 200 finite elements is calculated. The volume fractions in the cell are very similar to the overall measured volume fractions in the nano-CT scan. The microstructure-based cell is loaded uniaxially in each principal direction perpendicularly to the outer free surface. Thus, three different uniaxial stress states are obtained for which the respective Young's modulus is evaluated. The mean

Fig. 6 Results for the temperature-dependent Young's modulus from experiments and microstructure-based cell simulations

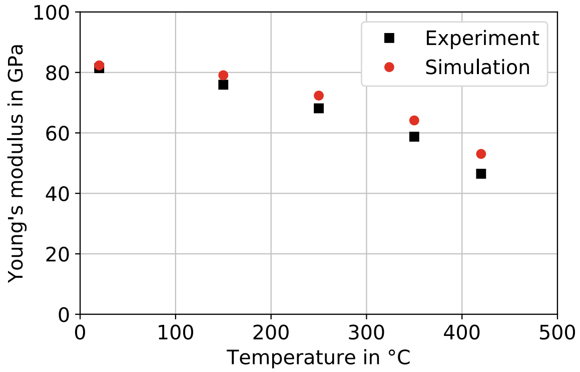

values, compared to the experimental results, are shown in Fig. 6. For all considered temperatures, the modulus of elasticity in the simulation is slightly higher than in the experiment and the deviation increases with increasing temperature. Because the numerical results correspond quite well to the experimental observations no further curve fitting is carried out.

3.4.2 Thermal Properties

In the following, the microstructure-dependent coefficient of thermal expansion is determined for the described cell model. In [26], partially non-isotropic thermal expansion coefficients α_{th} are determined for the different phases of the cast aluminium alloy. In this work, a thermal expansion coefficient of $\alpha_{\mathrm{th}} = 3.7 \cdot 10^{-6}\ 1/\mathrm{K}$ is assumed for silicon, which agrees well with the results in [26]. For the defined intermetallic phase 1, the values given in [26] for intermetallic phases AlFeMnSi, Al_9FeNi and Al_7Cu_4Ni are averaged, that is $\alpha_{\mathrm{th}} = 14.3 \cdot 10^{-6}\ 1/\mathrm{K}$. Averaged values determined by Chen [26] for Al_2Cu phase ($\alpha_{\mathrm{th}} = 17.7 \cdot 10^{-6}\ 1/\mathrm{K}$) are applied to the intermetallic phase 2. The thermal expansion coefficient of the aluminium matrix is considered as an adjustable parameter. The experimental results of the thermophysical analysis of the AlSi12CuNiMg-T7 alloy are shown in Fig. 7 (blue curve).

In order to investigate the thermal expansion of the microstructure-based model, a homogeneous temperature distribution is applied to the cell with an initial temperature of 150 °C and a maximum temperature of 420 °C. The computed macroscopic coefficient of thermal expansion of a first FE simulation is shown in Fig. 7 (orange curve). In a second FE simulation with a slight modification of the thermal expansion coefficient of the aluminium matrix the green curve is obtained that fits very well with the experimental data.

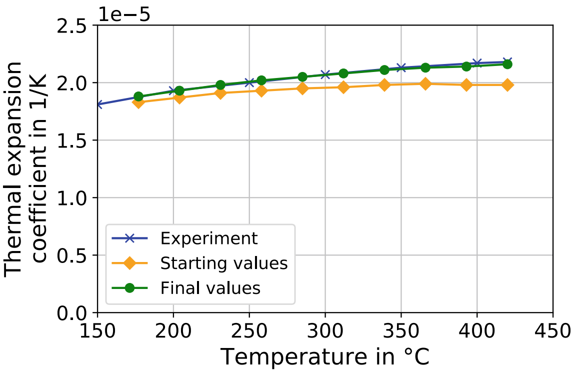

Fig. 7 Thermal expansion coefficients of the reference alloy and the microstructure cell for different temperatures

3.4.3 Viscoplastic Properties

In order to describe the time- and temperature-dependent plasticity of the aluminium matrix, a viscoplastic Chaboche model [33] is used. The model is able to describe the major deformation phenomena at elevated temperatures such as hardening, stress relaxation and recovery processes during dwell times as well as strain rate dependency. For adjusting the parameters of the time-dependent Chaboche model, a triangular, fully reversed loading cycle with a mechanical strain amplitude of $\varepsilon_{\text{a}}^{\text{mech}} = 0.4\%$ with a constant strain rate of $\text{d}\varepsilon/\text{d}t = 10^{-3}\ 1/\text{s}$ is applied to the microstructure cell with its 200 × 200 × 200 finite elements. The macroscopic stresses and strains are evaluated and compared with the experimental hysteresis loops of different LCF tests (see Wöhler curve in Fig. 2). The results of the five investigated temperatures (20, 150, 250, 350 and 420 °C) are shown in Fig. 8.

For all temperatures, the experimental stress-strain-hystereses can be described very well with the microstructure-based material model. For room temperature and 150 °C the strength of the alloy is nearly the same. However, the stresses between 150 and 250 °C reduce significantly. At 420 °C, stresses of only about 40 MPa are reached for the applied strain amplitude and the material tends to loose its hardening behavior. Although the isothermal test results are described very well, there is a significant difference between the experimental results and the FE analysis for the TMF cycle, see Fig. 8f. The elastic parts of the hysteresis loop at the beginning and at the point of load reversal are described well. Thus, the temperature-dependent parameters of the Chaboche model need to be optimised in future works.

4 Microstructure-Dependent Anisotropic Elastic Material Behavior

In this section, the elastic, macroscopic anisotropic material behavior is investigated by means of microstructure-dependent material properties at room temperature. Therefore, 64 different microstructure cells with a respective cell size of 200

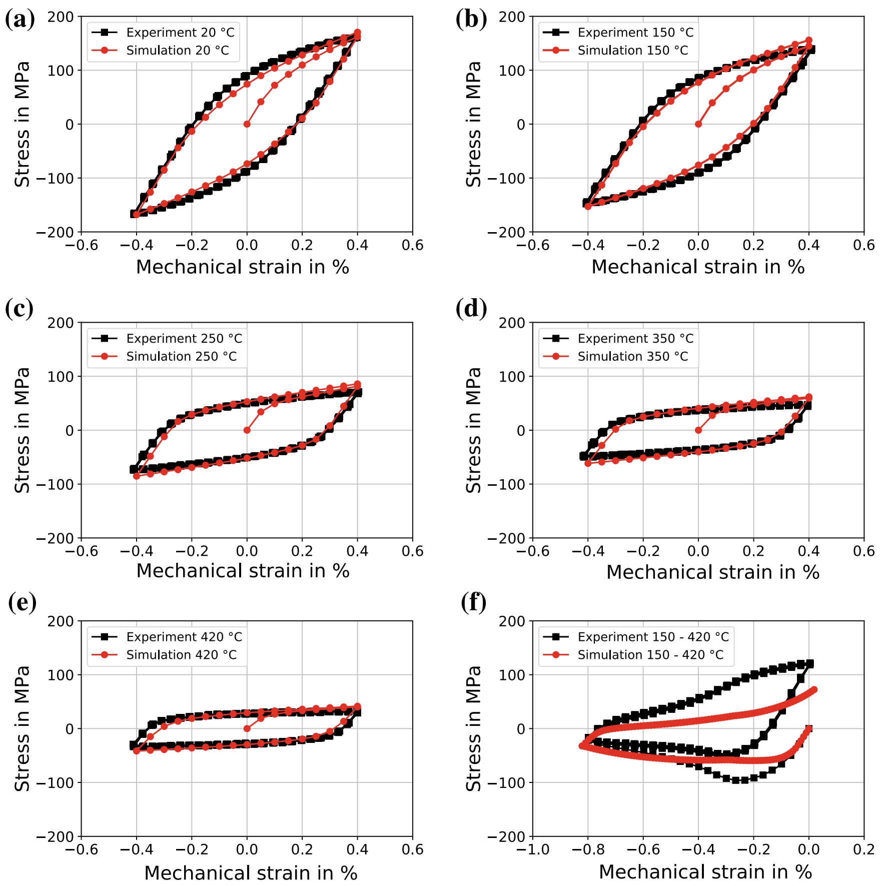

Fig. 8 Comparison of the elastic-viscoplastic deformation behavior between the reference material and the microstructure cell for **a** room temperature, **b** 150 °C, **c** 250 °C, **d** 350 °C, **e** 420 °C and **f** TMF between 150 and 420 °C

$\times\ 200 \times 200$ finite elements are reconstructed from the digitized nano-CT scan (see Fig. 3). Linear-elastic material properties are assigned according to Sect. 3.4. Again, each cell is loaded in the three directions in space normal to its outer surface so that a uniaxial stress state is obtained. The Young's modulus is then evaluated by means of the computed macroscopic uniaxial stress-strain curve. The results of the analyzes are shown in Fig. 9. It is found that the elastic response of the cells is almost independent of the loading direction. The averaged Young's modulus of $E = 82687$ MPa agrees well with the experimental value ($E = 80000$ MPa). The standard deviation of the presented results in Fig. 9 is 1288 MPa, which is about 1.5% of the averaged value of Young's modulus and the maximum deviation that was found in the analyses is 5%.

Fig. 9 Young's modulus as a function of the loading direction and the microstructure cell

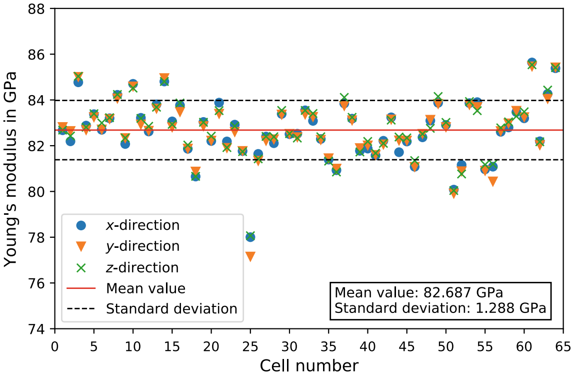

Fig. 10 Correlation of the volume fraction of the microstructure phases with the Young's modulus

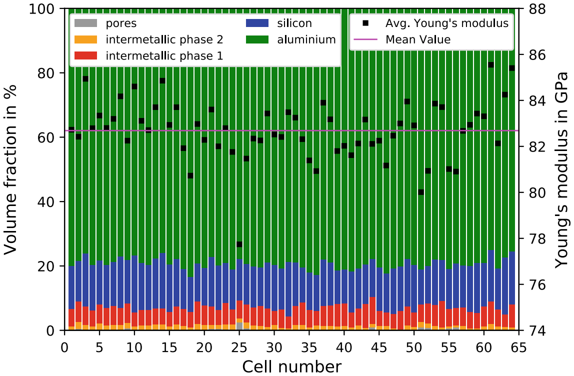

Only the results for cell number 25 deviate significantly from the other results. The deviation can be explained by means of Fig. 10, where the volume fractions of the microstructure phases are plotted against the cell number. The averaged Young's modulus is shown on the right axis and the magenta line marks the mean value for all cells. Cell 25 contains a porosity of approximately 2.6%, while the average value is only 0.17% and thus, a lower value for Young's modulus is obtained in the analyses. Figures 9 and 10 indicate, that a high percentage of hard phases (i.e. cells 61 and 64 with >15% silicon and >7% intermetallic phase 1) leads to an increased macroscopic Young's modulus, while the porosity (i.e. cells 51, 52, 55 and 56 with porosity between 0.72 and 0.95%) and a high percentage of aluminium matrix (i.e. cells 18 and 36 with >82% aluminium matrix) lead to a reduction of the macroscopic Young's modulus.

5 Microstructure-Dependent Thermal FE Analyses

Due to the mismatch in the thermal expansion behavior of the individual phases, mechanical (in)elastic strains and stresses can arise locally. In this section, the reconstructed microstructure-dependent cell is loaded with a homogeneous temperature distribution between 150 and 420 °C with a temperature rate of 10 K/s at zero macroscopic stresses. Two simulations are performed: One with microstructure-dependent linear-elastic material behavior and one with additionally elastic-viscoplastic material behavior for the aluminium matrix. In Fig. 11, the locally resolved maximum principal stress state of the microstructure-dependent cell from Fig. 5 is plotted after heating up from 150 to 420 °C in Fig. 11a for linear-elastic material behavior and in Fig. 11b for elastic-viscoplastic material behavior. For the linear-elastic material properties, high stresses localize around the complex shaped microstructure phases and in the near surrounding aluminium matrix. The local arising stresses in the microstructure phases are reduced significantly in the simulation with the elastic-viscoplastic material behavior.

Figure 12 shows the microstructure (upper figure) and the respective stress distribution for the linear-elastic analysis (lower left figure) and the simulation with the elastic-viscoplastic material law (lower right figure) for the aluminium matrix at 420 °C. The stresses are highly concentrated in a silicon particle with a rather bottleneck like geometry. In the linear-elastic simulation, the hard phases are consistently higher and uniformly loaded than in the simulation with the elastic-viscoplastic material behavior for the aluminium matrix due to the fact that the surrounding aluminium matrix is able to transfer also higher stresses. In the more realistic elastic-viscoplastic simulation, the particle stresses in the linear-elastic analysis of about 800 MPa are significantly reduced to approximately 400 MPa due to the plastic deformation of the matrix. In the elastic-viscoplastic simulation the particle stress is centered more locally, which leads to higher maximum principal stress values at the bottleneck than in the linear-elastic simulation.

The distribution of the accumulated plastic strain in Fig. 13 shows that the plastic strain in the aluminium matrix localizes in the surrounding of the hard particles and in dependence on their local morphology.

The first results indicate that the thermal mismatch between silicon and aluminium yields to not negligible stresses in the material, which are localized at points with complex microstructure morphology. In the following, the distribution of the stresses in the aluminium matrix and the silicon particles is analyzed for the whole microstructure cell statistically. As characteristic quantity the computed von Mises stress is evaluated at each integration point for the aluminium matrix and the maximum principal stress for the silicon particles. In Figs. 14 and 15, the computed stresses are compared at three different temperatures during the thermal cycle. Figure 14 shows the results of the FE simulation with the linear-elastic material model. The stresses in the silicon particles increase with the temperature (see Fig. 14a). At 250 °C, the max-

Fig. 11 Comparison of the macroscopic behavior of the microstructure cell at a temperature of 420 °C: **a** linear-elastic material behavior and **b** elastic-viscoplastic material behavior

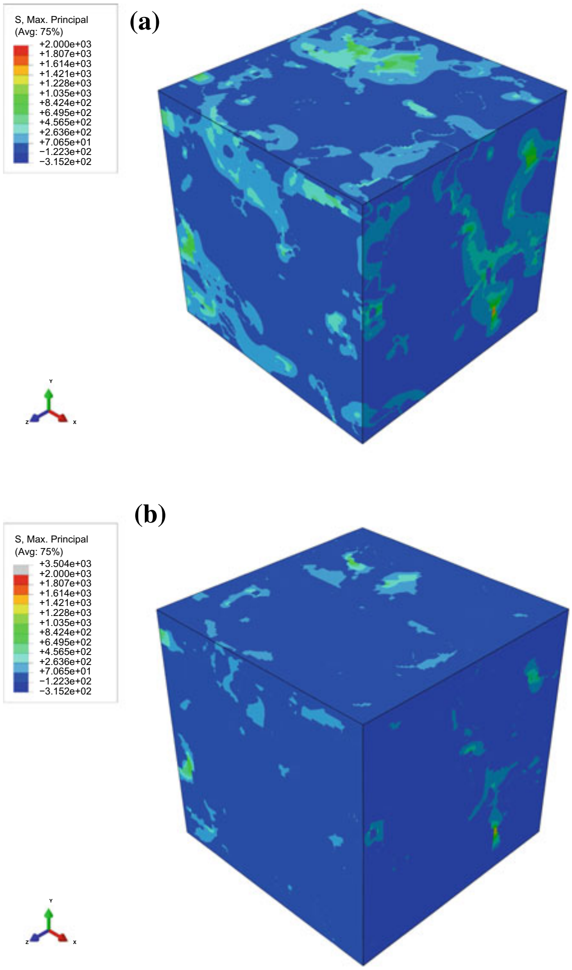

imum frequency occurs at a principal stress of 200 MPa, at 350 °C nearly at 400 MPa and at 420 °C at almost 500 MPa. The frequency distribution is shifted to higher stresses for higher temperatures. The plot of the cumulative frequency distribution in Fig. 14b shows that the overall stress level is increased with temperature. Maximum stresses above 1000 MPa are reached at a temperature of 420 °C. This means, that the mismatch in the coefficient of thermal expansion between the individual phases dominates the drop in Young's modulus with increasing temperature. The stress distribution in the aluminium matrix is shown in Fig. 14c, d. Higher stresses in the aluminium matrix occur with increasing temperature. The maximal frequency is almost independent of the temperature and is located at approximately 50 MPa (see Fig. 14c). In comparison to the computed stresses in the silicon phase, the stresses in the aluminium matrix are equally distributed for 350 °C and 420 °C (see Fig. 14d). Since the

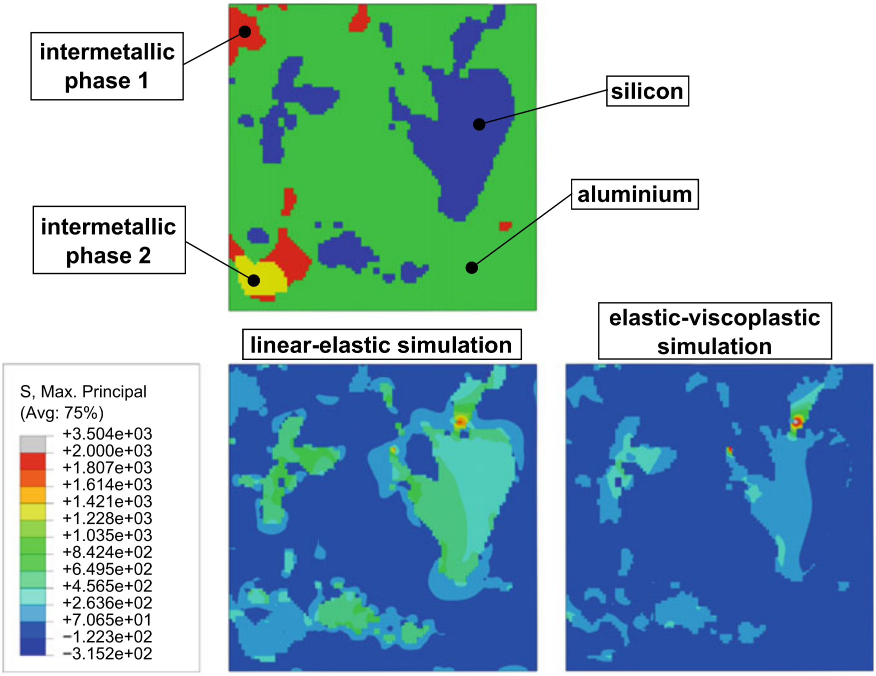

Fig. 12 Comparison of the maximal principal stress fields for the linear-elastic and elastic-viscoplastic simulation at 420 °C

Fig. 13 Distribution of the accumulated plastic strain at 420 °C

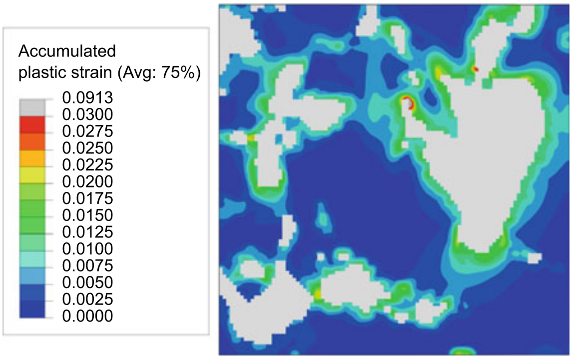

stresses exceed the temperature-dependent yield stress σ_Y of the AlSi12CuNiMg-T7 alloy significantly (i.e. 58 MPa at 250 °C, 40 MPa at 350 °C, 29 MPa at 420 °C) a simple linear-elastic FE analysis is not sufficient to study microstructure-dependent resulting stresses in the individual phases due their thermal mismatch.

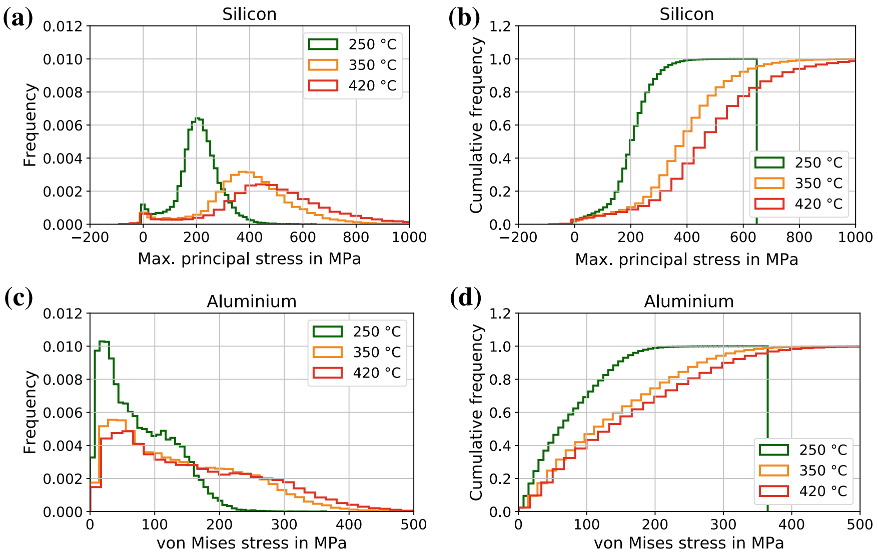

Fig. 14 Stress distribution in the silicon particles (**a**/**b**) and in the aluminium matrix (**c**/**d**) at different temperatures for the linear-elastic FE analyses

If the deformation behavior of the aluminium matrix is described with the viscoplastic Chaboche model, the stresses in the silicon particles are generally reduced. The maximum frequency in Fig. 15a has a corresponding stress value of 120 MPa for all three investigated temperatures. The stresses increase slightly with higher temperature (Fig. 15b), with hardly any difference between 350 and 420 °C. However, at these two temperatures, maximum stresses above 800 MPa are reached at some integration points of the silicon phase in the considered microstructure cell. Figure 15c, d show the stress distribution in the aluminium matrix. The stress level is now bounded and thus significantly reduced in comparison to the linear-elastic FE simulation. Furthermore, the stresses are now even reduced with increasing temperature. At 250 °C, the maximal frequency occurs at 45 MPa and at 25 MPa for 420 °C. This trend is also shown in the cumulative plot in Fig. 15d.

Finally, the results of the linear-elastic and the elastic-viscoplastic simulation are compared for 420 °C in Fig. 16. Figure 16a shows the results for the silicon particles and Fig. 16b for the aluminium matrix. Both graphs demonstrate that the stress level is significantly reduced due to the viscoplastic material behavior that is used for the aluminium matrix. In addition, the distribution is shifted to lower stresses for both phases.

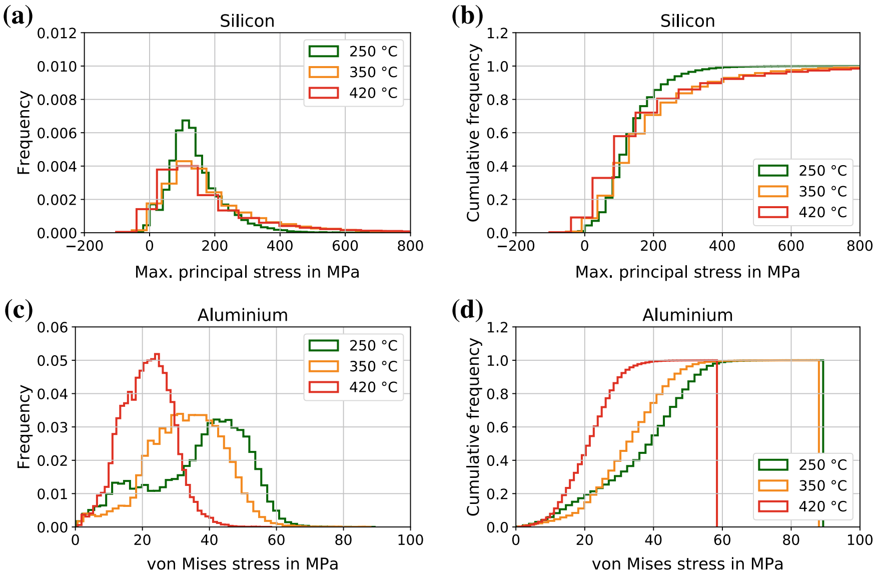

Fig. 15 Stress distribution in the silicon particles (**a**/**b**) and in the aluminium matrix (**c**/**d**) at different temperatures for the elastic-viscoplastic FE analyses

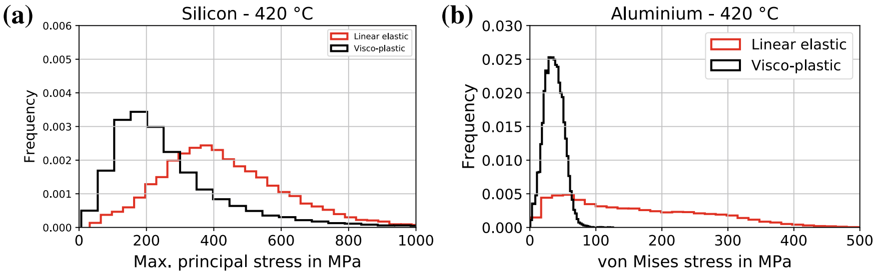

Fig. 16 Comparison of the stress distribution in the **a** silicon particles and in the **b** aluminium matrix at 420 °C for the linear-elastic and elastic-viscoplastic FE analyses

6 Summary and Conclusions

In this paper, microstructure-based analyses of the cast aluminium alloy AlSi12CuNiMg-T7 are presented. This alloy exhibits a complex microstructure morphology consisting of aluminium matrix, large primary silicon particles, various intermetallic phases and pores. A representative microstructure is digitized with nano-CT technology. In the nano-CT scan, the aluminium matrix, silicon particles, pores and two intermetallic phases are detected. With the digitized data, three-dimensional, microstructure-based cell models are reconstructed for the FE simulation in ABAQUS/Standard. Linear-elastic and thermal material properties for the microstructure phases from literature are assigned and viscoplastic material properties for the aluminium matrix are adapted to experimental half lifetime hysteresis loops of LCF and TMF tests.

Microstructure cells with 200 × 200 × 200 elements show nearly isotropic material behavior. The macroscopic deformation behavior of the aluminium alloy can be described very well with the microstructure-dependent microscopic material behavior. The microstructure cell is subjected to a thermal cycle between 150 and 420 °C. During heating and cooling under zero force, high stresses at the interfaces of silicon particles and the aluminium matrix occur due to the thermal mismatch of the two phases. In the linear-elastic simulation, high stress levels appear in all microstructure features. Elastic-viscoplastic material behavior of the aluminium matrix leads to a stress relief in the silicon particles and inelastic deformation occurs in the aluminium matrix. Thus, it can be concluded, that advanced plasticity models are necessary for reliable FE analyses.

The simulations predict significant high stresses in the silicon particles preferentially at points with complex shaped geometries. A significant amount of the particle areas is loaded beyond the fracture stress of 200 MPa given in [34]. The debonding of silicon particles at high temperatures is not considered yet, which is observed in fractographical investigations. Debonding between the silicon particles and the aluminium matrix could release the overall stresses and thus predict an even more realistic stress distribution in the microstructure.

The next step is to optimize the Chaboche model parameters, so that also TMF experiments can be described well. In order to analyze the damage caused by thermal fatigue, the heat transfer from the combustion process into the material has to be investigated more in detail. The gained knowledge about the temperature-dependent crack growth interaction between the aluminium matrix and the other microstructural phases can then be hopefully transferred establishing a mechanism- and microstructure-based lifetime model for the presented class of cast aluminium alloys.

Acknowledgements The authors from the Fraunhofer Institute for Mechanics of Materials IWM would like to thank Simon Zabler from the project group NanoCT Systeme at the Fraunhofer Institute for Integrated Circuits IIS in Würzburg and Maximilian Ullherr from the University of Würzburg for the digitization of the microstructure volume and the segmentation of the respective data.

References

1. Gao, Y.X., Yi, J.Z., Lee, P.D., et al.: A micro-cell model of the effect of microstructure and defects on fatigue resistance in cast aluminium alloys. Acta Materalia **52**, 5435–5449 (2004)
2. Teranishi, M., Kuwazuru, O., Gennai, S., et al.: Three-dimensional stress and strain around real shape Si particles in cast aluminum alloy under cylic loading. Mater. Sci. Eng. A **678**, 273–285 (2016)

3. Krätschmer, D.M.: Bewertung mikrostruktureller Werkstoffschädigung bei Schwingbeanspruchung mit stochastischen Methoden. Ph.D. Thesis, University of Stuttgart, Germany (2011)
4. Gall, K., Horstemeyer, M.F., McDowell, D.L., et al.: Finite element analysis of the stress distributions near damaged Si particle clusters in cast Al–Si alloys. Mech. Mater. **32**, 277–301 (1999)
5. Kenningley, S., Morgenstern, R.: Transient mircomechanical deformation and thermomechanical fatigue damage in AlSi based piston alloys under superimposed high cycle mechanical and low cycle thermal loading. Mater. Test. **57**, 155–159 (2015)
6. Moffat, A.J: Micromechanistic analysis of fatigue in aluminium silicon casting alloys. Ph.D. Thesis, University of Southampton, Great Britain (2007)
7. Fan, J., McDowell, D.L., Horstemeyer, M.F., et al.: Computational micromechanics analysis of cyclic crack-tip behavior for microstructurally small cracks in dual-phase Al–Si alloys. Eng. Fract. Mech. **68**, 1687–1706 (2001)
8. McDowell, D.L., Gall, K., Horstemeyer, M.F., et al.: Microstructure-based fatigue modeling of cast A356–T6 alloy. Eng. Fract. Mech. **70**, 49–80 (2003)
9. Needleman, A., Tvergaard, V.: An analysis of ductile rupture modes at a crack tip. J. Mech. Phys. Solids **35**(2), 151–183 (1987)
10. Chawla, N., Chawla, K.K.: Microstructure-based modeling of the deformation behavior of particle reinforced metal matrix composites. J. Mater. Sci. **41**, 913–925 (2006)
11. Chawla, N., Sidhu, R.S., Ganesh, V.V.: Three-dimensional visualization and microstructure-based modeling of deformation in particle-reinforced composites. Acta Materialia **54**, 1541–1548 (2006)
12. Ganesh, V.V., Chawla, N.: Effect of particle orientation anisotropy on the tensile behavior of metal matrix composites: experiments and microstructured-based simulation. Mater. Sci. Eng. A **391**, 342–353 (2005)
13. Chawla, N., Deng, X.: Microstructure and mechanical behavior of porous sintered steels. Mater. Sci. Eng. A **390**, 98–112 (2005)
14. Metzger, M., Seifert, T.: Computational assessment of the microstructure-dependent plasticity of lamellar gray cast iron - Part I: methods and microstructure-based models. Int. J. Solids Struct. **66**, 184–193 (2015)
15. Dezecot, S., Maurel, V., Buffiere, J.Y., et al.: 3D characterization and modeling of low cycle fatigue damage mechanisms at high temperature in a cast aluminium alloy. Acta Materialia **123**, 23–34 (2017)
16. Eckmann, S.: Entwicklung eines Finite-Elemente-Mikrostrukturmodells zur Untersuchung des Schädigungsverhaltens einer AlSi-Legierung. Seminar paper, University of Applied Sciences Offenburg, Germany (2014)
17. Asghar, Z., Requena, G., Degischer, H.P., et al.: Three-dimensional study of Ni aluminides in an AlSi12 alloy by means of light optical and synchrotron microtomography. Acta Materalia **57**, 4125–4132 (2009)
18. Schneiders, R., Schindler, R., Weiler, F.: Octree-based generation of hexahedral element meshes. In: Proceedings of the 5th International Meshing Roundtable (1996)
19. Owen, S.J., Brown, J.A., Ernst, C.D., et al.: Hexahedral mesh generation for computational materials modeling. Procedia Eng. **203**, 167–179 (2017)
20. Fan, J., McDowell, D.L., Horstemeyer, M.F., et al.: Cyclic plasticity at pores and inclusions in cast Al–Si alloys. Eng. Fract. Mech. **70**, 1281–1302 (2003)
21. Hill, R.: On constitutive macro-variables for heterogeneous solids at finite strains. Proceeding R. Soc. A **326**, 131–147 (1972)
22. Suquet, P.: Elements of homogenization theory for inelastic solid mechanics. In: Sanchez-Palencia, E. (eds.) Homogenization Techniques for Composite Media, pp. 194–275. Springer, Berlin (1987)
23. Python. https://www.python.org/ Accessed 18 Feb 2019
24. ABAQUS 6.14 Documentation

25. Smith, J.F., Zheng, S.: High temperature nanoscale mechanical property measurements. Surf. Eng. **16**(2), 143–146 (2000)
26. Chen, C.L.: Characterisation of intermetallic phases in multicomponent Al–Si alloys for piston applications. Ph.D. Thesis, Loughborough University, Great Britain (2006)
27. Hopcroft, A., Nix, W.D., Kenny, T.W.: What is the Young's modulus of silicon? J. Microelectromechanical Syst. **19**, 229–238 (2010)
28. Ang, W.C., Kroplinicki, P., Soe, O., et al.: Novel development of the micro-tensile test at elevated temperature using a test structure with integrated micro-heater. J. Micromechanics Microengineering **22**, 085015 (2012)
29. Cho, C.H.: Characterization of Young's modulus of silicon versus temperature using a "beam deflection" method with a four-point bending fixture. Curr. Appl. Phys. **9**(2), 538–545 (2009)
30. Nakao, S., Ando, T., Shikida, M., et al.: Mechanical properties of a micron-sized SCS film in a high-temperature environment. J. Micromechanics Microengineering **16**, 715–720 (2006)
31. Namazu, T., Isono, Y., Tanaka, T.: Plastic deformation of nanometric single crystal silicon wire in AFM bending test at intermediate temperatures. J. Microelectromechanical Syst. **11**(2), 125–135 (2002)
32. Belov, N.A., Eskin, D.G., Avxentieva, N.N.: Constituent phase diagrams of the Al–Cu–Fe–Mg–Ni–Si system and their application to the analysis of aluminium piston alloys. Acta Materialia **53**, 4709–4722 (2005)
33. Chaboche, J.L.: Constitutive equations for cyclic plasticity and cyclic viscoplasticity. Int. J. Plast. **5**, 247–302 (1989)
34. Hirsch, P.B., Roberts, S.G.: The brittle-ductile transition in silicon. Philos. Mag. **64**(1), 55–80 (1991)

Problems of Thick Functionally Graded Material Structures Under Thermomechanical Loadings

Artur Ganczarski and Damian Szubartowski

Abstract The present work is an extensive overview of several aspects of thick FGM structures subjected to thermomechanical loadings. The concept of reducing the full 3D thermo-mechanical FGM problem to the plane stress one is demonstrated in case of both classical and quasi- polar continua. Theorem on the stress free deformation accompanying linear gradation of thermomechanical properties of the material staying in constant temperature condition is presented. The influence of several approximations of FGM thermal barrier coatings on the temperature and stress distributions in thick-walled cylinder including FGM Thermal Barrier Coating is considered. A special graded finite element to discretize FGM properties is introduced.

1 Introduction

Functionally graded materials are special composite materials that have continuous and smooth spatial variations of physical and mechanical properties. An essential improvement of their thermomechanical properties such as coefficient of thermal conductivity, coefficient of thermal expansion or Young's modulus and simultaneous removal of thermomechanical mismatch allow for application in many fields such as high performance engines for aerospace vehicles, turbine blades and heat-resisting tools.

Numerous closed-form solutions of thermo-elastic plane problems of FGMs take advantage of specific power or exponential function in approximation methods of multi-layered composite plates. All above limitations can be overcome with general-

---

A. Ganczarski (✉) · D. Szubartowski
Institute of Applied Mechanics, Cracow University of Technology,
Al. Jana Pawła II 37,
30-860 Kraków, Poland
e-mail: artur.ganczarski@pk.edu.pl

D. Szubartowski
e-mail: dszubartowski@pk.edu.pl

K. Naumenko and M. Krüger (eds.), *Advances in Mechanics of High-Temperature Materials*, Advanced Structured Materials 117,
https://doi.org/10.1007/978-3-030-23869-8_3

ization of a theorem on the plane stress state in an isotropic thermo-elastic thick plate as is done by Sneddon and Lockett [27]. The authors presented convinced proof for a problem of semi-infinite thermo-elastic medium bounded by two parallel planes and loaded by an arbitrary temperature field on one surface. The method of employed solution was the double Fourier transforms. The results confirmed solution of analogous problems, being inspiration to their work, received earlier by Sternberg and McDowell [28], based on Green's function, and by Muki [17], who used method combining the theory of Fourier series and the Hankel transforms of integral order.

Contrary to aforementioned broad stream of papers, the number of works concerning fully 3D problems, like thick plate, semi-space or thick-walled vessels, is rather limited. Hence, let us mention several of them in chronological order. Senthil and Batra [26] analyzed 3D thermomechanical deformation of simply supported rectangular plate loaded by a temperature impulse. Authors applied Laplace's transform in order to reduce set of uncoupled and quasi-static equations of linear thermo-elasticity to the set ordinary differential equations containing power functions of effective thermomechanical constants. Magnitudes of aforementioned constants (bulk and shear modules, coefficients of thermal conductivity and expansion) were described by Mori–Tanaka or Self-Consistent rules and were directly dependent on a volume fraction of components (Al/SiC).

Next work by Batra [2] deals with functionally graded cylinders and spheres made of incompressible linearly elastic material. Author proved that the optimal magnitude of circumferential stress refers to the linear function of Kirchhoff's modulus along radial direction.

Dai et al. [6] applied the Meshless Method to active control and dynamic response of a plate supplied with piezoelectric sensors and actuators. Authors considered functionally graded plates made of ZrO_2 and aluminium alloy for which the volume fraction was changed along their thickness according to a power law. In order to determine shape functions the Meshless Galerkin Method was used.

Problem of transversely isotropic, functionally graded, piezoelectric half-space was presented by Pan and Han [20]. Authors introduced original concept based on graded Green's functions in order to better capturing of displacement, stress and electric potential fields in following functionally graded structures: PZT-4 half-space, functionally graded PZT-4 layer deposed on homogeneous substrate made of $BaTiO_3$. This work can be treated as a perfect generalization of paper by Sternberg and McDowell [28] since full analogy between electric potential and temperature fields appears.

Wang et al. [33] considered problem of functionally graded half-space subjected to a point heat source. In order to describe thermal conductivity, which changes in exponential manner along arbitrary direction, authors introduced 3D Green's functions.

Exact solution of thermo-elastic, thick, circular FGM plate was published by Jabbari et al. [12]. All material constants except Poisson's ratio were considered as exponential functions of thickness direction. Assuming rotational symmetry of the problem, authors presented exact analytical solution that comprised: temperature distribution, displacement and stress component fields for metallic phase Ti-6Al-4V and ceramic ZrO_2.

Yang et al. [36] presented new approach to 2D and 3D analyses of thermal stress in FGM's by use of analytical terms in Boundary Element integration. Application of fundamental Kelvin's solutions led to integral equations which comprised both inhomogeneity and temperature change. Next authors demonstrated efficiency of this approach solving problem of hexagonal prism. Discussed method, mainly based on BEM, is competitive to conventional FEM since saves over 60% computational time.

Kulikov and Plotnikova [14] presented new method of Sampling Surfaces applied to 3D multi-layered, FG plates under thermomechanical loadings. Aforementioned method is based on a choose of sampling surface for each laminate layer, at which temperature and displacement are treated as fundamental variables. Uniform convergence of the method is guaranteed by location of discussed surfaces inside each laminate layer, directly in nodes of Chebyshev's polynomials. Among authors whose works have been published recently or will be published in the nearest future it is worth to mention following: Seifi [25], Sburlati et al. [23], Popovych and Kalynyak [22], Manthena [16], Wang and Qin [34].

2 Technological and Numerical Problems of FGM's

The concept of FGM is based on a spatial gradient of physical and mechanical properties that allows to eliminate stress mismatch at the interface. The spatial gradient is achieved by mixture of composite constituents, the volume fraction of which varies spatially such that the effective thermo-mechanical properties change smoothly from one material (ceramic) to the other (metal). In this way, in the case of a Thermal Barrier Coating deposited on a metallic substrate, the heat-resistant ceramic layer and the solid metal are separated by functionally graded FG layer, the composition of which varies from pure ceramic to pure metal. As regards FG layer processing, Plasma Spray Thermal Barrier Coating leads to lamellar microstructures, whereas columnar-lamellar micro-structures are produced when using Electron Beam Physical Vapour Deposition, see Fig. 1a. Two other methods of fabrication FGMs share common base material, which is of the granular nature. In the first one, subsequent layers of FGM powder material are superimposed one onto another, and next all consolidated in conditions of high pressure and elevated temperature. Typical limitations accompanying an application of this method are necessity of forming complete element and requirement of different temperatures applied to subsequent layers of powder, see Fig. 1b. Aforementioned method is mainly used in manufacturing of electronic part based on silicon. In the other one, called 3D printing, printing heads spread functional inks containing nanoparticles, see Fig. 1c. Both methods give FGMs of

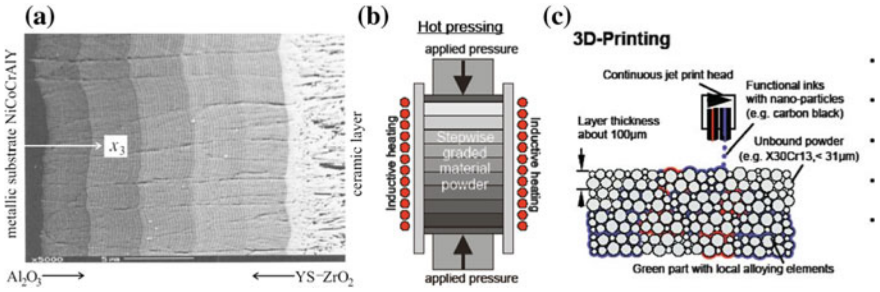

Fig. 1 Methods of fabrication FGMs: **a** microstructure of chemically graded electron beam physical vapour deposition thermal barrier coating, see Schulz et al. [24], **b** hot pressing, see Trumble [31], **c** 3D printing, see [35]

specific microstructure, in which sintered grains of powder or bounded nanoparticles may exhibit deformation typical for quasi-polar continuum.

When the classical FEM based on homogeneous elements is used for FGMs, the material properties stay the same for all integration points belonging to one finite element. This means that material properties may vary in a piecewise continuous manner, from one element to the other, and a unique possibility to model FGM structure is approximation by use of appropriately fine mesh. On the other hand, a too coarse mesh may lead to unrealistic stresses at the interface between the subsequent layers. To overcome this difficulty a special graded element has been introduced by Kim and Paulino [13] to discretize FGM properties. The material properties at Gauss quadrature points are interpolated there from the nodal material properties by the use of isoparametric interpolation functions. Contrary to the classical FEM formulation, the stiffness matrix of an element is expressed by the integral, in which constitutive matrix is a function of the coordinates. In the original formulation the same shape functions are used for approximation of the displacement field and material inhomogeneity. However, from the numerical point of view nothing stands in the way of implementation of shape functions referring directly to the individual character of inhomogeneity, for instance power functions or exponential functions.

3 Conditions of Plane Stress State

3.1 Classical Thermo-Elastic Continuum

A thermo-elastic three-layer plate under a temperature field $T + \theta(x_3)$, where T is the temperature of the solid corresponding to zero stress and strain is considered, see Fig. 2. The FGM interface of thermomechanical properties such as α, k, G and E are arbitrary functions of x_3. Surfaces of the plate are free from tractions and there are

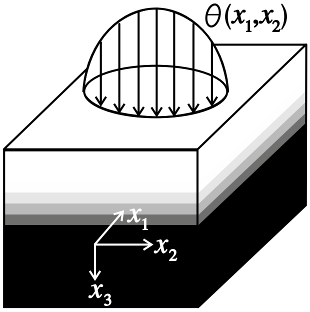

Fig. 2 Thermo-elastic three-layer plate with FGM interface under thermal loading

no body forces. The system of equations of uncoupled thermo-elasticity expressed in displacements format

$$
\begin{aligned}
&\nabla^2\theta + \frac{1}{k}\frac{\partial k}{\partial x_3}\frac{\partial \theta}{\partial x_3} = 0\\
&\nabla^2 u_i + \frac{1}{1-2}\frac{\partial \Theta}{\partial x_i} + \frac{1}{G}\frac{\partial G}{\partial x_3}\left(\frac{\partial u_i}{\partial x_3} + \frac{\partial u_3}{\partial x_i}\right) = 2\frac{1+\nu}{1-2\nu}\frac{\partial(\alpha\theta)}{\partial x_i} \qquad \forall\, i = 1,2\\
&\nabla^2 u_3 + \frac{1}{1-2\nu}\frac{\partial \Theta}{\partial x_3} + \frac{2}{G}\frac{\partial G}{\partial x_3}\left(\frac{\partial u_3}{\partial x_3} + \frac{\nu\Theta}{1-2\nu}\right) = 2\frac{1+\nu}{1-2\nu}\left[\frac{\partial(\alpha\theta)}{\partial x_3}\right.\\
&\qquad \left. + \frac{1}{E}\frac{\partial E}{\partial x_3}\alpha\theta\right]
\end{aligned}
\tag{1}
$$

where u_i denotes the displacement vector, $\Theta = \mathrm{div} u_i$ is the dilatation, whereas θ stands for temperature change. To solve Eqs. (1) the following potential, originally proposed by Iljushin et al. [11], is introduced

$$
\begin{aligned}
u_i &= \frac{\partial \phi}{\partial x_i}, & f(x_3) &= A x_3^2 + B x_3 + C\\
u_3 &= -\frac{\partial \phi}{\partial x_3} + f(x_3), & \alpha\theta &= 2\frac{1-\nu}{1+\nu}A x_3 - \frac{1}{1+\nu}\frac{\partial^2 \phi}{\partial x_3^2}
\end{aligned}
\tag{2}
$$

where function of displacement potential ϕ is of harmonic type $\nabla^2\phi = 0$ and A, B, and C are constants. Simple introducing of definitions (2)–Eqs. $(1)_{2-3}$ shows that only equations of mechanical state

$$\begin{aligned}&\frac{\partial}{\partial x_i}\Big(\underbrace{\nabla^2\phi}_{=0}\Big)+\frac{1}{1-2\nu}\Big(\underbrace{\nabla^2\phi}_{=0}-2\frac{\partial^2\phi}{\partial x_3^2}+2Ax_3+B\Big)+\frac{1}{G}\frac{\partial G}{\partial x_3}\\&\quad\times\Big(\underbrace{\frac{\partial^2\phi}{\partial x_3\partial x_i}-\frac{\partial^2\phi}{\partial x_i\partial x_3}}_{=0}\Big)=2\frac{1+\nu}{1-2\nu}\left(-\frac{1}{1+\nu}\frac{\partial^3\phi}{\partial x_i\partial x_3^2}\right)\qquad\forall\, i=1,2\end{aligned}\tag{3}$$

$$\begin{aligned}&-\frac{\partial}{\partial x_3}\Big(\underbrace{\nabla^2\phi}_{=0}\Big)+2A+\frac{1}{1-2\nu}\frac{\partial}{\partial x_3}\Big(\underbrace{\nabla^2\phi}_{=0}-2\frac{\partial^2\phi}{\partial x_3^2}+2Ax_3+B\Big)\\&+\frac{2}{G}\frac{\partial G}{\partial x_3}\Big[-\frac{\partial^2\phi}{\partial x_3^2}+2Ax_3+B+\frac{1}{1+\nu}\Big(\underbrace{\nabla^2\phi}_{=0}-2\frac{\partial^2\phi}{\partial x_3^2}+2Ax_3+B\Big)\Big]\\&=2\frac{1+\nu}{1-2\nu}\left[2\frac{1-\nu}{1+\nu}A-\frac{1}{1+\nu}\frac{\partial^3\phi}{\partial x_i\partial x_3^2}+\frac{1}{E}\frac{\partial E}{\partial x_3}\left(2\frac{1-\nu}{1+\nu}Ax_3-\frac{1}{1+\nu}\frac{\partial^3\phi}{\partial x_i\partial x_3^2}\right)\right]\end{aligned}$$

are satisfied as identity, contrary to the case of homogeneous material when also the equation of thermal state is satisfied as identity. The stress components referring to the plane stress state with respect to axis x_3

$$\tau_{i3}=G\left(\frac{\partial u_i}{\partial x_3}+\frac{\partial u_3}{\partial x_i}\right)=G\Big(\underbrace{\frac{\partial^2\phi}{\partial x_i\partial x_3}-\frac{\partial^2\phi}{\partial x_3\partial x_i}}_{=0}\Big)=0\qquad\forall\, i=1,2$$

$$\begin{aligned}\sigma_{33}&=2G\left[\frac{\partial u_3}{\partial x_3}-\alpha\theta+\frac{\nu}{1-2\nu}(\Theta-3\alpha\theta)\right]=2G\left\{-2\frac{\partial^2\phi}{\partial x_3^2}+2Ax_3+B\right.\\&-2\frac{1-\nu}{1+\nu}Ax_3+\frac{1}{1+\nu}\frac{\partial^2\phi}{\partial x_3^2}+\frac{\nu}{1-2\nu}\Big[\underbrace{\nabla^2\phi}_{=0}-2\frac{\partial^2\phi}{\partial x_3^2}+2Ax_3+B\\&\left.-3\left(2\frac{1-\nu}{1+\nu}Ax_3-\frac{1}{1+\nu}\frac{\partial^2\phi}{\partial x_3^2}\right)\Big]\right\}=2G\frac{1-\nu}{1-2\nu}B\end{aligned}\tag{4}$$

are also identically equal to zero when $B=0$ for any point x_i, what proves that Eqs. (2) transform original mechanical problem Eq. $(1)_{2-3}$ into plane stress one (see Ganczarski and Szubartowski [10])

$$\nabla^2\phi+2(1-\nu)Ax_3-(1+\nu)\alpha\theta=0\tag{5}$$

The general solution of Eq. (5) can be written in a form which is more suitable to plate problems, in which the thermo-elastic solid is bounded by two parallel planes $x_3=z$ and exhibits axial symmetry

$$\frac{\partial^2\phi}{\partial r^2}+\frac{1}{r}\frac{\partial\phi}{\partial r}+2(1-\nu)Az-(1+\nu)\alpha\theta=0 \tag{6}$$

Differentiation of Eq. (6) with respect to r and next substitution $u=\frac{\partial\phi}{\partial r}$, according to Eqs. $(2)_1$, lead to the classical Euler-type differential equation describing thermo-mechanical membrane state

$$\frac{\partial^2 u}{\partial r^2}+\frac{1}{r}\frac{\partial u}{\partial r}-\frac{u}{r^2}=(1+\nu)\frac{\partial(\alpha\theta)}{\partial r} \tag{7}$$

Unique solution of equation (7) that satisfies homogeneous boundary conditions $u(0)=0, \sigma_r(R)=0$ takes well known form

$$\begin{aligned} u &= \frac{1-\nu}{R^2}r\int_0^R \alpha\theta r\mathrm{d}r+\frac{1+\nu}{r}\int_0^r \alpha\theta\xi\mathrm{d}\xi \\ \sigma_r &= \frac{E}{R^2}\int_0^R \alpha\theta r\mathrm{d}r-\frac{E}{r^2}\int_0^r \alpha\theta\xi\mathrm{d}\xi \\ \sigma_\varphi &= \frac{E}{R^2}\int_0^R \alpha\theta r\mathrm{d}r+\frac{E}{r^2}\int_0^r \alpha\theta\xi\mathrm{d}\xi-E\alpha\theta \end{aligned} \tag{8}$$

which in case of constant temperature θ =const and linear gradation of coefficient of thermal expansion $\alpha(z)=a_0+a_1z$ leads to purely linear (stress-less) deformation $u(r,z)=\alpha\theta(z)r, \sigma_r=\sigma_\varphi\equiv 0$, what will be proven by use of stress formulation in Sect. 4.

3.2 Quasi-micro-polar Continuum

Methods of FGM fabrication, like high pressure consolidation of powder or 3D printing, reveal the granular nature of material. In other words, the classical deformation may be accompanied by additional rotation of a local particle equal to an average rotation of the displacement field. A system of the governing equations is as follows (see Szubartowski and Ganczarski [29])

$$\begin{aligned} &L(u_i)+\frac{1}{4}(\gamma+\psi)\nabla^2\mathrm{rot}_i(\mathrm{rot}\mathbf{u})+\frac{\partial\mu}{\partial x_3}\left(\frac{\partial u_i}{\partial x_3}+\frac{\partial u_3}{\partial x_i}\right)=\eta\frac{\partial\theta}{\partial x_i} \\ &L(u_3)+\frac{1}{4}(\gamma+\psi)\nabla^2\mathrm{rot}_3(\mathrm{rot}\mathbf{u})+2\frac{\partial\mu}{\partial x_3}\frac{\partial u_3}{\partial x_3}+\frac{\partial\lambda}{\partial x_3}\Theta=\eta\frac{\partial\theta}{\partial x_3}+\eta\frac{\partial\eta}{\partial x_3}\theta \end{aligned} \tag{9}$$

It is easy to notice that: symbol $L(\mathbf{u})=\mu\nabla^2u_i+(\lambda+\mu)\mathrm{grad}(\mathrm{div}\mathbf{u})$ stands for the partial differential operator of classical continuum, additional term $1/4(\gamma+$

$\psi)\nabla^2\mathrm{rot}(\mathrm{rot}\mathbf{u})$ directly results from quasi-micro-polar nature whereas terms in brackets, preceding by partial derivatives

$$\frac{\partial \mu}{\partial x_3} = 0, \qquad \frac{\partial \lambda}{\partial x_3} = 0$$

correspond to functional gradation of Kirchhoff's $\mu = G$ and bulk modules, respectively. Stationary heat flux equation takes format of $(1)_1$. Again, to solve Eqs. (9) the Iljushin potential (2) is applied transforming original thermo-mechanical quasi-micro-polar problem into plane stress one (5). In other words, quasi-micro-polar continuum under consideration reduces to classical continuum, that stays in the plane stress state.

3.3 Example—Thick Plate Made of FGM Al/ZrO$_2$ + Y$_2$O$_3$

Unique solution of equation (7) that satisfies boundary conditions

$$u(0) = 0, \qquad \lim_{r\to\infty} \sigma_{r,\varphi} = 0$$

takes format

$$\begin{aligned}
u(r,z) &= \alpha(z)\left[\frac{1-\nu}{2}\theta(\infty)r + \frac{1+\nu}{2}\int\limits_0^r \theta(\xi,z)\xi\mathrm{d}\xi\right] \\
\sigma_r(r,z) &= E(z)\alpha(z)\left[\frac{\theta(\infty)}{2} - \frac{1}{r^2}\int\limits_0^r \theta(\xi,z)\xi\mathrm{d}\xi\right] \\
\sigma_\varphi(r,z) &= E(z)\alpha(z)\left[\frac{\theta(\infty)}{2} + \frac{1}{r^2}\int\limits_0^r \theta(\xi,z)\xi\mathrm{d}\xi - \theta(r,z)\right]
\end{aligned} \tag{10}$$

Additionally, in case when temperature is bounded:

$$\lim_{r\to\infty} \theta(r,z) = 0$$

and simultaneously

$$\lim_{r\to\infty} \frac{1}{r^2}\int\limits_0^r \theta(\xi,z)\xi\mathrm{d}\xi < \infty$$

solution (10) reduces to

$$
\begin{aligned}
u(r,z) &= \alpha(z)\frac{1+\nu}{2}\int_0^r \theta(\xi,z)\xi\,\mathrm{d}\xi \\
\sigma_r(r,z) &= -E(z)\alpha(z)\left[\frac{1}{r^2}\int_0^r \theta(\xi,z)\xi\,\mathrm{d}\xi\right] \\
\sigma_\varphi(r,z) &= E(z)\alpha(z)\left[\frac{1}{r^2}\int_0^r \theta(\xi,z)\xi\,\mathrm{d}\xi - \theta(r,z)\right]
\end{aligned}
\tag{11}
$$

and it is clear that its dependence with respect to depth co-ordinate z comes from the functional gradation of Young's modulus $E(z)$ and thermal expansion coefficient $\alpha(z)$ as well the temperature field non-homogeneity $\theta(r,z)$, exclusively. The boundary value problem is formulated as follows: find temperature distribution θ, that fulfils Eq. $(1)_3$ and boundary conditions

$$
\begin{aligned}
&\theta(r,-\tfrac{h}{2}) = \theta_0,\ (r) \quad \frac{\partial\theta(0,z)}{\partial r} = 0 \\
&\frac{\partial\theta(r,\frac{h}{2})}{\partial z} = 0, \qquad \int_{-h/2}^{h/2} k(z)\frac{\partial\theta(r,z)}{\partial r}\mathrm{d}z = \mathrm{const}
\end{aligned}
\tag{12}
$$

and accompanying plane stress components satisfying Eq. (11) for a semi-infinite axially symmetric three-layer thick plate made of FGM composite Al/ZrO_2 stabilized by Y_2O_3. The magnitudes of both materials being constituents of FGM, after Wang et al. [32] and Lee et al. [15], are presented in Table 1. Assume that all thermomechanical properties of three-layer FGM depend on local magnitude of volume fraction of both constituents, which is subjected to the tangent hyperbolic approximation

$$
p(z) = \frac{p_\mathrm{c}+p_\mathrm{m}}{2} + \frac{p_\mathrm{c}+p_\mathrm{m}}{2}\tanh(az+b)
$$

where $p(z)$ stands for respective property $k(z)$, $\alpha(z)$ or $E(z)$, indices "c" and "m" refer to ceramic or metallic materials, parameters a and b define location and thickness of interface layer. Applying finite difference method to Eq. $(1)_1$ and boundary conditions (12) discrete format of difference operator

Table 1 Selected properties of constituents of FGM after Wang et al. [32] and Lee et al. [15]

Material	E [GPa]	ν	k [W/mK]	$\alpha \cdot 10^{-6}$ [1/K]
Al	73	0.3	154	23
Al/ZrO_2	205	–	2.0	9.8

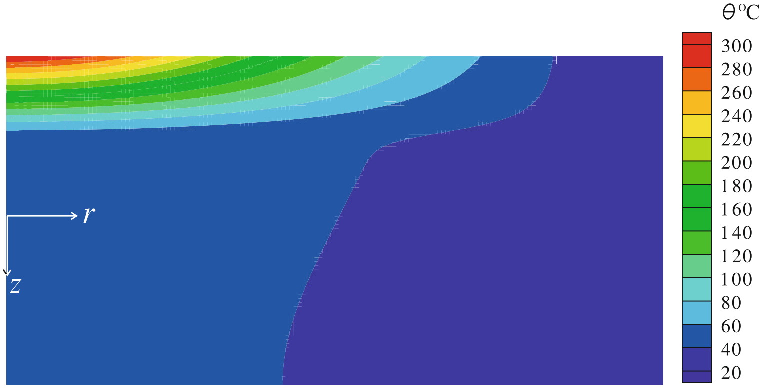

Fig. 3 Distribution of temperature field in thick plate

$$\frac{1}{\Delta r}\left(\frac{1}{\Delta r}-\frac{1}{2r_i}\right)\theta_{i-1,j}+\frac{1}{\Delta z}\left(\frac{1}{\Delta z}-\frac{1}{2k}\frac{\partial k}{\partial z}\right)\theta_{i,j-1}-\left[\frac{2}{(\Delta r)^2}+\frac{2}{(\Delta z)^2}\right]\theta_{i,j}$$
$$+\frac{1}{\Delta z}\left(\frac{1}{\Delta z}+\frac{1}{2k}\frac{\partial k}{\partial z}\right)\theta_{i,j+1}+\frac{1}{\Delta r}\left(\frac{1}{\Delta r}+\frac{1}{2r_i}\right)\theta_{i+1,j}=0 \tag{13}$$

is spanned over the mesh of 161 × 81 square elements $\Delta r = \Delta z$. The thermal load applied to the upper surface of the plate is subjected to the following relation $\theta_0 = 300[1 - \tanh^2(2r)]$. Temperature distribution is shown in Fig. 3. The temperature field exhibits a drastic decrease in temperature at top layer in comparison with the temperature distribution obtained for homogeneous material. This is a consequence of application of ceramic material having coefficient of thermal conductivity 77 times lower than analogous coefficient of metallic substrate. Hence, one may clearly observe effect of thermal barrier coating with characteristic strong temperature gradients in it and simultaneous homogenization of temperature field in middle and bottom layers.

Solution of mechanical problem is illustrated by distribution of hoop stress, which turns out to be the dominant component of stress, in Fig. 4. Application of functionally graded composite leads to the concentration of compressive stress in top layer, being ceramic material of high toughness. This convenient effect is accompanied by simultaneous unloading of middle and bottom layers built of metallic substrate. Nevertheless, another effect of tensile stress zone in ceramic layer occurs. This phenomenon is strictly associated with the structure of equations defining stress components (11).

Fig. 4 Distribution of hoop stress field in thick plate

4 Conditions of Stress Free Deformation

Analogous problem to the presented in Sect. 3 is considered, but now the system of equations of uncoupled thermo-elasticity expressed in stress format is as follows

$$\sigma_{ij|j} = 0, \quad \in_{ikl}\in_{jmn} \left(C_{knpq}\sigma_{pq} + \alpha_{kn}\theta\right)|_{lm} = 0, \quad (k_{ij}\theta|_i)|_j = 0. \tag{14}$$

Assuming constant temperature $\theta = \text{const}$, one can insert $\theta|_i = 0$ into $(14)_3$, hence the Fourier equation is satisfied as identity whereas thermal expansion term in $(14)_2$ simplifies to $(\alpha_{kn}\theta)|_{lm} = \alpha_{kn}|_{lm}\theta$. Assuming additionally $\sigma_{pq} = 0$, satisfying $(14)_1$ as identity, we look for such a distribution of thermal expansion α_{kn} that solves equations $\in_{ikl}\in_{jmn}\ \alpha_{kn}|_{lm}\theta = 0$. This turns out to be true only if covariant differential along direction of functional gradation reduces to the partial differential, or other words can be written down in format

$$\alpha_{ij,kl} + \alpha_{kl,ij} - \alpha_{ik,jl} - \alpha_{jl,ik} = 0 \tag{15}$$

and simultaneously gradation of thermal expansion tensor is linear with respect to x_3, see Fung [8], Nowacki [18], Ganczarski and Szubartowski [9]. According to above proof the generally anisotropic material of linear gradation of thermal expansion coefficient, subjected to constant temperature exclusively, is not stressed. In case of axial symmetry and transverse isotropy $\alpha_r = \alpha_\varphi = \alpha \neq \alpha_z$ the stress free deformation can be expressed by following equations

$$\varepsilon_r = \frac{\partial u}{\partial r} = \alpha_r\theta, \quad \varepsilon_\varphi = \frac{u}{r} = \alpha_\varphi\theta, \quad \varepsilon_z = \frac{\partial w}{\partial z} = \alpha_z\theta. \tag{16}$$

If structure composed of homogeneous metallic substrate (Al) and ceramic layer (Al_2O_3), joined by FGM interface, shown in Fig. 5a, and thermo-elastic properties presented in Table 2, such that linearly graded coefficient of thermal expansion exhibits polygonal function

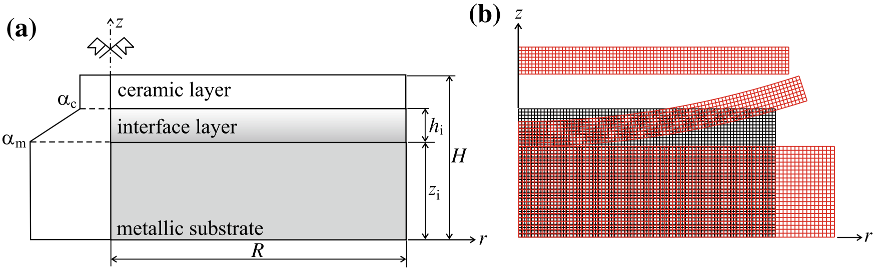

Fig. 5 Three layer FGM structure (**a**), stress-free but incompatible thermal deformation: initial mesh-black lines, deformed mesh-red lines (displacement magnified ×100) (**b**)

Table 2 Properties of constituents of alumina-based composite Al-Al_2O_3 after Chen and Tong [4], Cho and Shin [5], Wang et al. [32], Dusza [7]

Material	E [MN/cm^2]	ν	k [W/cmK]	$\alpha \cdot 10^{-6}$ [1/K]	Ratio α_z/α
Al	7.3	0.3	1.54	23	–
Al_2O_3	38	–	0.46	8.5	1.194

$$\alpha_{r,z} = \begin{cases} \alpha^{\mathrm{m}}_{r,z} & 0 \le z < z_i \\ \alpha^{\mathrm{m}}_{r,z} - (\alpha^{\mathrm{m}}_{r,z} - \alpha^{\mathrm{c}}_{r,z})\dfrac{z - z_i}{h_i} & z_i < z < z_i + h_i \\ \alpha^{\mathrm{c}}_{r,z} & z_i + h_i \le z < H \end{cases} \tag{17}$$

and one easily arrive at following of solution Eqs. (16) for u

$$u = \int \alpha_r \theta \mathrm{d}r = \begin{cases} \alpha^{\mathrm{m}}_r \theta r & 0 \le z < z_i \\ \left[\alpha^{\mathrm{m}}_r - (\alpha^{\mathrm{m}}_r - \alpha^{\mathrm{c}}_r)\dfrac{z - z_i}{h_i}\right]\theta r & z_i < z < z_i + h_i \\ \alpha^{\mathrm{c}}_r \theta r & z_i + h_i \le z < H \end{cases} \tag{18}$$

and for w respectively

$$w = \int \alpha_z \theta \mathrm{d}z = \begin{cases} \alpha^{\mathrm{m}}_z \theta z & 0 \le z < z_i \\ \left[\alpha^{\mathrm{m}}_z z - (\alpha^{\mathrm{m}}_z - \alpha^{\mathrm{c}}_z)\dfrac{(z - z_i)^2 - r^2}{2h_i}\right]\theta & z_i < z < z_i + h_i \\ \alpha^{\mathrm{c}}_z \theta z & z_i + h_i \le z < H \end{cases} \tag{19}$$

The displacement field corresponding to stress free deformation defined by Eqs. (17)–(19) is spanned over the mesh of 80 × 40 square elements and shown in Fig. 5b. It is well visible that both substrate and ceramic layers exhibit homogeneous deformation, whereas deformation of interface is curvilinear. Although all three deformations satisfy individually stress less state they are not compatible.

5 FGM Cylinder

5.1 Governing Equations

A thermo-elastic rotationally-symmetric cylinder including FGM TBC is considered. The cylinder is loaded by temperature field $\theta(r) + T$ as well as internal pressure p, see Fig. 6. The system of equations of uncoupled thermo-elasticity expressed by stress function formulation is as follows

$$\begin{aligned} &\theta'' + \left(\frac{k'}{k} + \frac{1}{r}\right)\theta' = 0 \\ &F'' + \left(\frac{1}{r} - \frac{E'}{E}\right)F' + \left(\frac{\nu}{1-\nu}\frac{E'}{E} - \frac{1}{r}\right)\frac{F}{r} = -\frac{E(\alpha\theta)'}{1-\nu^2} \end{aligned} \tag{20}$$

Stress components as well as heat flux are expressed by conventional relations

$$\begin{aligned} &\sigma_r = \frac{F}{r} && \sigma_\varphi = F' \\ &\sigma_z = \nu(\sigma_r + \sigma_\varphi) - E\alpha\theta && q = -k\theta' \end{aligned} \tag{21}$$

All thermomechanical properties of the FGM TBC such as α, k and E are arbitrary functions of radius r. Following five approximations are considered (Szubartowski and Ganczarski [30]):
benchmark problem of a ceramic layer deposed directly on metallic substrate

$$f_1(r) = f_\mathrm{c} \tag{22}$$

conventional power function

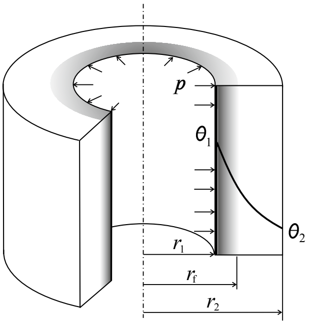

Fig. 6 FGM cylinder under thermo-mechanical loading

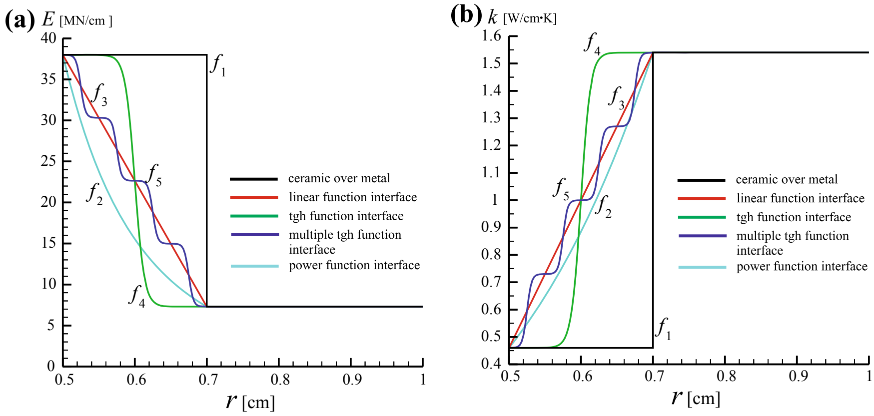

Fig. 7 Subsequent approximations of thermo-mechanical properties: **a** Youngs modulus, **b** coefficient of thermal conductivity

$$f_2(r) = (f_\mathrm{m} - f_\mathrm{c}) \frac{r^n}{r_\mathrm{f}^n - r_1^n} \quad \text{where} \quad n = \frac{\log\left(\frac{f_\mathrm{m}}{f_\mathrm{c}}\right)}{\log\left(\frac{r_\mathrm{f}}{r_1}\right)} \tag{23}$$

linear function

$$f_3(r) = (f_\mathrm{m} - f_\mathrm{c}) \frac{r - r_1}{r_\mathrm{f} - r_1} + f_\mathrm{c} \tag{24}$$

tangent hyperbolic (one step smooth) function

$$f_4(r) = \frac{f_\mathrm{m} + f_\mathrm{c}}{2} + \frac{f_\mathrm{m} - f_\mathrm{c}}{2} \tanh(ar + b) \tag{25}$$

multiple tangent hyperbolic (multi-step smooth) function

$$f_5(r) = \frac{f_\mathrm{m} + f_\mathrm{c}}{2} + \frac{f_\mathrm{m} - f_\mathrm{c}}{2} \sum_{i=1}^{4} \tanh(a_i r + b_i) \tag{26}$$

where $f_i(r)$ stand for respective property $\alpha(r)$, $k(r)$ or $E(r)$, parameters a_i and b_i define location and thickness of TBC sub-layer, see Fig. 7.

5.2 *Example*

A system of four first-order ordinary differential equations, corresponding to Eqs. (20), is numerically integrated from $r_1 = 0.5$ cm to $r_2 = 1.0$ cm by use of

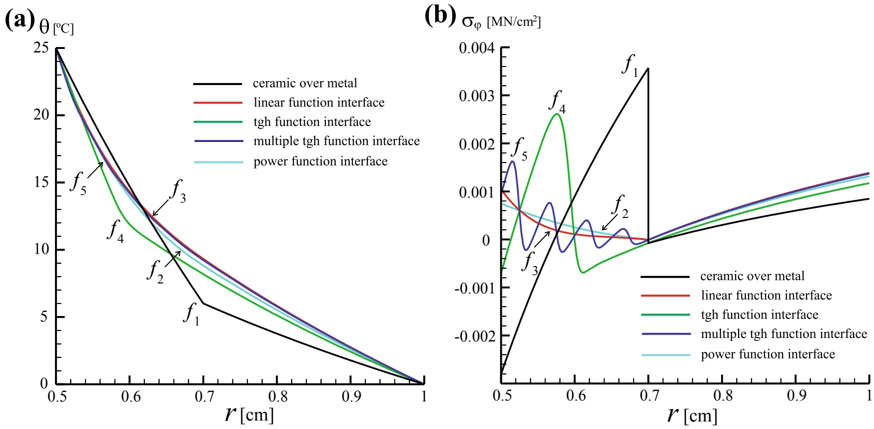

Fig. 8 Distributions of: **a** temperature, **b** hoop stress, for subsequent approximations of thermomechanical properties

shootf.for routine, being shooting to a fitting point $r_\mathrm{f} = 0.7$ cm implementation of multidimensional, globally convergent Newton-Raphson method. Thermomechanical boundary and continuity conditions are assumed as follows:

$$\begin{aligned} &\theta(r_1) = \theta_1, \qquad q_\mathrm{c}(r_\mathrm{f}) = q_\mathrm{m}(r_\mathrm{f}), \qquad \theta(r_2) = \theta_2 \\ &\sigma_{r\mathrm{c}}(\rho_1) = -p, \quad \sigma_{r\mathrm{c}}(r_\mathrm{f}) = \sigma_{r\mathrm{m}}(r_\mathrm{f}), \quad \sigma_{r\mathrm{c}}(r_2) = 0 \end{aligned} \tag{27}$$

where $p = 0.55$ kN/cm^2, $\theta_1 = 25\,^\circ$C and $\theta_2 = 0\,^\circ$C. Complete material data of both materials constituents of FGM, after Wang et al. [32], are presented in Table 2. Temperature distributions corresponding to all five types of TBC, described by Eqs. (22)–(26), are shown in Fig. 8a. In comparison with the temperature obtained for the benchmark problem (ceramic layer deposed directly over the metallic substrate), the temperature fields referring to subsequent types of TBC represent smooth and monotonously decreasing functions. All curves are located rather close each to other, although corresponding distributions of thermal conductivity (see Fig. 7b) essentially differ. This is a consequence of both Dirichlet's type of boundary conditions imposed on temperature Eq. $(20)_1$. Solution of mechanical problem is illustrated by distribution of hoop stress, which is the dominant component of stress, in Fig. 8b. In case of the benchmark problem, hoop stress exhibits strong discontinuity mainly caused by thermo-mechanical mismatch $E_\mathrm{c} \gg E_\mathrm{m}$, $\alpha_\mathrm{c} \ll \alpha_\mathrm{m}$. This inconvenient effect is successively eliminated by application of subsequent types of TBC's. Detailed analysis of subsequent distributions of hoop stress allows to distinguish two groups of TBC's. First one, represented by conventional power and linear functions, combines curves of rather monotonous character that are located relatively close each to other. Second one, represented by one-step and multi-step smooth functions, combines curves of oscillating character that profiles differ essentially. Detailed qualitative and quantitative analysis of hoop stress referring to subsequent types of TBC reveals that another inconvenient effect of tensile stress zone in ceramic layer occurs.

6 Concept of FGM Axisymmetric Finite Element

6.1 Formulation of FGM Thermo-Elastic Cylinder

The system of equations (20) takes the operator format (see Szubartowski and Ganczarski [30])

$$L_1\left[\theta(r)\right]=0, \quad L_2\left[F(r)\right]=-\frac{E}{1-\nu^2}(\alpha\theta)' \tag{28}$$

where the Poisson ratio ν is not subjected to any change. All thermomechanical properties of the FGM are arbitrary functions of radius r, subsequent global approximations are considered

$$f_6(r)=(f_{\mathrm{m}}-f_{\mathrm{c}})\,\frac{r_{\mathrm{f}}^n-r_1^n}{r^n-r_1^n}+f_{\mathrm{c}} \tag{29}$$

Voigt for $n=1$, Reuss for $n=-1$, and Hashin-Shtrikman (separate formulas for bulk modulus K and coefficient of thermal conductivity k)

$$\begin{aligned}
K^{\mathrm{HS}-}&=K_{\mathrm{m}}+\frac{(K_{\mathrm{c}}-K_{\mathrm{m}})V_{\mathrm{f}}}{1+\zeta_{\mathrm{m}}(1-V_{\mathrm{f}})\left(\dfrac{K_{\mathrm{c}}}{K_{\mathrm{m}}}-1\right)}\\
K^{\mathrm{HS}+}&=K_{\mathrm{c}}+\frac{(K_{\mathrm{m}}-K_{\mathrm{c}})(1-V_{\mathrm{f}})}{1+\zeta_{\mathrm{c}}V_{\mathrm{f}}\left(\dfrac{K_{\mathrm{m}}}{K_{\mathrm{c}}}-1\right)}, \qquad \zeta_{\mathrm{c/m}}=\frac{1+\nu_{\mathrm{c/m}}}{3(1-\nu_{\mathrm{c/m}})}\\
k^{\mathrm{HS}-}&=\frac{k_{\mathrm{m}}k_{\mathrm{c}}+2k_{\mathrm{c}}[k_{\mathrm{m}}V_{\mathrm{f}}+k_{\mathrm{c}}(1-V_{\mathrm{f}})]}{2k_{\mathrm{c}}+k_{\mathrm{c}}V_{\mathrm{f}}+k_{\mathrm{m}}(1-V_{\mathrm{f}})}\\
k^{\mathrm{HS}+}&=\frac{k_{\mathrm{m}}k_{\mathrm{c}}+2k_{\mathrm{m}}[k_{\mathrm{m}}V_{\mathrm{f}}+k_{\mathrm{c}}(1-V_{\mathrm{f}})]}{2k_{\mathrm{m}}+k_{\mathrm{c}}V_{\mathrm{f}}+k_{\mathrm{m}}(1-V_{\mathrm{f}})}, \qquad V_{\mathrm{f}}=\frac{r-r_1}{r_{\mathrm{f}}-r_1}
\end{aligned} \tag{30}$$

see Pobedria [21], Aboudi et al. [1], Calvo-Jurando and Parnell [3].

6.2 FEM Formulation

From the FEM point of view both the Fourier equation $(28)_1$ and the mechanical state equation $(28)_2$ are treated as differential equations of variable coefficients describing isotropic material, which inhomogeneity is subjected to smooth change form one element to other due to the global FGM approximation functions. In order to save Euler's type of both Eqs. (28) the following material inhomogeneity shape functions, that approximate the global FGM functions at a level of element, are assumed

$$k^{(e)} = k_0 r^n, \quad E^{(e)} = E_0 r^m, \quad \alpha^{(e)} = \alpha_0 r^s \tag{31}$$

Transformation of Eqs. (28) to FEM form is done by discretization, use of the Galerkin weighted residual process Kim and Paulino [13], Owen and Hinton [19], Zienkiewicz [37]

$$\int_V [L_{1,2}(\Phi) + Q] W \mathrm{d}V = 0 \tag{32}$$

and approximation of unknown function by N_i global shape functions $\Phi = \sum_{i=1}^{n} N_i \Phi_i$. The weighting functions W_i corresponding to node i are conveniently chosen such that $W_i = N_i$, hence substituting for Φ and W in Eq. (32) and assembling all elements results in $H_{ij}\Phi_j = Q_i$, in which typical element components of the element stiffness matrices $h_{ij}^{(e)}$ and the element nodal force vectors $q_i^{(e)}$ are

$$h_{ij}^{(e)} = \frac{k_0}{n+2} \frac{r_{l+1}^{n+2} - r_l^{n+2}}{R^2} \begin{bmatrix} 1 & -1 \\ -1 & 1 \end{bmatrix} \qquad q_i^{(e)} = k_0 \begin{bmatrix} -r_l^{n+1}\theta'(r_l) \\ r_{l+1}^{n+1}\theta'(r_{l+1}) \end{bmatrix}$$

$$\begin{aligned} h_{ij}^{(e)} &= \begin{bmatrix} \left(1 - \frac{m\nu}{1-\nu}\right)\frac{R}{3\bar{r}} + \frac{\bar{r}}{R} - \frac{m}{2} & \left(1 - \frac{m\nu}{1-\nu}\right)\frac{\bar{r}}{6R} - \frac{\bar{r}}{R} + \frac{m}{2} \\ \left(1 - \frac{m\nu}{1-\nu}\right)\frac{\bar{r}}{6R} - \frac{\bar{r}}{R} - \frac{m}{2} & \left(1 - \frac{m\nu}{1-\nu}\right)\frac{R}{3\bar{r}} + \frac{\bar{r}}{R} + \frac{m}{2} \end{bmatrix} \\ q_i^{(e)} &= \begin{bmatrix} -r_l F'(r_l) + A\frac{\alpha_0 E_0}{1-\nu}\bar{r}^{m+s}\left[\left(\frac{\bar{r}}{2} + \frac{sR}{6}\right)\theta_{l+1} - \left(\frac{\bar{r}}{2} - \frac{sR}{3}\right)\theta_l\right] \\ r_{l+1}F'(r_{l+1}) + A\frac{\alpha_0 E_0}{1-\nu}\bar{r}^{m+s}\left[\left(\frac{sR}{3} + \frac{\bar{r}}{2}\right)\theta_{l+1} - \left(\frac{\bar{r}}{2} - \frac{sR}{6}\right)\theta_l\right] \end{bmatrix} \end{aligned} \tag{33}$$

for thermal and mechanical problems, respectively, and $\bar{r}$ stands for mid radius of an element. For the case of a two-node element with a linear variation of Φ the shape functions are

$$N_1^{(e)} = \frac{r_{l+1} - \xi}{R}, \qquad N_2^{(e)} = \frac{\xi - r_l}{R}$$

where R is the length of an element.

6.3 Examples

This subsection comprises results obtained for the FGM cylinder by use of special finite elements defined in the previous subsection. The results are compared with results of other methods such numerical integration and conventional finite elements, without gradation of material properties, supplied by ANSYS.

In the first of numerical tests, a convergence of the new finite element, described in Sect. 6.2, is checked. All geometrical, material and loading parameters of the cylinder remain unchanged if compare with example shown in Sect. 5.2. Distributions of temperature and stress function are shown in Fig. 9.

Good convergence requires application of fine mesh for interface (40 elements) and relatively coarse mesh for homogeneous part of cylinder (15 elements). Such a mesh includes minimal number of elements and simultaneously guarantees convergence of the mechanical problem. It is worth to notice, that application of staggered algorithm (first the thermal problem is solved and next temperature is treated as right hand side in the mechanical problem) results in cumulative error in the second step of algorithm, usually ten times bigger than the error form the first step. Detailed qualitative and quantitative analysis of results confirms good convergence of FEM FGM and numerical integration but simultaneous lack of convergence in case of conventional FEM.

Aforementioned positive results are a starting point for further investigations when the FG modified FEM is applied to other types of interfaces. As it is shown in Sect. 6.2 following three interfaces are considered: Voigt's, Reuss' and Hashin-Shtrikman's. Results, comprising distributions of temperature, stress function and stress components in case of Voigt's versus Reuss' interface and lower versus upper Hashin-Shtrikman's interface, are presented in Fig. 10.

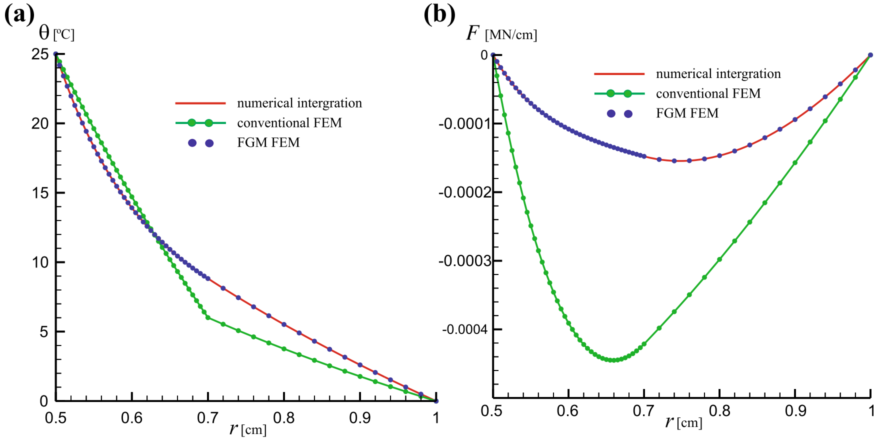

Fig. 9 Comparison of temperature and stress function distributions in case of FGM cylinder

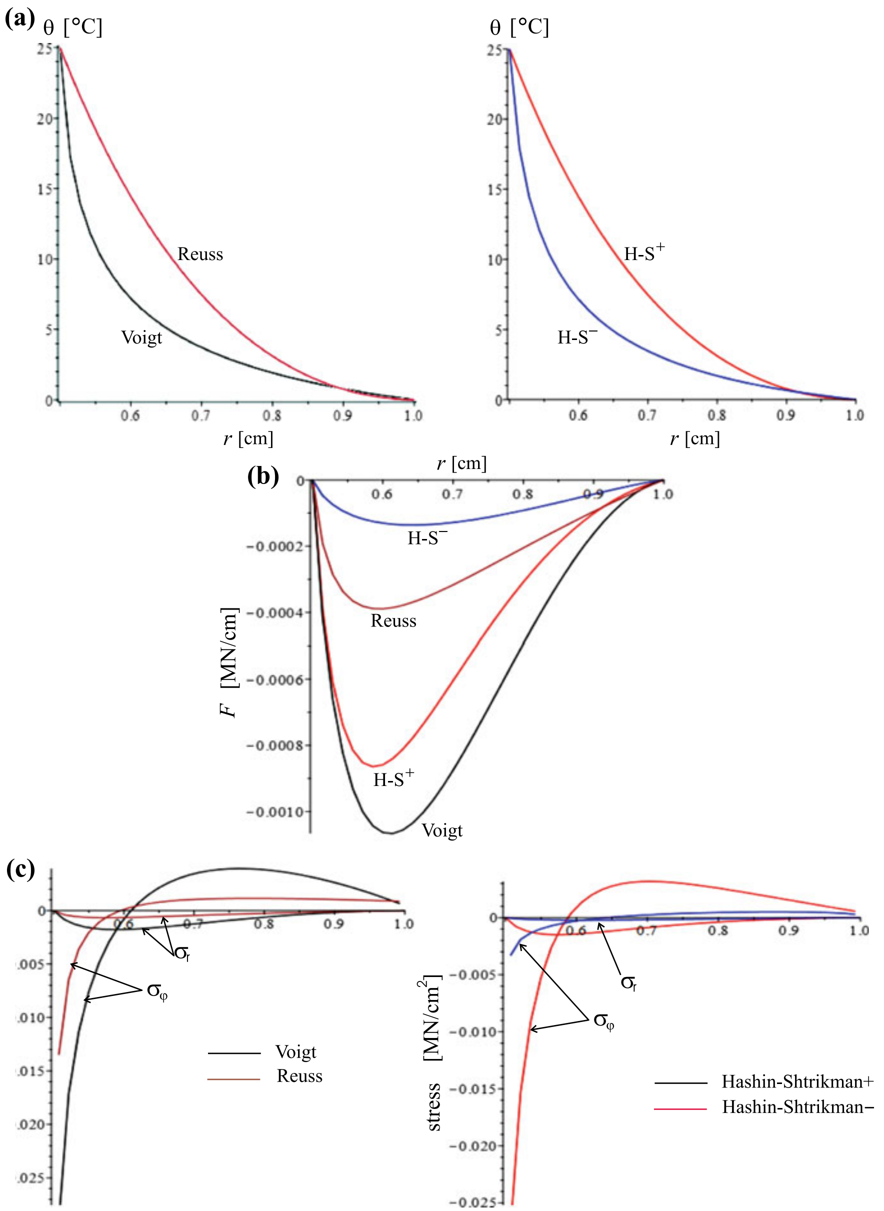

Fig. 10 Comparison of results for Voigt's, Reuss' and Hashin–Shrikman's interfaces: **a** temperature, **b** stress function, **c** stress components

The following general tendencies can be formulated: Voigt's and upper Hashin-Shtrikman's interfaces lead to lower average temperatures and higher levels of stress, contrary to Reuss' and lower Hashin-Shtrikman's interfaces resulting in higher average temperatures and lower levels of stress. This is logical consequence of assumed definitions of element stiffness matrices and element nodal force vectors (33), being integrals of appropriate approximation (29)–(30) and shape functions.

7 Conclusions

Following concluding remarks may be formulated:

- Thermal loading applied to the FGM plate treated as both classical and quasi-polar continua results in the plane stress state if only force-type boundary conditions are homogeneous and there are no body forces.
- Application of functionally graded composite Al/Al_2O_3 is very efficient since FGM layer works like thermomechanical barrier, successively protecting metallic cylinders from both high-temperature gradients and high stress concentration.
- Lack of compatibility makes stress free deformation of the FGM plate subjected to constant temperature impossible.
- Special graded FEM is very attractive tool to analyse thermomechanical structures built of FGMs.

References

1. Aboudi, J., Arnold, S.M., Bednarcyk, B.A.: Micromechanics of Composite Materials. Elsevier, Amsterdam (2013)
2. Batra, R.C.: Optimal design of functionally graded incompressible linear elastic cylinders and spheres. AIAA J. **46**, 2050–2057 (2008)
3. Calvo-Jurando, C., Parnell, W.J.: Hashin-Shtrikman bounds on the effective thermal conductivity of a transversely isotropic two-phase composite material. J. Math. Chem. **53**, 828–843 (2015)
4. Chen, W.F., Tong, L.: Sensitivity analysis of heat conduction for functionally graded materials. Mater Des. **25**, 633–672 (2004)
5. Cho, J.R., Shin, S.W.: Material composition optimization for heat-resisting FGMs by artificial neutral network. Compos. A **35**, 585–595 (2004)
6. Dai, K.Y., Liu, G.R., Han, X., Liu, K.M.: Thermomechanical analysis of functionally graded material (FGM) plates using element-free Galerkin method. Comput. Struct. **83**, 1487–1502 (2005)
7. Dusza, J.: High temperature properties. KMM-NoE Rep 3 (2005)
8. Fung, Y.C.: Foundations of Solid Mechanics. Prentice-Hall, New Jersey (1965)
9. Ganczarski, A., Szubartowski, D.: On the stress free deformation of linear FGM interface under constant temperature. Acta Mechanica et Automatica **9**, 135–139 (2015)
10. Ganczarski, A., Szubartowski, D.: Plane stress state of FGM thick plate under thermal loading. Arch. Appl. Mech. **86**, 111–120 (2016)

11. Iljushin, A.A., Lomakin, W.A., Shmakov, A.P.: Mechanics of Continuous Media. Moscow (1979)
12. Jabbari, M., Shahryari, E., Haghighat, H., Eslami, M.R.: An analytical solution for steady state three dimensional thermoelasticity of functionally graded circular plates due to axisymmetric loads. Eur. J. Mech. A/Solids **47**, 124–142 (2014)
13. Kim, J.H., Paulino, G.H.: Isoparametric graded finite elements for non-homogeneous isotropic and orthotropic materials. ASME J. Appl. Mech. **69**, 502–514 (2002)
14. Kulikov, G.M., Plotnikova, S.A.: A sampling method and its implementation for 3D thermal stress analysis of functionally graded plates. Compos. Struct. **120**, 315–325 (2015)
15. Lee, W.Y., Stinton, D.P., Berndt, C.C., Erdogan, F., Lee, Y.-D., Mutasin, Z.: Concept of functionally graded materials for advanced thermal barrier coating applications. J. Am. Ceram. Soc. **79**, 3003–3012 (1996)
16. Manthena, V.: Mathematical modeling of thermoelastic behavior of a functionally graded thermally sensitive thick hollow cylinder with internal heat generation. Arch Appl. Mech. (2018) (in print); Wang, H., Qin, Q.: Numerical thermal analysis for functionally graded coating/substrate system using the approximated transfer approach. Coatings (2018) (in print)
17. Muki, R.: Thermal stresses in a semi-infinite solid and a thick plate under steady distribution of temperature. Proc. Fac. Eng. Keio Univ. **9**, 42 (1957)
18. Nowacki, W.: Theory of Elasticity. PWN, Warszawa (1970)
19. Owen, D.R.J., Hinton, E.: Finite Elements in Plasticity: Theory and Practice. Pineridge Press, UK (1980)
20. Pan, E., Han, F.: Green's functions for transversely isotropic piezoelectric functionally graded multilayered half spaces. Int. J. Solid Struct. **42**, 3207–3233 (2005)
21. Pobedria, B.E.: Mechanics of composite materials. Issues of Moscow University (1984) (in Russian)
22. Popovych, V., Kalynyak, B.M.: Mathematical modeling and methods for the determination of the static thermoelastic state of multilayer thermally sensitive cylinders. J. Math. Sci. **215**, 218–242 (2016)
23. Sburlati, R., Atashipour, S.R., Atashipour, S.A.: Exact elastic analysis of a doubly coated thick circular plate using functionally graded interlayers. Arch Appl. Mech. **85**, 1779 (2015)
24. Schulz, U., Bach, F.W., Tegeder, G.: Graded coating for thermal, wear and corrosion barriers. Mater Sci. Eng. **A362**(1–2), 61–80 (2003)
25. Seifi, R.: Exact and approximate solutions of thermoelastic stresses in functionally graded cylinders. J. Thermal Stress. **38**, 1163–1182 (2015)
26. Senthil, S.V., Batra, R.C.: Three-dimensional analysis of transient thermal stresses in functionally graded plates. Int. J. Soilds Struct. **40**, 7181–7196 (2003)
27. Sneddon, I., Lockett, F.J.: On the steady-state thermoelastic problem for the half-space and the thick plate. Quart. Appl. Math. **18**(2), 145–153 (1960)
28. Sternberg, E., McDowell, E.L.: On the steady-state thermoelastic problem for the half-space. Quart. Appl. Math. **14**, 381 (1957)
29. Szubartowski, D., Ganczarski, A.: Problems of modeling of FGM interface under thermal loading. J. Pol.-Braz. Sci. Technol. **2**, 445–465 (2016)
30. Szubartowski, D., Ganczarski, A.: Problem of FGM TBC coated cylinder. AIP Conf. Proc. **1922** (2017). https://doi.org/10.1063/1.5019117
31. Trumble, K.: Technology and Controlled Tailoring of Functional Graded Materials. First Integration Summer School, Udine (2005)
32. Wang, B.L., Han, J.C., Du, S.Y.: Crack problems for functionally graded materials under transient thermal loading. J. Thermal Stress. **23**, 143–168 (2000)
33. Wang, K., Pan, E., Roy, A.K.: Three-dimensional Green's functions for a steady point heat source in a functionally graded half space and some related problems. Int. J. Eng. Sci. **45**, 930–950 (2007)
34. Wang, H., Qin, Q.: Numerical thermal analysis for functionally graded coating/substrate system using the approximated transfer approach. Coatings (2018) (in print)

35. Website of international knowledge-based multicomponent materials for durable and safe performance, Network of excellence. http://www.kmm-noe.org
36. Yang, K., Feng, W.-Z., Peng, H.-F., Lv, J.: A new analytical approach of functionally graded material structures for thermal stress BEM analysis. Int. Commun. Heat Mass Transf. **62**, 26–32 (2015)
37. Zienkiewicz, O.C., Taylor, R.L.: The Finite Element Method. Butterworth, Oxford (2000)

Structural Analysis of Gas Turbine Blades Made of Mo-Si-B Under Stationary Thermo-Mechanical Loads

Olha Kauss, Konstantin Naumenko, Georg Hasemann and Manja Krüger

Abstract This study focuses on the mechanical analysis of high temperature gas turbine blades based on finite element method. The aim is to evaluate the feasibility of a Mo-based alloy Mo-12Si-8.5B as a possible candidate as a new type of turbine blade material. For that purpose, the numerical analysis of typical turbine blades under common stationary load was carried out based on the finite element method. The alloy Mo-12Si-8.5B was compared to the state-of-the-art Ni-based superalloy CMSX-4. The creep deformation is taken into account, so that the stationary load under high temperatures could be represented.

1 Introduction

For further increase of the thermodynamic efficiency of gas turbines a significant increase of the gas inlet temperatures is required. This leads, nevertheless, to an increase of strains caused by material's creep especially in the turbine blades, which drastically reduces their service life. The application temperatures of state-of-the-art Ni-based superalloys cannot be further increased significantly [1]. Currently, they can withstand temperatures up to about 1150 °C, which is approximately 90% of their melting temperature [2]. Due to the advanced cooling systems and thermal barrier coatings the gas inlet temperature can reach up to 1600–1700 °C. The problem is that any further temperatures increase by using state-of-the-art Ni-based superalloys would lead to a significant lifetime reduction of the components [2]. This problem can probably be solved by the development of new alloys based on refractory metals with melting temperature several hundred degrees higher as compared to Ni-based materials. Therefore, new heat-resistant materials with high melting points are in the focus of current material's research.

O. Kauss (✉) · K. Naumenko
Otto von Guericke University Magdeburg, Magdeburg, Germany
e-mail: olha.popovych@ovgu.de

G. Hasemann · M. Krüger
Research Center Jülich, Jülich, Germany

K. Naumenko and M. Krüger (eds.), *Advances in Mechanics of High-Temperature Materials*, Advanced Structured Materials 117,
https://doi.org/10.1007/978-3-030-23869-8_4

Ni-based superalloys combine excellent fracture toughness, creep resistance and oxidation resistance at elevated temperatures [1]. The reason for the superior creep properties of these alloys is a cube-shaped microstructure of γ' phases in a γ matrix phase [1]. A typical example for materials with this microstructure is CMSX-4. It represents a second-generation single-crystal superalloy, which is of great interest for applications as high temperature gas turbine blades [1, 2] and will be used as a reference material in the present study.

Heat-resistant Mo-Si-B alloys have the potential to substitute Ni-based alloys for high-temperature applications in gas turbines in future. Their microstructures are mostly based on a Mo solid solution phase (Mo_{ss}) and two silicides, namely Mo_3Si and Mo_5SiB_2 [2]. Although they have higher density compared to Ni-based superalloys, their melting temperatures and their excellent mechanical properties allow operating temperatures up to 1300 °C and they can be further developed [2].

Nevertheless, several questions about the feasibility of Mo-based alloys under realistic turbine blade operating conditions remain unsolved. Experimental data of turbine blades under real thermal and mechanical loading conditions are in great demand but extremely challenging. Some problems of the complex thermal and mechanical analyses can partially be solved with numerical analysis based on the finite element method (FEM). Although any FEM calculations of gas turbine components require simplifications of the model and loading conditions, it still provides an efficient method to estimate the materials performance compared to expensive component tests. As a result of the FEM analysis, the stress-strain state can be examined with sufficient accuracy. These data could be used to showcase the potential and give first ideas on the feasibility of the newly developed Mo-Si-B alloys.

The numerical study of a turbine blade modeled under stationary loads is an important step in determining the feasibility of Mo-based alloys in gas turbine materials. In this study, the three-phase alloy Mo-12Si-8.5B is considered as a potential blade material in a comparative numerical analysis to the already used superalloy CMSX-4.

2 Requirements for Gas Turbine Blade Materials

The gas turbine blades are critical components of gas turbine engines, since a large part of all gas turbine failures (25.5–28%) are related to turbine blades [3, 4]. These blade failures are mainly caused by two basic types of loads: angular velocity that leads to huge centrifugal forces (and hence tensile stresses) and extreme temperatures (or temperature gradients). These two loads define the multiaxial stress state in turbine blades.

Creep deformation resistance is a very important point in the design of the blades, especially for industrial turbines. The reason for this is that they are used under constant centrifugal load at extremely high and relatively homogeneous temperatures for a very long operating time. It is assumed, that technically relevant creep processes generally occur at homologous temperatures $>0.3\ T_M$ of the blade material [5]. In

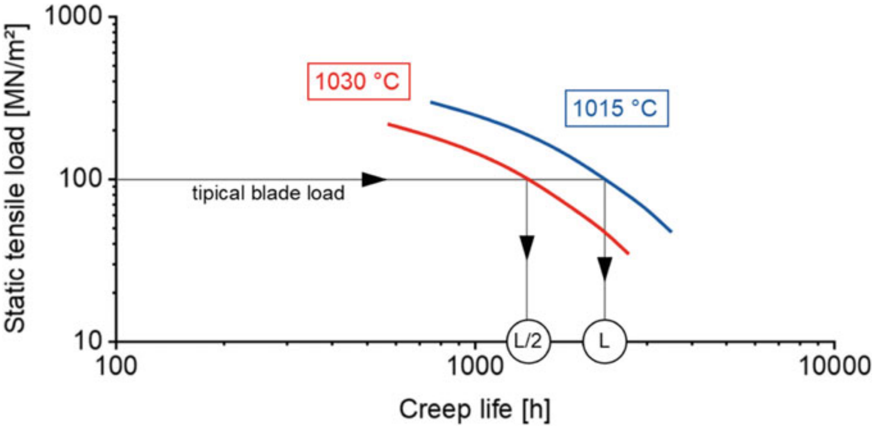

Fig. 1 Reduction of creep life due to temperature increase, reprinted after [6]

industrial gas turbines the damage costs due to creep failure of the rotating components can reach up to 24% of the whole turbine system value [6]. This is particularly dangerous for the first rows of high pressure turbine blades, which are exposed to the highest temperatures compared to medium and low pressure turbines. The creep failure can be due to initiation and growth of cracks [7] or extension of the blades which leads to contact with the turbine casing [8].

The increase of the temperature always serves as a hindering factor. For example raising the operating temperature of the turbine by 10–15 K using the same material and cooling system reduces the service life by half [6, 8, 9]. This effect is shown in Fig. 1.

The transition from combustion to gas turbine engines has required new materials due to the demanding thermal and mechanical conditions. In combustion engines, the materials operate at temperatures up to 800 °C (mostly under pressure). On the other hand, in gas turbine engines structural materials for disks and blades operate under static and dynamic tensile stresses as well as under varying thermal stress. In addition, only first turbine engines were operating at temperatures of 700–800 °C. The operating temperature was significantly increased during their further development.

Depending on the application as a blade or as a vane, the requirements for certain material properties are different. Besides this, there is also a drastic difference of working conditions in the first turbine stages as compared to the following sections. Vanes operate at significantly higher temperatures compared to blades. They operate under bending forces due to the gas flow and thermal loads, which are determined by an uneven temperature field under both stationary and transient loads. Vanes undergo significantly lower alternating loads. The stresses in the vanes are lower than in the blades, which operate under strong influence of centrifugal forces. One of the most common ways of vanes damage is oxidation due to lack of resistance against high temperature corrosion of the alloys. Therefore, the main requirements for alloys that are used for vanes are both high heat and corrosion resistance and fatigue resistance at high temperatures.

Even higher demands are placed on the alloys for blade applications in the high-temperature section of gas turbines. They are exposed to static, vibration, thermocycling, corrosion and erosion loads, which lead to numerous possible damage scenarios. Typical damage of the blades results from a lack of fatigue strength of the alloys used. During mechanical surface treatment of blades, overheating may occur, which causes plastic compression of the outer layers of the metal. This leads to significant residual stresses after such processing, which promotes the initiation of cracks. In uncontrolled surface grinding, residual stresses reach up to 350 MPa [10]. Since the strength limit of the cast Ni-based superalloys is 700–1000 MPa, cracking in the cold-worked metal at low temperatures may already occur at loads of 350–650 MPa, which is much lower than the normal strength limit [10]. Thus the tensile strength of samples, which were ground after casting, is 15–27% lower than the fracture stresses of samples with as-cast surfaces. At the same time, the cold-formed metal is characterized by a higher diffusion permeability. This leads to an intensification of the recrystallization processes on the surface layer and faster coagulation of the γ' phase. Thereby softening of the surface layer occurs, which leads to conditions that facilitates the nucleation and development of cracks [10].

The requirements for the heat-resistant cast alloys of the cooled blades are becoming more and more complex. One reason is a sharp temperature drop that occurs in the thin walls of the cooled blade, which leads to a high temperature gradient. This inevitably generates thermal tensile stresses, which reach up to 200–300 MPa under certain operating conditions on the inner surface of the blades [10]. Therefore, cracks may be induced as a result of the overall effect of thermal tensile stresses in addition to centrifugal forces on the inner surface of the hollow blades cast with equiaxed structure.

Another type of possible damage is fatigue. In endurance tests, fatigue damage mostly occurs in the blade root due to insufficient fatigue and creep strength.

However, both types of damage, described above, are sufficiently studied. The reasons and appropriate methods of their elimination as well as the calculation stage, during and after operation, are already developed (i.e. during construction, maintenance and repair).

New generations of gas turbine engines have higher gas inlet temperatures of about 1300 °C. Therefore, the used materials must ensure a higher thermal fatigue resistance. Besides the high maximum temperature, modern aircraft engines are characterized by high variation of their operating temperatures between start-up, stationary operation and shut-down. This results in a huge difference in the heating and cooling rates of the thick parts of the airfoil and their thin edges, leading to considerable thermal loads, in combination with the influence of the gas flow and the centrifugal loads. The increase of the gas inlet temperature in new turbines is not only attributed to the development of materials that are more heat resistant, but also to the improvement of cooling technology and resulting cooling efficiency. One critical condition is higher uniformity of the cooling film over the entire blade surface, because if this film is destructed, local temperature peaks occur on the blade's surface, which results in significant thermal stresses.

Another typical blades failure may occur in the area of the housing, which is caused by the increasing of its run-out and generating a gap in the housing gasket. The run-out depends on the run-out resistance, heat resistance and creep properties of the blade material.

In modern gas turbines, the blades of the first stages are cooled. Their internal hollow consists of a large number of pins and jumpers that form a cooling system, providing stiffness of the blade and guide the flow of cooling air. However, the connection of pins and pads with the inner surface of the airfoil is an area with a high stress concentration, which in some cases leads to failure. This damage can be prevented by reducing the roughness of the inner surface of the blade, pins and jumpers, as well as by increasing the transition radius (with a sharp change in cross sections) [10]. In addition, the materials should have high plasticity and fracture toughness. The problem of high stability of turbine blades to gas corrosion is particularly relevant with increasing operating temperatures. Therefore, a sufficiently high heat resistance is one of the most important requirements [10].

3 Methods and Computational Details

An idealized three-dimensional geometry of a high pressure jet turbine blade with the height of 58 mm was created (Fig. 2). The bottom surface of the blade was clamped for all types of movements (Fig. 2a). The blade was loaded with the centrifugal rotation for 100 h (rotation radius 170 mm, rotational velocity 10,200 min^{-1}). For the calculations a mesh with mostly hexahedral square mesh elements with 20 nodes was generated (Fig. 2). The calculation model consists of 6,280 elements and 30,796 nodes.

The deformation induced by secondary creep was considered using the Norton creep law to define a creep strain rate:

$$\dot{\varepsilon}_{cr} = A \cdot \sigma^n \cdot \mathrm{e}^{-Q/RT}, \tag{1}$$

where σ is stress; A—material specific coefficients; n—creep exponent; Q—activation energy, T—temperature.

3.1 Materials

In this study turbine blades made of Ni-based alloy CMSX-4 and Mo-based Mo-12Si-8.5B alloy are compared. CMSX-4 is a widely used Ni-based superalloy for turbine blades. Mo-12Si-8.5B is an alloy designed for the substitution of Ni-based

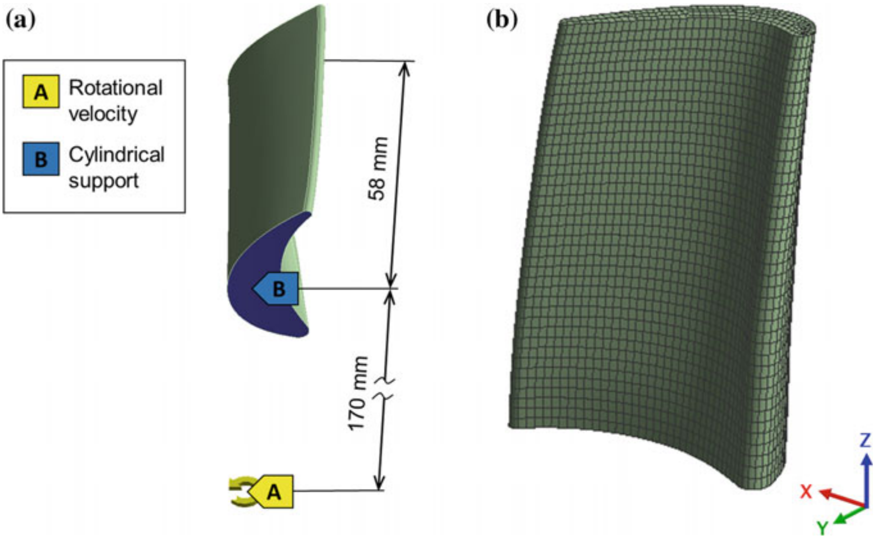

Fig. 2 **a** Boundary conditions, **b** Turbine blade geometry with mesh

superalloys in future, which possess improved creep resistance [11]. The CMSX-4 blade was analyzed under centrifugal load at 1100 °C. The blade made of alloy Mo-12Si-8.5B was considered in the range of 1100–1200 °C.

CMSX-4 is a monocrystalline Ni-based superalloy developed by Cannon Muskegon with γ' precipitations in a γ-matrix (Fig. 3) [1]. The blade made of the monocrystalline Ni-based alloy was assumed to be isotropic and the properties of this alloy, determined in the <100> direction, were used. Such a simplification is permissible because the load acts in the direction of <100> . The good agreement of such assumptions with experimental results has already been confirmed by Fokin and Semenov [12]. In the <100> direction the elastic modulus of this alloy is 94 GPa and the Poisson's ratio 0.44 at 1100 °C [13]. The yield stress at 1100 °C is 420 MPa [14]. The parameters for Eq. 1 for CMSX-4 at 1100 °C were derived from the experimental data by Hasemann et al. [15] and are $n = 5.2$ and $A \times e^{-Q/RT} = 6.8 \times 10^{-50}\,\mathrm{s^{-1}\,Pa^{-5.2}}$. The density of this alloy is 8.7 g/cm^3 [1].

Mo-12Si-8.5B has a microstructure composed of an intermetallic Mo_3Si matrix with inclusions of Mo_{ss} and Mo_5SiB_2 (Fig. 3), which provides excellent creep resistance [11, 16]. The Mo-based alloy do not have a texture in its microstructure and can be considered as isotropic [16]. The density of the Mo-12Si–8.5B alloy was calculated from the weight proportion of the phases and is ≈9.4 g/cm^3. The Young's modulus of the Mo-12Si-8.5B alloy is 274 GPa at 1100 °C and 269 GPa at 1200 °C [17]. The Poisson´s ratio is 0.309 at 1100 °C and 0.312 at 1200 °C [17]. The relation of elastic constants of this alloy to the temperature from RT to 1200 °C is almost linear [17]. Schneibel and Lin [11] reported following parameters for the Eq. 1 for this alloy: $n = 2.7$, $A = 1.8 \times 10^{-18}\,\mathrm{s^{-1}\,Pa^{-2.7}}$ and $Q = 338\,\mathrm{kJ/mol}$.

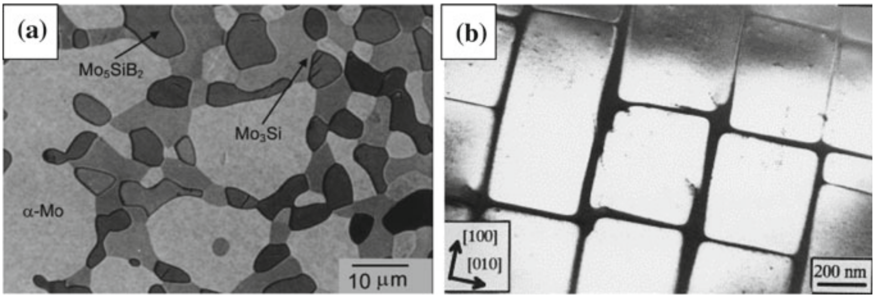

Fig. 3 Microstructure of **a** Mo-12Si-8.5B alloy [18] and **b** CMSX-4 alloy [19]

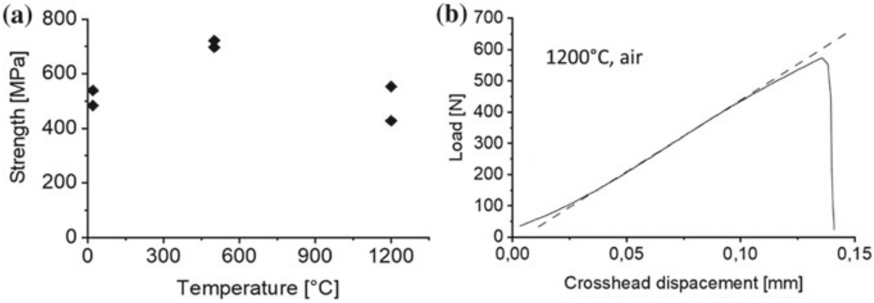

Fig. 4 **a** The three-point flexure strength of Mo-12Si-8.5B, **b** three-point flexure test of Mo-12Si-8.5B at 1200 °C in air, according to [20]

Schneibel et al. [20] determined the three-point flexure strength for Mo-12Si-8.5B at three different temperatures in air (Fig. 4a). Mo_{ss} phase induces significant ductile-phase toughening. Fracture toughness increases with the temperature. This causes a significantly higher strength at 500 °C comparing to room temperature with the increased ductility of the Mo_{ss} phase at 500 °C and the associated reduction in notch sensitivity of the specimen, but the total alloy is still rather brittle. Nevertheless, the strength at 1200 °C is lower than that at 500 °C because of softening mechanisms dominance. In the air at 1200 °C the load-displacement curves showed only a slight plasticity (Fig. 4b). However, the fracture of this alloy in tensile tests in flowing nitrogen at 1200 °C occurs in a brittle manner. The brittle behavior of Mo-12Si-8.5B alloy is caused by the brittleness of the intermetallic phases.

4 Results

In the considered model, the stresses arise because of the centrifugal force and are therefore tensile stresses. The highest stresses (and thus, strains) arise in the blade root (Fig. 5). For the blade with the same cross sections internal force can be described by the following equation:

$$N(r) = 0.5\rho A\omega^2\left(b^2 - r^2\right),$$

where b is the outer radius (rotation radius 170 mm + blade length 58 mm = 228 mm); r—radial coordinate (varies from 170 mm to 228 mm); A—cross-section;

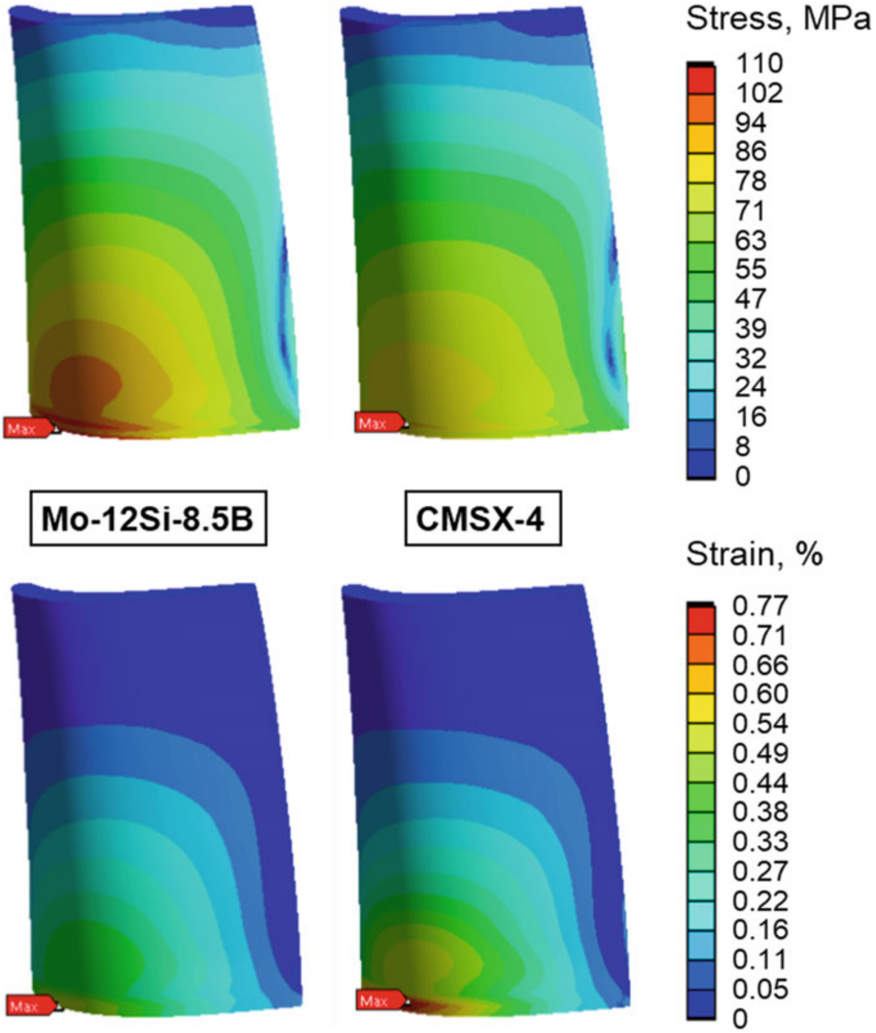

Fig. 5 Calculated stress and strain of Mo-12Si-8.5B and CMSX-4 alloy after 100 h operation considering creep deformation

ρ—material density; ω—angular velocity [21]. The material density and the angular velocity in every cross-section over the blade are the same, so the internal force and also the stress depends only on the difference ($b^2 - r^2$) and are therefore highest at the bottom cross-section and smallest at the upper cross-section. The calculations have also confirmed that the blade root is the most critical area, which corresponds to the crack initiation points during the blade operation. Using a power law stress function $f(x) = x^n$ for the creep deformation, the maximum displacement can be computed as follows [21]:

$$\dot{u}_{\max} = \dot{\varepsilon}_0 \left(\frac{\rho\omega^2}{2\sigma_0} \right)^n \int_a^b \left(b^2 - r^2 \right)^n \mathrm{d}r$$

Figure 5 shows a comparison of the resulting strain and stress of CMSX–4 and Mo-12Si-8.5B at 1100 °C.

In the Mo-12Si-8.5B blade stresses are higher as compared to CMSX-4 blade (Fig. 5). The maximum stress after 100 h in CMSX-4 blade is 89 and 110 MPa in Mo-12Si-8.5B. This correlates well with Eq. 2, because using the same blade geometry, radius of rotation and angular velocity, the stresses depend only on the density of the material and the Mo-based alloy has a higher density than CMSX-4 (9.4 vs. 8.7 g/cm^3). All calculated stresses are significantly lower than the yield strengths of the investigated materials (see Sect. 3.1). In this way, it is permissible not to consider plastic deformation at the initial point. Thus, the only considered inelastic deformation is creep, which takes place at high temperatures also at stresses below the yield stress and causes cracks.

When evaluating the strains, it should be taken into account that in the Mo-based blade higher stresses occur. Nevertheless, at 1100 °C due to a higher Young's modulus and lower creep rate they lead to a lower strain. Thus, the elastic strains, which occur right after the load is applied, and the strains after 100 h of loading are lower in the Mo-12Si-8.5B blades in comparison to CMSX-4 blade. The maximum values of the immediate elastic strains are 0.19% for CMSX-4 and 0.06% for Mo-12Si-8.5B blades. The strain values after 100 h at 1100 °C are 0.77% and 0.51%, respectively. With increasing temperature the creep rate rises exponentially, which leads to higher strain values. Hence, the strain distribution in the Mo-12Si-8.5B blades is almost the same at different temperatures, but the values slightly increase with increasing temperature. The strain rate in the Mo-12Si-8.5B blades at 1110°C are similar to those in CMSX-4 at 1100 °C, but the strain values are lower (maximum value after 100 h is 0.61%). This result shown in Fig. 6 means, that using Mo-12Si-8.5B the temperature can be increased to 1110 °C with benefit to CMSX-4 alloys. The ability to apply polycrystalline Mo-Si-B alloy instead of monocrystalline Ni-based alloy at temperatures increased by 10 K with equal strain rate and lower deformation is very promising, because such temperature increase would lead otherwise to significant reduction of creep life of state-of-the-art alloys (s. paragraph 2, Fig. 1). Furthermore, the producing technology of polycrystalline alloys is much easier than that of monocrystalline ones. A further increase of the temperature leads to exponential increase of the creep rate. So, after 100 h load at 1200 °C Mo-12Si-8.5B blade reaches the maximum calculated strain value of 3.1%.

When the body is at a high temperature under a given load system, the stress redistributes in that body with time. One reason for this is that immediately after loading, the material is not in equilibrium, because the external energy cannot immediately be distributed over the entire volume in accordance with the system's minimum total energy principle. It results in local spots with increased energy, whose redistribution over the sample volume requires time, but occurs faster at higher temperatures. Figure 7 shows the decrease of the maximum stress values. Another illustration of

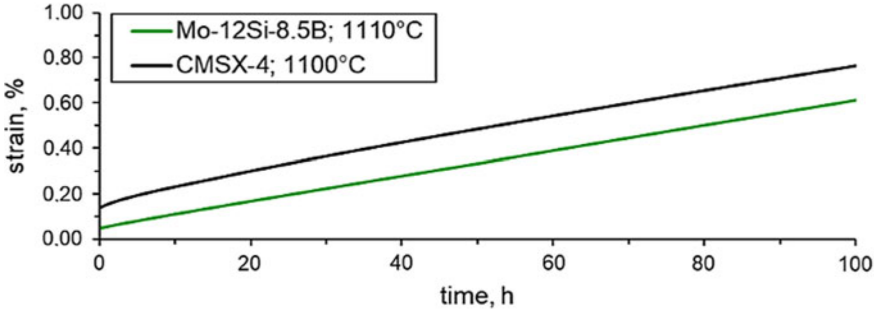

Fig. 6 Change of the maximum strain in the Mo-12Si-8.5B blades and CMSX-4

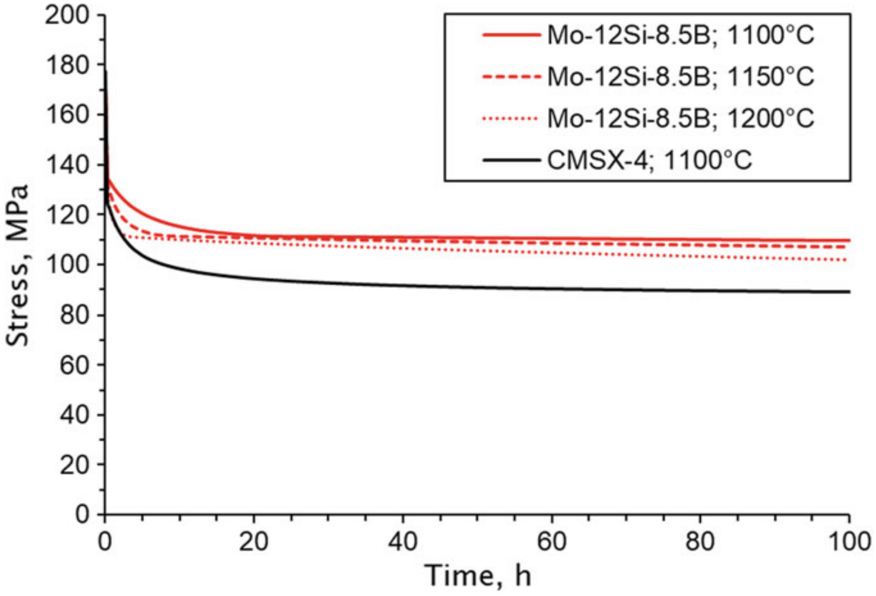

Fig. 7 Change of the calculated maximum stress in the blades made of Mo-12Si-8.5B and CMSX-4 with time

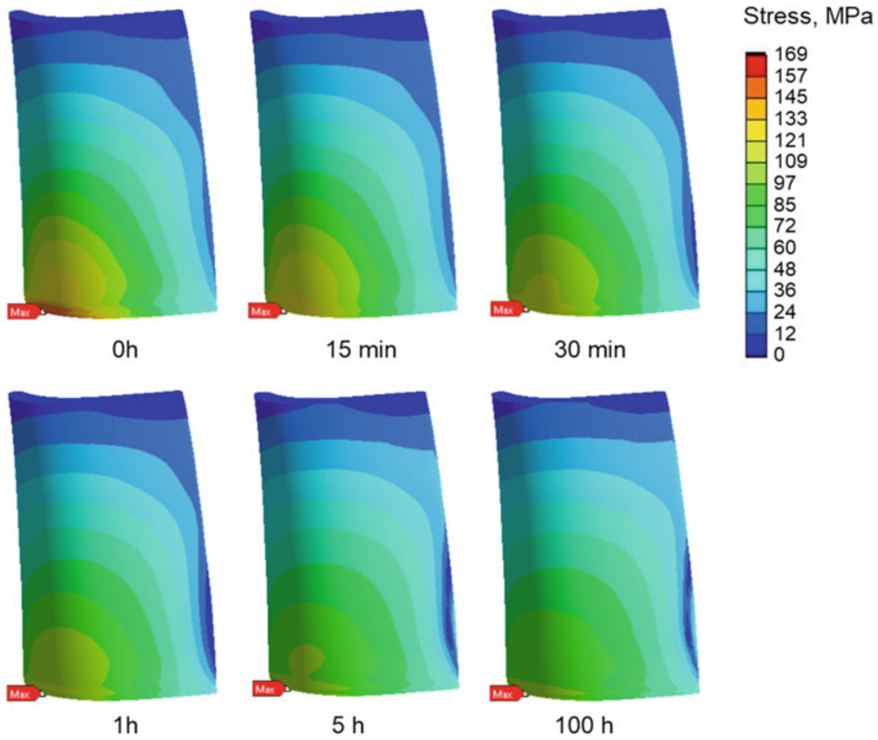

Fig. 8 Stress redistribution at 1100 °C for Mo-12Si-8.5B material

the stress redistribution is shown in Fig. 8 for Mo-12Si-8.5B blade at 1100 °C. The redistribution of the stresses in other calculated cases is similar. The highest stress occurs in the blade root at the starting point, which distributes through the blade with time with the decreasing speed. The highest stress value for the CMSX-4 blade is 177 and 169 MPa for the Mo-12Si-8.5B blade. The redistribution rate is higher at higher temperatures.

5 Conclusions

In this study calculations were performed for stationary operation of high temperature turbine blade considering creep deformation. Two alloys, Mo-12Si-8.5B and the monocrystalline Ni-based superalloy CMSX-4, were considered at 1100 °C. Additionally, the stress-strain states in a Mo-12Si-8.5B blade were calculated in a border temperature range between 1100 and 1200 °C. Due to the higher density of Mo-12Si-8.5B, higher stresses occur in this blade as compared to CMSX-4. Nevertheless, the elastic and creep properties are beneficial and thus, an application of Mo-12Si-8.5B is preferred at temperatures up to 1110 °C. Since the alloy Mo-12Si-8.5B has a better creep resistance in the polycrystalline state than the single-crystalline CMSX-4, the class of Mo-Si-B alloys appear promising for the application as a possible new type of turbine blade material. However, further alloy development will be necessary in terms of the ductility and toughness at low temperatures and the oxidation behavior of multi-phase Mo-Si-B alloys.

References

1. Reed, R.C.: The Superalloys: Fundamentals and Applications. Cambridge University Press, Cambridge (2006)
2. Lemberg, J.A., Ritchie, R.O.: Mo-Si-B alloys for ultrahigh-temperature structural applications. Adv. Mater. **24**(26), 3445–3480 (2012). https://doi.org/10.1002/adma.201200764
3. Boyce, M.P.: Gas Turbine Engineering Handbook, 4th edn. Butterworth-Heinemann; Elsevier, Waltham, Mass; Amsterdam (2012)
4. Schulenberg, T.: Zuverlässige Gasturbinen. Vorlesung am Institut für Thermische Strömungsmaschinen der Universität Karlsruhe. Karlsruhe
5. Nabarro, F.R.N., de Villiers, F.: Physics of Creep and Creep-Resistant Alloys. Chapman and Hall/CRC, Boca Raton (2018)
6. Rossmann, A.: Industrie-Gasturbinen: Problemorientierter Ratgeber für Betreiber; mit Diagrammen. Turboconsult Rossmann, Karlsfeld (2009)
7. Carter, T.J.: Common failures in gas turbine blades. Eng. Fail. Anal. **12**(2), 237–247 (2005). https://doi.org/10.1016/j.engfailanal.2004.07.004
8. Bräunling, W.J.G.: Flugzeugtriebwerke: Grundlagen, Aero-Thermodynamik, ideale und reale Kreisprozesse, Thermische Turbomaschinen, Komponenten, Emissionen und Systeme, 3., vollst. überarb. u. erw. Aufl. VDI-Buch. Springer, Berlin (2009)
9. Lechner, C., Seume, J. (eds.): Stationäre Gasturbinen, 2, neu bearb. Aufl. VDI-Buch. Springer, Berlin (2010)
10. Kablov, E.N.: Litye lopatki gasoturbinnyh dvigatelei: splavy, tehnolohii, pokrytiya, 2nd edn. Nauka, Moskva (2006)
11. Schneibel, J.H., Lin, H.T.: Creep properties of molybdenum silicide intermetallics containing boron. Mater. High Temp. **19**(1), 25–28 (2002). https://doi.org/10.1179/mht.2002.19.1.004
12. Fokin, D.Y., Semenov, A.S.: Vliyanie anizotropii i polyuchesti materiala na NDS lopatok gazovoi turbiny. XXXIV Nedelya nauki SPbGPU IV, pp. 76–78 (2006)
13. Siebörger, D., Knake, H., Glatzel, U.: Temperature dependence of the elastic moduli of the nickel-base superalloy CMSX-4 and its isolated phases. Mater. Sci. Eng.: A **298**(1–2), 26–33 (2001). https://doi.org/10.1016/S0921-5093(00)01318-6
14. Sengupta, A., Putatunda, S.K., Bartosiewicz, L., et al.: Tensile behavior of a new single-crystal nickel-based superalloy (CMSX-4) at room and elevated temperatures. JMEP **3**(1), 73–81 (1994). https://doi.org/10.1007/BF02654502
15. Hasemann, G., Bogomol, I., Schliephake, D., et al.: Microstructure and creep properties of a near-eutectic directionally solidified multiphase Mo–Si–B alloy. Intermetallics **48**, 28–33 (2014). https://doi.org/10.1016/j.intermet.2013.11.022
16. Schneibel, J.H.: High temperature strength of Mo–Mo3Si–Mo5SiB2 molybdenum silicides. Intermetallics **11**(7), 625–632 (2003). https://doi.org/10.1016/S0966-9795(03)00044-X
17. Biragoni, P.G.: Modelling the influence of microstructure on elastic properties and tensile damage behaviour of Mo-base silicide alloys. Ph.D. thesis, Otto-von-Guericke University, Magdeburg, Germany (2007)
18. Choe, H., Schneibel, J.H., Ritchie, R.O.: On the fracture and fatigue properties of Mo-Mo3Si-Mo5SiB2 refractory intermetallic alloys at ambient to elevated temperatures (25 °C to 1300 °C). Metall. Mater. Trans. A **34**(2), 225–239 (2003). https://doi.org/10.1007/s11661-003-0325-4

19. Hemmersmeier, U., Feller-Kniepmeier, M.: Element distribution in the macro- and microstructure of nickel base superalloy CMSX-4. Mater. Sci. Eng.: A **248**(1), 87–97 (1998). https://doi.org/10.1016/S0921-5093(98)00516-4
20. Schneibel, J.H., Kramer, M.J., Ünal, Ö., et al.: Processing and mechanical properties of a molybdenum silicide with the composition Mo–12Si–8.5B (at.%). Intermetallics **9**(1), 25–31 (2001). https://doi.org/10.1016/S0966-9795(00)00093-5
21. Naumenko, K., Altenbach, H.: Modeling High Temperature Materials Behavior for Structural Analysis: Part II. Solution Procedures and Structural Analysis Examples. Springer, Berlin (2019)

Effects of Second Phases in Mo-Zr Alloys-A Study on Phase Evolution and Mechanical Properties

Julia Becker, Heiko F. Siems and Manja Krüger

Abstract In this study the microstructure evolution and the mechanical properties of different cast Mo-XZr ($X = 5, 10, 15, 20$ at.%) alloys were investigated. It focuses on the effect of Zr concentrations on the second phase formation in binary Mo-Zr alloys. All alloys exhibit polycrystalline Mo_2Zr precipitations as well as a (Mo, Zr) solid solution phase, which in most cases forms the matrix phase. Microhardness measurements were carried out by the Vickers indentation method. The Mo_2Zr precipitations show a strengthening effect in addition to the solid solution hardening. Additionally, constant displacement tests in the compressive mode at room temperature confirm these findings. However, the homogeneously distributed Mo_2Zr phases offer an extraordinary potential to improve the strength of Mo-based alloys without decreasing the ductility.

1 Introduction

In terms of preserving resources and reducing environmental impacts, improving the efficiency of turbines for power plants and aircraft engines is an increasingly important research subject. A comparably slight increase of the gas inlet temperature would already improve the efficiency of turbines significantly [1].

However, currently used nickel-based superalloys are limited in their maximum operating temperatures due to their melting point of about 1400 °C. Therefore, despite complex cooling systems and coatings, the turbine's efficiency cannot be substantially improved using nickel-based superalloys [2]. Molybdenum-based materials are predestined for such high temperature applications because of their high melting point above 2000 °C as well as their excellent mechanical properties, and are thus promising candidates to replace nickel-based superalloys. Especially multi-phase

---

J. Becker (✉) · H. F. Siems
Otto-von-Guericke University Magdeburg, Magdeburg, Germany
e-mail: julia.becker@ovgu.de

M. Krüger
Research Center Jülich GmbH, Jülich, Germany

K. Naumenko and M. Krüger (eds.), *Advances in Mechanics of High-Temperature Materials*, Advanced Structured Materials 117,
https://doi.org/10.1007/978-3-030-23869-8_5

Mo-Si-B alloys are focused in current research studies since they combine good ambient and high temperature mechanical properties as well as a satisfying oxidation resistance [3–5]. It is well known that the materials properties are significantly correlating to the microstructural features.

Therefore, the approach of Berczik [6] is the most constructive development for Mo-Si-B alloys, aiming in a microstructure in which the hard, but brittle silicide particles are embedded in a continuous Mo solid solution (Mo_{ss}) matrix. Such a microstructure helps to improve the mechanical properties, particularly the fracture toughness at ambient temperatures and simultaneously to ensure sufficient oxidation properties and creep resistance at ultra-high temperatures [3, 7, 8].

Another important issue for the potential application of Mo-Si-B alloys as turbine blade materials in jet engines is to reduce their density. Previous research shows, that comparatively lightweight alloying elements like Ti, V and Zr can be solved in the Mo_{ss} phase (up to their individual solubility limits) and therefore, affect the fracture toughness, the ductility and the strength of this microstructural constituent and, additionally, the density [9]. Especially for Zr doped samples, excellent high temperature properties were reached. In this regard, the alloy Mo-5Zr benefits from the Mo_2Zr particles as effective strengthening phases in addition to the solid solution hardening effect. Therefore, this type of alloy provides a significantly improved strength level compared to single-phase Mo_{ss} alloys. Based on these findings the present study shows systematic investigations on the effects of Zr alloying on the phase formation and resulting mechanical properties in binary Mo-Zr alloys.

2 Effect of Zr in Mo-Based Alloys

In terms of density reduction of Mo alloys, Zr ($\rho = 6.5$ g/cm^3) [10] is a very promising alloying partner. Additionally, Zr operates as getter for oxygen and thus, seems to have a ductilizing effect in powder metallurgically (PM) processed Mo-based materials. Experiments showed that the addition of 1 at.% Zr to the base alloy composition Mo-1.5Si led to a fourfold increase of strength and, simultaneously, an increase of ductility even at room temperature was recognized. Different reasons could be found for these improvements: (I) Zr works as getter for the detrimental oxygen and forms nm-sized ZrO_2 particles, (II) a reduced grain size during PM processing which reduces the overall concentration of interstitial impurities at grain boundaries [11], and (III) the segregation of Si to grain boundaries is reduced which alleviates the grain boundary embrittlement [12, 13]. A computational screening evaluating the Rice-Thomson parameter predicts a more fundamental effect of Zr in terms of ductilizing Mo [14]. However, the solubility of Zr in Mo at room temperature is quite low, i.e. < 1 at.% according to Fig. 1 [15]; higher alloying additions lead to the formation of the secondary phase Mo_2Zr, having a bcc crystal structure as described by Blazina et al. [16, 17]. So, the phase diagram provides a two-phase region composed of (Mo, Zr)$_{ss}$ and Mo_2Zr.

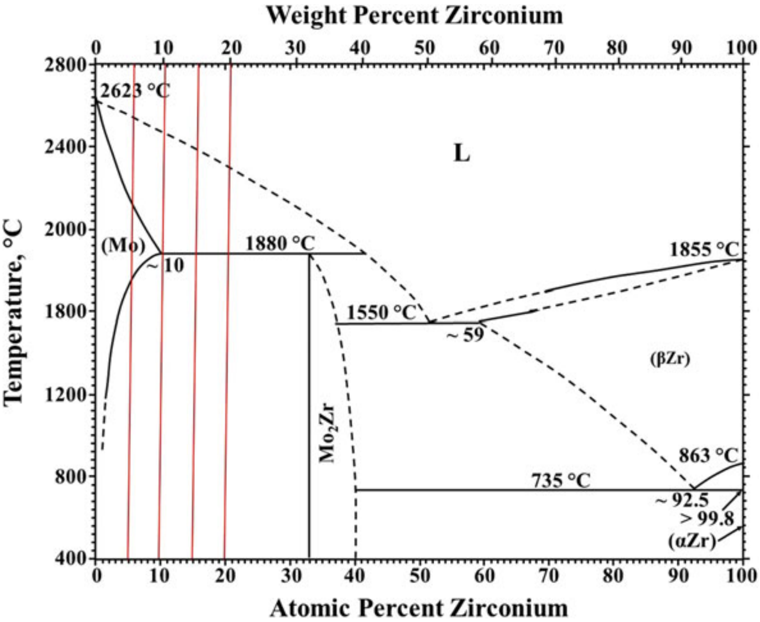

Fig. 1 Binary alloy phase diagram of Mo-Zr, reprinted according to [15]; the compositions chosen for this study are marked by red lines

Microstructural investigations by Mousa et al. [18] have shown the additional Mo_2Zr and $MoZr_2$ nano-phase formation in a Mo-1.5Si-1Zr alloy which might contribute to an extra strengthening beyond the effect of the ZrO_2 particles, which was demonstrated in [9, 19, 20]. Even for three-phase Mo-Si-B alloys a positive effect of Zr alloying (≤ 1at.%) on the strength and ductility was shown [21]. However, for multi-phase Mo-Zr alloys, no systematic investigations were carried out so far regarding the influence of higher concentrations of Zr beyond the results described above. A fundamental understanding is essential to identify the working mechanisms, which can be used for technical relevant multi-phase Mo-based alloys. Therefore, the aim of this work is to systematically investigate the phase formation in binary Mo-Zr alloys which will be discussed in the context of data from alloy Mo-5Zr [9]. Accordingly, the effect of gradually increased Zr concentrations (5, 10, 15, 20 at.%) in Mo alloys is investigated regarding the phase evolution and the resulting mechanical properties of two-phase alloys.

3 Materials and Methods

Since previous research demonstrated the potential of Zr additions to Mo (about 1–5 at.% Zr), higher concentrations of Zr are subject of the present study to observe relevant effects on the mechanical properties of Mo-Zr alloys. Therefore, the Zr additions were chosen as follows: 5 at.% [9], 10 at.%, 15 at.% and 20 at.%.

The alloys were fabricated via arc-melting (AM) in an argon atmosphere to produce the binary alloys having compositions of Mo-5Zr, Mo-10Zr, Mo-15Zr and Mo–20Zr (at.%). All compositions used for this study are marked in the phase diagram in Fig. 1. The pure metal sheets with purities of 99.95% for Mo and 99.2% for Zr were cut into flakes and mixed to obtain the target alloy composition.

After remelting the samples five times on a water-cooled copper mold they solidify typically drop-shaped. Due to the high cooling rates of the arc-melting process disequilibrium conditions could remain after solidification. Therefore, the ingots were subsequently homogenized in an argon atmosphere for 24 h at 1400 °C. The investigation of the microstructure was carried out by scanning electron microscopy (SEM—FEI ESEM XL30 FEG equipped with EDS) on ground and polished samples. Therefore, the compact samples were hot mounted, ground, wet-grinded using SiC paper with a grit of 500, 800, 1200 and polished with a 3 and 1 μm diamond suspension.

The concentration of Zr in the $\mathrm{Mo_{ss}}$ was measured using energy dispersive X-ray analysis (EDS). Electron backscatter diffraction (EBSD) analysis was performed to identify the crystal structure of the precipitations and the matrix phase using a Zeiss Merlin SEM equipped with a Nordlys EBSD camera and Aztec software package (Oxford Instruments). Grain sizes of the alloys were evaluated by means of optical microscopy (OM) via linear intercept method (DIN EN ISO 643 [22]). Due to differences of the grey values in the SEM micrographs, the fractions of phases were evaluated using the program Image J. Additionally, the phase fractions were measured using EBSD analyses. Density measurements of the specimens were carried out according to the Archimedes' method.

X-ray diffraction (XRD) measurements were performed using an X'Pert X-ray diffractometer (PANalytical) with Cu $\mathrm{K}_{\alpha 1,2}$ radiation. The phase identification was performed using the analyzing software X'Pert HighScore Plus (PANalytical).

Vickers microindentation tests referring to DIN EN ISO 6507–1 [23] were conducted with a force of 0.1 N (HV 0.01) and a hold period of 5 s. The microhardness measurements were performed by generating a series of 30 indents set within the grains by considering a defined minimum distance between the indents and grain boundaries. The mechanical behavior was determined by constant displacement tests at a nominal strain rate of $1 \cdot 10^{-4}\ \mathrm{s}^{-1}$ in uniaxial compression at room temperature. The specimens with dimensions of ($2 \times 2 \times 3.5$) mm, prepared by electro-discharge machining, were tested using a Zwick/Roell Z100 electro-mechanical testing machine. The yield stresses were measured by the 0.2% offset method.

4 Results and Discussion

4.1 Microstructures

The microstructures were observed via OM and SEM coupled with EDS as well as EBSD analysis. According to the phase diagram the Mo-Zr alloys show a two-phase microstructure (Fig. 2) with the (Mo, Zr)$_{ss}$ phase as the main phase and the intermetallic phase Mo_2Zr as homogeneously distributed second phase particles. A comparison of the Mo-Zr alloys indicates that the amount of secondary phases rises with increasing Zr additions in agreement with the phase diagram (Fig. 1).

In contrast to the Mo-5Zr alloy, in which finely distributed individual particles were formed (Fig. 2a), the microstructure of Mo–Zr alloys with higher Zr concentrations reveals extended phase dimensions of Mo_2Zr (Fig. 2b–d). Accordingly, there is an enormous increase of secondary phase proportions from 9 vol.% for Mo–5Zr to 44 vol.% for Mo-20Zr (Table 1), which corresponds quite well with the phase diagram. The appearance of the Mo_2Zr phase changes from individual particles in Mo-5Zr to a network-like structure in Mo-20Zr (Fig. 2).

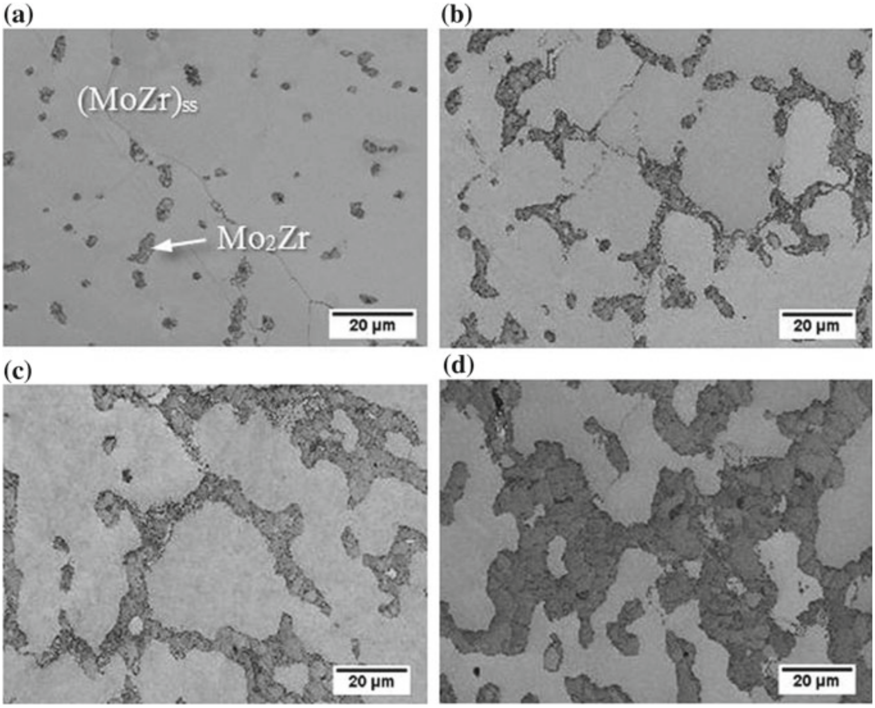

Fig. 2 SEM images of **a** Mo-5Zr [9] **b** Mo-10Zr **c** Mo-15Zr and **d** Mo-20Zr alloy

Table 1 Microstructural parameters of Mo-XZr alloys compared to pure Mo

Nominal alloy composition, at.%	Mo	−5Zr	−10 Zr	−15 Zr	−20 Zr
Calculated density after [24], g/cm^3	10.21	9.91	9.83	9.50	9.21
Measured density, g/cm^3	10.19	9.95	9.87	9.51	9.23
Median grain size, μm	–	176	59	56	32
Concentration of Zr in Mo$_{ss}$, at.%	–	4.1	4.4	6.5	8.9
Amount of Mo$_2$Zr phases, vol.%	–	9	12	22	44

A summary of the microstructural properties and the density of the alloys is given in Table 1, which represents the significant impact of increasing Zr additions. It can clearly be seen that not only rising amounts of Zr, which is dissolved in Mo$_{ss}$, but also the increased fraction of Mo$_2$Zr phase with a density of 8.63 g/cm^3 (calculation based on [24]) contributes to the density reduction of the Mo alloys.

Additionally, the grain size decreases with increasing Zr concentrations due to the nucleation of Mo$_2$Zr grains, limiting the grain growth of the Mo$_{ss}$ phase during solidification and heat treatment. Hence, the Hall-Petch theory as well as second phase hardening have to be considered when discussing the mechanical properties. EDS measurements show that the concentration of dissolved Zr in the (Mo, Zr)$_{ss}$ phase tends to increase despite of forming Mo$_2$Zr particles (Table 1). However, based on the phase diagram, presented in Fig. 1, lower concentrations of dissolved Zr in the Mo$_{ss}$ phase would be expected. This might be due to a still incomplete equilibrium state of the alloys even after heat treatment or to ambiguous solubility ranges in the phase diagram at lower temperatures.

The XRD diffractograms in Fig. 3 (left) verify the presence of the (Mo, Zr)$_{ss}$ phase in all alloys. There is just a weak peak of the Mo$_2$Zr phase detectable in the alloy Mo-5Zr and Mo-10Zr, whereas for higher Zr-doped Mo alloys this phase was clearly identified. A more detailed depiction of one of the respective (Mo, Zr)$_{ss}$ reflexes (Fig. 3, right) represents the shifting of the (Mo, Zr)$_{ss}$ peaks to smaller diffraction angles with respect to that one of pure Mo, which indicates changes in the lattice parameters. This is based on the Bragg's equation [26]. The site occupation by Zr atoms in the Mo lattice leads to lattice distortion, which is due to deviations of the atomic radii (Mo: 145 pm; Zr: 155 pm) [25].

The EDS measurements (Table 1) showed the following trend: the higher the Zr addition in the alloy the higher the concentration of Zr dissolved in the Mo lattice. This is confirmed by the shifting of the (Mo, Zr)$_{ss}$ reflexes as visible in Fig. 3. The higher intensities of the reflexes of Mo-5Zr as compared to Mo-Zr with 10, 15 and 20% Zr are due to longer settings at each single step during the measurement.

All alloys were investigated by EBSD analyses as shown in Fig. 4. A phase mapping clearly identified the phases Mo$_{ss}$ and Mo$_2$Zr and corresponds very well with the results of XRD measurements (Fig. 3). Additional EDS analyses confirm that the last-mentioned phase consists of about 66 at.% Mo and 34 at.% Zr according to the stoichiometric composition of Mo$_2$Zr.

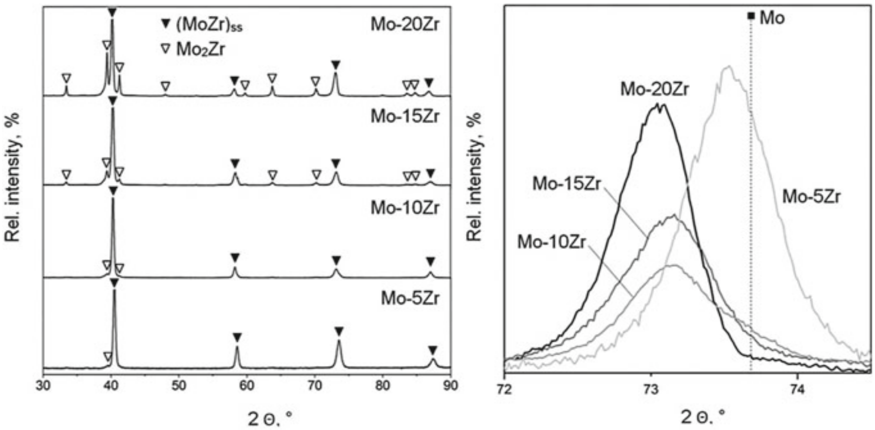

Fig. 3 XRD data in (left) standardized representation and (right) direct comparison visualizing the shifting of reflexes in comparison to pure Mo

Figure 4a gives an impression on the finely distributed Mo_2Zr precipitations in the microstructure of Mo-5Zr. It also reveals that the Mo_2Zr phases appear at the grain boundaries, but also within the grains (Fig. 4b). It is assumed, that the high cooling rates in the arc melting process could hinder a peritectic reaction (according to Fig. 1). Due to this reason a supersaturated $(Mo, Zr)_{ss}$ phase could remain after cooling, so that the Mo_2Zr precipitations inside the grains could be formed during the subsequent heat treatment procedure, so that they appear next to the Mo_2Zr precipitations decorating the grain boundaries.

The occupation of the grain boundaries with the Mo_2Zr phase becomes more dense in the alloys with 10 at.% Zr and 15 at.% Zr (Fig. 4c, d). For the Mo-20Zr alloy, EBSD orientation mappings show that the extended Mo_2Zr phases appear in a network-like structure at the grain boundaries (Fig. 4e, f). Due to the pronounced precipitation of the Mo_2Zr phase during solidification, grain growth is limited which results in a decreasing grain size by an increasing fraction of Mo_2Zr (Table 1).

The EBSD orientation mappings of the Mo_2Zr phases shown in Fig. 4 indicate that the precipitated phases are polycrystalline. Polycrystalline phases exhibit a huge advantage by acting as effective obstacles to dislocations while still allowing some degree of deformation. In other words, in case of alloy Mo-20Zr, small grain sizes of $(Mo, Zr)_{ss}$ combined with a high amount of Mo_2Zr phases at the grain boundaries show promising potential for high strength while keeping the plastic deformability at an acceptable level (Sect. 4.3).

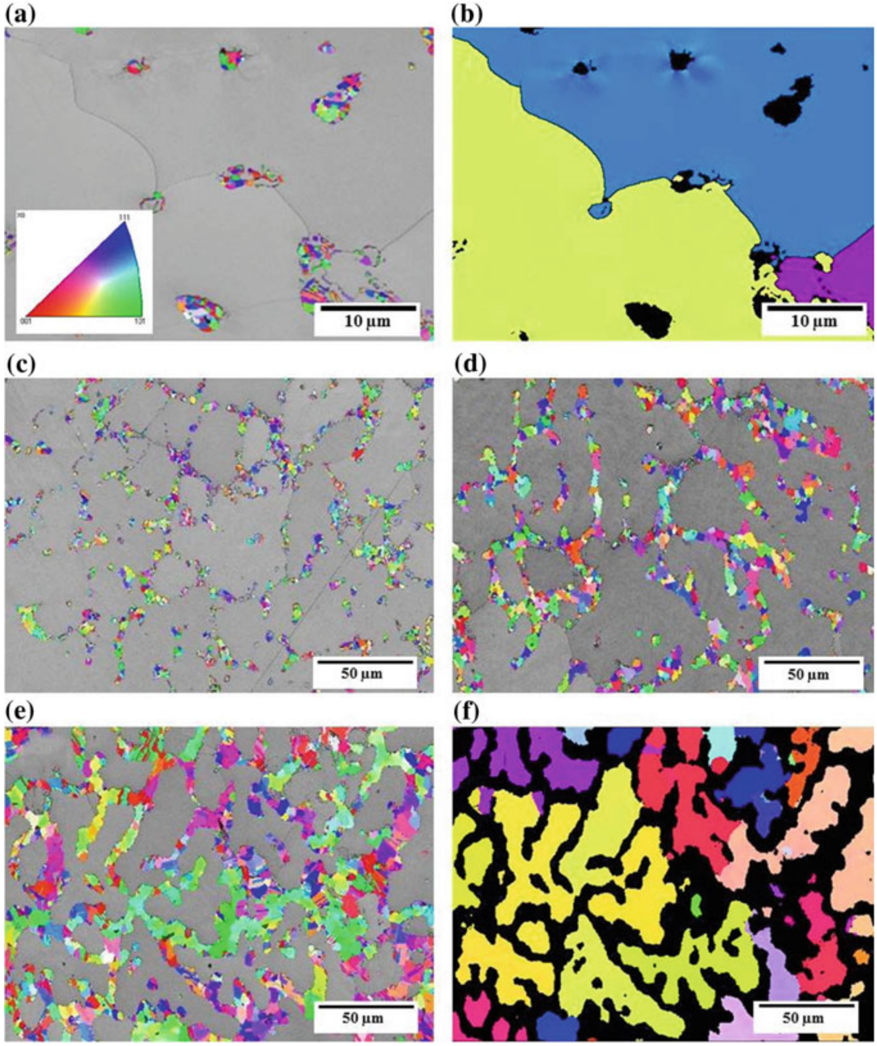

Fig. 4 Results of EBSD orientation mappings: IPF color-coded images of Mo_2Zr phases in **a** Mo-5Zr, **c** Mo-10Zr, **d** Mo-15Zr and **e** Mo-20Zr and additional IPF color-coded images of (Mo, Zr)$_{ss}$ phase in **b** Mo-5Zr and **f** Mo-20Zr

Fig. 5 Hardness of Mo-XZr alloys compared to pure Mo

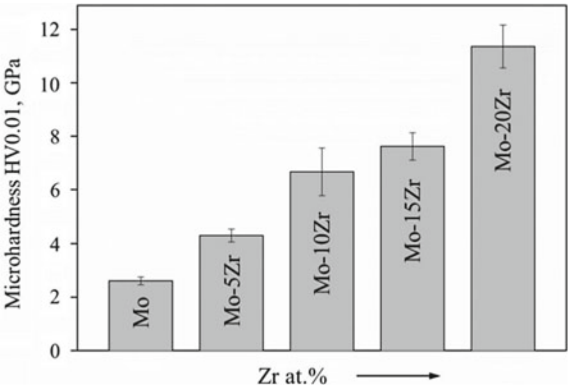

4.2 *Microhardness*

The microhardness measurements were performed using a pyramidal Vickers indenter. To avoid the effect of dislocation pile-up at the grain boundaries it is necessary to consider a defined minimum distance between the indents and grain boundaries. According to [23] the minimum interval between the center of neighboring indents as well as the distance between the indent and the grain boundary should be the threefold of the diagonal length. This requirement has been fulfilled. Although the present materials are two-phase alloys, only indents in the (Mo, Zr)$_{ss}$ phase are considered for the hardness data to analyze only the solid solution effects. The results compared to data of pure Mo are shown in Fig. 5, which demonstrate the improvement of hardness of the (Mo, Zr)$_{ss}$ phase by increasing Zr additions. In general, this effect is mainly due to solid solution hardening, since the hardness increase corresponds very well with the dissolved Zr concentration in the solid solution (Table 1). In previous studies [9] we already demonstrated that Zr is a very effective solid solution strengthener as compared to Ti and V, which is due to an effective lattice distortion.

The hardness values of all alloys especially in Mo-20Zr are significantly higher than the reference of pure Mo and can be understood as an increasing level of solid solution strengthening in dependence on the dissolved Zr concentration. Calculated strengthening contributions based on the model of Labusch [27] show that additional strengthening from 0.17 GPa (Mo-5Zr) up to 0.5 GPa (Mo-20Zr) is possible in the solid solution phase. It is noticeable that the total hardness of the alloys will be additionally influenced by Hall-Petch hardening and precipitation or second phase hardening.

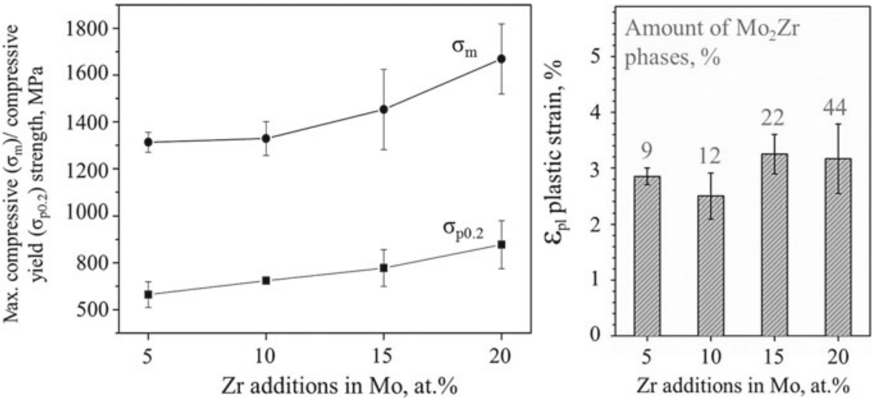

Fig. 6 Results of compression tests at room temperature: (left) maximum compressive (σ_m) and yield ($\sigma_{p0.2}$) strength, (right) plastic strain depending on the Zr additions

4.3 Uniaxial Compression Tests

By using constant displacement tests at a nominal strain rate of $1 \cdot 10^{-4}\ s^{-1}$ in uniaxial compression at room temperature (RT), the influence of Zr on the compressive strength and plastic deformability was analyzed. The results are presented in Fig. 6, depending on the Zr concentration in the respective alloys.

Regarding the maximum compressive and yield strength (left), all Mo alloys show an increase of strength with rising Zr additions. So the general tendency of the microhardness measurements (Fig. 5) is validated by the uniaxial compressive tests. For detailed understanding of the measured data it is necessary to have a closer look at the microstructural parameters as presented above. Following the approach of Hall and Petch [28, 29] the contribution of the grain size (GS) effect must be considered as follows: $\Delta GS_{\text{Mo-5zr, 176}\mu\text{m}} < \Delta GS_{\text{Mo-10Zr, 59}\mu\text{m}} < \Delta GS_{\text{Mo-15Zr, 56}\mu\text{m}} < \Delta GS_{\text{Mo-20Zr, 32}\mu\text{m}}$ (Table 1). Hence, the Mo_2Zr precipitations cause the stabilization of a small grain size during solidification, which means that a smaller grain size was generated by increasing Zr concentrations and results in an increased strength according to the Hall-Petch theory. Not only the grain size but also the concentration of Zr dissolved in the Mo phase plays a major role. After Northcott [30], investigations on Mo alloys containing up to 3% Zr showed that the lattice parameter increases linearly with Zr additions, indicating that at least 3% is soluble in Mo. For the present alloys the dissolved Zr concentrations are higher than expected by the literature data. This might be due to a not completely achieved equilibrium state of the alloys after annealing. Thus, the additionally dissolved Zr causes an extra distortion within the Mo lattice leading to a more pronounced solid solution strengthening effect.

An additional effect on the strength is given by the secondary Mo_2Zr phases. In general, the homogeneous distribution of this phase has an improving effect on the strength level, since this second phase acts as obstacles for the dislocation motion.

Especially for alloy Mo-20Zr which exhibits the highest amount of Mo_2Zr phases, the strength level is significantly improved (Fig. 6). This effect may also be due to the continuous formation (network-like) of Mo_2Zr phase.

On the other hand, all Mo-XZr alloys provide plastic strains between 2 and 4% in compressive mode (Fig. 6, right), showing the potential of materials' deformability, even though hard and brittle Mo_2Zr is present in comparably high concentrations. Surprisingly, the plastic strain was not significantly decreased with increasing amount of Mo_2Zr.

5 Conclusions

The effects of Zr additions on the mechanical properties of the Mo solid solution (Mo_{ss}) phase and two-phase Mo_{ss}-Mo_2Zr alloys were investigated using different compositions of Mo-XZr (X = 5, 10, 15, 20 at.%). These alloys were characterized by microstructure analysis, Vickers microhardness measurements as well as constant displacement tests in uniaxial compression at room temperature. According to the experimental results described above, the following conclusions can be drawn:

1. The Mo-Zr alloys exhibit a two-phase microstructure as expected from the binary phase diagram. The secondary phases were identified as Mo_2Zr, which are homogeneously embedded in a $(Mo, Zr)_{ss}$ phase, occurring as precipitations at the grain boundaries and within the grains. The amount of second phases increase with rising Zr additions whereas the grain size is decreased.
2. Detailed EBSD analyses indicate that the phase regions of Mo_2Zr are polycrystalline. In case of Mo-20Zr the Mo_2Zr phase decorates the grain boundaries completely and forms large and continuous network-like structures.
3. Zr causes effective distortion of the Mo lattice. The significant contribution of solid solution strengthening is due to the high concentration of dissolved Zr in Mo, which is beyond the solubility limits as given in the phase diagram.
4. In general, Zr has a positive effect on the mechanical properties, which is represented by the results of microhardness and compression tests. This is mainly due to the following reasons: First, higher amounts of Mo_2Zr phases lead to a smaller grain size, which results in an increased strength according to the Hall-Petch theory. Second, significant concentrations of Zr dissolved in the Mo phase cause a strong solid solution strengthening effect. Third, an additional increase of strength is given by the second phase Mo_2Zr particles, which are homogeneously distributed.
5. The alloys investigated offer a constant level of plastic deformability at room temperature, even though the amount of Mo_2Zr varies significantly from 9 to 44%.

Acknowledgements The authors gratefully acknowledge for the financial support by the DFG Graduate School 1554 "Micro-Macro-Interactions in structured Media and Particle Systems". We thank Dr. E. Wessel from Forschungszentrum Jülich GmbH for the SEM and EBSD analyses. M. K. acknowledges the MDZ WP e.V. for the support of this research.

References

1. Dimiduk, D.M., Perepezko, J.H.: Mo-Si-B Alloys: Developing a revolutionary turbine-engine material. MRS Bull. **28**, 639–645 (2003). https://doi.org/10.1557/mrs2003.191
2. Jackson, J.E., Olson, D.L., Mishra, B., Lasseigne-Jackson, A.N.: Deposition and characterization of Al-Si metallic TBC precursor on Mo-Si-B turbine materials. Int. J. Hydrogen Energy **32**, 3789–3796 (2007). https://doi.org/10.1016/j.ijhydene.2006.08.053
3. Krüger, M., Franz, S., Saage, H., Heilmaier, M., Schneibel, J.H., Jéhanno, P., Böning, M., Kestler, H.: Mechanically alloyed Mo-Si-B alloys with a continuous α-Mo matrix and improved mechanical properties. Intermetallics **16**, 933–941 (2008). https://doi.org/10.1016/j.intermet.2008.04.015
4. Parthasarathy, T.A., Mendiratta, M.G., Dimiduk, D.M.: Oxidation mechanisms in Mo-reinforced Mo_5SiB_2(T2)-Mo_3Si alloys. Acta Mater. **50**, 1857–1868 (2002). https://doi.org/10.1016/S1359-6454(02)00039-3
5. Nieh, T.G., Wang, J.G., Liu, C.T.: Deformation of a multiphase Mo-9.4Si-13.8B alloy at elevated temperatures, Intermetallics. **9,** 73–79 (2001). https://doi.org/10.1016/s0966-9795(00)00098-4
6. Berczik, D.M.: U.S. Patents 5,595,616 und 5,693,156 (1997)
7. Krüger, M., Jain, P., Kumar, K.S., Heilmaier, M.: Correlation between microstructure and properties of fine grained Mo-Mo_3Si-Mo_5SiB_2 alloys. Intermetallics **48**, 10–18 (2014). https://doi.org/10.1016/j.intermet.2013.10.025
8. Kruzic, J.J., Schneibel, J.H., Ritchie, R.O.: Fracture and fatigue resistance of Mo-Si-B alloys for ultrahigh-temperature structural applications. Scr. Mater. **50**, 459–464 (2004). https://doi.org/10.1016/j.scriptamat.2003.11.002
9. Becker, J., Betke, U., Wessel, E., Krüger, M.: Alloying effects in Mo-5X (X = Zr, Ti, V) - microstructural modifications and mechanical properties. Mater. Today Commun. **15**, 314–321 (2018)
10. Binder, H.H.: Lexikon der chemischen Elemente. S. Hirzel Verlag, Leipzig, Stuttgart (1999)
11. Becker, J., Krüger, M.: Impact of Phase Distribution on the Fracture Toughness of High Temperature Resistant Mo-Si-B Alloys. Pract. Metallogr. **52**, 295–313 (2015)
12. Sturm, D., Heilmaier, M., Schneibel, J.H., Jéhanno, P., Skrotzki, B., Saage, H.: The influence of silicon on the strength and fracture toughness of molybdenum. Mater. Sci. Eng. A **463**, 107–114 (2007). https://doi.org/10.1016/j.msea.2006.07.153
13. Northcott, L.: Metallurgy of the Rarer Metals-5 Molybdenum. Academic Press INC. Pulbishers, New York (1956)
14. Geller, C.B., Smith, R.W., Hack, J.E., Saxe, P., Wimmer, E.: A computational search for ductilizing additives to Mo. Scr. Mater. **52**, 205–210 (2005). https://doi.org/10.1016/j.scriptamat.2004.09.034
15. ASM, ASM Handbook vol.3, Alloy Phase Diagrams, ASM International (1992)
16. Blazina, Z., Trojko, R., Ban, Z.: High temperature equilibria in the Zr1-xHfxM2, Zr1-xTixM2 and Hf1-xTixM2 (M = Mo orW) Systems. J. Less-Common Met. **83**, 175–183 (1982)
17. Blazina, Z., Trojko, R., Ban, Z.: Metal-metalloid exchange in the Zr1-xMxMo2 (M = Ge, Si, Al) System. J. Less-Common Met. **97**, 91–98 (1984)
18. Mousa, M., Wanderka, N., Timpel, M., Singh, S., Krüger, M., Heilmaier, M., Banhart, J.: Modification of Mo-Si alloy microstructure by small additions of Zr. Ultramicroscopy **111**, 706–710 (2011). https://doi.org/10.1016/j.ultramic.2010.12.002
19. Cui, C., Gao, Y., Wei, S., Zhang, G., Zhou, Y., Zhu, X.: Microstructure and high temperature deformation behavior of the Mo-ZrO_2 alloys. J. Alloys Compd. **716**, 321–329 (2017). https://doi.org/10.1016/j.jallcom.2017.05.013

20. Lenchuk, O., Rohrer, J., Albe, K.: Cohesive strength of zirconia/molybdenum interfaces and grain boundaries in molybdenum: A comparative study, Acta Mater. (2017). https://doi.org/10.1016/j.actamat.2017.05.070
21. Hochmuth, C., Schliephake, D., Völkl, R., Heilmaier, M., Glatzel, U.: Influence of zirconium content on microstructure and creep properties of Mo-9Si-8B alloys. Intermetallics **48**, 3–9 (2014). https://doi.org/10.1016/j.intermet.2013.08.017
22. DIN Deutsches Institut für Normung e.V., DIN EN ISO 643 (2012)
23. DIN Deutsches Institut für Normung e.V., DIN EN ISO 6507-1 (2006)
24. Schumann, H., Oettel, H.: Metallografie. Wiley-VHC, Weinheim (2011)
25. Pintat, T., Wellinger, K., Gimmel, P.: Werkstofftabellen der Metalle: Bezeichnung, Festigkeitswerte, Zusammensetzung, Verwendung und Lieferquellen, Aufllage 8, Alfred Kröner Verlag (2000)
26. Bargel, H.-J., Schulze, G.: Werkstoffkunde, 10. Auflag, Springer, Heidelberg (2008)
27. Labusch, R.: A statistical theory of solid solution hardening. Phys. Status Solidi. **41**, 659–669 (1970). https://doi.org/10.1002/pssb.19700410221
28. Hall, E.O., Sylwestrowicz, W., Hall, E.O., Wain, H.L.: The Deformation and Ageing of Mild Steel: III Discussion of Results (1951)
29. Petch, N.J.: The cleavage strength of polycrystals. Iron Steel Inst. **174**, 25–28 (1953)
30. Northcott, L., Office, W.: Some Featur. **3** (1961)

Investigating the Effect of Creep Properties Mismatch in Very Thin Pipes Within High-Temperature Facilities

Martin Packham and Daniele Barbera

Abstract Most industrial structures are affected by material mismatch effects, due to the design necessity that leads to the use of dissimilar materials like welding of different parts. In other circumstances, this mismatch is introduced by material transformation like radiation embrittlement, hydrogen attack or carburisation, which can drastically change the material response of a restricted area of the component. Such an outcome can have an unpredicted effect on the behaviour and endurance of the component. Carburisation has been identified within the thin stainless steel pipes of UK Advanced Gas-cooled Reactors (AGR). This carburisation is known to affect crack initiation and creep-fatigue properties, ultimately impacting on service life. The current assessment procedure for UK AGRs has several limitations when addressing carburisation and is believed in some circumstances to be overly conservative and in other conditions non-conservative. The work of this study aims to aid in clarifying the effect of creep properties mismatch due to carburisation in thin pipes within such high-temperature facilities. A numerical study is undertaken to investigate the effect of creep properties mismatch in a thin pipe subjected to a combination of primary (load controlled) and secondary (displacement controlled) cyclic loading. In order to perform an extensive parametric study, a special numerical procedure based on the finite element commercial code Abaqus is used to predict the cyclic behaviour of the structure. The effect of creep properties mismatch on global shakedown and creep ratcheting will be investigated providing new insight in the field of structural integrity of pressurised components.

M. Packham · D. Barbera (✉)
University of Glasgow, University Avenue G12 8QQ, Glasgow, UK
e-mail: daniele.barbera@glasgow.ac.uk

M. Packham
e-mail: martin.packham2@btinternet.com

K. Naumenko and M. Krüger (eds.), *Advances in Mechanics of High-Temperature Materials*, Advanced Structured Materials 117,
https://doi.org/10.1007/978-3-030-23869-8_6

1 Introduction

EDF Energy currently operate 14 Advanced Gas-cooled Reactors (AGRs) across six sites in the UK. The majority of these AGRs have been in operation for around 35 years, with the first site, Hinkley Point B, starting operation in 1976. The UK's commitment to an increasing energy demand as well as environmental targets have called for numerous life time extension plans. These have been both announced and implemented allowing for considerable extension over the original intended service lives of 25–30 years.

There are two major limiting factors in the service lives of UK Advanced Gas-cooled Reactors (Fig. 1), the first of these being cracking and damage to the graphite components associated with the reactor core and the second, creep-fatigue damage to irreplaceable stainless steel pipework. The AGR's boilers contain many stainless steel components that are exposed to temperatures as high as 650 °C whilst operating over hundreds of thousands of hours. Water within the pipes is heated via a coolant gas mixture primarily consisting of carbon dioxide with carbon monoxide, methane and water vapour also present. This gas in turn cools the reactor core. This investigation

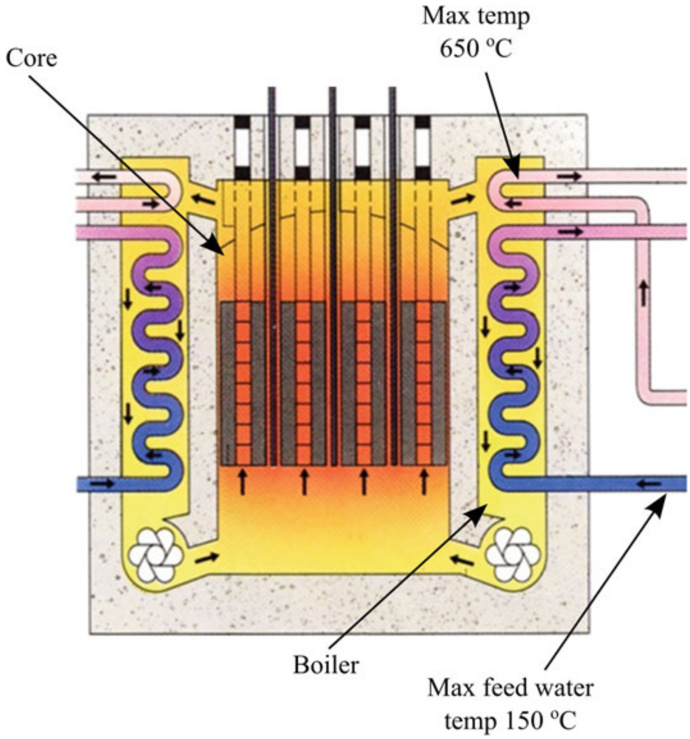

Fig. 1 Advanced gas cooled reactor schematic [1]

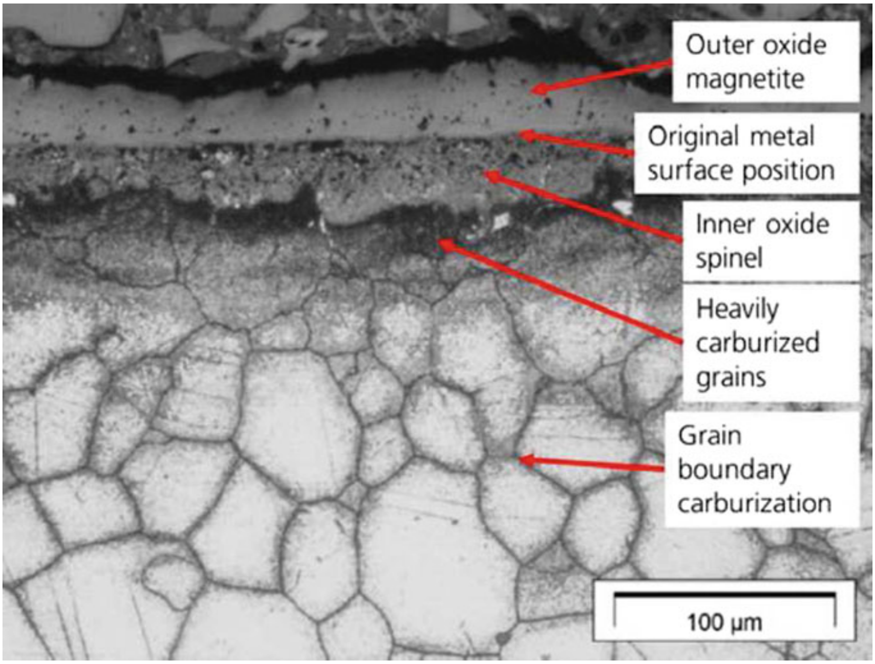

Fig. 2 Etched 316 H stainless steel sample after exposure to AGR coolant gas [1]

will focus on the hottest regions of the boiler, generally associated with the re-heater. Here, components are subject to a wide range of loading conditions resulting from high internal pressures and variations in temperature. This leads to a combination of primary, load controlled, and secondary, displacement controlled, cyclic loading. At temperatures greater than 480 °C it has been observed that exposure to the coolant gas may lead to carburisation of the austenitic 316 H stainless steel of which boiler components are fabricated [1]. Oxidation occurs rapidly at temperatures higher than 480 °C. Initially a thin chromia (Cr_2O_3) layer forms; in most cases this gives way to the formation of a duplex oxide consisting of an outer magnetite (Fe_3O_4) layer and an inner spinel layer rich in chromium and nickel [2]. This oxidation process leads to carburisation of the austenitic stainless steel via diffusion, with diffusion occurring more rapidly along the grain boundaries as shown in Fig. 2 [1].

At temperatures greater than 600 °C, the initial duplex oxide formation may be very rapid, however a chromium-silicon rich healing layer may form providing a protective barrier at the interface of the metal and oxide [3]. This oxide layer prevents further carburisation occurring, whereas at temperatures in the region of 480–600 °C carburisation may continue throughout the material life. Carburisation leads to a considerable increase in the hardness of the material due to the ingress of carbon and the formation of carbides. The depth of carburisation can be assessed using micro hardness tests where an exponentially decaying curve can be fitted to the test data until the bulk material is reached at a particular depth. The extent of carburisation is generally defined as the depth until the hardness falls to a value of 110% of the bulk material [1]. After an exposure to the coolant gas for more than approximately 12 years a carburised layer depth of 0.2–0.8 mm may be expected, resulting in a material mismatch. This depth will be heavily dependent on several factors including temperature, surface finish and proximity to welded joints.

Damage and structural defects in the UK AGRs are both predicted and assessed using the R5 defect assessment procedures, which have been developed and revised over many years [4]. It is written as a series of step-by-step instructions in a series of five volumes with the purpose of assessing damage at high temperature [5]. The five volumes are Volume 1: Overview, Volume 2/3: Creep-fatigue initiation procedure for defect free structures, Volume 4/5: Procedure for assessing defects under creep and creep-fatigue loading, Volume 6: Assessment procedure for dissimilar metal welds and Volume 7: Behaviour of similar welds: guidance for steady creep loading of CrMoV pipework components [4]. It is Volume 2/3 that relates specifically to the work of this study and involves assessment of damage via shakedown analysis.

At present the R5 [6] does not directly consider carburisation but rather makes a series of assumptions and relies on conservatism to account for it, as described by Chevalier [1]. For a start, as carburisation is likely to occur within the first few years of operation and given a healing layer is likely to form preventing further carburisation. Following this assumption, the depth of the carburised layer may be treated as metal loss. Alternately, the presence of carburisation may be ignored on the provision that a full creep fatigue crack initiation assessment is carried out. The simplifying assumptions of the R5 assessment procedure can in some cases be conservative and in other cases non-conservative. This is dependent on the extent of carburisation, the magnitude of the loading and the nature of the loading (primary or secondary). It is understood that the conservatism or non-conservatism is directly related to the presence of surface cracking in the carburised layer. The brittle nature of the hard carburised layer makes it particularly susceptible to cracking at higher levels of loading. Should cracking initiate, then a perceived increased creep rate would be expected, leading to a reduced time to failure as cracking effectively leads to metal loss. However, at lower levels of loading the carburised layer may not crack. In this case the higher yield stress of the carburised material may be of benefit and an increased creep rate would be observed, ultimately increasing the material life. This work aims to investigate the effects of a creep properties mismatch, as a result of carburisation, on a section of thin walled stainless steel pipe found in an AGR. The simulated pipe section, represented as a Bree cylinder, is subjected to cyclic thermal gradient and a constant mechanical load. The model is subject to a creep dwell when the temperature across the pipe section is constant and at its maximum temperature. The numerical study is performed for several models with increasing thickness of the carburised material. The effects of various magnitudes of mechanical loading are also investigated. This paper details the simulation and modelling approaches before providing and discussing results of the study.

2 Cyclic Response of Structures at Elevated and High-Temperature

Over the last 50 years one of the most intuitive and reliable method of classifying the cyclic behaviour of a structure has been the famous Bree diagram [7]. Within his research work Bree identified the relationship between the cyclic behaviour and the level of combined mechanical and thermal load. In accordance with his diagram the following mechanisms can be exhibited: elastic shakedown, plastic shakedown or ratcheting. To represent the interaction between the cyclic and constant load, he proposed an interaction diagram as shown in Fig. 3. Within the diagram (Fig. 3) the thermal stress and the constant mechanical load are normalised for the yield stress and limit load respectively and are reported on the vertical and horizontal axes. If the combined loads applied are small enough, the entire component will remain elastic during the operating life. However, if the load is increased the component can exhibit elastic shakedown. If the cyclic thermal load is increased, the component can fall in plastic shakedown domain. In this region the cyclic response is characterized by the typical closed hysteresis loop, which is responsible for subsequent low cycle

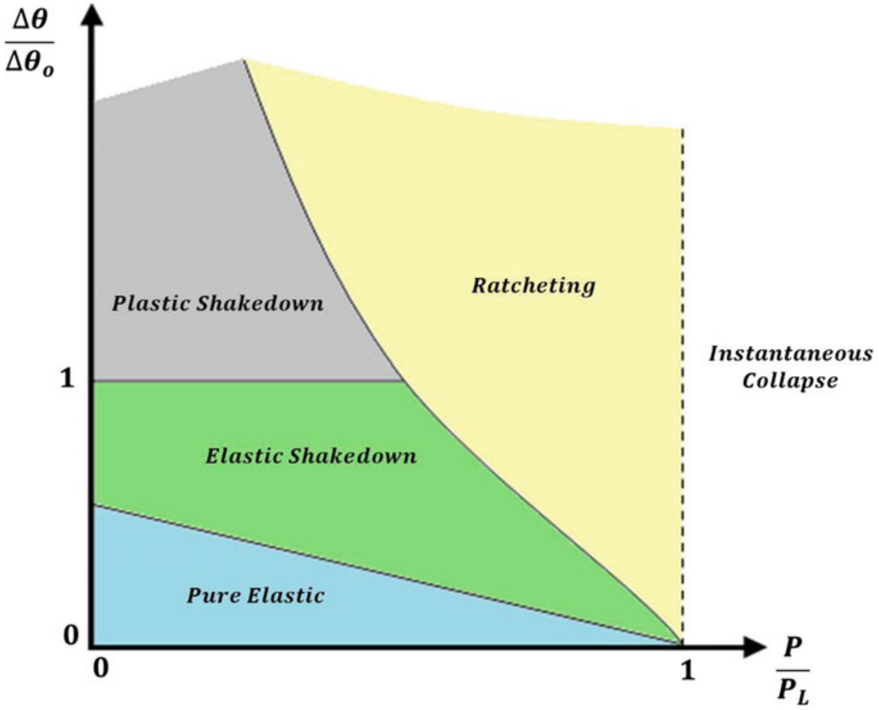

Fig. 3 Classical Bree type diagram for a cylinder subjected to cyclic thermal load and constant mechanical load

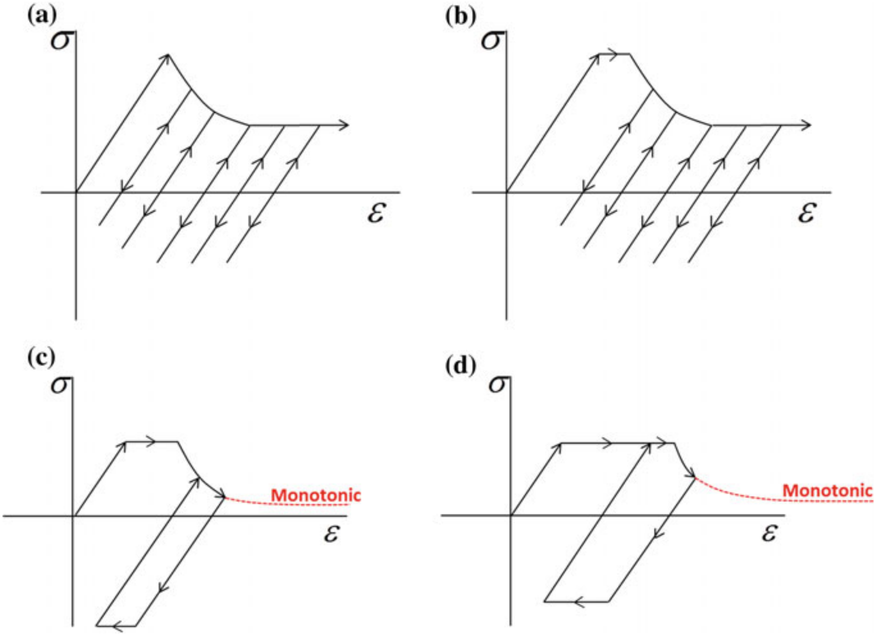

Fig. 4 Different material responses due to cyclic loading with creep dwell period at the tensile peak **a** elastic response, **b** elastic shakedown, **c** creep enhanced reversed plasticity and **d** creep enhanced plastic shakedown

fatigue cracking. If mechanical load is increased, leaving the thermal load level constant, ratcheting occurs. This behaviour is particularly detrimental, since it causes a continuous accumulation of plastic strain at each cycle that can lead to premature collapse of the structure. Finally, if the mechanical load is increased further, the limit load can be reached causing the instantaneous plastic collapse of the structure.

However, due to the interaction between creep and fatigue, the application of the Bree diagram becomes less accurate when high temperature creep occurs during the cycle. The presence of creep dwell can change drastically the cyclic behaviour of a structure, and a schematic representation is given in Fig. 4.

In this representation, for simplicity, a single creep dwell is considered which acts at the end of the tensile peak. If the load at this point is within the elastic limit, no plastic strain is accumulated during the first cycle (Fig. 4a). Due to the creep dwell, a progressive stress relaxation occurs, and unloading also remains purely elastic. A similar behaviour can occur in the presence of a small initial plastic strain (Fig. 4b), but also in this case the progressive stress relaxation leads to elastic behaviour.

In some case the stress relaxation can promote a plastic response during the unloading phase (Fig. 4c), known creep enhanced plasticity. This mechanism is particularly dangerous because it introduces low cycle fatigue in conjunction with creep. In addition, if the applied load is over the shakedown limit, the hysteresis loop response shows plasticity during both the loading and unloading phases, causing more severe fatigue damage which interacts with the creep damage (Fig. 4d). In both Fig. 4c and Fig. 4d, the accumulated creep damage is larger than that obtained by a monotonic load, due to the higher stress level which cyclically occurs during the creep dwell. For this reason, this response is known as "Cyclically Enhanced Creep". In some particular conditions, an open hysteresis loop response is possible and it is known as "Creep ratcheting".

As mentioned before creep dwell is capable of altering the cyclic response of a structure introducing a closed loop response (Fig. 4c, d) for cyclic loading conditions within the shakedown limit. The closure of the hysteresis loop is due to the balance of all the inelastic strains within the entire cycle. However, the non-closed hysteresis loop would still be possible, when an inelastic strain accumulation occurs due to the dominant creep or reversed plastic strains [8]. For example, a large dwell time could produce a creep strain greater than the limited plastic strain, leading to an inelastic strain accumulation dominated by creep. In other loading conditions a large stress relaxation, which results in a low level of overall creep stress, leads to insignificant creep strain but large plastic strain during the unloading phase. This could produce an open hysteresis loop dominated by the reversed plastic strain. Hence creep ratcheting is instead a much more complex mechanism, and it is dependent on the dwell time, the type of load applied and load levels [9].

3 Numerical Model

The geometry of this study was based upon the well-established Bree cylinder, which was originally used to study cyclic behaviour of nuclear fuel casing behaviour [7]. The model geometry is shown in Fig. 5, due to the type of problem an axisymmetric model has been used. The cylinder has been also divided into two domains, one modelled with the bulk material (316H), and the other one on the external side as the carburised material. The presence of two different materials had impact also on the mesh strategies, which is depicted in Fig. 5 for different cases. The mesh is composed of quadratic quadrilateral elements CAX8R, with a reduced integration scheme. The pipe features a wall thickness of 2.4 mm and an internal diameter of 13.8 mm. After initial analysis, carburisation is introduced to the outer side of the pipe at a thickness of 0.1 mm and then 0.4 mm. The initial mesh featured 16 elements across the thickness of the pipe. This is increased to 24 for the 0.1 mm carburised model with a bias ratio of 10 towards the carburisation. The number of elements is then increased for the 0.4 mm carburised model with a total of 36, again with biasing towards the carburisation. For this particular case study due to the symmetry of boundary conditions and both mechanical and thermal load applied the aspect ratio of the element do not represent a crucial factor. However, it is important to ensure a good number of elements at the interface between the two materials. It is worth noting that despite this approach a numerical discontinuity will be always present.

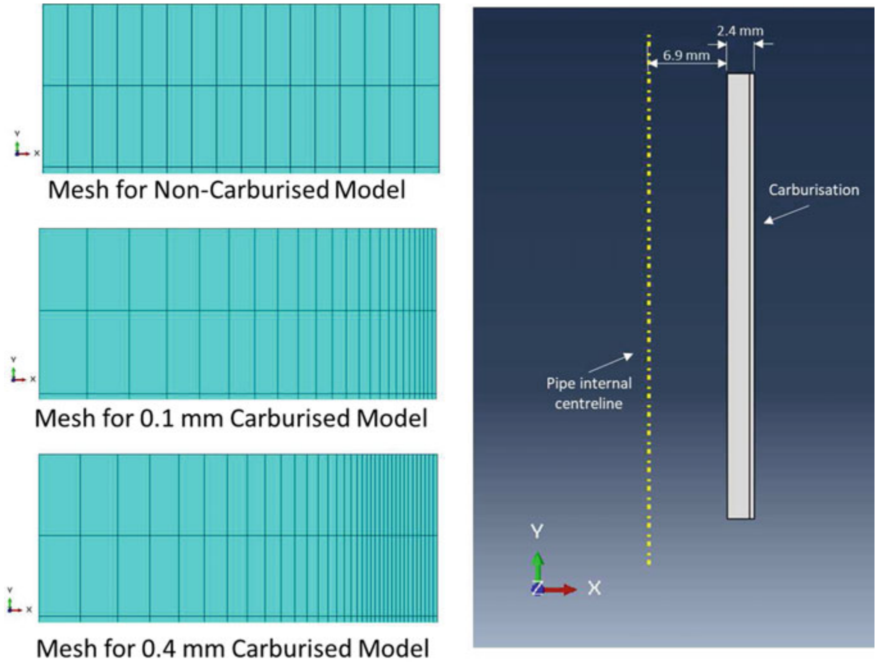

Fig. 5 Classical Bree's like diagram for a cylinder subjected to cyclic thermal load and constant mechanical load

The model is constrained from motion at the bottom. When required a constant axial tensile load is applied to the top of the model. This simulates the axial effect of static mechanical loading due to the internal pressure. For simplicity, radial or hoop stresses are not considered. Temperature is varied cyclically from a reference of 600 °C with higher temperatures occurring externally and propagating inwards through the wall thickness.

The bulk material considered is the 316H and material properties are obtained from the NIMS database [10]. Yield stress, thermal conductivity and coefficient of thermal expansion are taken as functions of temperature. For simplicity, Young's modulus is assumed to be temperature dependent with linear trend between data points available (Table 1 in Appendix), and a constant Poisson's ratio is considered. High-temperature creep is modelled using Norton's law neglecting primary and tertiary phase. The plastic behaviour of the material has been modelled as elastic perfect plastic and no hardening rule is considered.

Poor access to material data for the carburised layer meant a number of assumptions had to be made. Firstly, properties are assumed constant across the thickness of the layer. Then based on the work of Chevalier [1] Young's Modulus is increased by 30% from the bulk material value and yield point is increased by 50.6% over the full temperature range. Conflicting information on the effect of carburisation on strain creep rate lead to firstly assuming the creep rate reduced by a factor of 10 for the carburised layer. Following this the problem is remodelled with creep rate increased by a factor of 10. All the data used within this work are reported in tabulated form in the Appendix.

4 Results

4.1 Bree Like Diagram for Non-carburised Cylinder

Before introducing creep and carburisation effects, a detailed study of cyclic response of the structure has been undertaken. This involved determining the reference limit load P_L, which is found to be approximately 115 MPa at 600 °C. A reference thermal load of 50 °C is selected to be applied on the datum temperature of 600 °C.

During this research work along with traditional finite element analysis a well-established direct method, known as the Linear Matching Method (LMM) has been used. The LMM is capable of calculating shakedown, ratcheting and plastic collapse limits, more efficiently than other numerical procedures such as the Direct Cyclic Analysis (DCA) for a wide range of problems [11]. Within this work it has been used for providing an efficient solution to particular calculation like the shakedown limit calculation and the assessment of the steady state response due to cyclic loading at high-temperature. To calculate a fully shakedown limit a series of step by step analysis has been carried out, trialling values for mechanical and thermal loading ratios. At the same time for verification purpose the Linear Matching Method has been used to calculate the same limit.

The limit is depicted in Fig. 6, which shows a typical behaviour when a cyclic temperature and a constant mechanical load is applied.

By analysing the plastic strain accumulated over time, the type of cyclic responses could be determined and hence points added to the Bree diagram for the selected loading ratios. From these points, a boundary line could be interpolated that divides the plot up into the regions as shown in Fig. 6.

The step by step results are also verified using the linear matching method with results shown as a dashed red line in Fig. 6. The verification of the limit calculated is depicted in Fig. 7, where three cyclic load points just inside the shakedown limits A_1(0.0, 0.9), B_1(0.4, 0.9), C_1(0.65, 0.3), and three outside A_2(0.0, 1.1), B_2(0.4, 1.1), C_2(0.65, 0.5) as shown in Fig. 6. By comparing plastic strain histories, as shown in (Fig. 7), firstly, it is observed that elastic shakedown behaviour occurs for load point A_1, B_1 and C_1. These points are predicted to lie inside the limit. Instead when they are taken outside reversed plasticity is predicted for A_2 and B_2. For the cyclic point C_2 a well defined ratcheting mechanism is visible (Fig. 7). The results obtained demonstrates that the limit calculated with a temperature dependent yield stress is accurate. On the basis of this shakedown limit specific cyclic load points are going to be analysed with the presence of a carburised layer.

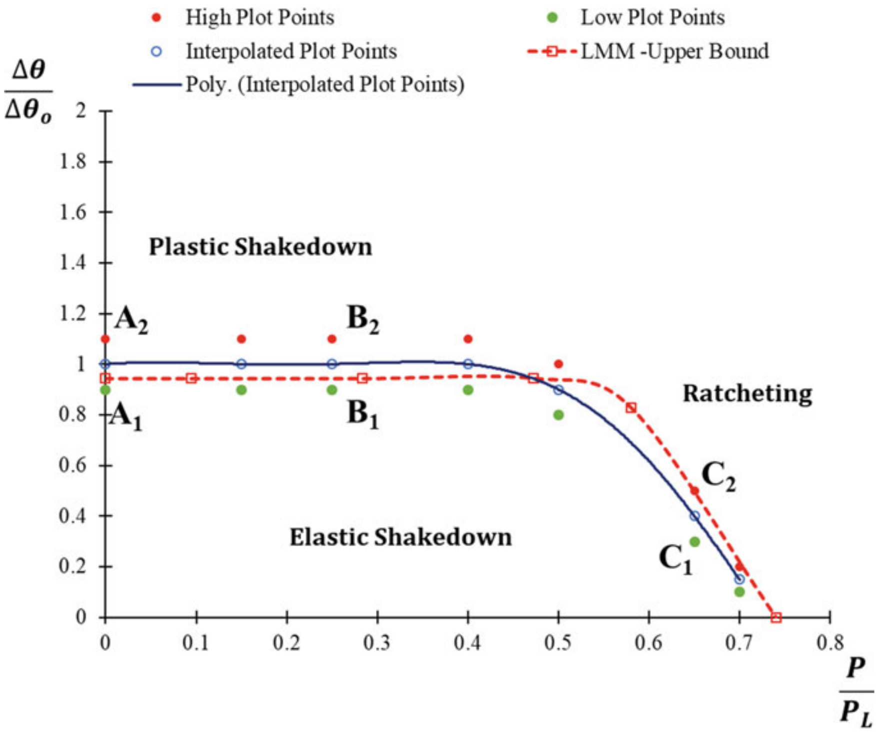

Fig. 6 Bree's like diagram for the non-carburised cylinder subjected to cyclic thermal load and constant mechanical load

4.2 *Creep-Fatigue Analyses of the Non-carburiesed Cylinder*

In order to study the effect of the carburisation on the cyclic behaviour at high temperature of the cylinder a reference case is constructed considering only the bulk material. The cyclic history has been modified considering the presence of a creep dwell at constant temperature and constant primary load. The creep dwell length considered has been 500 h, and the maximum temperature considered is 650 °C, which is consistent with the operating temperature in the AGR reactor. Three different mechanical loading situations are simulated, firstly with no mechanical load, and then the other two with an incremental increased mechanical loading. This is important to study the effect on the cyclic response and the possible presence of creep-ratcheting.

The type of response, at the inner side of the cylinder, obtained from the three load case with increasing mechanical load are shown in Fig. 8. Figure 8a shows the response without any mechanical load applied. The absence of any primary load makes it impossible to obtain creep-ratcheting [9]. In addition, in all the responses reported the creep dwell is always compressive and for this reason no creep damage

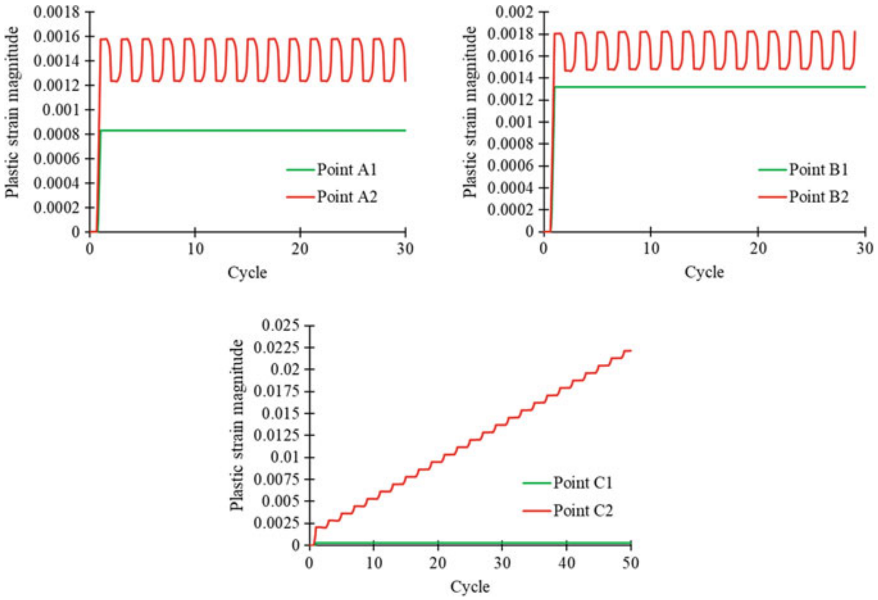

Fig. 7 Verification through step-by-step analysis of the shakedown limit for the cylinder structure by comparing plastic strain histories

is expected to occur. During the first step the strain-stress response is caused by the thermal gradient across the thickness. Then the thermal gradient is removed and the entire section is at the highest temperature, consequently stress relaxes and redistributes due to the change of flow stress caused by the associated change in temperature field. At this point the creep dwell starts and once concluded it is followed by unloading to return to datum temperature (600 °C), forming a closed loop.

When the mechanical load is introduced, creep-ratcheting occurs as shown in Fig. 8b, c. This mechanism is caused by the type of the load applied that promotes creep-ratcheting in the direction of the applied load. Despite this the ratchet strain per cycle accumulated is relatively small, but not insignificant, as it is depicted in Fig. 8b. In addition, the direction of the ratchet strain is negative. This type of mechanism is dramatically affected by the length of the creep dwell and by the magnitude of the mechanical load. Figure 9 shows the cyclic responses across the thickness, from left to right, without the carburised layer on the right side. In all plots a well-defined ratcheting is defined. The creep dwell at the mid-wall and at outer-wall positions occurs with tensile stresses. In particular, at the mid-wall elastic shakedown is associated with an increase in inelastic strain due to the accumulation of creep deformation. However, in this case as it is shown in Fig. 9 the accumulated strain per cycle is not significant.

The von-Mises stress across the pipe wall is shown in Fig. 10a, b. It is clear how the stress increases with the thermal gradient before redistributing as the material

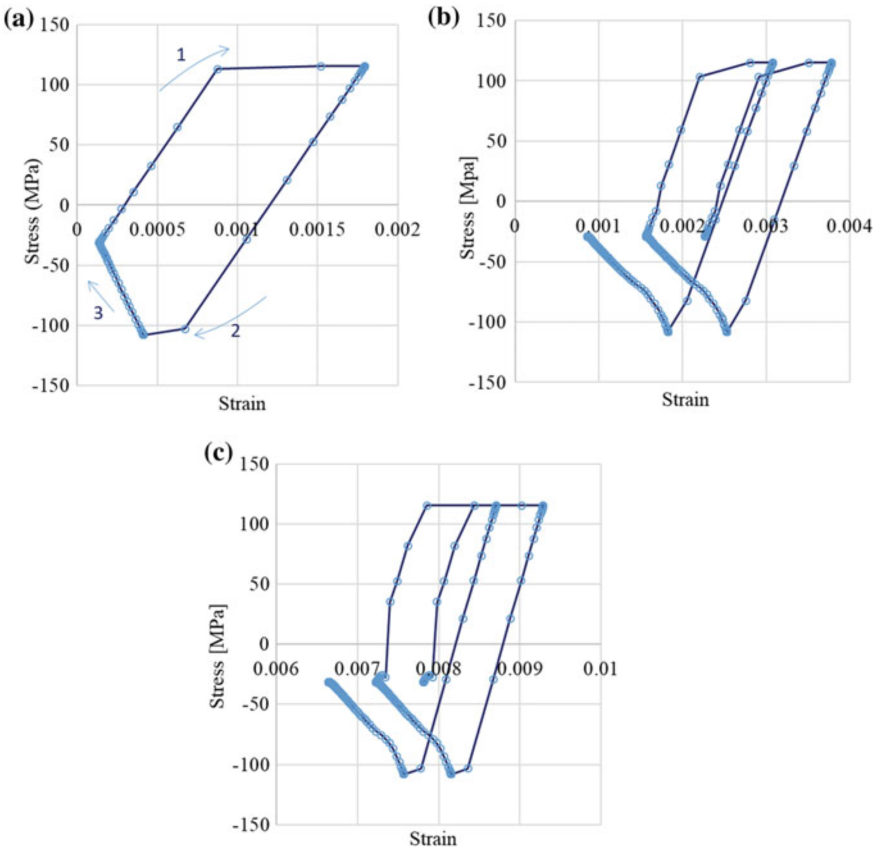

Fig. 8 Cyclic response of the non-carburised cylinder subjected to cyclic thermal load and constant mechanical load. **a** Zero mechanical load, **b** 0.15 times the limit load, **c** 0.3 times the limit load

relaxes, before again decreasing during the creep dwell. When the mechanical load is applied (Fig. 10b) it can be seen how it interacts with the thermal gradient causing an asymmetric stress field. Furthermore, also the minimum stress at the core of the wall is increased.

4.3 Creep-Fatigue Analyses of a Cylinder with Carburised Layer

In order to investigate the effect of the carburised layer, firstly a 0.1 mm layer is considered, and for simplicity, the interface area between the parent material and the carburised one is considered straight and homogeneous. Due to the discrepancies in

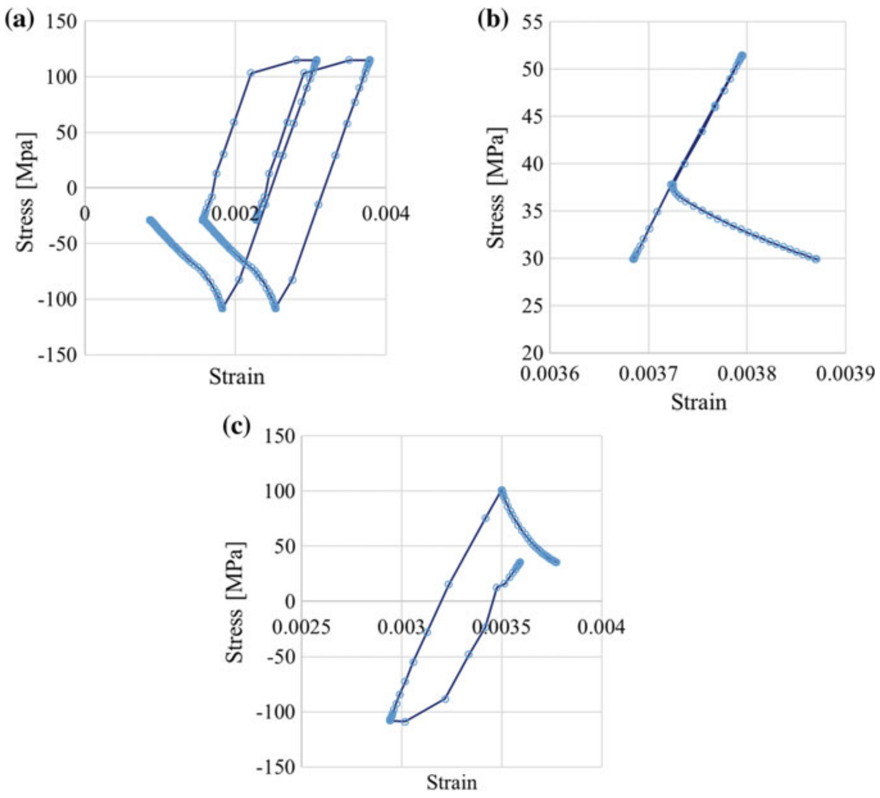

Fig. 9 Cyclic stabilised responses across the thickness, at the inner side (**a**), at the centre (**b**) and on the outer side (**c**) without a carburised layer

the literature on the creep properties, two cases have been considered. It has been decided to simulate the creep behaviour for the carburised layer with an increased and then a decreased creep multiplier, leaving the exponent constant.

In Fig. 11 the cyclic response predicted is shown for both cases on the inner side of the pipe away from the carburisation. The results correspond to the final loading cycle of simulation with firstly an increased creep rate (Fig. 11a, b, c) and then secondly with a decreased rate (Fig. 11d, e, f). For the case with a decreased creep rate the cyclic response does not change remarkably, and only a slight creep ratcheting can be observed. In fact, all the effects of creep are less significant than when there is no carburisation. This would suggest a carburised layer is beneficial in terms of preventing creep ratcheting. In addition, at this stage, the total strain range remains almost constant.

However, a significant change in the response is obtained if the carburised layer is assumed to have an increased creep strain rate. For the case, without mechanical load, the total strain range is significantly larger, as expected due to the contribution

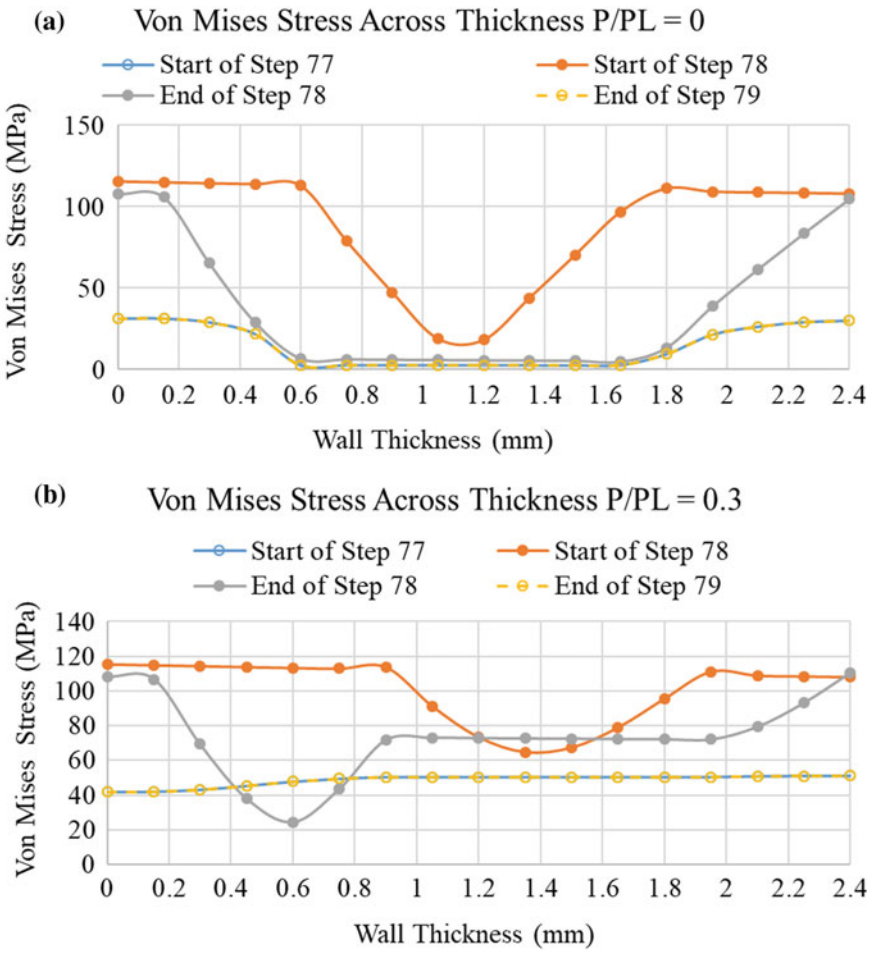

Fig. 10 von Mises stress along the cylinder thickness for **a** no mechanical load and **b** with a mechanical load 0.3 times the limit load

of the creep strain accumulated over the dwell time. Indeed, the larger stress relaxation occurring during the creep dwell enhance the subsequent phase, generating more plastic strain. The results obtained with the mechanical load shows a different mechanism, as it is shown in Fig. 11e, f. The results then become a little unusual when the mechanical loading is applied. The mechanism affects the stress relaxation during the creep dwell. An unusual creep relaxation occurs, it as the direction of the creep changes from compressive to tension. This mechanism is known as structural creep strain recovery [12]. When this occurs, it has been demonstrated that a large stress relaxation can be identified during the start of the creep dwell. This process is caused by the rapid relaxation of thermally induced stress. In this work, the rule of sign or Dominant Principal direction is used to determine the sign to be assigned

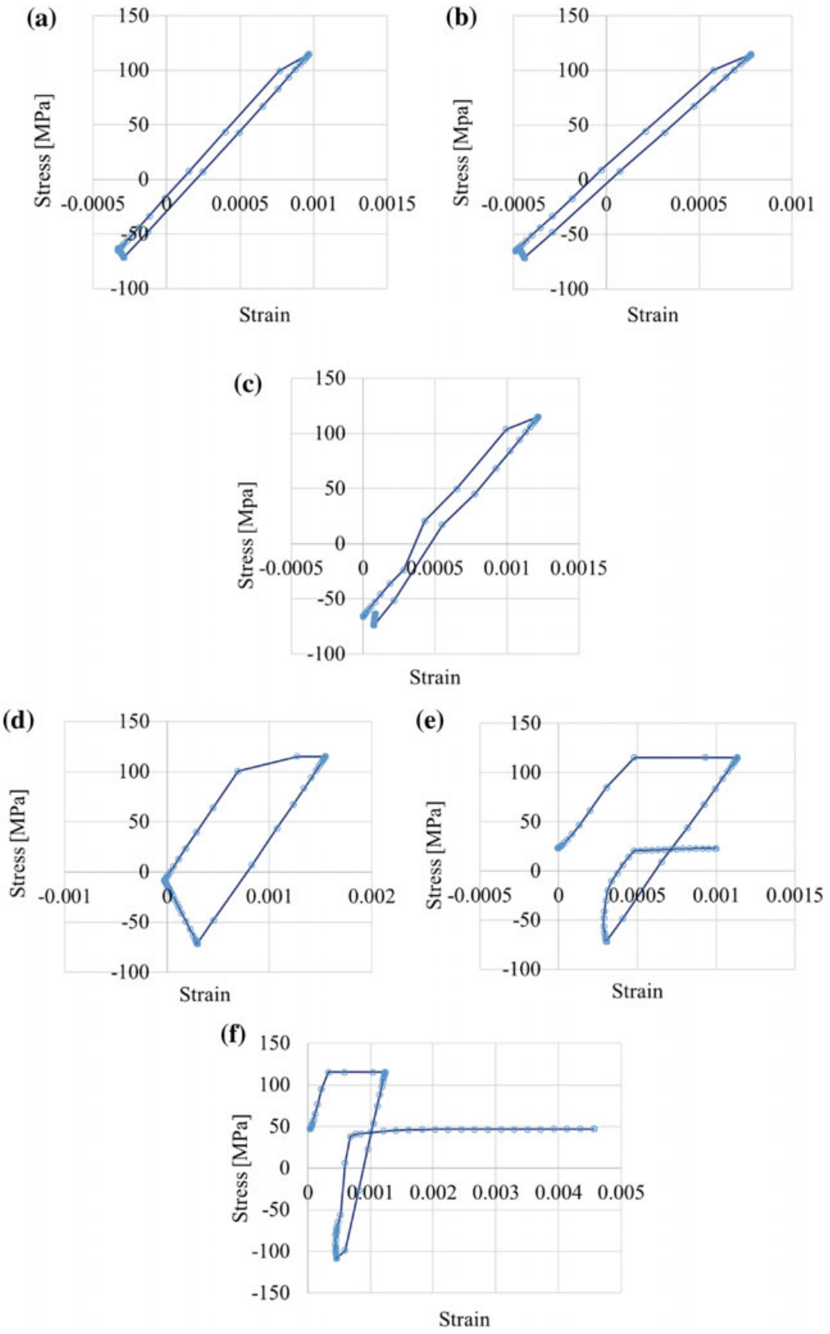

Fig. 11 Steady state cyclic response at the inner surface of the cylinder for decreased creep strain rate and increasing mechanical load (**a** No mechanical load, **b** 0.15 P_L, **c** 0.3 P_L) and for decreased creep strain rate and increasing mechanical load (**d** No mechanical load, **e** 0.15 P_L, **f** 0.3 P_L)

to the equivalent stress [13]. To do this the three principal components are evaluated, estimating which gives the largest stress range. Within this work, the maximum principal stress has been found to be the largest one.

As it is shown in Fig. 11e, f, the transition is very rapid and only few data points are currently available to show the transition, but the overall behaviour of principal stress and von-Mises stress are in line with the observation of Cho et al. [12]. As the mechanical load increases the total strain range also increases, as does the rate of ratcheting. Clearly, in this case, the carburised layer would be detrimental. It is worth noting that the stress reached during the stress relaxation is close to the level of stress caused by the mechanical load. This is caused by the progressive relaxation of secondary loads caused by the thermal gradient

The mechanism at the origin of this behaviour is the creep properties mismatch that allows a significant stress redistribution and a different creep deformation between the bulk and carburised material. All the behaviours identified have the potential to decrease significantly the fatigue life of the pipe.

Figure 12a, b depict the effect of the carburised layer on the stress distribution across the thickness of the pipe wall, without mechanical load. In both the cases when the carburised creep rate is increased and decreased relative to the bulk material it can be seen clearly that the harder carburised material is associated with higher stress. This allows the presence for low stress, well within the elastic limit, in the central cylinder core. In both cases, the Linear Matching Method has been used for further verification of the stress field determined using the non-linear analyses. The agreement between the two methods is very good especially the creep area.

It can be concluded that the stresses occurring at the start and end of the cycle, at the edges of the pipe wall, are higher for the case where the creep rate is decreased and lower for when it is increased. This is likely because in this scenario the stresses are completely displacement driven due to it only being thermally loaded and so the final stress will be dependent on the creep multiplier factor of the Norton's law.

Lastly, the effect of the thickness of the carburised layer has been investigated by considering a layer of 0.4 mm. Since the most critical response occurs for an increased creep strain rate, this case has been investigated due to its importance. In Fig. 13a, b, c the cyclic response of the stabilised cycle at the inner side is shown for a mechanical load of 0.15 times the limit load respectively and for a carburised layer of 0, 0.1 and 0.4 mm thick respectively. The introduction of the carburised layer drastically changes the response and introduces the creep strain recovery. The increase in carburised layer thickness does not further change the cyclic response as it can be seen in Fig. 13b, c.

For the external pipe surface (Fig. 13d, e, f) it is clear that once carburisation is introduced, the amount of ratcheting considerably increases. Due to a large amount of creep strain accumulated the overall cycle width increases remarkably. In addition, the stress at the start of the creep dwell is always positive, causing damage that could lead to failure (cracking) of the carburised layer. At the same time, the creep-ratcheting is very large and increases with the thickness of the carburised layer. In addition, it can be seen that the total strain range is less than for the inner side elements and this is due to the greater hardness of the carburised material.

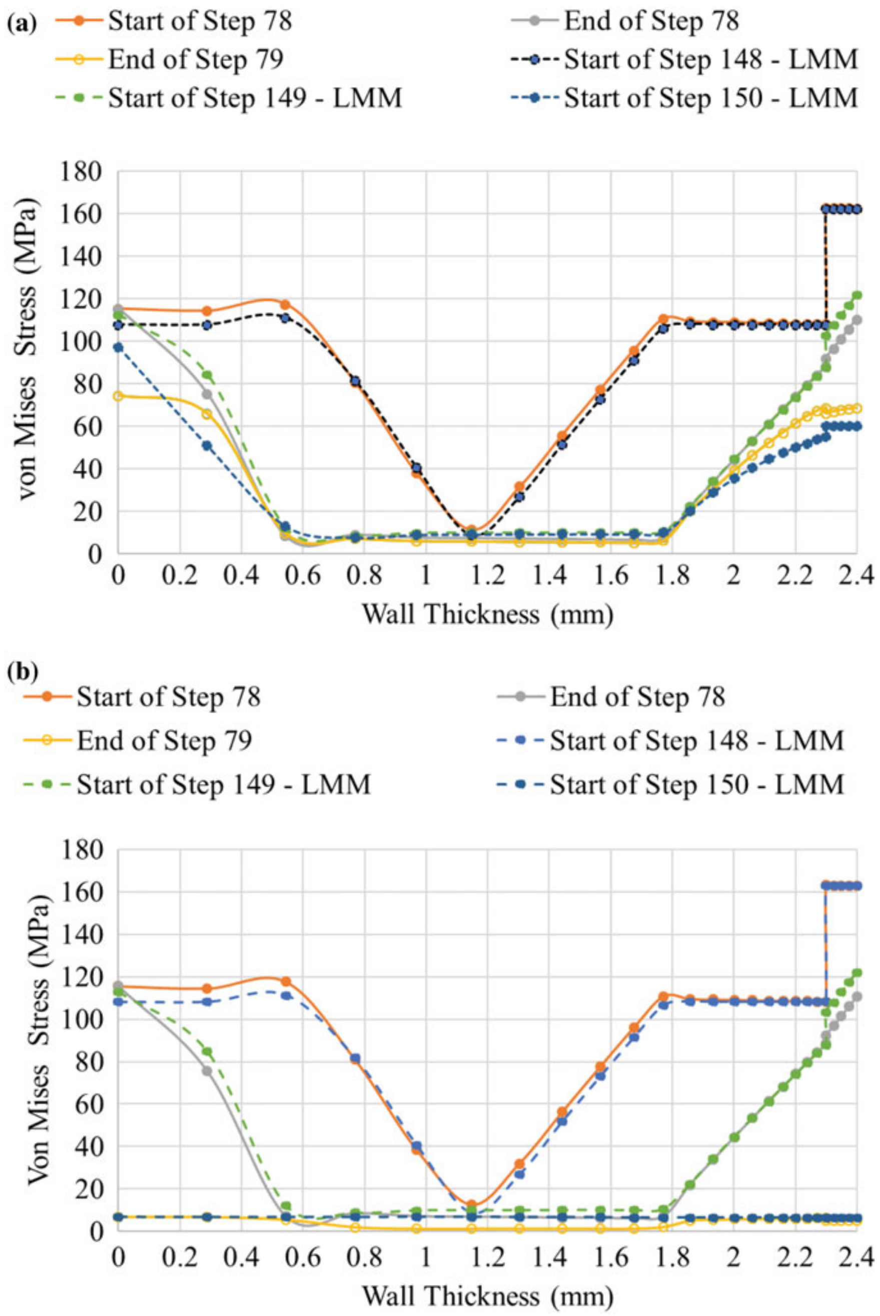

Fig. 12 von Mises stress along the cylinder thickness without mechanical load **a** for decreasing and **b** increasing creep strain rate

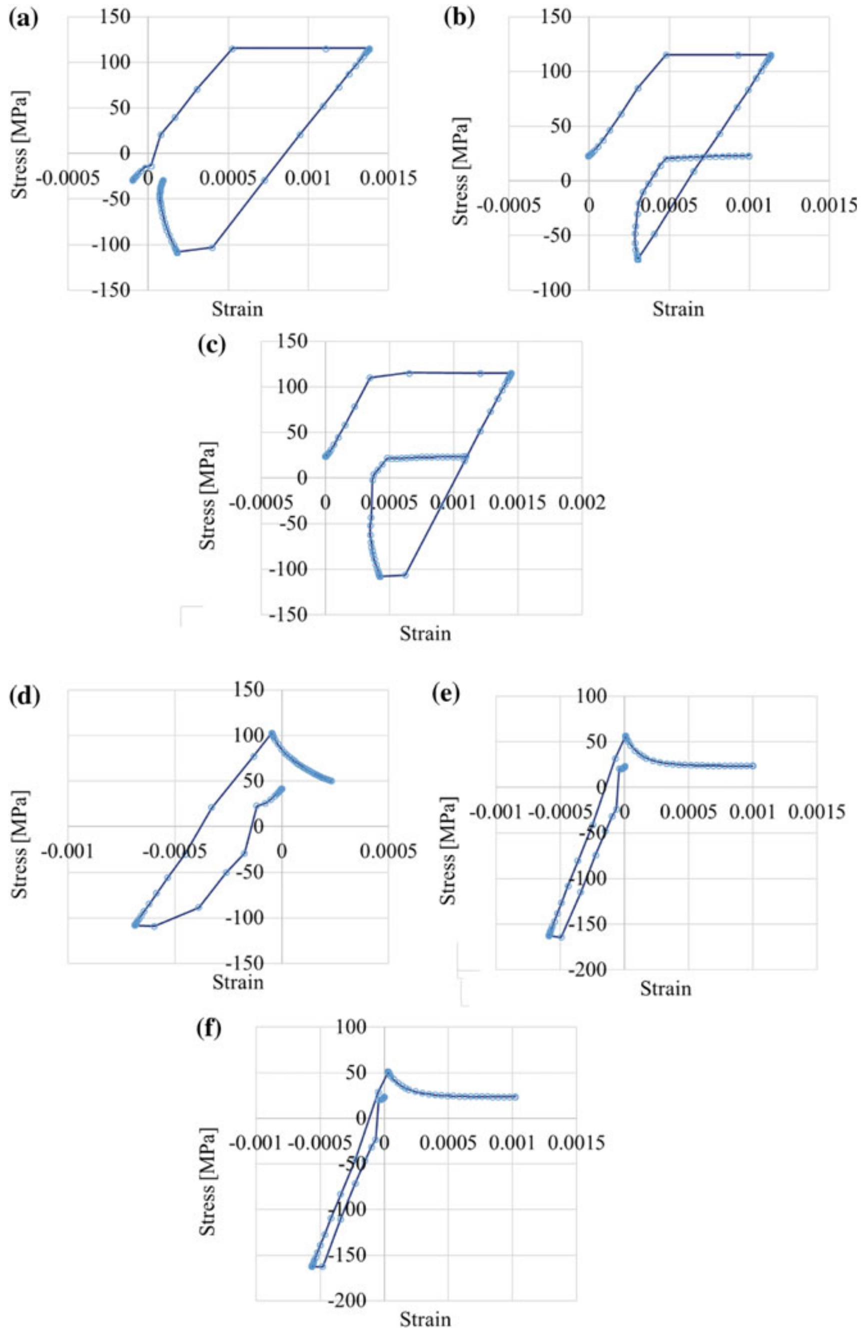

Fig. 13 Steady state cyclic response at the inner surface (top) and outer surface (bottom) of the cylinder for an increasing thickness of carburised layer, 0, 0.1 and 0.4 mm. All the responses area obtained for a mechanical load of 0.15 P_L

5 Conclusion

In this work, a numerical study on the cyclic response at high-temperature of a structure containing a progressively thicker carburised layer has been carried out. The model has been analysed accounting for temperature dependent material properties and considering different possible creep behaviours of the carburised material. The main results obtained within this research work are as follow:

1. A comprehensive study on the effect of creep properties mismatch has been achieved, demonstrating how the presence of a carburised material can alter largely the cyclic behaviour of the associated bulk material. It is therefore important to pay particular attention when considering if the presence of carburisation can be simply neglected.
2. The most detrimental mechanisms have been observed when considering a creep softer carburised layer. In this case the cyclic response is highly sensitive to the applied internal pressure (primary load). A progressive increase of inelastic strain is predicted to occur due to creep-ratcheting.
3. When considering the effect of increased carburised layer thickness on both the bulk and carburised material, a significant increase in creep-ratcheting strain per cycle is observed. In addition, should the carburised layer be subject to a particularly harmful tensile dwell, with the potential to produce additional cracking, this would greatly enhance the penetration of coolant gas via the newly formed cracks.
4. Most of the observed mechanisms are due to the complex stress redistribution caused by the presence of several material properties mismatch, including yield stress and creep properties. It is worth noting, that in this study the coefficient of thermal expansion of the two materials has been kept constant. However, studies are undergoing to evaluate this assumption. A mismatch also in this property would increase the interface stress between the two materials.

Acknowledgements The authors acknowledge the EPSRC Summer Vacation Scholarship Scheme and the University of Glasgow for their financial support and the GCEC for providing the computational facilities.

Appendix

See Tables 1, 2, 3, 4 and 5.

Table 1 Temperature dependent yield stress

Temperature (°C)	Bulk material yield stress (MPa)	Carburised material yield stress (MPa)
20	251.12	378.1845
40	244.48	368.1913
60	238.02	358.4622
80	231.73	348.9901
100	225.61	339.7683
120	219.65	330.7902
140	213.84	322.0493
160	208.19	313.5395
180	202.69	305.2544
200	197.34	297.1883
220	192.12	289.3354
240	187.05	281.6899
260	182.10	274.2465
280	177.29	266.9998
300	172.61	259.9445
320	168.04	253.0757
340	163.60	246.3884
360	159.28	239.8778
380	155.07	233.5392
400	150.97	227.3681
420	146.99	221.3601
440	143.10	215.5108
460	139.32	209.8161
480	135.64	204.2719
500	132.05	198.8742
520	128.57	193.6191
540	125.17	188.5029
560	121.86	183.5218
580	118.64	178.6724
600	115.51	173.9512
620	112.45	169.3546
640	109.48	164.8796
660	106.59	160.5228
680	103.77	156.2811
700	101.03	152.1515
720	98.36	148.131
740	95.76	144.2168
760	93.23	140.406
780	90.77	136.6958
800	88.37	133.0838

Table 2 Temperature dependent young's modulus

Temperature (°C)	Bulk material yield stress (MPa)	Carburised material yield stress (MPa)
20	251.12	378.1845
40	244.48	368.1913
60	238.02	358.4622
80	231.73	348.9901
100	225.61	339.7683
120	219.65	330.7902
140	213.84	322.0493
160	208.19	313.5395
180	202.69	305.2544
200	197.34	297.1883
220	192.12	289.3354
240	187.05	281.6899
260	182.10	274.2465
280	177.29	266.9998
300	172.61	259.9445
320	168.04	253.0757
340	163.60	246.3884
360	159.28	239.8778
380	155.07	233.5392
400	150.97	227.3681
420	146.99	221.3601
440	143.10	215.5108
460	139.32	209.8161
480	135.64	204.2719
500	132.05	198.8742
520	128.57	193.6191
540	125.17	188.5029
560	121.86	183.5218
580	118.64	178.6724
600	115.51	173.9512
620	112.45	169.3546
640	109.48	164.8796
660	106.59	160.5228
680	103.77	156.2811
700	101.03	152.1515
720	98.36	148.131
740	95.76	144.2168
760	93.23	140.406
780	90.77	136.6958
800	88.37	133.0838

Table 3 Temperature dependent coefficient of thermal expansion

Temperature (°C)	Coefficient of thermal expansion (1/°C)
20	15.42
40	15.72
60	16.02
80	16.32
100	16.62
120	16.92
140	17.21
160	17.51
180	17.81
200	18.11
220	18.42
240	18.72
260	19.02
280	19.32
300	19.62
320	19.92
340	20.22
360	20.53
380	20.83
400	21.13
420	21.43
440	21.74
460	22.04
480	22.34
500	22.65
520	22.95
540	23.25
560	23.56
580	23.86
600	24.17
620	24.47
640	24.78
660	25.08
680	25.39
700	25.70
720	26.00
740	26.31
760	26.61
780	26.92
800	27.23

Table 4 Temperature dependent thermal conductivity

Temperature (°C)	Thermal conductivity [W/(mm*C°)]
20	1.335E-02
40	1.368E-02
60	1.402E-02
80	1.435E-02
100	1.468E-02
120	1.501E-02
140	1.533E-02
160	1.566E-02
180	1.598E-02
200	1.630E-02
220	1.662E-02
240	1.694E-02
260	1.726E-02
280	1.757E-02
300	1.788E-02
320	1.820E-02
340	1.851E-02
360	1.881E-02
380	1.912E-02
400	1.942E-02
420	1.973E-02
440	2.003E-02
460	2.033E-02
480	2.063E-02
500	2.092E-02
520	2.122E-02
540	2.151E-02
560	2.180E-02
580	2.209E-02
600	2.238E-02
620	2.267E-02
640	2.295E-02
660	2.324E-02
680	2.352E-02
700	2.380E-02
720	2.408E-02
740	2.435E-02
760	2.463E-02
780	2.490E-02
800	2.517E-02

Table 5 Norton law creep parameters for different temperatures and stress levels

550 °C	A [MPa$^{-1}h^{-1}$]	n
LS	–	–
HS (123 MPa)	6.64E-23	7.7039
600 °C	A [MPa$^{-1}h^{-1}$]	n
LS	2.67E-11	2.3
HS (98 MPa)	4.22E-22	7.5
650 °C	A [MPa$^{-1}h^{-1}$]	n
LS	1.05E-10	2.3
HS (76 MPa)	1.62E-20	7.5
700 °C	A [MPa$^{-1}h^{-1}$]	n
LS	7.75E-10	2.3
HS (50 MPa)	2.58E-19	7.5
750 °C	A [MPa$^{-1}h^{-1}$]	n
LS	4.19E-09	2.3
HS (38 MPa)	7.17E-18	7.5

References

1. Chevalier, M.: ASME 2018 Symposium on Elevated Temperature Application of Materials for Fossil, Nuclear, and Petrochemical Industries (American Society of Mechanical Engineers), pp. V001T03A003–V001T03A003 (2018)
2. Nasser, M., Davies, C.M., Nikbin, K.: ASME 2016 Pressure Vessels and Piping Conference (American Society of Mechanical Engineers, 2016), pp. V005T09A009–V005T09A009 (2016)
3. Dean, D., Chevalier, M.: The FESI Bulletin. pp. 9–17 (2017)
4. Ainsworth, R.: The FESI Bulletin. pp. 18–25 (2017)
5. Ainsworth, R.: Int. Mater. Rev. **51**(2), 107 (2006)
6. Energy, E.: Assessment Procedure for the High Temperature Response of Structures, R5 Issue 3 (2014)
7. Bree, J.: J. Strain Anal. Eng. Design **2**(3), 226 (1967)
8. Chen, H., Chen, W., Ure, J.: J. Press. Vessel. Technol. **136**(6), 061404 (2014). https://doi.org/10.1115/1.4028164
9. Barbera, D., Chen, H., Liu, Y.: J. Press. Vessel. Technol. (2015). https://doi.org/10.1115/1.4032278
10. N.R.I. for Metals, Data Sheets on the elevated temperature properties of 18Cr-12Ni-Mo stainless steel tubes for boiler and heat exanchger (SUS 316H TB) (National Reseach Institute for Metals, 2000)
11. Chen, H., Ponter, A.R.: Int. J. Press. Vessel. Piping **78**(6), 443 (2001)
12. Cho, N.K., Chen, H., Boyle, J.T., Xuan, F.Z.: Int. J. Fatigue **113**, 149 (2018)
13. Manson, S., Halford, G.R.: Fatigue and Durability of Metals at High Temperatures (ASM International, 2009)

Cohesive Zone Models—Theory, Numerics and Usage in High-Temperature Applications to Describe Cracking and Delamination

Joachim Nordmann, Konstantin Naumenko and Holm Altenbach

Abstract This treatise deals with Cohesive Zone Models which were developed around 1960 through Barenblatt and Dugdale. At first, we present an overview about these models and the numerical treatment of these models in the sense of the Finite Element Method. Further on, a rate-dependent Cohesive Zone Model is presented and tested through a simulation of a Four-Point-Bend-Test with a metal compound. The required material parameters are determined through numerical optimisation by using a neural network which is explained, as well.

1 Introduction

In the past decades it was ascertained that metal alloys are not capable to sustain complex loading collectives for a long time, like it is the case in combustion engines or steam and gas turbines. In these units the parts are subjected to very complex and high loadings, especially in the combustion chamber where thermal and mechanical loads interact cyclic (TMF) and next to that corrosion, oxidation and wear occur which reduce the strength of the material, constantly and finally the durability is reduced. As a result of this used metal alloys are improved, permanent. But at the same time the loadings increased, hence, the limits of the materials were reached again and the durability did not increase much.

For further improvement the used alloys are coated to protect them against some influences, for example a coating to increase the wear resistance or a coating to reduce

---

J. Nordmann (✉) · K. Naumenko · H. Altenbach
Chair of Engineering Mechanics, Faculty of Mechanical Engineering,
Institute of Mechanics, Otto von Guericke University Magdeburg,
39106 Magdeburg, Germany
e-mail: joachim.nordmann@ovgu.de

K. Naumenko
e-mail: konstantin.naumenko@ovgu.de

H. Altenbach
e-mail: holm.altenbach@ovgu.de

K. Naumenko and M. Krüger (eds.), *Advances in Mechanics of High-Temperature Materials*, Advanced Structured Materials 117,
https://doi.org/10.1007/978-3-030-23869-8_7

the temperature influence on the alloy (thermal-barrier-coating). However, the design process and the simulation of these components is more difficult and additionally it is necessary to simulate the failure, now.

In this treatise we use the Cohesive Zone Model (CZM) to analyse and simulate the failure behaviour of an aluminium specimen coated with iron aluminide which is tested in a Four-Point-Bend-Test (4PBT) at 400 °C. At first, we present the theory of CZMs and the Traction-Separation-Law (TSL) which describes the failure behaviour. After this it follows the description how a novel rate-dependent TSL is derived with the capability to simulate heat conduction through the interface. Subsequently, it follows a section which explains how a CZM is treated in the Finite Element Method (FEM). After all these explanations the simulation of the aforementioned compound is presented. Required material parameters are determined through numerical optimisation by using a neural network and the software tool ABAQUS2MATLAB [1]. The simulation is performed until the coating fails and starts to delaminate. To be able to simulate the cracking and the delamination the model is equipped with cohesive zones. The failure of the coating is modelled with a standard TSL and the delamination is modelled with the novel rate-dependent TSL.

We conclude with a summary and an outlook for future work.

2 Preliminaries and Notation

Throughout the whole text, the direct tensor notation is preferred. Scalars are symbolised by italic letters (e.g. a), vectors by italic lowercase bold letters (e.g. $\boldsymbol{a} = a_i\, \boldsymbol{e}_i$), second order tensors by italic uppercase bold letters (e.g. $\boldsymbol{A} = A_{lm}\, \boldsymbol{e}_l \otimes \boldsymbol{e}_m$), and fourth order tensors by italic uppercase bold calligraphic letters (e.g. $\boldsymbol{\mathcal{A}} = A_{pqrs}\, \boldsymbol{e}_p \otimes \boldsymbol{e}_q \otimes \boldsymbol{e}_r \otimes \boldsymbol{e}_s$), where Einstein's summation convention is applied. Considering a Cartesian coordinate system and orthonormal bases, e.g. $\boldsymbol{e}_i$ with $i \in \{1, 2, 3\}$, basic operations for tensors used in this paper are the scalar product of two vectors

$$\boldsymbol{a} \cdot \boldsymbol{b} = a_i\, b_j\, \boldsymbol{e}_i \cdot \boldsymbol{e}_j = a_i\, b_i = \alpha \qquad\qquad \alpha \in \mathbb{R}\,,$$

the dyadic product

$$\boldsymbol{a} \otimes \boldsymbol{b} = a_i\, b_j\, \boldsymbol{e}_i \otimes \boldsymbol{e}_j = \boldsymbol{C}\,,$$

the composition of a second and a first order tensor

$$\boldsymbol{A} \cdot \boldsymbol{a} = A_{lm}\, a_i\, \boldsymbol{e}_l \otimes \boldsymbol{e}_m \cdot \boldsymbol{e}_i = A_{li}\, a_i\, \boldsymbol{e}_l = \boldsymbol{d}\,,$$

the composition of two second order tensors

$$\boldsymbol{A} \cdot \boldsymbol{B} = A_{lm}\, B_{no}\, \boldsymbol{e}_l \otimes \boldsymbol{e}_m \cdot \boldsymbol{e}_n \otimes \boldsymbol{e}_o = A_{lm}\, B_{mo}\, \boldsymbol{e}_l \otimes \boldsymbol{e}_o = \boldsymbol{D}\,,$$

the double scalar product between a fourth and a second order tensor

$$\begin{aligned}\boldsymbol{\mathcal{A}} : \boldsymbol{B} &= A_{pqrs}\, B_{no}\, \boldsymbol{e}_p \otimes \boldsymbol{e}_q \otimes \boldsymbol{e}_r \otimes \boldsymbol{e}_s : \boldsymbol{e}_n \otimes \boldsymbol{e}_o \\ &= A_{pqrs}\, B_{sr} \boldsymbol{e}_p \otimes \boldsymbol{e}_q = \boldsymbol{F}\end{aligned}$$

and the definition of a transposed second order tensor $\boldsymbol{A}$

$$\boldsymbol{A}^\top = A_{ji}\, \boldsymbol{e}_i \otimes \boldsymbol{e}_j = A_{ij}\, \boldsymbol{e}_j \otimes \boldsymbol{e}_i \,.$$

In the following equation, the Kronecker delta δ_{ij} is used to represent the second order unit tensor

$$\mathbf{1} = \delta_{ij}\, \boldsymbol{e}_i \otimes \boldsymbol{e}_j = \boldsymbol{e}_i \otimes \boldsymbol{e}_i \qquad \text{with} \quad \delta_{ij} = \begin{cases} 1 & \text{if } i = j \\ 0 & \text{if } i \neq j \end{cases}$$

Using the tensor notation, Latin indices run through the values 1, 2, and 3, while Greek indices represent the normal and the two tangential directions of the local coordinate system (n, t_1, t_2). The vector valued nabla operator is defined as $\boldsymbol{\nabla} = \boldsymbol{e}_i\, {}^{\partial}\!/\!{}_{\partial x_i}$ at three dimensions. $\boldsymbol{\nabla} \cdot \square$ is the divergence, and $\boldsymbol{\nabla} \otimes \square$ is the gradient of a tensor. The transposed gradient is defined as $\square \otimes \boldsymbol{\nabla} = [\boldsymbol{\nabla} \otimes \square]^\top$ where $\square$ holds for all first and second order tensors. An extended overview of tensor algebra and analysis is given in basic textbooks on continuum mechanics featuring mathematical propaedeutics, e.g. in Altenbach [2], Lai, Rubin and Krempl [3], Bertram [4] or Lebedev, Cloud and Eremeyev [5].

In vector-matrix notation, vectors are denoted as upright lowercase sans serif bold letters (e.g. displacement vector $\mathbf{u} = [u_1\ u_2\ u_3]^\top$) and matrices as upright uppercase sans serif bold letters (e.g. stiffness matrix $\mathbf{K}$).

3 Basics of a Cohesive Zone Model and the Traction-Separation-Law

This section is divided into two subsections. In the first one we give a brief overview over CZMs, mention important works in this field and present the main assumptions of these models. The second subsection is dedicated to the different types of TSLs which can be used in a CZM and in which situation a specific law is applied.

3.1 The Cohesive Zone Model

A CZM is a phenomenological framework to model crack evolution and crack nucleation in solid bodies. The advantages of CZMs are that the existence of a pre-crack,

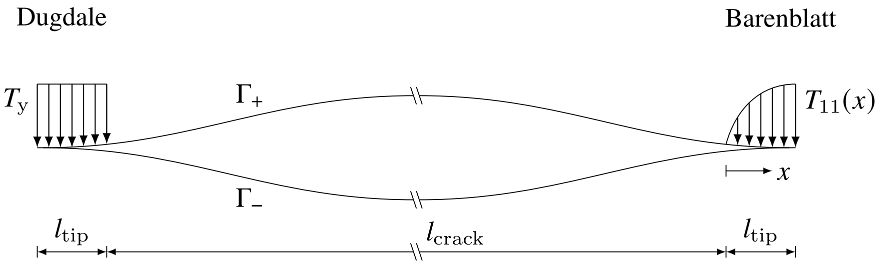

Fig. 1 Stress distribution at a crack in the sense of Dugdale (left) and Barenblatt (right) after [6]

like it is in classical fracture mechanics, is not necessary and that no stress singularity at the crack tip occurs, any more.

All CZMs are based on the pioneering works of Barenblatt [7] and Dugdale [8]. Through the cracking of the solid new surfaces Γ_+ and Γ_- are created (see Fig. 1) which are unconnected, stress-free and the behaviour of them depends only on local quantities and not on global ones. This is the stress-free zone of a crack. The second zone of a crack is the crack tip which is called process or cohesive zone in which damage and fracture occurs. To avoid an infinite stress in this zone the stress is prescribed through the introduction of a TSL. Further on, it is assumed that the crack tip is small compared to the size of the crack ($l_{\text{tip}} \ll l_{\text{crack}}$). Dugdale assumed that the stress at the crack tip is the yield strength T_y and that this stress is constant (see Fig. 1, left-hand side) to analyse the yielding of a steel sheet containing slits. In contrast to that Barenblatt analysed crack evolution in a perfect brittle solid. A schematic stress distribution in his sense is presented in Fig. 1 on the right-hand side.

State of the art is to formulate the traction acting in the cohesive zone as a function of the distance between the surfaces Γ_+ and Γ_- (separation). However, Barenblatt formulated his TSL as a function of the distance x from the end of the crack to the end of the cohesive zone.

After introducing this theory to the scientific community nearly two decades nothing happened on this field because the effort to solve the arising problem was too high. But with the advance of the numerical solution techniques, especially the Finite Element Method (FEM), it got possible to solve the arising systems of partial differential equations what led to a big interest in CZMs to describe cracking and crack evolution in a solid. The CZM is added to a FE mesh by introducing cohesive or interface elements. From this follows that it is necessary to know the crack path. This is one disadvantage of CZMs. Further disadvantages are that a length scale is added to the model [9] and that the stress starts to oscillate. But this is the topic of Sect. 4, next to the destabilisation of the Newton–Raphson procedure due to a strong softening behaviour.

From our knowledge one of the first users of this theory was Hillerborg [10] in 1976 to describe failure of concrete.

3.2 The Traction-Separation-Law

The TSL is the key part of every CZM, therefore, we dedicate one section to this topic. The TSL has a strong influence on how the crack will open and how the crack will propagate. Next to that the choice of TSL depends on the failure mechanism (e.g. brittle or ductile), the opening mode (Mode I, II, III), the material of which the solid is made and to which problem the TSL is applied. Further on, the crack propagation could depend on the crack opening velocity or it could exist a coupling between the different opening modes. All these information can have an influence on the crack growth and have to be considered when the TSL is formulated. That is the reason why a lot of different TSLs were formulated from researchers to analyse their specific problems. Here, we can only present an overview of frequently used TSLs. They are shown in Fig. 2 for pure Mode I opening.

Brittle cracking can be modelled with simple linear TSLs which were presented and used by Hillerborg or Bažant to model cracking of concrete for example (Fig. 2 top, left and bottom, left). These TSLs have no elastic range because for brittle failure it can be assumed that any inelastic deformation is material separation [6], but the introduction of a small elastic zone is useful for the numerical treatment.

In contrast to that smooth TSLs with an elastic range are used to describe ductile failure mechanisms. Some examples for these TSLs are presented in the diagrams

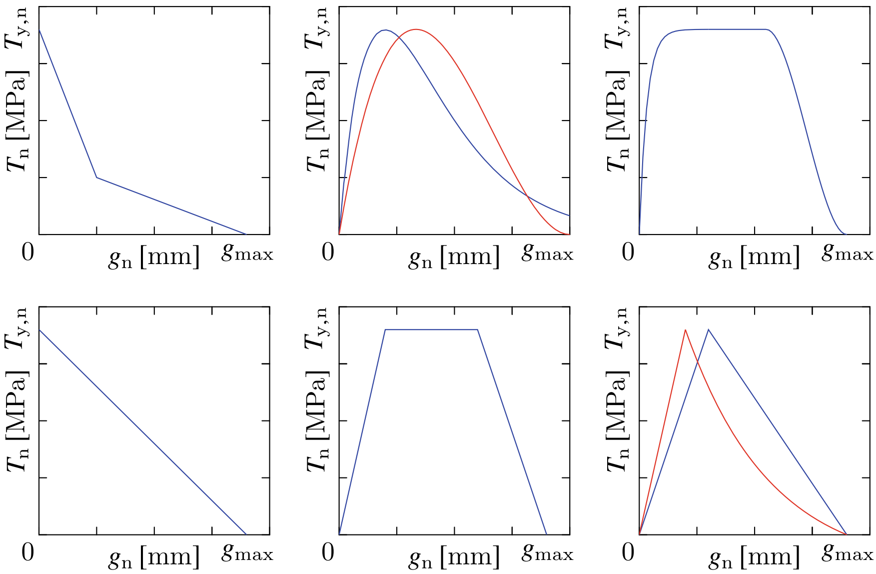

Fig. 2 Types of TSLs fore Mode I opening after: Bažant [11] (top, left); Needleman [12, 13] blue—exponential TSL, red—polynomial TSL (top, centre); Scheider [14] (top, right); Hillerborg [10] (bottom, left); Tveergard and Hutchinson [15] (bottom, centre); ABAQUS [16] blue—linear softening, red—exponential softening (bottom, right)

in Fig. 2 top, centre and right position and in Fig. 2 bottom, centre position. The bottom, right diagram in Fig. 2 presents schematically the two possible shapes of TSLs which are implemented in the commercial software tool ABAQUS. Both TSLs can be adjusted in that way that it gets possible to model brittle or ductile failure. However, application of these TSLs is limited because of their simplicity.

All presented TSLs have in common that they are characterised through two parameters because all other usually depend or are formulated with a dependence on them. The area below the TSL is the cohesive energy which is the work needed to create a unit area of fracture surface. It is calculated as

$$G_\mathrm{i} = \int\limits_0^{g_\mathrm{max}} T_\mathrm{n} \, \mathrm{d}g_\mathrm{n} \tag{1}$$

In reality not only Mode I cracking occurs, especially not without another mode and in general the modes influence each other. To consider this in the TSL description a mix-mode behaviour is introduced. This is done by introducing and effective separation which is a combination of normal and tangential separation and finally the TSL is formulated with the effective separation.

Next to that it is necessary to guarantee that the TSL fulfils thermodynamic restrictions. To ensure this it is state of the art to derive the traction formulation from a potential (see [17]), similar to the procedure in standard continuum mechanics. Hence, the TSL is usually prescribed (e.g. [18, 19]) and then the global behaviour is analysed, of course the inverse way is possible (see e.g. [20]) but then it is difficult to fulfil thermodynamics, therefore, it is uncommon.

If someone wants to model unloading of the TSL, respectively the cohesive zone, it is important to add a contact formulation to the TSL and maybe a friction formulation for the tangential direction when required. For more detailed informations concerning TSLs and for what problems they are used we refer to the book of Schwalbe [6] or the reviews of Needleman [9] and Chandra [21].

4 Development of the Novel Traction-Separation-Law for High-Temperature Applications

4.1 Equations of Balance for an Arbitrary Body with a Thin Interface

Figure 3 shows an arbitrary body Ω which is homogeneous and isotopic with constant density ρ and constant volume V in reference and current configuration which is separated by an interface Γ into two parts Ω_+ and Ω_-. Hence, interface is split into Γ_+ and Γ_-, as well as the boundary of the body $\partial\Omega$ where the body is subjected to a load $\boldsymbol{t}_{\partial\Omega}$. At the beginning of separation the surfaces Γ_+ and Γ_- are in contact. But

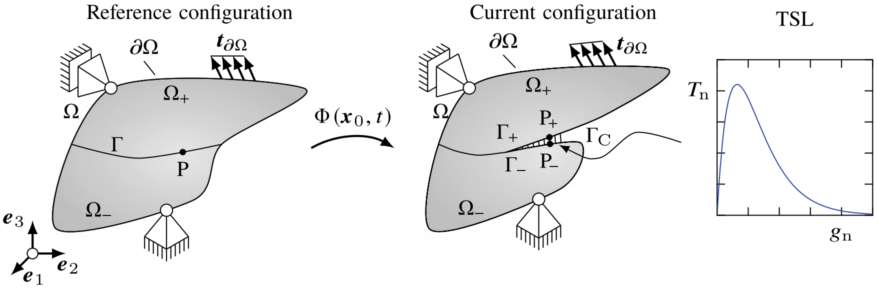

Fig. 3 Arbitrary body with a thin (zero thickness) interface in the Euclidian space $\mathbb{E}^3$ in reference and current configuration subjected to a mechanical load and a TSL for pure Mode I opening (T_n-traction in normal direction, g_n-separation in normal direction)

evolving separation leads to failure of this connection and as result a crack starts to propagate along the interface Γ. The connection between the interface surfaces Γ_+ and Γ_- is described by a TSL. One feasible shape of a TSL is presented in Fig. 3 for pure Mode I opening. This TSL is applied to every point P which is placed on the interface to describe crack propagation. In Fig. 4 the vectors are presented which act on upper and lower surface of the interface when the body Ω is subjected to a mechanical load and a temperature field. Next to that, Fig. 4 presents the resulting vectors which act on the midsurface of the interface. This midsurface is introduced to simplify resulting equations to describe the body. Here, we just give a brief overview how the basic equations are derived and refer the interested reader to Naumenko and Altenbach [22], Fagerström and Larsson [23] and others for further informations. All equations are derived in the context of large deformations and with respect to the current configuration. First equation which must be valid for the body is the balance of linear momentum. The equation is derived by neglecting inertia effects (quasi-static) and body forces. It follows

$$\int\limits_{\partial\Omega} \boldsymbol{t}_{\partial\Omega}\,\mathrm{d}a + \int\limits_{\Gamma_+} \boldsymbol{t}_+\,\mathrm{d}a + \int\limits_{\Gamma_-} \boldsymbol{t}_-\,\mathrm{d}a = \boldsymbol{o} \tag{2}$$

The vectors $\boldsymbol{t}_+$ and $\boldsymbol{t}_-$ are the tractions acting on the deformed interface surfaces (see Fig. 4). With the force equilibrium for the interface tractions

$$\int\limits_{\Gamma_+} \boldsymbol{t}_+\,\mathrm{d}a + \int\limits_{\Gamma_-} \boldsymbol{t}_-\,\mathrm{d}a = \boldsymbol{o}\,,$$

Cauchy's theorem and Gauss' divergence theorem, it results the common formulation for the balance of linear momentum in the global form for the whole deformed body Ω

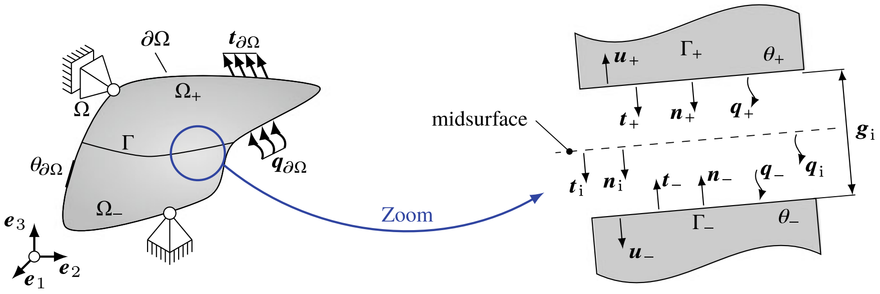

Fig. 4 Definition of the vectors acting on the interface (Cohesive Zone) when the arbitrary body Ω is subjected to mechanical and thermal boundary conditions

$$\int\limits_{\Omega} \boldsymbol{T} \cdot \nabla \, \mathrm{d}v = \boldsymbol{o} \tag{3}$$

The second equation is the balance of angular momentum which for a Cauchy continuum leads to the restriction that the stress tensor $\boldsymbol{T}$ is symmetric

$$\boldsymbol{T} = \boldsymbol{T}^{\top} \tag{4}$$

The first law of thermodynamics or balance of energy is the third equation which is necessary for the formulation of an interface constitutive model. First law of thermodynamics states that the rate of kinetic $\dot{E}_{\mathrm{kin}}$ and internal energy $\dot{E}_{\mathrm{int}}$ is equal the mechanical P_{mech} and non-mechanical power P_{non} supplied to a body

$$\dot{E}_{\mathrm{kin}} + \dot{E}_{\mathrm{int}} = P_{\mathrm{mech}} + P_{\mathrm{non}} \, . \tag{5}$$

Whereby, kinetic energy of the body Ω is zero because only quasi-static processes are considered. The internal energy is assumed to be the sum of a bulk (index “b”) and an interface part (index “i”) with the specific internal energy e, see [23] as well

$$E_{\mathrm{int}} = \int\limits_{\Omega} \rho e_{\mathrm{b}} \, \mathrm{d}v + \int\limits_{\Gamma} e_{\mathrm{i}} \, \mathrm{d}a \tag{6}$$

Additionally, the split into a bulk and an interface part is used for the mechanical and non-mechanical power but without a heat source r for the interface. The vector $\boldsymbol{q}_{\mathrm{b}}$ in the non-mechanical power represents the heat vector of the bulk material

$$
\begin{aligned}
P_{\text{mech}} &= \int\limits_{\Omega} \boldsymbol{T} : \boldsymbol{D}\, \mathrm{d}v && + \int\limits_{\Gamma} \boldsymbol{t}_{\mathrm{i}} \cdot \dot{\boldsymbol{g}}_{\mathrm{i}}\, \mathrm{d}a \\
P_{\text{non}} &= \int\limits_{\Omega} \left(\rho r - \nabla \cdot \boldsymbol{q}_{\mathrm{b}}\right) \mathrm{d}v && - \int\limits_{\Gamma} q_{\mathrm{i}}\, \mathrm{d}a \\
q_{\mathrm{i}} &= \boldsymbol{n}_{\mathrm{i}} \cdot \boldsymbol{q}_{\mathrm{i}}
\end{aligned}
\tag{7}
$$

In these equations $\boldsymbol{t}_{\mathrm{i}}$, $\boldsymbol{q}_{\mathrm{i}}$ and $\boldsymbol{n}_{\mathrm{i}}$ are the natural traction, heat and normal vector of the interface which act on the midsurface (see Fig. 4) and $\boldsymbol{D}$ represents the work-conjugate strain rate tensor corresponding to the Cauchy stress tensor $\boldsymbol{T}$. Separation vector is defined as

$$\boldsymbol{g}_{\mathrm{i}} = \boldsymbol{u}_{+} - \boldsymbol{u}_{-}$$

and heat vector as

$$\boldsymbol{q}_{\mathrm{i}} = \boldsymbol{q}_{+} - \boldsymbol{q}_{-}$$

After inserting internal energy, mechanical and non-mechanical power into Eq. (5) and rearrange the terms, final form is derived with one contribution for the bulk material and another one for the interface.

$$\underbrace{\int\limits_{\Omega} \left(\rho \dot{e}_{\mathrm{b}} - \boldsymbol{T} : \boldsymbol{D} - \rho r + \nabla \cdot \boldsymbol{q}_{\mathrm{b}}\right) \mathrm{d}v}_{\text{bulk}} + \underbrace{\int\limits_{\Gamma} \left(\dot{e}_{\mathrm{i}} - \boldsymbol{t}_{\mathrm{i}} \cdot \dot{\boldsymbol{g}}_{\mathrm{i}} + q_{\mathrm{i}}\right) \mathrm{d}a}_{\text{interface}} = 0 \tag{8}$$

The last equation required is the second law of thermodynamics or entropy inequality. This inequality states that entropy production of a process is non-negative. It follows

$$
\begin{aligned}
0 &\leqslant \dot{H}_{\eta} - \frac{q_{\eta}}{\theta} \qquad \text{with} \\
\frac{q_{\eta}}{\theta} &= \int\limits_{\Omega} \rho \frac{r}{\theta}\, \mathrm{d}v - \int\limits_{\partial\Omega} \boldsymbol{n}_{\partial\Omega} \cdot \frac{\boldsymbol{q}_{\mathrm{b}}}{\theta}\, \mathrm{d}a - \int\limits_{\Gamma} \frac{q_{\mathrm{i}}}{\theta}\, \mathrm{d}a
\end{aligned}
\tag{9}
$$

In this equation H_{η} is the entropy and $\frac{q_{\eta}}{\theta}$ is the entropy flux. Required interface temperature is determined through the heat conduction equation for the interface which is determined in the subsequent section.

The entropy is divided into a bulk and an interface part, similar as it is done for the internal energy, with η as the specific entropy

$$H_{\eta} = \int\limits_{\Omega} \rho \eta_{\mathrm{b}}\, \mathrm{d}v + \int\limits_{\Gamma} \eta_{\mathrm{i}}\, \mathrm{d}a$$

By using Gauss' divergence theorem, the final form is obtained which is divided into a bulk and an interface part, as well

$$\underbrace{\int\limits_{\Omega}\left[\rho\dot{\eta}_{\mathrm{b}}-\rho\frac{r}{\theta}+\nabla\cdot\left(\frac{\boldsymbol{q}_{\mathrm{b}}}{\theta}\right)\right]\,\mathrm{d}v}_{\text{bulk}}+\underbrace{\int\limits_{\Gamma}\left[\dot{\eta}_{\mathrm{i}}+\frac{q_{\mathrm{i}}}{\theta}\right]\,\mathrm{d}a}_{\text{interface}}\geqslant 0 \tag{10}$$

Bulk and interface part of derived balance equations are used independently to develop constitutive models of bulk material and interface.

4.2 The Novel Traction-Separation-Law

The basic equations of continuum mechanics for an arbitrary body with an interface were presented in the foregoing section. Now, the deductive development of the TSL begins. Therefore, only interface parts of derived equations are considered. As a first step, Helmholtz free energy [24] for the interface is introduced

$$\psi_{\mathrm{i}}=e_{\mathrm{i}}-\theta\eta_{\mathrm{i}} \tag{11}$$

The time derivative of this variable yields

$$\dot{\psi}_{\mathrm{i}}=\dot{e}_{\mathrm{i}}-\dot{\theta}\eta_{\mathrm{i}}-\theta\dot{\eta}_{\mathrm{i}} \tag{12}$$

Combining balance of energy and entropy inequality as well as replacing specific internal energy by Helmholtz free energy yields the global form of Clausius [25], Duhem [26] inequality

$$\int\limits_{\Gamma}\boldsymbol{t}_{\mathrm{i}}\cdot\dot{\boldsymbol{g}}_{\mathrm{i}}-\left(\dot{\psi}_{\mathrm{i}}+\eta_{\mathrm{i}}\dot{\theta}\right)\,\mathrm{d}a\geqslant 0 \tag{13}$$

for the interface. The name of Eq. (13) was introduced by Truesdell [27, 28]. This equation is valid for the whole interface. Hence, it can be localised

$$\boldsymbol{t}_{\mathrm{i}}\cdot\dot{\boldsymbol{g}}_{\mathrm{i}}-\left(\dot{\psi}_{\mathrm{i}}+\eta_{\mathrm{i}}\dot{\theta}\right)\geqslant 0 \tag{14}$$

The Clausius–Duhem inequality must be fulfilled for any arbitrary process, hence, this equation is the origin of a thermodynamic consistent constitutive model. At first, the separation is additive decomposed into an elastic and an inelastic part

$$\boldsymbol{g}_{\mathrm{i}}=\boldsymbol{g}_{\mathrm{el}}+\boldsymbol{g}_{\mathrm{in}} \tag{15}$$

This is done to account for a viscous behaviour of the interface because the bulk material shows a strong creep behaviour which influences the cohesive zone, too. In general, the overall rate dependence can arise as a consequence of rate dependence of the bulk material's behaviour, of the interface response itself, or of both [29].

Next to that the experiment shows a relaxation behaviour during the delamination process (see Fig. 10) which is captured by the inelastic part. Further on, the additive decomposition is valid although large deformations are considered because metals are investigated and hence the strains keep small. Large deformations are only considered to capture the effects of large rotations.

The free energy depends on the temperature θ, an isotropic damage variable d and the elastic separation $\boldsymbol{g}_{\mathrm{el}}$

$$\psi_{\mathrm{i}} = f\left(\boldsymbol{g}_{\mathrm{el}}, d, \theta\right) \tag{16}$$

Next to that split of separation into elastic and inelastic part acts like a viscous regularisation (see [30, 31]) for the numerical solution scheme, later on.

Only one isotropic damage variable is introduced which captures the effects of creep as well as fatigue damage. This has the advantage that no further equation is necessary to describe the interaction between creep and fatigue damage, which is the case when independent damage variables for these two damage types are defined.

By applying the chain rule, the time derivative of Helmholtz free energy follows as

$$\dot{\psi}_{\mathrm{i}} = \frac{\partial \psi_{\mathrm{i}}}{\partial \boldsymbol{g}_{\mathrm{el}}} \cdot \dot{\boldsymbol{g}}_{\mathrm{el}} + \frac{\partial \psi_{\mathrm{i}}}{\partial d}\dot{d} + \frac{\partial \psi_{\mathrm{i}}}{\partial \theta}\dot{\theta} \tag{17}$$

Inserting Eq. (17) into Clausius–Duhem inequality while considering the additive split of separation at the same time and rearrange terms leads to

$$\left(\boldsymbol{t}_{\mathrm{i}} - \frac{\partial \psi_{\mathrm{i}}}{\partial \boldsymbol{g}_{\mathrm{el}}}\right) \cdot \dot{\boldsymbol{g}}_{\mathrm{el}} - \left(\eta_{\mathrm{i}} + \frac{\partial \psi_{\mathrm{i}}}{\partial \theta}\right)\dot{\theta} + \boldsymbol{t}_{\mathrm{i}} \cdot \dot{\boldsymbol{g}}_{\mathrm{in}} - \frac{\partial \psi_{\mathrm{i}}}{\partial d}\dot{d} \geqslant 0 \tag{18}$$

This equation must be fulfilled for any process, thus, it follows directly the relation for traction and specific entropy

$$\boldsymbol{t}_{\mathrm{i}} = \frac{\partial \psi_{\mathrm{i}}}{\partial \boldsymbol{g}_{\mathrm{el}}}\,, \tag{19}$$

$$\eta_{\mathrm{i}} = -\frac{\partial \psi_{\mathrm{i}}}{\partial \theta}\,, \tag{20}$$

These results follow from the rate independence of Eq. (16). For further informations we refer to [22]. It remains the dissipation inequality

$$\boldsymbol{t}_{\mathrm{i}} \cdot \dot{\boldsymbol{g}}_{\mathrm{in}} + Y_{\mathrm{E}}\dot{d} \geqslant 0\,, \qquad Y_{\mathrm{E}} = -\frac{\partial \psi_{\mathrm{i}}}{\partial d} \tag{21}$$

which is used to develop evolution equations for the inelastic separation and the damage, later on. For specification of free energy this one is split into a mechanical and a pure thermal part

$$\psi_{\mathrm{i}} = \psi_{\mathrm{i}}^{\mathrm{mech}} + \psi_{\mathrm{i}}^{\mathrm{therm}} \tag{22}$$

The mechanical part of Helmholtz free energy is specified first. This part is formulated as a quadratic function of elastic separation in combination with a degradation function f_d which is introduced with the effective stress concept [32]

$$\psi_\mathrm{i}^\mathrm{mech} = \frac{1}{2} f_\mathrm{d}(d)\, \boldsymbol{g}_\mathrm{el} \cdot \boldsymbol{C}_\mathrm{TSL} \cdot \boldsymbol{g}_\mathrm{el} \qquad \text{with} \qquad f_\mathrm{d}(d) = (1-d)^p \tag{23}$$

Dependence of degradation function f_d to parameter p leads to a finite value for the thermodynamic driving force when $p > 1$ and $d = 1$ [33].

Thermal part is specified in such a way that heat capacity λ_i is a linear function of the temperature ($\lambda_\mathrm{i} = C_{\lambda 1}\theta + C_{\lambda 2}$). This is done due to the fact that for metals thermal material parameters (heat capacity, thermal expansion, density, etc.) depend linearly on the temperature in the range from room to near melting temperature, approximately [34, 35]. By integrating this function with the relation

$$\lambda_\mathrm{i} = -\theta \frac{\partial^2 \psi_\mathrm{i}}{\partial \theta^2}$$

one gets following thermal part of Helmholtz free energy

$$\psi_\mathrm{i}^\mathrm{therm} = C_{\lambda 2}\,(\theta - \theta_0) - \frac{C_{\lambda 1}}{2}\left(\theta^2 + \theta_0^2\right) + C_{\lambda 1}\theta\theta_0 - C_{\lambda 2}\theta \ln\left(\frac{\theta}{\theta_0}\right) \tag{24}$$

Herein, θ_0 is the reference temperature. The last part of the interface model are the evolution equations for the inelastic separation and the damage. To derive these Eq. (21), the dissipation inequality is used because this equation must be fulfilled at every time. For inelastic separation a power-law type is defined with extension to damage [36, 37], hence, secondary and tertiary stages of inelastic separation can be described

$$\dot{\boldsymbol{g}}_\mathrm{in} = \frac{a}{(1-d)^{N_1}} \left[\frac{|\boldsymbol{t}_\mathrm{i}|}{T_0}\right]^{N_2} \frac{\boldsymbol{t}_\mathrm{i}}{|\boldsymbol{t}_\mathrm{i}|} \qquad \text{if} \qquad |\boldsymbol{t}_\mathrm{i}| > T_\mathrm{y} \tag{25}$$

Therein, evolution of inelastic separation starts when traction $\boldsymbol{t}_\mathrm{i}$ is bigger as the threshold T_y. This equation fulfils Eq. (21) because the term $\boldsymbol{t}_\mathrm{i} \cdot \dot{\boldsymbol{g}}_\mathrm{in}$ is always positive or zero with this evolution equation.

Damage evolution equation follows from dissipation inequality after introducing the damage driving force or elastic energy release rate Y_E and assume that the damage rate is always positive ($\dot{d} \geqslant 0$), hence, healing effects of the material are excluded. Next to that damage can only evolve from 0 to 1

$$\boldsymbol{t}_\mathrm{i} \cdot \dot{\boldsymbol{g}}_\mathrm{in} + Y_\mathrm{E}\dot{d} \geqslant 0\,, \qquad Y_\mathrm{E} = -\frac{\partial \psi_\mathrm{i}}{\partial d} \tag{26}$$

A suitable damage evolution equation which fulfils this inequality is

$$\dot{d} = (1-d)^{s_1} \left(\frac{Y_\mathrm{E}}{S_0}\right)^{s_2} \frac{\left|\dot{\boldsymbol{g}}_\mathrm{in}\right|}{g_\mathrm{dim}} \tag{27}$$

This form is similar to an evolution equation used by Bouvard [19]. Damage evolves when the normal separation is positive (no contact), material is under loading, elastic energy release rate is bigger as the threshold Y_{E0} and an inelastic evolution takes place

$$\boldsymbol{g}_{\mathrm{el}} \cdot \boldsymbol{n}_{\mathrm{i}} > 0\,, \qquad Y_{\mathrm{E}} > Y_{\mathrm{E0}}\,, \qquad \dot{Y}_{\mathrm{E}} \geqslant 0, \qquad \dot{\boldsymbol{g}}_{\mathrm{in}} \neq 0$$

With Eqs. (25) and (27) each term of the dissipation inequality is fulfilled at every time, thus, the complete dissipation inequality is fulfilled, as well. Finally, we present the complete set of equations in a close form.

$$\boldsymbol{t}_{\mathrm{i}} = (1-d)^p\, \boldsymbol{C}_{\mathrm{TSL}} \cdot \boldsymbol{g}_{\mathrm{el}}\,, \tag{28}$$

$$\boldsymbol{g}_{\mathrm{el}} = \boldsymbol{g}_{\mathrm{i}} - \boldsymbol{g}_{\mathrm{in}}\,, \tag{29}$$

$$\dot{\boldsymbol{g}}_{\mathrm{in}} = \frac{a}{(1-d)^{N_1}} \left[\frac{|\boldsymbol{t}_{\mathrm{i}}|}{T_0}\right]^{N_2} \frac{\boldsymbol{t}_{\mathrm{i}}}{|\boldsymbol{t}_{\mathrm{i}}|}\,, \tag{30}$$

$$Y_{\mathrm{E}} = \frac{p}{2}\,(1-d)^{p-1}\, \boldsymbol{g}_{\mathrm{el}} \cdot \boldsymbol{C}_{\mathrm{TSL}} \cdot \boldsymbol{g}_{\mathrm{el}}\,, \tag{31}$$

$$\dot{d} = (1-d)^{s_1} \left(\frac{Y_{\mathrm{E}}}{S_0}\right)^{s_2} \frac{|\dot{\boldsymbol{g}}_{\mathrm{in}}|}{g_{\mathrm{dim}}}\,, \tag{32}$$

$$\eta_{\mathrm{i}} = C_{\lambda 2} \ln\left(\frac{\theta}{\theta_0}\right) + C_{\lambda 1}\,(\theta - \theta_0) - \frac{\partial \psi_{\mathrm{i}}^{\mathrm{mech}}}{\partial \theta}\,, \tag{33}$$

$$\lambda_{\mathrm{i}} = C_{\lambda 1}\theta + C_{\lambda 2} - \theta \frac{\partial^2 \psi_{\mathrm{i}}^{\mathrm{mech}}}{\partial \theta^2} \tag{34}$$

4.3 Heat Transfer Through an Arbitrary Body with a Thin Interface

The heat conduction equation follows from Eq. (8)

$$\int\limits_{\Omega} \rho \dot{e}_{\mathrm{b}} - \boldsymbol{T} : \boldsymbol{D} - \rho r \,\mathrm{d}v - \int\limits_{\partial\Omega} q_{\mathrm{b}}\,\mathrm{d}a + \int\limits_{\Gamma} \dot{e}_{\mathrm{i}} - \boldsymbol{t}_{\mathrm{i}} \cdot \dot{\boldsymbol{g}}_{\mathrm{i}} + q_{\mathrm{i}}\,\mathrm{d}a = 0 \tag{35}$$

Up next, Helmholtz free energy [24] for the arbitrary body is introduced. It is assumed that the free energy is additively composed of a bulk and an interface portion

$$\psi = \psi_{\mathrm{b}} + \psi_{\mathrm{i}} \tag{36}$$

Further on, the bulk portion is a function of temperature and the elastic part of Almansi strain tensor

$$\psi_{\mathrm{b}} = f\left(\boldsymbol{E}_{\mathrm{A}}^{\mathrm{el}}, \theta\right)$$

and the interface portion is a function of temperature, elastic separation and a scalar damage variable

$$\psi_{\mathrm{i}} = f\left(\boldsymbol{g}_{\mathrm{el}}, d, \theta\right)$$

The relations between internal energy, free energy, temperature and entropy are

$$\begin{aligned} e_{\mathrm{b}} &= \psi_{\mathrm{b}} - \eta_{\mathrm{b}}\theta \\ e_{\mathrm{i}} &= \psi_{\mathrm{i}} - \eta_{\mathrm{i}}\theta \end{aligned}$$

From Clausius–Duhem inequality the following relations for the bulk and interface portion are derived

$$\begin{aligned} \boldsymbol{t}_{\mathrm{i}} &= \frac{\partial \psi_{\mathrm{i}}}{\partial \boldsymbol{g}_{\mathrm{el}}}, & \eta_{\mathrm{i}} &= -\frac{\partial \psi_{\mathrm{i}}}{\partial \theta}, & Y_{\mathrm{E}} &= -\frac{\partial \psi_{\mathrm{i}}}{\partial d}, \\ \boldsymbol{T} &= \rho \frac{\partial \psi_{\mathrm{b}}}{\partial \boldsymbol{E}_{\mathrm{A}}^{\mathrm{el}}}, & \eta_{\mathrm{b}} &= -\frac{\partial \psi_{\mathrm{b}}}{\partial \theta} \end{aligned}$$

With these relations, the time derivative of the internal energy and the time derivative of the entropy it follows the heat conduction equation for a fully coupled thermomechanical problem

$$\begin{aligned} &\int\limits_{\Omega} \rho\lambda_{\mathrm{b}}\dot{\theta} - \rho r - \theta \frac{\partial \boldsymbol{T}}{\partial \theta} : \boldsymbol{D} + \left[\theta \frac{\partial \boldsymbol{T}}{\partial \theta} - \boldsymbol{T}\right] : \boldsymbol{D}_{\mathrm{in}} \, \mathrm{d}v - \int\limits_{\partial\Omega} q_{\mathrm{b}} \, \mathrm{d}a \\ &+ \int\limits_{\Gamma} \lambda_{\mathrm{i}}\dot{\theta} + q_{\mathrm{i}} - \theta \frac{\partial \boldsymbol{t}_{\mathrm{i}}}{\partial \theta} \cdot \dot{\boldsymbol{g}}_{\mathrm{i}} + \left[\theta \frac{\partial Y_{\mathrm{E}}}{\partial \theta} - Y_{\mathrm{E}}\right]\dot{d} + \left[\theta \frac{\partial \boldsymbol{t}_{\mathrm{i}}}{\partial \theta} - \boldsymbol{t}_{\mathrm{i}}\right] \cdot \dot{\boldsymbol{g}}_{\mathrm{in}} \, \mathrm{d}a = 0 \end{aligned} \tag{37}$$

Wherein, the external and internal work of the bulk material are

$$W_{\mathrm{b,ext}} = \theta \frac{\partial \boldsymbol{T}}{\partial \theta} : \boldsymbol{D} \qquad W_{\mathrm{b,int}} = \left[\theta \frac{\partial \boldsymbol{T}}{\partial \theta} - \boldsymbol{T}\right] : \boldsymbol{D}_{\mathrm{in}}$$

and the external and internal work of the interface are

$$W_{\mathrm{i,ext}} = \theta \frac{\partial \boldsymbol{t}_{\mathrm{i}}}{\partial \theta} \cdot \dot{\boldsymbol{g}}_{\mathrm{i}} \qquad W_{\mathrm{i,int}} = \left[\theta \frac{\partial Y_{\mathrm{E}}}{\partial \theta} - Y_{\mathrm{E}}\right]\dot{d} + \left[\theta \frac{\partial \boldsymbol{t}_{\mathrm{i}}}{\partial \theta} - \boldsymbol{t}_{\mathrm{i}}\right] \cdot \dot{\boldsymbol{g}}_{\mathrm{in}}$$

Heat flux q_{b} is determined after the common procedure

$$q_{\mathrm{b}} = -\boldsymbol{n}_{\partial\Omega} \cdot \boldsymbol{q}_{\mathrm{b}} \tag{38}$$

The negative sign ensures that a heat flux pointing into the body increases the internal energy and not vice versa. The heat flux vector $\boldsymbol{q}_{\mathrm{b}}$ is determined after Fourier's law [38]

$$\boldsymbol{q}_{\mathrm{b}} = -\,\kappa_{\mathrm{b}}\,(\boldsymbol{\nabla}\theta) \tag{39}$$

With these considerations and Gauss divergence theorem it follows from Eq. (37)

$$\begin{aligned} &\int\limits_{\Omega} \rho\lambda_{\mathrm{b}}\dot{\theta} - \kappa_{\mathrm{b}}\boldsymbol{\nabla}\cdot(\boldsymbol{\nabla}\theta) - \rho r - W_{\mathrm{b,ext}} + W_{\mathrm{b,int}}\,\mathrm{d}v \\ +&\int\limits_{\Gamma} \lambda_{\mathrm{i}}\dot{\theta} + q_{\mathrm{i}} - W_{\mathrm{i,ext}} + W_{\mathrm{i,int}}\,\mathrm{d}a = 0 \end{aligned} \tag{40}$$

Coming to the end it is necessary to determine the heat flux through the interface q_{i}, as well. This flux is based on heat conduction and the temperature difference of the two interface surfaces and makes it possible to simulate a discrete temperature jump in the interface which occurs because of cracking and crack propagation (delamination), respectively.

$$q_{\mathrm{i}} = q_{+} + q_{-} = -\boldsymbol{n}_{\mathrm{i}}\cdot\boldsymbol{q}_{\mathrm{i}} = \kappa_{\mathrm{i}}(d)\,(\theta_{+} - \theta_{-}) \tag{41}$$

Due to damage evolution the heat conductivity of the interface changes. This is considered through the dependence of heat conductivity κ_{i} on the damage variable. Thus, when damage starts to evolve heat conductivity begins to change from the value of the bulk material in direction of the value of air. This value is reached when the CZM fails

$$\kappa_{\mathrm{i}}(d) = d\kappa_{\mathrm{air}} + (1-d)\,\kappa_{\mathrm{b}} \tag{42}$$

The fluxes of the interface surfaces are

$$\begin{aligned} q_{+} &= -\boldsymbol{n}_{\mathrm{i}}\cdot\boldsymbol{q}_{+} = \kappa_{\mathrm{i}}\,(\theta - \theta_{+}) \\ q_{-} &= \boldsymbol{n}_{\mathrm{i}}\cdot\boldsymbol{q}_{-} = \kappa_{\mathrm{i}}\,(\theta_{-} - \theta) \end{aligned}$$

It follows the final form of heat conduction equation by replacing the interface heat flux in Eq. (40) with Eq. (41) and neglecting internal heat supply.

$$\begin{aligned} &\int\limits_{\Omega} \rho\lambda_{\mathrm{b}}\dot{\theta} - \kappa_{\mathrm{b}}\boldsymbol{\nabla}\cdot(\boldsymbol{\nabla}\theta) - W_{\mathrm{b,ext}} + W_{\mathrm{b,int}}\,\mathrm{d}v \\ +&\int\limits_{\Gamma} \lambda_{\mathrm{i}}\dot{\theta} + \kappa_{\mathrm{i}}(d)\,(\theta_{+} - \theta_{-}) - W_{\mathrm{i,ext}} + W_{\mathrm{i,int}}\,\mathrm{d}a = 0 \end{aligned} \tag{43}$$

5 Numerics of Cohesive Zone Models and the Novel Traction-Separation-Law

This section is about how CZMs are treated numerically and how they are implemented in a Finite Element (FE) model.

5.1 Deriving Basic FEM Equations

The starting point to derive the FE formulation is to formulate the balance of linear momentum of the body Ω (see Fig. 1) without an interface as a global equation, add Cauchy's relation and multiply this equation with the test function $\delta \boldsymbol{u}$. All equations are written for the current configuration. In contrast to Sect. 4 the acceleration of the body is considered for the beginning. For detailed informations about the procedure we refer to Holzapfel [39], Wriggers [40] and Allix and Corigliano [41].

$$\int\limits_{\Omega} \delta \boldsymbol{u} \cdot \Big(\rho \ddot{\boldsymbol{u}} - \boldsymbol{T} \cdot \nabla\Big) \, \mathrm{d}v + \int\limits_{\partial\Omega} \delta \boldsymbol{u} \cdot \Big(\boldsymbol{T} \cdot \boldsymbol{n}_{\partial\Omega} - \boldsymbol{t}_{\partial\Omega}\Big) \, \mathrm{d}a = 0 \tag{44}$$

In the next step the interface is introduced through the split of Eq. (44) into two parts and add the variation of interface tractions to the balance of linear momentum. One part reads

$$\int\limits_{\Omega_+} \delta \boldsymbol{u} \cdot \Big(\rho \ddot{\boldsymbol{u}} - \boldsymbol{T} \cdot \nabla\Big) \, \mathrm{d}v + \int\limits_{\partial\Omega_+} \delta \boldsymbol{u} \cdot \Big(\boldsymbol{T} \cdot \boldsymbol{n}_{\partial\Omega} - \boldsymbol{t}_{\partial\Omega}\Big) \, \mathrm{d}a + \int\limits_{\Gamma_+} \delta \boldsymbol{u}_+ \cdot \boldsymbol{t}_+ \, \mathrm{d}a = 0$$

and the other one

$$\int\limits_{\Omega_-} \delta \boldsymbol{u} \cdot \Big(\rho \ddot{\boldsymbol{u}} - \boldsymbol{T} \cdot \nabla\Big) \, \mathrm{d}v + \int\limits_{\partial\Omega_-} \delta \boldsymbol{u} \cdot \Big(\boldsymbol{T} \cdot \boldsymbol{n}_{\partial\Omega} - \boldsymbol{t}_{\partial\Omega}\Big) \, \mathrm{d}a + \int\limits_{\Gamma_-} \delta \boldsymbol{u}_- \cdot \boldsymbol{t}_- \, \mathrm{d}a = 0$$

Combine these two equations, introduce a displacement jump, use the equilibrium of interface forces and neglect inertia effects yields

$$\begin{aligned} &\int\limits_{\partial\Omega} \delta \boldsymbol{u} \cdot \Big(\boldsymbol{T} \cdot \boldsymbol{n}_{\partial\Omega}\Big) \, \mathrm{d}a - \int\limits_{\Omega} \delta \boldsymbol{u} \cdot \Big(\boldsymbol{T} \cdot \nabla\Big) \, \mathrm{d}v \\ &- \int\limits_{\partial\Omega} \delta \boldsymbol{u} \cdot \boldsymbol{t}_{\partial\Omega} \, \mathrm{d}a + \int\limits_{\Gamma} \Big(\delta \boldsymbol{u}_+ - \delta \boldsymbol{u}_-\Big) \cdot \boldsymbol{t}_+ \, \mathrm{d}a = 0 \end{aligned}$$

The final form of the variation of balance of linear momentum is achieved through the transformation of the second integrand with the product rule for the divergence, Gauss' divergence theorem and a pull-back from the current into the reference configuration. Next to that is the interface traction vector replaced by the traction vector of the interface midsurface.

$$\underbrace{\underbrace{\int\limits_{\Omega} \delta \boldsymbol{E}_{\mathrm{G}} : \boldsymbol{T}_{2\mathrm{PK}} \, \mathrm{d}V}_{\delta W_{\mathrm{b}}} + \underbrace{\int\limits_{\Gamma} \delta \boldsymbol{g}_{\mathrm{i}} \cdot \boldsymbol{t}_{\mathrm{i}} \, \mathrm{d}a}_{\delta W_{\mathrm{i}}}}_{\delta W_{\mathrm{int}}} = \underbrace{\int\limits_{\partial\Omega} \delta \boldsymbol{u} \cdot \boldsymbol{t}_{\partial\Omega} \, \mathrm{d}a}_{\delta W_{\mathrm{ext}}} \tag{45}$$

In Eq. (45) $\boldsymbol{E}_{\mathrm{G}}$ represents the Green–Lagrange strain tensor and $\boldsymbol{T}_{2\mathrm{PK}}$ the second Piola–Kirchhoff stress tensor. The pull-back is not performed on the other two integrands, thus, Eq. (45) corresponds to the formulation which is used in the commercial FE software package ABAQUS [16]. In Eq. (45) it is necessary to reformulate the internal work of the interface, thus, this term is a variation of the displacement vector and not the separation vector. This yields

$$\delta W_{\mathrm{i}} = \int\limits_{\Gamma} \delta \boldsymbol{u} \cdot \frac{\partial \boldsymbol{g}_{\mathrm{i}}}{\partial \boldsymbol{u}} \cdot \boldsymbol{t}_{\mathrm{i}} \, \mathrm{d}a \tag{46}$$

Generally, a zero-thickness cohesive element is formulated without the ability to model heat conduction. We overcome this problem. In Sect. 4.3 the equation of heat conduction for a body with an interface is derived. We start with Eqs. (37)–(39) and perform the variation

$$\begin{aligned} &\int\limits_{\Omega} \delta\theta \big[\rho\lambda_{\mathrm{b}}\dot{\theta} - \rho r - W_{\mathrm{b,ext}} + W_{\mathrm{b,int}}\big] \, \mathrm{d}v - \int\limits_{\partial\Omega} \delta\theta q_{\mathrm{b}} \, \mathrm{d}a \\ &+ \int\limits_{\Gamma} \delta\theta \big[\lambda_{\mathrm{i}}\dot{\theta} + q_{\mathrm{i}} - W_{\mathrm{i,ext}} + W_{\mathrm{i,int}}\big] \, \mathrm{d}a \\ &+ \int\limits_{\partial\Omega} \delta\theta \big[q_{\mathrm{b}} + \boldsymbol{n}_{\partial\Omega} \cdot \boldsymbol{q}_{\mathrm{b}}\big] \, \mathrm{d}a = 0 \end{aligned}$$

Internal heat production is neglected and with the product rule of divergence it follows

$$\begin{aligned} &\underbrace{\int\limits_{\Omega} \delta\theta \big[\rho\lambda_{\mathrm{b}}\dot{\theta} - W_{\mathrm{b,ext}} + W_{\mathrm{b,int}}\big] + \kappa_{\mathrm{b}} \left(\nabla\theta\right) \cdot \left(\nabla\delta\theta\right) \mathrm{d}v}_{\delta H_{\mathrm{b}}} \\ &+ \underbrace{\int\limits_{\Gamma} \delta\theta \big[\lambda_{\mathrm{i}}\dot{\theta} + q_{\mathrm{i}} - W_{\mathrm{i,ext}} + W_{\mathrm{i,int}}\big] \, \mathrm{d}a}_{\delta H_{\mathrm{i}}} = \underbrace{\int\limits_{\partial\Omega} \delta\theta q_{\mathrm{b}} \, \mathrm{d}a}_{\delta H_{\mathrm{ext}}} \end{aligned} \tag{47}$$

The short form of Eq. (47) is

$$\delta H_{\mathrm{int}} = \delta H_{\mathrm{b}} + \delta H_{\mathrm{i}} = \delta H_{\mathrm{ext}}$$

5.2 Discretisation of the Variational Statements of the Interface

In a cohesive element all quantities are referred to a midsurface (see Fig. 2), to determine the position of this midsurface in the current configuration the average position of the positive (Γ_+) and the negative (Γ_-) surface is calculated

$$\bar{\boldsymbol{x}} = \frac{1}{2}\left(\boldsymbol{x}_+ + \boldsymbol{x}_-\right) \tag{48}$$

From Eq. (48) the local coordinate system ($\boldsymbol{e}_{\mathrm{t}_1}, \boldsymbol{e}_{\mathrm{t}_2}, \boldsymbol{e}_{\mathrm{n}}$) of the cohesive element is determined. At first, the two tangential directions of the midsurface are determined through the calculation of the derivatives of the midsurface with respect to the curvilinear coordinates ζ_1 and ζ_2

$$\boldsymbol{z}_1 = \frac{\partial \bar{\boldsymbol{x}}}{\partial \zeta_1}\,, \qquad \boldsymbol{z}_2^* = \frac{\partial \bar{\boldsymbol{x}}}{\partial \zeta_2}$$

With the cross product between these two vectors the normal vector $\boldsymbol{z}_3$ is determined

$$\boldsymbol{z}_3 = \boldsymbol{z}_1 \times \boldsymbol{z}_2^*$$

In a general curvilinear coordinate system the two tangential vectors $\boldsymbol{z}_1$ and $\boldsymbol{z}_2^*$ must not be perpendicular to each other, to overcome this a new tangential vector $\boldsymbol{z}_2$ is determined

$$\boldsymbol{z}_2 = \boldsymbol{z}_3 \times \boldsymbol{z}_1$$

Finally, this set of vectors is normalised to form the base of the local coordinate system

$$\boldsymbol{e}_\alpha = \frac{\boldsymbol{z}_\alpha}{|\boldsymbol{z}_\alpha|} \qquad \forall \quad \alpha \in \{1, 2, 3\} \tag{49}$$

The area of the midsurface in the current configuration is determined as the norm of the normal vector

$$\mathrm{d}a = |\boldsymbol{z}_3|\,\mathrm{d}\zeta_1 \mathrm{d}\zeta_2 \tag{50}$$

TSLs for a cohesive element are formulated in the local coordinate system because of this fact it is necessary to transform all global quantities of the problem into the local coordinate system. This is done by a orthogonal rotation tensor which is defined as follows for one node.

$$\boldsymbol{R} = \begin{bmatrix} \boldsymbol{e}_3 \\ \boldsymbol{e}_1 \\ \boldsymbol{e}_2 \end{bmatrix} \tag{51}$$

The continues variables displacement, node coordinates and temperature are approximated by discrete nodal values through the use of shape functions, which order depends on the choice of element type. Therefore, we do this in general and do not specify the sizes

$$\begin{aligned}
\boldsymbol{u} &\approx \tilde{\boldsymbol{u}} = \boldsymbol{N} \cdot \boldsymbol{u}^{\mathrm{e}}\,, \\
\delta\boldsymbol{u} &\approx \delta\tilde{\boldsymbol{u}} = \boldsymbol{N} \cdot \delta\boldsymbol{u}^{\mathrm{e}}\,, \\
\boldsymbol{x} &\approx \tilde{\boldsymbol{x}} = \boldsymbol{N} \cdot \boldsymbol{x}^{\mathrm{e}}\,, \\
\boldsymbol{x}_0 &\approx \tilde{\boldsymbol{x}}_0 = \boldsymbol{N} \cdot \boldsymbol{x}_0^{\mathrm{e}}\,, \\
\theta &\approx \tilde{\theta} = \boldsymbol{N} \cdot \boldsymbol{\theta}^{\mathrm{e}}\,, \\
\delta\theta &\approx \delta\tilde{\theta} = \boldsymbol{N} \cdot \delta\boldsymbol{\theta}^{\mathrm{e}}
\end{aligned} \tag{52}$$

The upper index $(\cdot)^{\mathrm{e}}$ at the vectors $\boldsymbol{u}$, $\boldsymbol{x}$ and $\boldsymbol{\theta}$ is introduced to denote this variable as a discrete element variable and tilde over a variable $\tilde{(\cdot)}$ denotes the approximated variable of the problem.

Up next, it is necessary to approximate the separation vector $\boldsymbol{g}_{\mathrm{i}}$. At first, the global displacement vector is rotated from the global into the local coordinate system with a rotation tensor $\boldsymbol{Q}$. This rotation tensor depends on $\boldsymbol{R}$. Further on, a separation-displacement-relation tensor $\boldsymbol{L}_{\mathrm{u}}$ is introduced which subtract the displacement values of nodes which are placed on opposite surfaces. It follows the approximated separation vector as

$$\tilde{\boldsymbol{g}}_{\mathrm{i}} = \boldsymbol{N}_{\mathrm{u}} \cdot \boldsymbol{L}_{\mathrm{u}} \cdot \boldsymbol{Q} \cdot \boldsymbol{u}^{\mathrm{e}} = \boldsymbol{Z}_{\mathrm{lin}} \cdot \boldsymbol{u}^{\mathrm{e}}\,, \quad \boldsymbol{Z}_{\mathrm{lin}} = \boldsymbol{N}_{\mathrm{u}} \cdot \boldsymbol{L}_{\mathrm{u}} \cdot \boldsymbol{Q} \tag{53}$$

The differentiation with respect to the displacement vector from Eq. (53) yields

$$\frac{\partial \tilde{\boldsymbol{g}}_{\mathrm{i}}}{\partial \boldsymbol{u}^{\mathrm{e}}} = \boldsymbol{Z} = \boldsymbol{Z}_{\mathrm{lin}} + \boldsymbol{Z}_{\mathrm{nl}} \cdot \boldsymbol{u}^{\mathrm{e}}\,, \quad \boldsymbol{Z}_{\mathrm{nl}} = \boldsymbol{N}_{\mathrm{u}} \cdot \boldsymbol{L}_{\mathrm{u}} \cdot \frac{\partial \boldsymbol{Q}}{\partial \boldsymbol{u}^{\mathrm{e}}} \tag{54}$$

The second term is usually neglected but we want to present the full formulation of the principle of virtual work for a cohesive element. The approximated midsurface is determined through the introduction of a second relation tensor $\boldsymbol{M}_{\mathrm{u}}$. It yields

$$\tilde{\bar{\boldsymbol{x}}} = \frac{1}{2}\boldsymbol{N}_{\mathrm{u}} \cdot \boldsymbol{M}_{\mathrm{u}} \cdot \left(\boldsymbol{x}_0^{\mathrm{e}} + \boldsymbol{u}^{\mathrm{e}}\right) = \boldsymbol{X}_{\mathrm{u}} \cdot \left(\boldsymbol{x}_0^{\mathrm{e}} + \boldsymbol{u}^{\mathrm{e}}\right) \quad \text{with} \quad \boldsymbol{X}_{\mathrm{u}} = \frac{1}{2}\boldsymbol{N}_{\mathrm{u}} \cdot \boldsymbol{M}_{\mathrm{u}} \tag{55}$$

The derivatives of Eq. (55) with respect to the natural element coordinates (ξ_1, ξ_2) lead to the approximated tangential vectors for the local coordinate system

$$\begin{aligned} \tilde{z}_1 &= \frac{\partial \tilde{\bar{\boldsymbol{x}}}}{\partial \xi_1} = \frac{1}{2}\boldsymbol{B}_1 \cdot \boldsymbol{M}_\mathrm{u} \cdot \left(\boldsymbol{x}_0^\mathrm{e} + \boldsymbol{u}^\mathrm{e}\right) \,, \quad \boldsymbol{B}_1 = \frac{\partial \boldsymbol{N}_\mathrm{u}}{\partial \xi_1} \\ \tilde{z}_2^* &= \frac{\partial \tilde{\bar{\boldsymbol{x}}}}{\partial \xi_2} = \frac{1}{2}\boldsymbol{B}_2 \cdot \boldsymbol{M}_\mathrm{u} \cdot \left(\boldsymbol{x}_0^\mathrm{e} + \boldsymbol{u}^\mathrm{e}\right) \,, \quad \boldsymbol{B}_2 = \frac{\partial \boldsymbol{N}_\mathrm{u}}{\partial \xi_2} \end{aligned} \tag{56}$$

and the cross product leads to the approximated normal vector

$$\tilde{z}_3 = \tilde{z}_1 \times \tilde{z}_2^* \tag{57}$$

Again, to ensure that all vectors are perpendicular to each other the second tangential vector is redetermined

$$\tilde{z}_2 = \tilde{z}_3 \times \tilde{z}_1$$

Now, all quantities are approximated, thus, Eq. (46) yields

$$\delta W_\mathrm{i} = \delta \boldsymbol{u}^\mathrm{e} \cdot \int_\Gamma \boldsymbol{Z}^\top \cdot \boldsymbol{t}_\mathrm{i} \, |\tilde{z}_3| \;\, \mathrm{d}\xi_1 \mathrm{d}\xi_2 = \delta \boldsymbol{u}^\mathrm{e} \cdot \boldsymbol{r}_{\mathrm{i,u}}^\mathrm{e} \tag{58}$$

The discretisation of δH_i from Eq. (47) leads to the thermal part for the interface

$$\begin{aligned} \delta H_\mathrm{i} = \delta \boldsymbol{\theta}^\mathrm{e} \cdot \int_\Gamma \boldsymbol{X}_\theta^\top \cdot \Bigg[& \lambda_\mathrm{i} \boldsymbol{N}_\theta \cdot \dot{\boldsymbol{\theta}}^\mathrm{e} + \kappa_\mathrm{i} \boldsymbol{N}_\theta \cdot \boldsymbol{L}_\theta \cdot \boldsymbol{\theta}^\mathrm{e} - \boldsymbol{X}_\theta \cdot \boldsymbol{\theta}^\mathrm{e} \left[\frac{\partial \boldsymbol{t}_\mathrm{i}}{\partial \theta} \cdot \dot{\boldsymbol{g}}_\mathrm{i} \right] \\ & + \boldsymbol{X}_\theta \cdot \boldsymbol{\theta}^\mathrm{e} \left[\frac{\partial Y_\mathrm{E}}{\partial \theta} + \frac{\partial \boldsymbol{t}_\mathrm{i}}{\partial \theta} \cdot \dot{\boldsymbol{g}}_\mathrm{in} \right] - Y_\mathrm{E} \dot{d} - \boldsymbol{t}_\mathrm{i} \cdot \dot{\boldsymbol{g}}_\mathrm{in} \Bigg] |\tilde{z}_3| \;\, \mathrm{d}\xi_1 \mathrm{d}\xi_2 \\ = \delta \boldsymbol{\theta}^\mathrm{e} \cdot \boldsymbol{r}_{\mathrm{i},\theta}^\mathrm{e} \quad & \text{with} \quad \boldsymbol{X}_\theta = \frac{1}{2} \boldsymbol{N}_\theta \cdot \boldsymbol{M}_\theta \end{aligned} \tag{59}$$

Equations (58) and (59) are arranged in a global residual vector for the interface which is varied with the global degrees of freedom (*DOF*) vector.

$$\delta P_\mathrm{i} = \delta \boldsymbol{p}^\mathrm{e} \cdot \boldsymbol{r}_\mathrm{i}^\mathrm{e} \tag{60}$$

This is the starting point to derive the stiffness tensor of the interface $\boldsymbol{K}_\mathrm{i}$ for the thermo-mechanical problem which is explained in detail in the subsequent section.

5.3 Deriving the Cohesive Element Stiffness Matrix

The stiffness tensor of the cohesive element is one part of the varied global residual vector $\boldsymbol{r}$ of the whole problem with respect to the global *DOF* vector

$$\delta P = \delta \boldsymbol{p}^\mathrm{e} \cdot \boldsymbol{r}^\mathrm{e}$$

The global residual vector is additively composed of a bulk and an interface portion. This residual vector follows from the statement that the global test function ($\delta \boldsymbol{p}^{\mathrm{e}}$) is arbitrary and non-zero, hence, the residual vector should be zero

$$\boldsymbol{r}^{\mathrm{e}} = \boldsymbol{r}^{\mathrm{e}}_{\mathrm{b}} + \boldsymbol{r}^{\mathrm{e}}_{\mathrm{i}} = \boldsymbol{o}$$

The derivation of the interface residual vector is explained in the foregoing sections and for the bulk portion we skip this derivation because later on for this portion a standard ABAQUS model is used. However, the residual vector of the bulk portion consists of a displacement and a temperature part, as well. The solution is obtained by performing the linearisation of the residual vector what leads to

$$\tilde{\boldsymbol{r}}^{\mathrm{e}} \approx \boldsymbol{r}^{\mathrm{e}} + \underbrace{\left(\boldsymbol{K}^{\mathrm{e}}_{\mathrm{b}} + \boldsymbol{K}^{\mathrm{e}}_{\mathrm{i}}\right)}_{\boldsymbol{K}^{\mathrm{e}}} \cdot \Delta \boldsymbol{p}^{\mathrm{e}} = \boldsymbol{o}\,, \quad \boldsymbol{K}^{\mathrm{e}}_{\mathrm{b}} = \frac{\partial \boldsymbol{r}^{\mathrm{e}}_{\mathrm{b}}}{\partial \boldsymbol{p}^{\mathrm{e}}}\,, \quad \boldsymbol{K}^{\mathrm{e}}_{\mathrm{i}} = \frac{\partial \boldsymbol{r}^{\mathrm{e}}_{\mathrm{i}}}{\partial \boldsymbol{p}^{\mathrm{e}}} \tag{61}$$

with $\boldsymbol{K}^{\mathrm{e}}_{\mathrm{i}}$ as the stiffness tensor of the interface, $\boldsymbol{K}^{\mathrm{e}}_{\mathrm{b}}$ as the stiffness tensor of the bulk material and $\boldsymbol{K}^{\mathrm{e}}$ as the stiffness tensor of the whole problem. The global stiffness tensor consists of four sub-parts and consequently the bulk and interface stiffness tensors, as well. The structure of the global stiffness tensor is

$$\boldsymbol{K}^{\mathrm{e}} = \begin{bmatrix} \boldsymbol{K}^{\mathrm{e}}_{\mathrm{b,uu}} & \boldsymbol{K}^{\mathrm{e}}_{\mathrm{b,u\theta}} \\ \boldsymbol{K}^{\mathrm{e}}_{\mathrm{b,\theta u}} & \boldsymbol{K}^{\mathrm{e}}_{\mathrm{b,\theta\theta}} \end{bmatrix} + \begin{bmatrix} \boldsymbol{K}^{\mathrm{e}}_{\mathrm{i,uu}} & \boldsymbol{K}^{\mathrm{e}}_{\mathrm{i,u\theta}} \\ \boldsymbol{K}^{\mathrm{e}}_{\mathrm{i,\theta u}} & \boldsymbol{K}^{\mathrm{e}}_{\mathrm{i,\theta\theta}} \end{bmatrix}$$

To simplify this highly non-linear problem it is assumed that the coupling between the mechanical and thermal problem is weak, hence, all sub-tensors are zero

$$\boldsymbol{K}^{\mathrm{e}}_{\mathrm{b,u\theta}} = \boldsymbol{K}^{\mathrm{e}}_{\mathrm{b,\theta}u} = \boldsymbol{K}^{\mathrm{e}}_{\mathrm{i,u\theta}} = \boldsymbol{K}^{\mathrm{e}}_{\mathrm{i,\theta}u} = \boldsymbol{0}$$

It remains

$$\boldsymbol{K}^{\mathrm{e}} = \begin{bmatrix} \boldsymbol{K}^{\mathrm{e}}_{\mathrm{b,uu}} & \boldsymbol{0} \\ \boldsymbol{0} & \boldsymbol{K}^{\mathrm{e}}_{\mathrm{b,\theta\theta}} \end{bmatrix} + \begin{bmatrix} \boldsymbol{K}^{\mathrm{e}}_{\mathrm{i,uu}} & \boldsymbol{0} \\ \boldsymbol{0} & \boldsymbol{K}^{\mathrm{e}}_{\mathrm{i,\theta\theta}} \end{bmatrix}$$

Now, it is usually possibly to solve the mechanical and thermal problem separately. Here, this is not the case because damage evolution in the interface influences the heat conduction through the interface. Thus, the problems must be solved and integrated in time together.

At last, for finite element implementation it is necessary to determine the sub-tensors $\boldsymbol{K}^{\mathrm{e}}_{\mathrm{i,uu}}$ and $\boldsymbol{K}^{\mathrm{e}}_{\mathrm{i,\theta\theta}}$ which represent the derivatives of the displacement and thermal part of the interface residual vector with respect to the displacement and temperature *DOF*, respectively. We begin with the displacement part. This stiffness tensor is very complex because all quantities inside the integral depend on the displacement vector. Only the second derivative of the rotation tensor $\boldsymbol{Q}$ with respect to the displacement vector is neglected because this tensor depends linearly on the displacement vector

$$\boldsymbol{K}^{\mathrm{e}}_{\mathrm{i,uu}} = \frac{\partial \boldsymbol{r}^{\mathrm{e}}_{\mathrm{i,u}}}{\partial \boldsymbol{u}^{\mathrm{e}}} = \int\limits_{\Gamma} 2\, \boldsymbol{Z}^{\top}_{\mathrm{nl}} \cdot \boldsymbol{t}_{\mathrm{i}}\, |\tilde{z}_3| + \boldsymbol{Z}^{\top} \cdot \boldsymbol{C}_{\mathrm{i}} \cdot \boldsymbol{Z}\, |\tilde{z}_3| + \boldsymbol{Z}^{\top} \cdot \boldsymbol{t}_{\mathrm{i}} \cdot \frac{\partial\, |\tilde{z}_3|}{\partial \boldsymbol{u}^{\mathrm{e}}}\, \mathrm{d}\xi_1 \mathrm{d}\xi_2$$

The variable $\boldsymbol{C}_{\mathrm{i}}$ represents the material tangent stiffness tensor of the cohesive element and is defined as

$$\boldsymbol{C}_{\mathrm{i}} = \frac{\partial \boldsymbol{t}_{\mathrm{i}}}{\partial \tilde{\boldsymbol{g}}_{\mathrm{i}}}$$

The assumption that the separation is small leads to the common formulation of the stiffness tensor for a cohesive element

$$\boldsymbol{K}^{\mathrm{e}}_{\mathrm{i,uu}} = \int\limits_{\Gamma} \boldsymbol{Z}^{\top}_{\mathrm{lin}} \cdot \boldsymbol{C}_{\mathrm{i}} \cdot \boldsymbol{Z}_{\mathrm{lin}}\, |\tilde{z}_3|\;\, \mathrm{d}\xi_1 \mathrm{d}\xi_2 \tag{62}$$

and the residual vector

$$\boldsymbol{r}^{\mathrm{e}}_{\mathrm{i,u}} = \int\limits_{\Gamma} \boldsymbol{Z}^{\top}_{\mathrm{lin}} \cdot \boldsymbol{t}_{\mathrm{i}}\, |\tilde{z}_3|\;\, \mathrm{d}\xi_1 \mathrm{d}\xi_2 \tag{63}$$

which are used in commercial FE software (ABAQUS, ANSYS, ...), as well. The thermal part follows from Eq. (59). But before, we neglect internal and external work contributions and introduce a heat capacity tensor $\boldsymbol{C}_{\lambda}$ and a heat conduction tensor $\boldsymbol{C}_{\kappa}$. With this Eq. (59) is rearranged to

$$\begin{aligned} \delta H_{\mathrm{i}} &= \delta \boldsymbol{\theta}^{\mathrm{e}} \cdot \int\limits_{\Gamma} \left[\boldsymbol{C}_{\lambda} \cdot \dot{\boldsymbol{\theta}}^{\mathrm{e}} + \boldsymbol{C}_{\kappa} \cdot \boldsymbol{\theta}^{\mathrm{e}} \right] |\tilde{z}_3|\;\, \mathrm{d}\xi_1 \mathrm{d}\xi_2 = \delta \boldsymbol{\theta}^{\mathrm{e}} \cdot \boldsymbol{r}^{\mathrm{e}}_{\mathrm{i},\theta} \\ \boldsymbol{C}_{\lambda} &= \lambda_{\mathrm{i}} \boldsymbol{X}^{\top}_{\theta} \cdot \boldsymbol{X}_{\theta}\,, \quad \boldsymbol{C}_{\kappa} = \kappa_{\mathrm{i}} \boldsymbol{X}^{\top}_{\theta} \cdot \boldsymbol{N}_{\theta} \cdot \boldsymbol{L}_{\theta} \end{aligned} \tag{64}$$

With the approximation of the temperature rate vector by the backward Euler scheme it follows the thermal part for the interface stiffness tensor with the time increment Δt

$$\boldsymbol{K}^{\mathrm{e}}_{\mathrm{i},\theta\theta} = \frac{\partial \boldsymbol{r}^{\mathrm{e}}_{\mathrm{i},\theta}}{\partial \boldsymbol{\theta}^{\mathrm{e}}} = \int\limits_{\Gamma} \left[\frac{\partial \boldsymbol{C}_{\lambda}}{\partial \boldsymbol{\theta}^{\mathrm{e}}} \cdot \dot{\boldsymbol{\theta}}^{\mathrm{e}} + \frac{1}{\Delta t} \boldsymbol{C}_{\lambda} + \frac{\partial \boldsymbol{C}_{\kappa}}{\partial \boldsymbol{\theta}^{\mathrm{e}}} \cdot \boldsymbol{\theta}^{\mathrm{e}} + \boldsymbol{C}_{\kappa} \right] |\tilde{z}_3|\;\, \mathrm{d}\xi_1 \mathrm{d}\xi_2$$

The influence of the temperature derivatives of heat capacity and heat conduction tensor are usually benign and are neglected due to this fact [42]. It results the final form

$$\boldsymbol{K}^{\mathrm{e}}_{\mathrm{i},\theta\theta} = \int\limits_{\Gamma} \left[\frac{1}{\Delta t} \boldsymbol{C}_{\lambda} + \boldsymbol{C}_{\kappa} \right] |\tilde{z}_3|\;\, \mathrm{d}\xi_1 \mathrm{d}\xi_2 \tag{65}$$

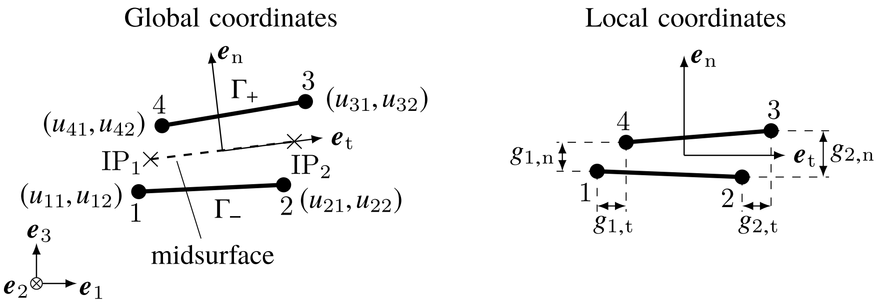

Fig. 5 2D linear cohesive element with global and local quantities after [43]; and position of integration points for Newton–Cotes integration

with the corresponding residual vector

$$\boldsymbol{r}^{\mathrm{e}}_{\mathrm{i},\theta} = \int_{\Gamma} \left[\boldsymbol{C}_{\lambda} \cdot \dot{\boldsymbol{\theta}}^{\mathrm{e}} + \boldsymbol{C}_{\kappa} \cdot \boldsymbol{\theta}^{\mathrm{e}} \right] |\tilde{z}_3| \; \mathrm{d}\xi_1 \mathrm{d}\xi_2 \tag{66}$$

5.4 2D Cohesive Element Formulation

In this section we present the formulation of a 2D cohesive element with four nodes. All equations are written down in a vector-matrix notation. The element is then used in the simulation which is presented in Sect. 5. Further on, we introduce the abbreviation *NN* for number of nodes.

At first, a node numbering scheme is required. We use the scheme of ABAQUS, hence, we number the corner nodes first and then the middle nodes, if they exist. The numbering begins in the lower left corner and ends in the upper left corner rotating counter clockwise. Every node has three *DOF*, two displacement *DOF* and one temperature *DOF*. This results in a number of twelve *DOF* for the four node element in the fully coupled thermo-mechanical case. The arranging of the vectors and matrices can be seen in the Appendix and the element is presented in Fig. 5.

In the three-dimensional case the cohesive zone is represented by a zero-thickness surface which reduces in the two-dimensional case to a line. Hence, it remains only the element coordinate ξ_1 and the stiffness matrix of the displacement part follows as

$$\mathbf{K}^{\mathrm{e}}_{\mathrm{i,uu}} = b \int_{-1}^{1} \mathbf{Z}^{\top}_{\mathrm{lin}} \cdot \mathbf{C}_{\mathrm{i}} \cdot \mathbf{Z}_{\mathrm{lin}} \left| \tilde{\mathbf{z}}_3 \right| \; \mathrm{d}\xi_1 \, , \quad \mathbf{Z}_{\mathrm{lin}} = \mathbf{N}_{\mathrm{u}} \cdot \mathbf{L}_{\mathrm{u}} \cdot \mathbf{Q} \tag{67}$$

and the residual vector to

$$\mathbf{r}^{\mathrm{e}}_{\mathrm{i,u}} = b\int_{-1}^{1} \mathbf{Z}^{\top}_{\mathrm{lin}} \cdot \mathbf{t}_{\mathrm{i}} \left|\tilde{\mathbf{z}}_3\right| \,\mathrm{d}\xi_1 \tag{68}$$

with the element width b. The thermal part gives the following stiffness matrix

$$\mathbf{K}^{\mathrm{e}}_{\mathrm{i},\theta\theta} = b\int_{-1}^{1} \left[\frac{1}{\Delta t}\mathbf{C}_{\lambda} + \mathbf{C}_{\kappa}\right] \left|\tilde{\mathbf{z}}_3\right| \,\mathrm{d}\xi_1 \tag{69}$$

$$\mathbf{C}_{\lambda} = \lambda_{\mathrm{i}}\mathbf{X}^{\top}_{\theta} \cdot \mathbf{X}_{\theta}\,, \quad \mathbf{C}_{\kappa} = \kappa_{\mathrm{i}}\mathbf{X}^{\top}_{\theta} \cdot \mathbf{N}_{\theta} \cdot \mathbf{L}_{\theta}\,, \quad \mathbf{X}_{\theta} = \frac{1}{2}\mathbf{N}_{\theta} \cdot \mathbf{M}_{\theta}$$

with the residual vector

$$\mathbf{r}^{\mathrm{e}}_{\mathrm{i},\theta} = b\int_{-1}^{1} \left[\mathbf{C}_{\lambda} \cdot \dot{\boldsymbol{\theta}}^{\mathrm{e}} + \mathbf{C}_{\kappa} \cdot \boldsymbol{\theta}^{\mathrm{e}}\right] \left|\tilde{\mathbf{z}}_3\right| \,\mathrm{d}\xi_1 \tag{70}$$

5.5 *Algorithm to Solve the Novel Traction-Separation-Law*

The solution of the TSL is obtained by applying the backward Euler scheme to the equations and obtain the solution through a Newton–Raphson procedure. At first, it is assumed that the influence of the derivatives with respect to the temperature is slight and can by neglected. With this the equations simplify to

$$\mathbf{t}_{\mathrm{i}} = (1-d)^{p}\, \mathbf{C}_{\mathrm{TSL}} \cdot \mathbf{g}_{\mathrm{el}}\,, \tag{71}$$

$$\mathbf{g}_{\mathrm{el}} = \mathbf{g}_{\mathrm{i}} - \mathbf{g}_{\mathrm{in}}\,, \tag{72}$$

$$\dot{\mathbf{g}}_{\mathrm{in}} = \frac{a}{(1-d)^{N_1}} \left[\frac{|\mathbf{t}_{\mathrm{i}}|}{T_0}\right]^{N_2} \frac{\mathbf{t}_{\mathrm{i}}}{|\mathbf{t}_{\mathrm{i}}|}\,, \tag{73}$$

$$Y_{\mathrm{E}} = \frac{p}{2}\,(1-d)^{p-1}\, \mathbf{g}_{\mathrm{el}} \cdot \mathbf{C}_{\mathrm{TSL}} \cdot \mathbf{g}_{\mathrm{el}}\,, \tag{74}$$

$$\dot{d} = (1-d)^{s_1} \left(\frac{Y_{\mathrm{E}}}{S_0}\right)^{s_2} \frac{|\dot{\mathbf{g}}_{\mathrm{in}}|}{g_{\mathrm{dim}}}\,, \tag{75}$$

$$\lambda_{\mathrm{i}} = C_{\lambda 1}\theta + C_{\lambda 2} \tag{76}$$

in vector-matrix form. Up next, the backward Euler scheme is applied to discretise the equations and then we arrange these equations in a residual vector. For a more compact notation we introduce the following abbreviations and normalise the separation $\boldsymbol{g}_{\mathrm{i}}$ with the parameter $g_{\mathrm{dim}} = 1$ mm and get a strain $\boldsymbol{e}_{\mathrm{i}}$ which has the magnitude of the separation (see e.g. [16]).

$$c_1 = \Delta t \frac{a}{\left(1 - d_{j+1}\right)^{N_1} |\mathbf{t}_{\mathrm{i},j+1}| \, g_{\mathrm{dim}}} \left[\frac{|\mathbf{t}_{\mathrm{i},j+1}|}{T_0} \right]^{N_2} ,$$

$$c_2 = \left(1 - d_{j+1}\right)^{s_1} \left[\frac{Y_{\mathrm{E},j+1}}{S_0} \right]^{s_2} ,$$

$$\mathbf{c}_1 = \mathbf{e}_{\mathrm{i},j+1} - \mathbf{e}_{\mathrm{in},j+1} ,$$

$$\mathbf{c}_2 = \mathbf{e}_{\mathrm{in},j+1} - \mathbf{e}_{\mathrm{in},j} ,$$

$$\mathbf{C}_1 = \mathbf{1} + \frac{(N_2 - 1)}{|\mathbf{t}_{\mathrm{i},j+1}|^2} \mathbf{t}_{\mathrm{i},j+1} \cdot \mathbf{t}^{\top}_{\mathrm{i},j+1}$$

Notice that through the matrix $\mathbf{C}_1$ a coupling between normal and tangential separation occurs, hence, mix-mode occurs when $N_2 > 1$. It is a result of the creep behaviour. This coupling can be avoided by assume that the interface behaves linear visco-elastic ($N_2 = 1$), see [44]. Additionally, from this follows that the constitutive matrix of the cohesive zone $\mathbf{C}_{\mathrm{TSL}}$ (see Appendix) has a diagonal structure only for the beginning, so long no inelastic separation occurs. The traction part of the residual vector is

$$\mathbf{r}_{\mathrm{t}} = \frac{1}{\left(1 - d_{j+1}\right)^{p}} \mathbf{C}^{-1}_{\mathrm{TSL}} \cdot \mathbf{t}_{\mathrm{i},j+1} - \mathbf{e}_{\mathrm{i},j+1} + \mathbf{e}_{\mathrm{i},j} + c_1 \mathbf{t}_{\mathrm{i},j+1} = \mathbf{o} \qquad (77)$$

and the damage part yields

$$r_{\mathrm{d}} = d_{j+1} - d_j - c_2 |\mathbf{c}_2| = 0 \qquad (78)$$

These parts form the residual vector $\mathbf{r}_{\mathrm{TSL}}$ which is linearised

$$\mathbf{r}_{\mathrm{TSL}} \approx \mathbf{r}^k_{\mathrm{TSL}} + \frac{\partial \mathbf{r}^k_{\mathrm{TSL}}}{\partial \mathbf{y}^k_{j+1}} \cdot \Delta \mathbf{y}^k_{j+1} = \mathbf{r}^k_{\mathrm{TSL}} + \mathbf{J}^k_{j+1} \cdot \Delta \mathbf{y}^k_{j+1} = \mathbf{o} \qquad (79)$$

and the resulting system of equations is solved by applying the common Newton–Raphson procedure with iteration index k

$$\Delta \mathbf{y}^k_{j+1} = - \left[\mathbf{J}^k_{j+1} \right]^{-1} \cdot \mathbf{r}^k_{\mathrm{TSL}} \qquad (80)$$

Followed is this by the update of the unknown vector $\mathbf{y}$ for the next iteration until the residual reaches a user specified tolerance

$$\mathbf{y}^{k+1}_{j+1} = \mathbf{y}^k_{j+1} + \Delta \mathbf{y}^k_{j+1} \qquad (81)$$

The Jacobian matrix consists of four sub-matrices which are

$$\mathbf{J}_{11} = \frac{\partial \mathbf{r}_{\mathrm{t}}}{\partial \mathbf{t}_{\mathrm{i},j+1}} = \frac{1}{\left(1-d_{j+1}\right)^{p}} \mathbf{C}_{\mathrm{TSL}}^{-1} + c_1 \mathbf{C}_1$$

$$\mathbf{J}_{12} = \frac{\partial \mathbf{r}_{\mathrm{t}}}{\partial d_{j+1}} = \left[\frac{p}{\left(1-d_{j+1}\right)^{p+1}} \mathbf{C}_{\mathrm{TSL}}^{-1} + \frac{c_1}{\left(1-d_{j+1}\right)} \mathbf{1} \right] \cdot \mathbf{t}_{\mathrm{i},j+1}$$

$$\mathbf{J}_{21} = \frac{\partial r_{\mathrm{d}}}{\partial \mathbf{t}_{\mathrm{i},j+1}} = c_1 c_2 \left[\frac{p s_2 S_0 \left(1-d_{j+1}\right)^{p-1} |\mathbf{c}_2|}{Y_{\mathrm{E},j+1}} \mathbf{c}_1^{\top} \cdot \mathbf{C}_{\mathrm{TSL}} - \frac{1}{|\mathbf{c}_2|} \mathbf{c}_2^{\top} \right] \cdot \mathbf{C}_1$$

and

$$\mathbf{J}_{22} = \frac{\partial r_{\mathrm{d}}}{\partial d_{j+1}} = 1 - \frac{c_1 |\mathbf{c}_2|}{\left(1-d_{j+1}\right)} \left[\frac{c_1 N_1}{|\mathbf{c}_2|^2} \mathbf{c}_2^{\top} \cdot \mathbf{t}_{\mathrm{i},j+1} \right.$$
$$\left. + s_1 p \left(1-d_{j+1}\right)^{p-2} \mathbf{c}_1^{\top} \cdot \mathbf{C}_{\mathrm{TSL}} \cdot \left[\frac{p-1}{2} \mathbf{c}_1 + c_1 N_1 \mathbf{t}_{\mathrm{i},j+1} \right] \right]$$

which are aligned as followed

$$\mathbf{J}_{j+1}^{k} = \begin{bmatrix} \mathbf{J}_{11} & \mathbf{J}_{12} \\ \mathbf{J}_{21} & \mathbf{J}_{22} \end{bmatrix}$$

After the successful solution the inelastic separation and the elastic energy release rate for the next time increment are recalculated

$$\mathbf{e}_{\mathrm{in},j+1} = \mathbf{e}_{\mathrm{in},j} + c_1 \mathbf{t}_{\mathrm{i},j+1} \tag{82}$$

$$Y_{\mathrm{E},j+1} = \frac{p}{2} \left(1-d_{j+1}\right)^{p-1} \mathbf{c}_1^{\top} \cdot \mathbf{C}_{\mathrm{TSL}} \cdot \mathbf{c}_1 \tag{83}$$

Because of this implementation of the TSL the material tangent stiffness matrix for the element stiffness matrix follows from the inversion of $\mathbf{J}_{11}$ (see [40] for more details)

$$\mathbf{C}_{\mathrm{i}} = \mathbf{J}_{11}^{-1} \tag{84}$$

5.6 Numerical Problems Arising Through the Use of Cohesive Elements

The simulation of crack propagation along a predefined path by using cohesive elements leads to two main problems. First, the numerical solution scheme gets unstable due to strain localisation resulting from a softening behaviour [30, 45] and second, spurious traction oscillations occur orthogonal to the crack propagation direction because of a high cohesive zone stiffness [46–49].

At first, we comment on the unstable solution scheme and then the latter problem. To stabilise the solution scheme, which is usually the Newton–Raphson procedure, an additional damping term is added to the quasi-static residual vector. This additional term consumes the released energy due to crack propagation and leads to a finite separation between the interface surfaces. This is called viscous regularisation and is common for many unstable analysis [30, 50]. The problem with viscous regularisation is that the user has to make an initial guess for the damping factor because, if the damping factor is too high no deformation will take place because all energy is consumed. In contrast to that, if the damping factor is too low the procedure will not converge. Hence, to find a proper damping factor a trial and error procedure is applied. Another possibility is to use other solution schemes like the Riks method. But other numerical solutions scheme suffer from the problem that they do not converge quadratically and are more complex, as the Newton–Raphson procedure, which leads in the end to higher calculation times. The user has to decide, if it is worth it to use another solution scheme, or start a trial and error procedure to find a suitable damping factor.

Now, the latter mentioned problem is discussed, the spurious traction oscillations. Many author mentioned and investigated these oscillations and found out that these oscillations result from the high stiffness of the cohesive zone which is necessary to ensure that the cohesive zone is not present in the virgin body until the crack starts to propagate. The occurrence of these oscillations can be influenced by the numerical integration scheme for the element stiffness matrix. Usually, full Gauss integration is used to evaluate the stiffness matrix, which results in a stiffness matrix with the following structure in the local coordinate system for a four node plane element with two displacement *DOF*

$$\mathbf{K}^{\mathrm{e}}_{\mathrm{i,uu}} = \frac{1}{3}\begin{bmatrix} 2\mathbf{C}_{\mathrm{i}} & \mathbf{C}_{\mathrm{i}} & -\mathbf{C}_{\mathrm{i}} & -2\mathbf{C}_{\mathrm{i}} \\ \mathbf{C}_{\mathrm{i}} & 2\mathbf{C}_{\mathrm{i}} & -2\mathbf{C}_{\mathrm{i}} & -\mathbf{C}_{\mathrm{i}} \\ -\mathbf{C}_{\mathrm{i}} & -2\mathbf{C}_{\mathrm{i}} & 2\mathbf{C}_{\mathrm{i}} & \mathbf{C}_{\mathrm{i}} \\ -2\mathbf{C}_{\mathrm{i}} & -\mathbf{C}_{\mathrm{i}} & \mathbf{C}_{\mathrm{i}} & 2\mathbf{C}_{\mathrm{i}} \end{bmatrix}$$

Hence, this matrix is fully coupled. In contrast to that it results following stiffness matrix by using Newton–Cotes integration

$$\mathbf{K}^{\mathrm{e}}_{\mathrm{i,uu}} = \begin{bmatrix} \mathbf{C}_{\mathrm{i}} & \mathbf{0} & \mathbf{0} & -\mathbf{C}_{\mathrm{i}} \\ \mathbf{0} & \mathbf{C}_{\mathrm{i}} & -\mathbf{C}_{\mathrm{i}} & \mathbf{0} \\ \mathbf{0} & -\mathbf{C}_{\mathrm{i}} & \mathbf{C}_{\mathrm{i}} & \mathbf{0} \\ -\mathbf{C}_{\mathrm{i}} & \mathbf{0} & \mathbf{0} & \mathbf{C}_{\mathrm{i}} \end{bmatrix}$$

The difference in these two schemes is that, through the use of Newton–Cotes integration for the element, only nodes placed at opposite sides influences each other and hence, the oscillations are reduced. By using Gauss integration all nodes of the element influences each other. Therefore, it is recommended to use Newton–Cotes integration for cohesive elements.

6 Application of the Cohesive Zone Model to Describe Cracking and Delamination of a Coating at High-Temperature

In this section we demonstrate the application of cohesive elements to a FE simulation to describe the cracking of a coating, at first and later on, the delamination of this cracked coating from the substrate material at high temperature. With high temperature we mean applications where the material is subjected to a homologous temperature of 30–90%. Thus, creep phenomena can occur.

6.1 *Experimental Setup and Numerical Model*

The tested specimen is a beam which is made of aluminium (AlSi10MgT6) and coated on one side with an iron aluminde (Fe24Al0.6Nb). This compound is then tested in a 4PBT at 400 °C which leads to a strong creep behaviour in the substrate material. The coating behaves at this temperature linear-elastic. This experiment is

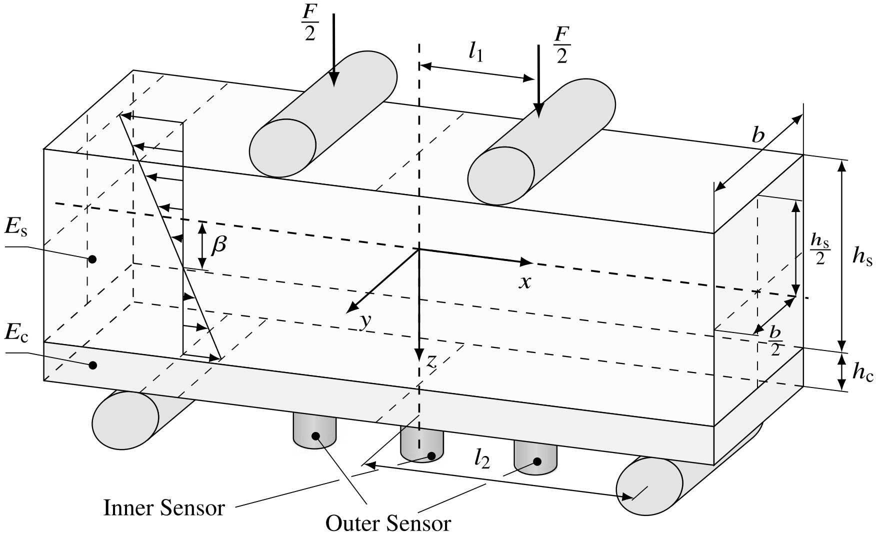

Fig. 6 Dimensions and loading of the specimen in a 4PBT with the assumed strain distribution and shifting of the neutral axis through inelastic deformations

Table 1 Material parameters and dimensions of the specimen after [51] ($i \in \{\mathrm{s}, \mathrm{c}\}$)

	E_i (MPa)	ν_i (–)	a_i ($\mathrm{MPa}^{-N_i}\,\mathrm{s}^{-1}$)	N_i (–)	h_i (mm)	b_i (mm)
Substrate	32979.9	0.33	4.4356E−11	4.0317	3.015	3.485
Coating	54784.8	0.30	–	–	1.240	3.485

in detail explained and analysed in [51] by using layer-wise theory until the coating starts to fail. Here, we want to use this setup (see Fig. 6), create a FE model and apply CZMs through the use of cohesive elements to this model and simulate the cracking of the coating and subsequently the delamination. Also, the material parameters of the substrate and the coating material are determined from experiments in [51]. They are summarised in Table 1 with all dimensions of the specimen, additionally.

The distance from the middle of the beam to an inner support is $l_1 = 10$ mm and to an outer support is $l_2 = 20$ mm. Because a load is only in z-direction applied on the specimen, only a plane simulation is performed under the plane stress assumption. Further on, because of the symmetry of the experiment with respect to the y-z-plane only the right half is modelled. Figure 7 shows the resulting FE model with boundary conditions, contact and cohesive zones. The contact interaction between supports and the specimen is modelled as hard contact with sliding, but friction is not considered. The creep behaviour of the substrate material is modelled with Norton's power law and the linear-elastic behaviour is modelled with Hooke's law. For the coating Hooke's law is used, additionally. Both materials are assumed to be isotropic. All these constitutive laws exist in ABAQUS, already. Then the discretisation is performed by using a quadratic plane stress element with reduced integration to prevent locking effects. The ABAQUS name for this element is `CPS8R`. Further on, a large displacement analysis is performed because the ratio between applied displacement and total height of the specimen is too large. Up next, a convergence study is performed to see how many elements are required to determine the stresses in the specimen, accurately. But without the cohesive zones because the parameters of the cohesive zones are not known for now. The results are presented in Fig. 8. The

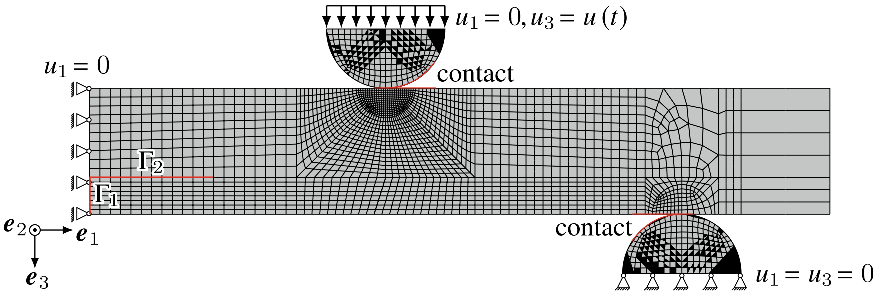

Fig. 7 FE model with boundary conditions, contact and cohesive zones

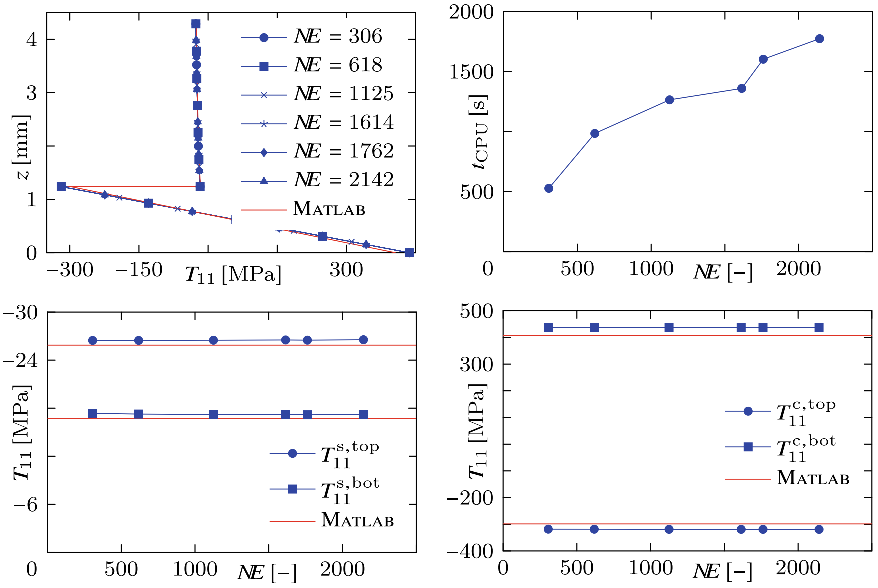

Fig. 8 Results of the convergence study

reference solution for this study is shown in red in Fig. 8. This solution is obtained with the model of [51]. The top left diagram in Fig. 8 presents the stress distribution over the cross section of the beam after 1845 s. The distribution looks like it is expected and fits very well to the reference solution. Due to the creep deformation in the substrate the stress reduces there and increases in the coating. Further on, a discrete jump in the stress occurs at the interface between substrate and coating which results from the difference of the Young's moduli. The bottom left and right diagrams of Fig. 8 present the stresses at the top and bottom of the substrate, respectively, the coating over the number of elements (*NE*). It can be seen, like in the top left diagram, that the stresses have already converged for all investigated *NE*. The top right diagram shows the calculation times for the different *NE*. For the highest *NE* the calculation time is half an hour, approximately.

From the convergence study, it can be concluded that all further calculations could be performed with the model of $NE = 306$. The stresses will be accurately calculated. We choose the model with $NE = 2142$ because later on cohesive elements are added to this model and due to localisation effects a finer mesh is necessary. And usually a much finer mesh has to be used but this is here impossible because we need this model to perform a numerical optimisation procedure to determine material parameters. Hence, the calculation time of half an hour for one model can easily increase to a week for the optimisation procedure. Besides, it is possible to do simulations which involve cohesive elements with a coarser mesh [52–54]. This leads to adjusted material parameters. We will see this in the following section.

Table 2 Prescribed cohesive zone parameters ($i \in \{\mathrm{n}, \mathrm{t}\}$)

	C_i (MPa)	p (–)	a (mms^{-1})	N_1 (–)	N_2 (–)	T_0 (MPa)	s_1 (–)	s_2 (–)
Γ_1	54784.8	–	–	–	–	–	–	–
Γ_2	43882.4	2	2.2178E−11	1	2.0158	1	1	1

The first cohesive zone Γ_1 is used to describe the cracking of the coating and the second Γ_2 to describe the delamination of the coating. Because of the linear elastic behaviour of the coating, it is expected that the coating shows more brittle failure behaviour. Therefore, the ABAQUS TSL with exponential degradation without mix-mode behaviour is used (see [16] for more informations) with the four parameters maximum normal traction $T_{\max,\mathrm{n}}$, maximum tangential traction $T_{\max,\mathrm{t}}$, maximum separation to failure $g_{\max}$ and alpha α. Due to the fact that ABAQUS normalises the separation which was mentioned earlier, already, the cohesive zone stiffness is set to the value of the Young's modulus of the coating. The second cohesive zone is equipped with the novel TSL of Sect. 4.2. Also, some parameters for this zone are prescribed. These are the creep parameters and the cohesive stiffness plus the damage exponents. These parameters are determined as mean values from the substrate and coating parameters. All parameters are summed up in Table 2.

6.2 *Determination of the CZM Parameters by Numerical Optimisation*

All cohesive zone parameters are determined simultaneously. In the experiment the force and the time for the middle of the beam is measured. From this we can derive a moment-time curve ($M - t$ curve). To get a similar curve from the simulation we have to integrate over the axial stress T_{11} along the z-direction. But because the neutral axis of the beam shifts as a result of the creep deformation, this shifting β has to be considered in the integration. This leads to

$$M = b \int_{z_{\mathrm{bot}}}^{z_{\mathrm{top}}} T_{11}(z - \beta)\ \mathrm{d}z \tag{85}$$

When this shifting is not considered in the integration the amount in the resulting moment coming from the coating is overestimated and the amount from the substrate is too low. But interestingly the resulting moment is correct calculated. This integration is later on performed by using the trapezoidal rule.

Now, we can begin with the optimisation process. Therefore, we connect the commercial software packages ABAQUS and MATLAB by using the tool ABAQUS2MATLAB [1]. The optimisation procedure is described in Fig. 9 in detail.

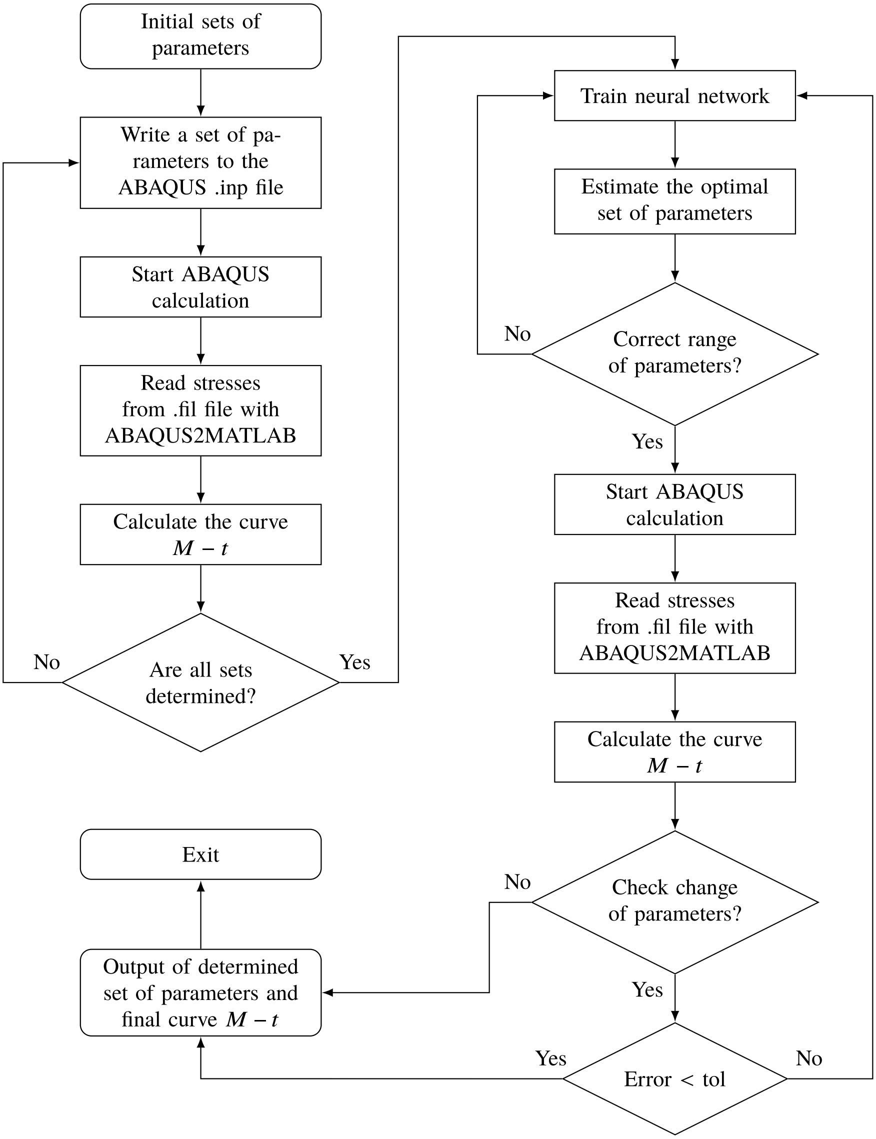

Fig. 9 Flowchart of the optimisation algorithm

Table 3 Determined cohesive zone parameters

	$T_{\max,\mathrm{n}}$ (MPa)	$T_{\max,\mathrm{t}}$ (MPa)	$g_{\max}$ (mm)	α (–)	S_0 (MPa)	$Y_{\mathrm{E}0}$ (MPa)
Γ_1	290.98	33.38	1.0344E−2	1.03	–	–
Γ_2	–	–	–	–	4.3901E−5	6.5815E−3

At first, initial sets of the parameters are defined which should be determined. Then is a FE simulation for every initial set performed and the $M - t$ curve is obtained by integrate the moment of the beam with Eq. (85). These initial sets and curves are the input for the optimisation process. For the optimisation we use the neural network toolbox of MATLAB. After every training of the network and estimating the new set of parameters it is at first checked if the estimated set is in the expected range and if every parameter is greater as zero, otherwise, the set is forgotten and the training starts again. When the set of parameters fulfills all requirements a new FE simulation is performed and the $M - t$ curve is calculated. The training algorithm is repeated until the change in the parameters is less than 1% or the error of the $M - t$ curve is less than the specified tolerance. Finally, the algorithm gives as output the determined set of parameters and the belonging $M - t$ curve. The determined parameters are summed up in Table 3. In Sect. 6.1 we mentioned the fact that cohesive zone parameters are adjusted to compensate the effects due to a coarse mesh. This can be seen by comparing the determined cohesive strength $T_{\max,\mathrm{n}}$ with the experimental determined strength of the interface which is 381 MPa [51]. Usage of a fine mesh would have led to a cohesive strength near the experimental determined value.

6.3 Comparison Between Experiment and Simulation

In Fig. 10 the result of the final simulation is presented and compared to the experiment of [51]. The simulation is performed for 2100 s with a final displacement of the upper support of $u\,(t = 2100\,\mathrm{s}) = 1.749\,\mathrm{mm}$. The displacement is increased from 0mm to 1.749 mm linearly over this time period. The diagram in Fig. 10 shows the experimental curve and the simulated one. It can be seen that the onset of cracking of the coating is simulated very well. But after this the simulation has a deviation to the experiment which is a consequence of the missing hardening of the compound after the coating has failed. But for this complex simulation the result is acceptable.

The missing hardening of the compound after the cracking of the coating (see Fig. 10; $t \approx 1750\,\mathrm{s}$) is a result of the early onset of the delamination and that the crack through the coating propagates to slow. But because the comparison between the experimental delamination curve and the simulated one is very similar (just shifted) we suppose that the false cracking behaviour of the coating is the main problem which causes the difference between experiment and simulation. Therefore, this will be investigated in the future.

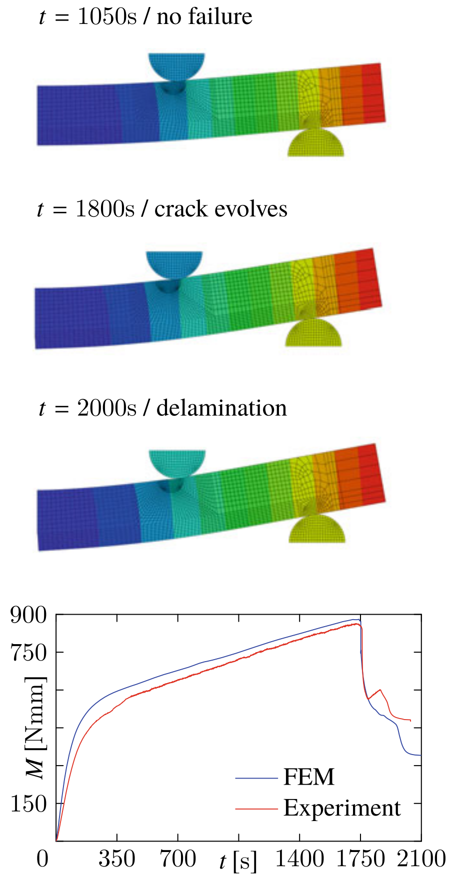

Fig. 10 Comparison between experiment and simulation and visualisation of the simulation at specific time points; red—smallest displacement, blue—highest displacement

Further on, Fig. 10 presents some pictures of the deformed specimen at specific time points to visualise the cracking and the delamination of the coating. The colors represent the displacement distribution over the specimen, red is the smallest displacement in every picture and blue the highest one. Due to the fact that the specimen is made of aluminium and iron aluminde, it is stiff and consequently the deformations are small. Therefore, a zoom is presented in Fig. 10 to see the delamination.

7 Summary and Outlook

In this treatise we presented an overview on CZMs and TSLs. Further on, we presented a rate-dependent TSL with mix-mode behaviour and explained the implementation into the FEM. Finally, the result of a 4PBT simulation is presented and compared to an experiment. Slight deviations between simulation and experiment occurred but they are acceptable.

Up next, the presented thermal model is implemented and tested and afterwards a thermal-mechanical simulation is performed. After this we want to analyse the influence of different TSLs on the failure behaviour of the coating to see if it is possible to simulate the hardening of the compound and finally get a better approximation of the experiment (see Sect. 6.3).

Acknowledgements The financial support rendered by the German Research Foundation (DFG) in context of the research training group 'Micro-Macro-Interactions of Structured Media and Particle Systems' (RTG 1554) is gratefully acknowledged.

Appendix

Arranging of displacement, position and temperature vector for a 2D cohesive element

$$\begin{aligned} \mathbf{u}^{\mathrm{e}} &= \left[u_{1x}\ u_{1y}\ u_{2x}\ \ldots\ u_{ny}\right]^{\top}, \quad n = NN \\ \mathbf{x}^{\mathrm{e}} &= \left[x_{1x}\ x_{1y}\ x_{2x}\ \ldots\ x_{ny}\right]^{\top}, \quad n = NN \\ \boldsymbol{\theta}^{\mathrm{e}} &= \left[\theta_1\ \theta_2\ \ldots\ \theta_n\right]^{\top}, \quad n = NN \end{aligned}$$

Arranging of total *DOF* and residual vector for a 2D cohesive element

$$\mathbf{p}^{\mathrm{e}} = \begin{bmatrix} \mathbf{u}^{\mathrm{e}} \\ \boldsymbol{\theta}^{\mathrm{e}} \end{bmatrix}$$

$$\mathbf{r}_{\mathrm{i}}^{\mathrm{e}} = \begin{bmatrix} \mathbf{r}_{\mathrm{i,u}}^{\mathrm{e}} \\ \mathbf{r}_{\mathrm{i},\theta}^{\mathrm{e}} \end{bmatrix}$$

Shape functions for a 2D cohesive element

$$\begin{aligned} N_1 &= \frac{1}{2}(1 - \xi_1) \\ N_2 &= \frac{1}{2}(1 + \xi_1) \end{aligned}$$

Arranging of the displacement and temperature shape function matrix

$$\mathbf{N}_\mathrm{u} = \begin{bmatrix} N_1 & 0 & N_2 & 0 \\ 0 & N_1 & 0 & N_2 \end{bmatrix}$$

$$\mathbf{N}_\theta = \begin{bmatrix} N_1 & N_2 \end{bmatrix}$$

Arranging of the displacement and temperature mean value matrix

$$\mathbf{M}_\mathrm{u} = \begin{bmatrix} 1&0&0&0&0&0&1&0 \\ 0&1&0&0&0&0&0&1 \\ 0&0&1&0&1&0&0&0 \\ 0&0&0&1&0&1&0&0 \end{bmatrix}$$

$$\mathbf{M}_\theta = \begin{bmatrix} 1&0&0&1 \\ 0&1&1&0 \end{bmatrix}$$

Arranging of the displacement and temperature separation relation matrix

$$\mathbf{L}_\mathrm{u} = \begin{bmatrix} -1&0&0&0&0&0&1&0 \\ 0&-1&0&0&0&0&0&1 \\ 0&0&-1&0&1&0&0&0 \\ 0&0&0&-1&0&1&0&0 \end{bmatrix}$$

$$\mathbf{L}_\theta = \begin{bmatrix} -1&0&0&1 \\ 0&-1&1&0 \end{bmatrix}$$

Arranging of the elasticity matrix

$$\mathbf{C}_\mathrm{TSL} = \begin{bmatrix} C_\mathrm{n} & 0 \\ 0 & C_\mathrm{t} \end{bmatrix}$$

References

1. Papazafeiropoulos, G., Muñiz-Calvente, M., Martínez-Pañeda, E.: Adv. Eng. Softw. **105**, 9 (2017). https://doi.org/10.1016/j.advengsoft.2017.01.006
2. Altenbach, H.: Kontinuumsmechanik: Einführung in die materialunabhängigen und materialabhängigen Gleichungen, 4th edn. Springer, Berlin (2018). https://doi.org/10.1007/978-3-662-57504-8
3. Lai, W., Rubin, D., Krempl, E.: Introduction to Continuum Mechanics, 4th edn. Butterworth-Heinemann, Oxford (2009)
4. Bertram, A.: Elasticity and Plasticity of Large Deformations: An Introduction, 3rd edn. Springer, Berlin (2012). https://doi.org/10.1007/978-3-642-24615-9
5. Lebedev, L.P., Cloud, M.J., Eremeyev, V.A.: Tensor Analysis with Applications in Mechanics. World Scientific, Singapore (2010). https://doi.org/10.1142/9789814313995
6. Schwalbe, K.H., Scheider, I., Cornec, A.: Guidelines for Applying Cohesive Models to the Damage Behaviour of Engineering Materials and Structures. Springer, Berlin (2013). https://doi.org/10.1007/978-3-642-29494-5
7. Barenblatt, G.: J. Appl. Math. Mech. **23**(3), 622 (1959). https://doi.org/10.1016/0021-8928(59)90157-1

8. Dugdale, D.: J. Mech. Phys. Solids **8**(2), 100 (1960). https://doi.org/10.1016/0022-5096(60)90013-2
9. Needleman, A.: Procedia IUTAM **10**, 221 (2014). https://doi.org/10.1016/j.piutam.2014.01.020
10. Hillerborg, A., Modéer, M., Petersson, P.E.: Cem. Concr. Res. **6**(6), 773 (1976)
11. Bažant, Z.P.: Eng. Fract. Mech. **69**(2), 165 (2002). https://doi.org/10.1016/s0013-7944(01)00084-4
12. Needleman, A.: J. Mech. Phys. Solids **38**(3), 289 (1990)
13. Needleman, A.: Non-linear Fracture, pp. 21–40. Springer, Netherlands (1990). https://doi.org/10.1007/978-94-017-2444-9_2
14. Scheider, I., Brocks, W.: Eng. Fract. Mech. **70**(14), 1943 (2003). https://doi.org/10.1016/s0013-7944(03)00133-4
15. Tvergaard, V., Hutchinson, J.W.: J. Mech. Phys. Solids **40**(6), 1377 (1992). https://doi.org/10.1016/0022-5096(92)90020-3
16. Dassault Systèmes, SIMULIA Corp., ABAQUS version 2017 documentation (2017)
17. Gurtin, M.E.: J. Appl. Math. Phys. (ZAMP) **30**(6), 991 (1979). https://doi.org/10.1007/BF01590496
18. Rice, J.R., Wang, J.S.: Mater. Sci. Eng.: A **107**, 23 (1989)
19. Bouvard, J., Chaboche, J., Feyel, F., Gallerneau, F.: Int. J. Fatigue **31**(5), 868 (2009). https://doi.org/10.1016/j.ijfatigue.2008.11.002
20. Nase, M., Rennert, M., Naumenko, K., Eremeyev, V.A.: J. Mech. Phys. Solids **91**, 40 (2016). https://doi.org/10.1016/j.jmps.2016.03.001
21. Chandra, N., Li, H., Shet, C., Ghonem, H.: Int. J. Solids Struct. **39**(10), 2827 (2002). https://doi.org/10.1016/s0020-7683(02)00149-x
22. Naumenko, K., Altenbach, H.: Modeling High Temperature Materials Behavior for Structural Analysis. Springer International Publishing, New York (2016). https://doi.org/10.1007/978-3-319-31629-1
23. Fagerström, M., Larsson, R.: J. Mech. Phys. Solids **56**(10), 3037 (2008). https://doi.org/10.1016/j.jmps.2008.06.002
24. Helmholtz, H.: Physical Memoirs Selected and Translated from Foreign Sources. Physical Society of London, vol. 1, pp. 43–97. Taylor & Francis, London (1882) (1888)
25. Clausius, R.: The Mechanical Theory of Heat. Macmillan, London (1879)
26. Duhem, P.: Mixture and Chemical Combination, pp. 291–309. Springer, Netherlands (1901) (2002). https://doi.org/10.1007/978-94-017-2292-6_22
27. Truesdell, C.: J. Ration. Mech. Anal. **1**, 125 (1952)
28. Coleman, B.D.: The Rational Spirit in Modern Continuum Mechanics, pp. 1–13. Kluwer Academic Publishers, New York (2003). https://doi.org/10.1007/1-4020-2308-1_1
29. Musto, M.: On the formulation of hereditary cohesive-zone models. Ph.D. thesis, Brunel University School of Engineering and Design (2014)
30. Gao, Y.F., Bower, A.F.: Model. Simul. Mater. Sci. Eng. **12**(3), 453 (2004). https://doi.org/10.1088/0965-0393/12/3/007
31. Needleman, A.: Comput. Methods Appl. Mech. Eng. **67**(1), 69 (1988). https://doi.org/10.1016/0045-7825(88)90069-2
32. Lemaitre, J., Desmorat, R.: Engineering Damage Mechanics. Springer, Berlin (2005). https://doi.org/10.1007/b138882
33. Miehe, C., Hofacker, M., Welschinger, F.: Comput. Methods Appl. Mech. Eng. **199**(45–48), 2765 (2010). https://doi.org/10.1016/j.cma.2010.04.011
34. Abu-Eishah, S., Haddad, Y., Solieman, A., Bajbouj, A.: J. Lat. Am. Appl. Res. (LAAR) **34**, 257 (2004)
35. Narender, K., Rao, A.S.M., Rao, K.G.K., Krishna, N.G.: J. Mod. Phys. **04**(03), 331 (2013). https://doi.org/10.4236/jmp.2013.43045
36. Leckie, F., Hayhurst, D.: Acta Metall. **25**(9), 1059 (1977). https://doi.org/10.1016/0001-6160(77)90135-3

37. Cocks, A., Ashby, M.: Prog. Mater. Sci. **27**(3–4), 189 (1982). https://doi.org/10.1016/0079-6425(82)90001-9
38. Fourier, J.B.J.: Théorie Analytique de la Chaleur. Cambridge University Press, Cambridge (2009). https://doi.org/10.1017/cbo9780511693229
39. Holzapfel, G.A.: Nonlinear Solid Mechanics. Wiley, New York (2000)
40. Wriggers, P.: Nonlinear Finite Element Methods. Springer, Berlin (2008). https://doi.org/10.1007/978-3-540-71001-1
41. Allix, O., Corigliano, A.: Int. J. Solids Struct. **36**(15), 2189 (1999). https://doi.org/10.1016/s0020-7683(98)00079-1
42. Dhondt, G.: The Finite Element Method for Three-Dimensional Thermomechanical Applications. Wiley-Blackwell, Hoboken (2004)
43. Park, K., Paulino, G.H.: Eng. Fract. Mech. **93**, 239 (2012). https://doi.org/10.1016/j.engfracmech.2012.02.007
44. Musto, M., Alfano, G.: Comput. Struct. **118**, 126 (2013). https://doi.org/10.1016/j.compstruc.2012.12.020
45. de Borst, R., Sluys, L., Mühlhaus, H.B., Pamin, J.: Eng. Comput. **10**(2), 99 (1993). https://doi.org/10.1108/eb023897
46. Gens, A., Carol, I., Alonso, E.: Comput. Geotech. **7**(1–2), 133 (1989). https://doi.org/10.1016/0266-352x(89)90011-6
47. Schellekens, J.C.J., Borst, R.D.: Int. J. Numer. Methods Eng. **36**(1), 43 (1993). https://doi.org/10.1002/nme.1620360104
48. Svenning, E.: Comput. Methods Appl. Mech. Eng. **310**, 460 (2016). https://doi.org/10.1016/j.cma.2016.07.031
49. Vignollet, J., May, S., de Borst, R.: Int. J. Numer. Methods Eng. **102**(11), 1733 (2015). https://doi.org/10.1002/nme.4867
50. Yu, H., Olsen, J.S., Olden, V., Alvaro, A., He, J., Zhang, Z.: Eng. Fract. Mech. **166**, 23 (2016). https://doi.org/10.1016/j.engfracmech.2016.08.019
51. Nordmann, J., Thiem, P., Cinca, N., Naumenko, K., Krüger, M.: J. Strain Anal. Eng. Des. **53**(4), 255 (2018). https://doi.org/10.1177/0309324718761305
52. Alfano, G., Crisfield, M.A.: Int. J. Numer. Methods Eng. **50**(7), 1701 (2001). https://doi.org/10.1002/nme.93
53. Turon, A., Dávila, C., Camanho, P., Costa, J.: Eng. Fract. Mech. **74**(10), 1665 (2007). https://doi.org/10.1016/j.engfracmech.2006.08.025
54. Ersoy, N., Ahmadvashaghbash, S., Engül, M., Öz, F.E.: Eur. Conf. Compos. Mater. (2018)

Stability of Parameter Identification Using Experiments with a Heterogeneous Stress State

Alexey V. Shutov and Anastasiya A. Kaygorodtseva

Abstract We analyze different strategies used for the identification of material parameters, which appear in a certain model of finite strain viscoplasticity. The main focus is set on the sensitivity of the parameters with respect to measurement errors. In different strategies we combine experimental data obtained from various torsion tests with a heterogeneous stress state. A direct problem is solved using the nonlinear FEM. To estimate the stability of a certain identification strategy we perform Monte Carlo simulations for a series of noisy experimental data. A distance between two sets of material parameters is measured using a special mechanics-based metric. Both the identification of material parameters and the estimation of their stability are illustrated by an example. In this example we employ a set of synthetic experimental data obtained for the steel 42CrMo4. As a material model, we choose a model of finite strain plasticity with a combined isotropic-kinematic hardening.

1 Introduction

Advanced phenomenological models describe the elasto-visco-plastic behaviour of high-temperature materials with a good accuracy, accounting for a number of nonlinear phenomena. A substantial progress has been achieved in the simulation of stress response under non-monotonic loading conditions, including ductile damage (cf. [21]), creep damage (cf. [8, 19]), and viscoplasticity under thermo-mechanical loading (cf. [13]). Unfortunately, the phenomenological models contain numerous material parameters, which can not be measured in the experiment directly. The situation may become even more difficult: models suitable for thermo-mechanical loadings may contain twice as much parameters when compared to their isother-

---

A. V. Shutov (✉) · A. A. Kaygorodtseva
Lavrentyev Institute of Hydrodynamics, pr. Lavrentyeva 15,
630090 Novosibirsk, Russia
e-mail: alexey.v.shutov@gmail.com

A. V. Shutov · A. A. Kaygorodtseva
Novosibirsk State University, ul. Pirogova 1, 630090 Novosibirsk, Russia

K. Naumenko and M. Krüger (eds.), *Advances in Mechanics of High-Temperature Materials*, Advanced Structured Materials 117,
https://doi.org/10.1007/978-3-030-23869-8_8

mal counterparts. A common approach is to identify these parameters by solving an inverse problem. Herein, an error functional reflecting the average deviation of the simulation results from the experimental data is minimized [2]. In order to gain more freedom in choosing the experimental setup one may go beyond experiments with a homogeneous distribution of stresses and strains in the gage area (cf. [1]). Apart from gaining a greater freedom in experimental setup, heterogeneous tests may carry more information than the homogeneous ones, since different parts of the sample experience various loadings. In order to solve a direct problem involving a heterogeneous deformation of the sample, the nonlinear finite element method is typically employed as a universal tool (cf. [7]). In the current study, we focus on torsion tests since they allow for large stable deformations without undesired influence of friction; hot torsion tests can be carried out in a robust way [1].

An important issue is the *sensitivity* of the identified material parameters with respect to the inevitable measurement errors. For instance, dealing with overparameterized models, a very good correspondence between simulation and experiment can be achieved, but even a smallest change in the experimental data may cause a finite variation of the identified material parameters. In the current study we estimate the sensitivity of the parameters by Monte Carlo simulations considering a large number of noisy experimental data. Motivated by the central limiting theorem of the probability theory, we consider the so-called white noise. As a result, a cloud of points in the space of material parameters is obtained. The size of this cloud is estimated using a special mechanics-based metric, which is advantageous over the conventional Euclidean metric.

For demonstration purposes, only two types of torsion samples are considered: circular rods and thick-walled tubes. In both cases the stress-strain state is heterogeneous. As a material model, constitutive equations proposed by Shutov and Kreißig [17] are used. This model accounts for a combined nonlinear isotropic-kinematic hardening in the finite strain range. For simplicity, isothermal conditions are considered. As the experimental basis, synthetic experimental data on non-monotonic torsion of heterogeneous samples made from the steel 42CrMo4 are employed. The synthetic data are obtained by using an accurate version of the material model with two evolving back-stresses. The parameter identification, in turn, is carried out using a simplified version of the model with only one back-stress.

2 Material Model

As already mentioned, the material model from [17] is implemented here. It accounts for the nonlinear isotropic hardening of Voce type and the nonlinear kinematic hardening according to Armstrong and Frederick. The rheological motivation of the model is shown in Fig. 1. The rheological model comprises one friction element (St.-Venant body), one elastic spring (Hooke body) and a number of rate-independent Maxwell bodies: only one body within a simplified model (Fig. 1, left) and two bodies in a refined model (Fig. 1, right). Each of the rate-independent Maxwell bodies,

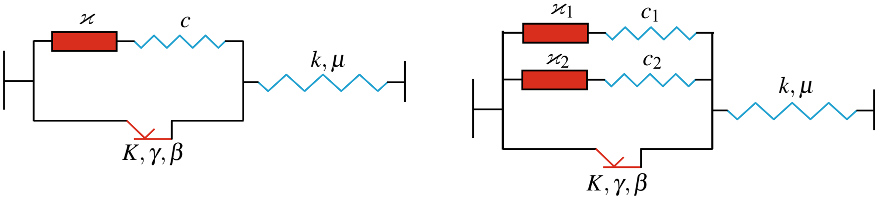

Fig. 1 Rheological explanation of the viscoplastic material model with nonlinear kinematic hardening. Left: simplified model with a single rate-independent Maxwell body. Right: refined model employing two Maxwell bodies

in turn, consists of an elastic spring and a modified (rate-independent) dashpot. Rate-independent dashpots are depicted as boxes in Fig. 1. They differ from the classical (rate-dependent) dashpots in that the physical time t is replaced by the monotonically increasing Odqvist parameter s. The stresses in each of the rate-independent Maxwell bodies are understood as back-stresses, which are used to account for the shift of the yield surface in the stress space (Bauschinger effect). In other words, a single back-stress tensor appears in the simplified model and two back-stress tensors are used in the refined model.

The geometrically nonlinear kinematics of the model is based on the nested multiplicative split of the deformation gradient, suggested by Lion in [6]. An example of practical application of this model is given in [10]. Modifications of this model to the high-temperature creep [19], ductile damage [21], and thermo-mechanical loading [13] are known.

We briefly recall the constitutive equations of the refined model, which uses two backstresses. Let $\mathbf{C} := \mathbf{F}^{\mathrm{T}}\mathbf{F}$ be the right Cauchy–Green tensor at a certain material point. Three tensor-like state variables of the same type are introduced: $\mathbf{C}_{\mathrm{i}}$ for the current inelastic strain and $\mathbf{C}_{1\mathrm{i}}$, $\mathbf{C}_{2\mathrm{i}}$ for the current inelastic strain of substructure. Quantities $\mathbf{C}$, $\mathbf{C}_{\mathrm{i}}$, $\mathbf{C}_{1\mathrm{i}}$, and $\mathbf{C}_{2\mathrm{i}}$ are symmetric and strictly positive definite. To capture the isotropic hardening, two scalar-valued quantities are used: Odqvist parameter (accumulated plastic arc-length) s and its dissipative part s_{d}.

Let ψ be the Helmholz free energy per unit mass. Assume that (cf. [18]):

$$\psi = \psi_{\mathrm{el}}(\mathbf{C}\mathbf{C}_{\mathrm{i}}^{-1}) + \psi_{\mathrm{kin1}}(\mathbf{C}_{\mathrm{i}}\mathbf{C}_{1\mathrm{i}}^{-1}) + \psi_{\mathrm{kin2}}(\mathbf{C}_{\mathrm{i}}\mathbf{C}_{2\mathrm{i}}^{-1}) + \psi_{\mathrm{iso}}(s - s_{\mathrm{d}}), \tag{1}$$

where $\psi_{\mathrm{el}}(\mathbf{C}\mathbf{C}_{\mathrm{i}}^{-1})$ stands for the energy storage associated to macroscopic elastic strains; $\psi_{\mathrm{kin1}}(\mathbf{C}_{\mathrm{i}}\mathbf{C}_{1\mathrm{i}}^{-1})$, $\psi_{\mathrm{kin2}}(\mathbf{C}_{\mathrm{i}}\mathbf{C}_{2\mathrm{i}}^{-1})$ and $\psi_{\mathrm{iso}}(s - s_{\mathrm{d}})$ are parts of the free energy stored in defects of crystal lattice. Contributions ψ_{kin} and ψ_{iso} are related to mechanisms of kinematic and isotropic hardening, respectively. The functions ψ_{el}, ψ_{kin1}, and ψ_{kin2} are assumed to be isotropic. To be definite, we set in this study

$$\rho_{\mathrm{R}}\psi_{\mathrm{el}}(\mathbf{A}) = \frac{k}{2}(\ln\sqrt{\det\mathbf{A}})^2 + \frac{\mu}{2}(\mathrm{tr}\overline{\mathbf{A}} - 3), \tag{2}$$

$$\rho_{\mathrm{R}}\psi_{\mathrm{kin1}}(\mathbf{A}) = \frac{c_1}{4}(\mathrm{tr}\overline{\mathbf{A}} - 3), \quad \rho_{\mathrm{R}}\psi_{\mathrm{kin2}}(\mathbf{A}) = \frac{c_2}{4}(\mathrm{tr}\overline{\mathbf{A}} - 3), \tag{3}$$

$$\rho_{\mathrm{R}}\psi_{\mathrm{iso}}(s_{\mathrm{e}}) = \frac{\gamma}{2}(s_{\mathrm{e}})^2, \quad \overline{\mathbf{A}} := (\det \mathbf{A})^{-1/3}\mathbf{A}, \tag{4}$$

for any $\mathbf{A}$ and s_{e}. Here, k, μ, c_1, c_2, γ are constant material parameters; ρ_{R} stands for the referential mass density. Following the Coleman–Noll procedure, the second Piola-Kirchhoff stress $\widetilde{\mathbf{T}}$ is computed through

$$\widetilde{\mathbf{T}} = 2\rho_{\mathrm{R}} \frac{\partial \psi_{\mathrm{el}}(\mathbf{C}\mathbf{C}_{\mathrm{i}}^{-1})}{\partial \mathbf{C}}|_{\mathbf{C}_{\mathrm{i}}=const}. \tag{5}$$

In Sect. 5 we will also need the Cauchy stress (true stress) $\mathbf{T}$:

$$\mathbf{T} = \frac{1}{\det(\mathbf{F})}\mathbf{F}\,\widetilde{\mathbf{T}}\,\mathbf{F}^{\mathrm{T}}. \tag{6}$$

Backstresses $\widetilde{\mathbf{X}}_1$ and $\widetilde{\mathbf{X}}_2$ and the overall backstress $\widetilde{\mathbf{X}}$ are employed in the refined model to capture the Bauschinger effect:

$$\widetilde{\mathbf{X}}_1 = 2\rho_{\mathrm{R}} \frac{\partial \psi_{\mathrm{kin1}}(\mathbf{C}_{\mathrm{i}}\mathbf{C}_{1\mathrm{i}}^{-1})}{\partial \mathbf{C}_{\mathrm{i}}}|_{\mathbf{C}_{1\mathrm{i}}=const}, \quad \widetilde{\mathbf{X}}_2 = 2\rho_{\mathrm{R}} \frac{\partial \psi_{\mathrm{kin2}}(\mathbf{C}_{\mathrm{i}}\mathbf{C}_{2\mathrm{i}}^{-1})}{\partial \mathbf{C}_{\mathrm{i}}}|_{\mathbf{C}_{2\mathrm{i}}=const}, \tag{7}$$

$$\widetilde{\mathbf{X}} = \widetilde{\mathbf{X}}_1 + \widetilde{\mathbf{X}}_2. \tag{8}$$

By $R \in \mathbb{R}$ we denote a hardening variable which is responsible for isotropic expansion of the yield surface:

$$R = \rho_{\mathrm{R}} \frac{\partial \psi_{\mathrm{iso}}(s - s_{\mathrm{d}})}{\partial s}|_{s_{\mathrm{d}}=const}. \tag{9}$$

Within viscoplastic models, stress states beyond the elastic domain are possible due to occurrence of a viscous overstress f which depends on the applied strain rate. The overstress is defined by

$$f := \mathfrak{F} - \sqrt{\frac{2}{3}}(K + R), \quad \mathfrak{F} := \sqrt{\mathrm{tr}[(\mathbf{C}\widetilde{\mathbf{T}} - \mathbf{C}_{\mathrm{i}}\widetilde{\mathbf{X}})^{\mathrm{D}}]^2}, \tag{10}$$

where K stands for the initial uniaxial quasi-static yield stress, $(\cdot)^{\mathrm{D}}$ denotes the deviatoric part, $\mathfrak{F}$ stands for the driving force of the viscoplastic flow (equivalent stress). The inelastic strain rate λ_{i} equals the norm of the inelastic strain rate tensor; λ_{i} is computed employing the Perzyna law of viscoplasticity using the current overstress f

$$\lambda_{\mathrm{i}} = \frac{1}{\eta}\Big\langle \frac{f}{k_0} \Big\rangle^m, \quad \langle x \rangle := \max(x, 0). \tag{11}$$

Here, η and m are fixed material parameters; k_0 equals 1 MPa (it is not a material parameter). The temporal changes of the internal variables are governed by the constitutive relations

$$\dot{\mathbf{C}}_{\mathrm{i}} = 2\frac{\lambda_{\mathrm{i}}}{\mathfrak{F}}(\mathbf{C}\widetilde{\mathbf{T}} - \mathbf{C}_{\mathrm{i}}\widetilde{\mathbf{X}})^{\mathrm{D}}\mathbf{C}_{\mathrm{i}}, \tag{12}$$

$$\dot{\mathbf{C}}_{1\mathrm{i}} = 2\lambda_{\mathrm{i}}\varkappa_1(\mathbf{C}_{\mathrm{i}}\widetilde{\mathbf{X}}_1)^{\mathrm{D}}\mathbf{C}_{1\mathrm{i}}, \quad \dot{\mathbf{C}}_{2\mathrm{i}} = 2\lambda_{\mathrm{i}}\varkappa_2(\mathbf{C}_{\mathrm{i}}\widetilde{\mathbf{X}}_2)^{\mathrm{D}}\mathbf{C}_{2\mathrm{i}}, \tag{13}$$

$$\dot{s} = \sqrt{\frac{2}{3}}\lambda_{\mathrm{i}}, \quad \dot{s}_{\mathrm{d}} = \frac{\beta}{\gamma}\dot{s}R. \tag{14}$$

Here, $\varkappa_1$, $\varkappa_2$ are parameters related to the saturation of the kinematic hardening; β is responsible for the saturation of the isotropic hardening; $\dot{(\cdot)}$ stands for the material time derivative. Here we assume that at $t = 0$ the material is isotropic, undeformed, and stress free, which yields the following initial conditions

$$\mathbf{C}_{\mathrm{i}}|_{t=0} = \mathbf{C}_{1\mathrm{i}}|_{t=0} = \mathbf{C}_{2\mathrm{i}}|_{t=0} = \mathbf{1}, \quad s|_{t=0} = s_{\mathrm{d}}|_{t=0} = 0. \tag{15}$$

The model exhibits the following properties:

- It is suitable for large elastic and inelastic strains. Various isotropic hyperelastic potentials can be implemented for the description of elastic properties and kinematic hardening.
- The model is thermodynamically consistent (the Clausius-Duhem inequality is satisfied for arbitrary processes) [17].
- The model is objective (thus providing a correct transformation of the Cauchy stress under superimposed rigid body motion).
- The model is w-invariant under the change of the reference configuration (cf. [14, 20]).
- Efficient numerical schemes are available in case of neo-Hookean hyperelastic potentials (cf. [11]). When the kinematic hardening is modelled using the Mooney-Rivlin potential, efficient algorithm from [12] can be used as well.

Some of the material parameters can be identified from experiments in a relatively simple way [18]. The elastic properties are captured by the shear modulus μ and the bulk modulus k. These parameters can be restored from the experimental data in the elastic mode. The initial yield stress under uniaxial tension K is identified from the uniaxial stress-strain curve. The parameters of the Perzyna-type viscosity η and the exponent m can be identified from a series of dynamic tension tests. The pre-identified values are taken from [18] and listed in Table 1.

Table 1 Pre-identified parameters for the steel 42CrMo4

k [MPa]	μ [MPa]	η [s]	m [-]	K [MPa]
135 600	52000	5×10^5	2.26	335

The remaining material parameters need to be identified simultaneously. Dealing with simplified model (employing a single Maxwell body) they are: the parameters of the isotropic hardening γ and β as well as the ones of the kinematic hardening c and $\varkappa$. Here, γ/β gives the saturation value of the isotropic hardening and $1/\beta$ gives the characteristic saturation strain. The parameter c can be seen as the stiffness of the elastic spring within the Maxwell body and $1/\varkappa$ corresponds to its generalized viscosity. Thus, the saturation level of the backstress is proportional to $1/\varkappa$ and the saturation strain is proportional to $1/(c\varkappa)$.

3 Synthetic Experimental Data

We analyze two types of torsion samples: a solid rod of the radius 10 mm and a thick-walled tube with the inner and outer radii of 5 and 10 mm, respectively. In both samples the length of the gage area equals 25 mm. The loading consist of monotonic torsion up to the maximum angle $\phi_{\max}$ followed by a reverse torsion bringing the sample back to the undeformed state finally followed by the second torsion up to the $\phi_{\max}$. Two different amplitudes are considered: $\phi_{\max} = 0.75$ rad and $\phi_{\max} = 1.5$ rad.

Unfortunately, real experimental data are missing for these samples and loading conditions. Therefore, in order to test the stability of the parameter identification strategy, we employ so-called synthetic experimental data. The synthetic data are generated by means of an FEM computation using the refined model (with two Maxwell bodies). The material parameters correspond to the high-strength steel 42CrMo4. The parameters are taken from the previous study [16]; they are shown in Table 2. Since the refined model describes the real stress response very accurately (see. Fig. 1 in Ref. [16]), the generated synthetic data are believed to be a reasonable representation of the real test results.

The FEM analysis is carried out using MSC.Marc. Isoparametric elements with a quadratic approximation of the geometry and displacements are used (element type Hex20) with a full integration scheme. The constitutive model is implemented using the Hypela2 interface as a user-defined material subroutine. In this, a robust and efficient numerical algorithm from [11] is employed. The overall deformation process is subdivided into 150 steps: 50 steps for the initial torsion up to $\phi_{\max}$, 50 steps for the reduction of the torsion angle back to zero, and, finally, 50 steps for the second loading up to $\phi_{\max}$. In order to speed-up the computations, the “cyclic symmetry” option is activated. Only a 10-degree sector is analyzed. The synthetic experimental data generated by FEM are shown in Fig. 2. Since the modelled sector

Table 2 Material parameters for the steel 42CrMo4 used to generate synthetic data

γ [MPa]	β [-]	c_1 [MPa]	c_2 [MPa]	$\varkappa_1$ [1/MPa]	$\varkappa_2$ [1/MPa]
141.18	0.037501	1692.6	23255.0	0.0038419	0.0045175

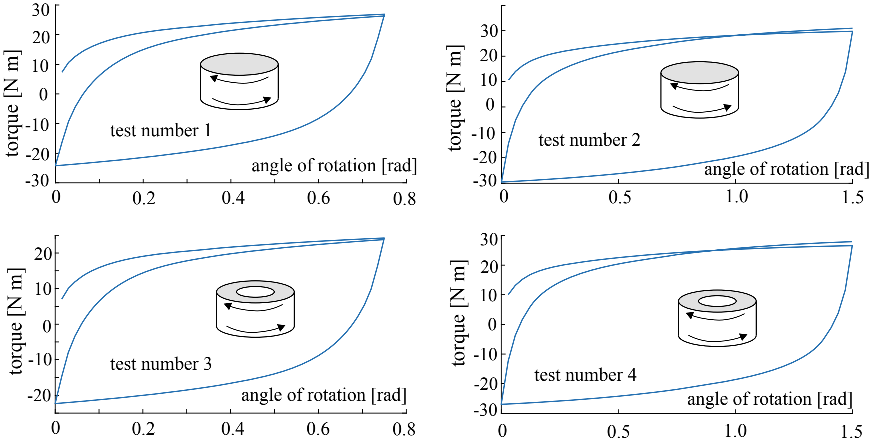

Fig. 2 Synthetic experimental data corresponding to torsion of samples made from 42CrMo4 steel. Top left: rod with $\phi_{\max} = 0.75$ rad (test number 1); top right: rod with $\phi_{\max} = 1.5$ rad (test number 2); bottom left: thick-walled sample with $\phi_{\max} = 0.75$ rad (test number 3); bottom right: thick-walled sample with $\phi_{\max} = 1.5$ rad (test number 4)

represents only $1/36$ of the real sample, the torque must be multiplied by the factor 36 to obtain the overall torque applied to the sample.

In the following, the synthetic data will be used to identify the material parameters pertaining to the simplified material model with a single rate-independent Maxwell body. Since the simplified model is less accurate, it cannot reproduce the synthetic data exactly, even for a well-identified set of material parameters. Thus, a real-life situation is reproduced that there is an unrecoverable discrepancy between simulation and experiment.

4 Identification Strategies and Optimization Results

In this section we consider all possible strategies of parameter identification which include exactly two different tests from the set shown in Fig. 2. In order to designate each identification strategy we introduce its signature as a 4-tuple (x_1, x_2, x_3, x_4). We set $x_i = 1$ if the test number i is included and $x_i = 0$ otherwise. For instance, strategy signature equals $(1, 0, 1, 0)$ if it includes tests 1 and 3.

Based on the synthetic experimental data we identify the four hardening parameters of the simplified material model which employs only one rate-independent Maxwell body (see Fig. 1(left)). All the torsion tests are simulated using FEM combined with the simplified model. For consistency, exactly the same FEM mesh is employed as the one used in the previous section to generate the synthetic data. Just as for the synthetic data, the loading process is subdivided into 150 time steps.

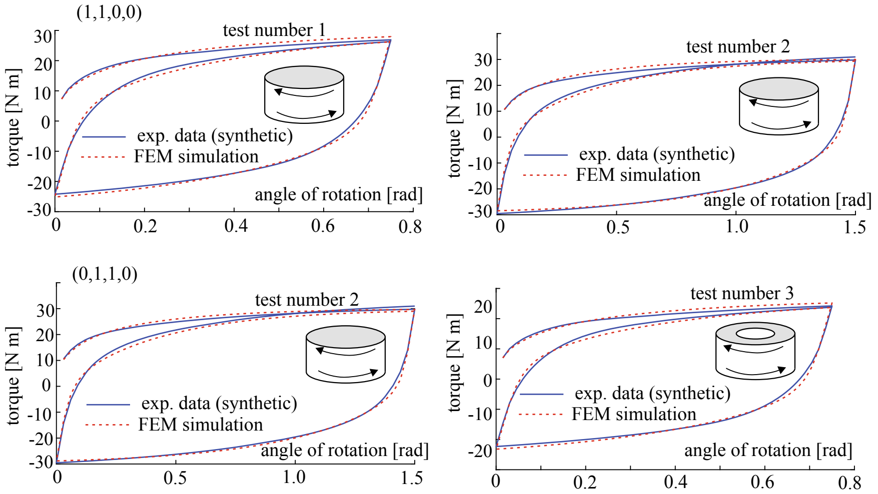

Fig. 3 Optimization results showing the best possible fit of the (synthetic) experimental data by a simplified model. Top: optimization strategy (1, 1, 0, 0); bottom: optimization strategy (0, 1, 1, 0)

Thus, we have exactly 300 data points pertaining to two tests. Following the standard approach we build the following error functional Φ, which reflects an average deviation of the simulation from the (synthetic) experiment:

$$\Phi(\gamma, \beta, c, \varkappa) = \sum_{i=1}^{300} [Exp_i - Mod_i(\gamma, \beta, c, \varkappa)]^2. \qquad (16)$$

Here, Exp_i is the i-th experimental (synthetic) torque and $Mod_i(\gamma, \beta, c, \varkappa)$ is the corresponding model prediction, which depends on the (unknown) material parameters. The error functional is minimized using the gradient-based Levenberg–Marquardt method. The identified vector of material parameters will be denoted as $\mathbf{p}_*$. For all 6 possible strategies, a good (but not perfect) correspondence between simulation and synthetic experiment can be observed. For example, the optimization results are shown in Fig. 3 for the strategies (1, 1, 0, 0) and (0, 1, 1, 0). The identified material parameters are listed in Table 3.

5 Mechanics-Based Metric

In order to measure a distance between two sets of material parameters we introduce a local strain-controlled loading programm. Let T be the duration of the deformation process, $\mathbf{F}(t)$ be the deformation gradient explicitly prescribed as a function of time $t \in [0, T]$. Since the analyzed material model represents a simple material of Noll's

Table 3 Material parameters of the simplified model pertaining to different identification strategies

Strategy	γ [MPa]	β [-]	c [MPa]	$\varkappa$ [1/MPa]
(1, 1, 0, 0)	19951	94.361	3893.2	0.0032882
(1, 0, 1, 0)	30237	155.09	4172.9	0.0035359
(1, 0, 0, 1)	21019	99.340	3878.5	0.0032836
(0, 1, 1, 0)	20346	94.433	3814.4	0.0033129
(0, 1, 0, 1)	14207	67.174	4093.1	0.0032441
(0, 0, 1, 1)	21889	101.52	3801.2	0.0033082

type [9], the local history of the true (Cauchy) stress $\mathbf{T}(t)$ depends on the deformation history $\mathbf{F}(t)$ and the material parameters $\mathbf{p} = (\gamma, \beta, c, \varkappa)^{\mathrm{T}}$:

$$\mathbf{T}(t, \mathbf{p}) = \underset{0 \leq t' \leq t}{\mathfrak{T}} \big(\mathbf{F}(t'), \mathbf{p}\big), \quad \text{for all } t \in [0, T]. \tag{17}$$

The dependence of the stress on the initial conditions is assumed but omitted for brevity. The mechanics-based distance between two sets of material parameters $\mathbf{p}^{(1)} = (\gamma^{(1)}, \beta^{(1)}, c^{(1)}, \varkappa^{(1)})$ and $\mathbf{p}^{(2)} = (\gamma^{(2)}, \beta^{(2)}, c^{(2)}, \varkappa^{(2)})$ is introduced as

$$\mathrm{dist}^{\mathbf{F}}(\mathbf{p}^{(1)}, \mathbf{p}^{(2)}) := \max_{t \in [0,T]} \|\mathbf{T}(t, \mathbf{p}^{(1)}) - \mathbf{T}(t, \mathbf{p}^{(2)})\|. \tag{18}$$

The idea behind the mechanics-based metric is to test the stress response predicted by the material model for a rather general deformation history. While computing the stress response which appears in (18), the viscous part of the model is switched off. For additional details regarding the definition of the metric as well as its advantages over the conventional Euclidian norm, the reader is referred to [15].

To be definite, the following deformation history is used here. In the time interval $t \in [0, 4]$ (t is non-dimensional) we set

$$\mathbf{F}(t) = \overline{\mathbf{F}'(t)}, \tag{19}$$

where $\mathbf{F}'(t)$ is a linear interpolation between key-points $\mathbf{F}_1$, $\mathbf{F}_2$, $\mathbf{F}_3$, and $\mathbf{F}_4$:

$$\mathbf{F}'(t) := \begin{cases} (1-t)\mathbf{F}_1 + (t)\mathbf{F}_2 & \text{if } t \in [0, 1] \\ (2-t)\mathbf{F}_2 + (t-1)\mathbf{F}_3 & \text{if } t \in (1, 2] \\ (3-t)\mathbf{F}_3 + (t-2)\mathbf{F}_4 & \text{if } t \in (2, 3] \\ (4-t)\mathbf{F}_4 + (t-3)\mathbf{F}_1 & \text{if } t \in (3, 4] \end{cases},$$

$$\mathbf{F}_1 := \mathbf{1},\ \mathbf{F}_2 := 1.2\,\mathbf{e}_1 \otimes \mathbf{e}_1 + (1.2)^{-1/2}\,(\mathbf{e}_2 \otimes \mathbf{e}_2 + \mathbf{e}_3 \otimes \mathbf{e}_3),$$

$$\mathbf{F}_3 := \mathbf{1} + 0.2\mathbf{e}_1 \otimes \mathbf{e}_2,\ \mathbf{F}_4 := 1.2\,\mathbf{e}_2 \otimes \mathbf{e}_2 + (1.2)^{-1/2}\,(\mathbf{e}_1 \otimes \mathbf{e}_1 + \mathbf{e}_3 \otimes \mathbf{e}_3).$$

6 Analysis of Stability with Respect to Measurement Errors

In order to estimate the dependence of identified material parameters on the experimental errors the following procedure is employed. Recall that for each identification strategy the optimal vector of material parameters is denoted by $\mathbf{p}_*$ (cf. Table 3). Now, the used experimental data Exp_i are replaced by the noisy ones $Exp_i + Noise_i$ (cf. [3, 4]). In the current contribution the white noise is used, which corresponds to uncorrelated normally distributed noise with a zero expectation:

$$Noise_i \in \mathcal{N}(\mu, \sigma^2), \quad \mu = 0. \tag{20}$$

Then, following the Monte Carlo approach, for the j-th instance of the noisy data the corresponding vector $\mathbf{p}^{(j)}$ of material parameters is identified. In the current study, the applied noise is relatively small. Therefore the parameter vector $\mathbf{p}^{(j)}$ is expected to be close to $\mathbf{p}_*$. Thus, a simplified identification procedure can be used, which is based on the linearization of the model response (see Eq. (24) in Ref. [16]). In total, we use $N_{noise} = 10000$ realizations of the noisy data with the standard deviation $\sigma = 0.3\ N \cdot m$. Finally, the average size of the cloud of material parameters is computed through

$$Size = \frac{1}{N_{noise}} \sum_{j=1}^{N_{noise}} \mathrm{dist}^{\mathbf{F}}(\mathbf{p}_*, \mathbf{p}^{(j)}). \tag{21}$$

The strategy is assumed to be reliable if for realistic standard deviation σ the size of the cloud is sufficiently small. The computed sizes of the clouds for six different strategies are listed in Table 4. Note that the distance has a dimension of pressure (or mechanical stress); here its is measured in MPa. An interesting result is as follows: *Although the analyzed strategies operate with essentially different (synthetic) experimental data, the parameter sensitivity is nearly the same*. The computed sizes of the clouds are sufficiently small: in most applications involving the high-strength steel, an error below 3 MPa is acceptable. The strategy $(1, 1, 0, 0)$ is the most stable with respect to the applied noise. Surprisingly, the size of the parameter cloud pertaining to the strategy $(1, 1, 0, 0)$ is somewhat smaller than for the $(0, 0, 1, 1)$. One explanation is as follows: For both strategies, the stochastic model (20) introduces the same noise in terms of absolute values. But in terms of relative values, the noise for the strategy $(0, 0, 1, 1)$ is larger than for $(1, 1, 0, 0)$.

Table 4 Sizes of the clouds of material parameters in terms of mechanics-based metric

Strategy:	(1, 1, 0, 0)	(1, 0, 1, 0)	(1, 0, 0, 1)	(0, 1, 1, 0)	(0, 1, 0, 1)	(0, 0, 1, 1)
Cloud size:	2.336 MPa	2.598 MPa	2.433 MPa	2.445 MPa	2.818 MPa	2.515 MPa

7 Discussion and Conclusion

In the current study, a simple procedure is demonstrated which allows us to estimate the impact of measurement errors on the resulting vector of material parameters **p**. Various strategies involving different sets of heterogeneous experiments are compared in terms of their sensitivity. For the considered material model, the possibility of material parameter identification based on heterogeneous test data is tested. An important conclusion is that all the strategies exhibit nearly the same sensitivity, which lies in the acceptable range. In the follow-up publication, the set of torsion experiments will be extended by introducing samples with non-circular cross-sections thus bringing us to the problem of optimal experimental design (cf. [5]). The use of different types of samples seems to be promising in obtaining a big variety of loading scenarios. This, in turn, would yield more reliable/stable identification strategies.

Acknowledgements The financial support provided by the RFBR (grant number 17-08-01020) is acknowledged.

References

1. Barraclough, D., Whittaker, H.J., Nair, K.D., Sellars, C.M.: Effect of specimen geometry on hot torsion test results for solid and tubular specimens. J. Test. Evaluat. **1**(3), 220–226 (1973)
2. Beck, J.V., Arnold, K.J.: Parameter Estimation in Engineering and Science. Wiley, New York (2007)
3. Harth, T., Lehn, J.: Identification of material parameters for inelastic constitutive models using stochastic methods. GAMM-Mitt. **30**(2), 409–429 (2007)
4. Harth, T., Schwan, S., Lehn, J., Kollmann, F.G.: Identification of material parameters for inelastic constitutive models: statistical analysis and design of experiments. Int. J. Plast. **20**, 1403–1440 (2004)
5. Herzog, R., Ospald, F.: Parameter identification for short fiber-reinforced plastics using optimal experimental design. Int. J. Numer. Methods Eng. **110**(8), 703–725 (2017)
6. Lion, A.: Constitutive modelling in finite thermoviscoplasticity: a physical approach based on nonlinear rheological elements. Int. J. Plast. **16**, 469–494 (2000)
7. Mahnken, R., Stein, E.: A unified approach for parameter identification of inelastic material models in the frame of the finite element method. Comput. Methods Appl. Mech. Eng. **136**, 225–258 (1996)
8. Naumenko, K., Altenbach, H., Kutschke, A.: A combined model for hardening, softening, and damage processes in advanced heat resistant steels at elevated temperature. Int. J. Damage Mech. **20**, 578–597 (2011)
9. Noll, W.: A new mathematical theory of simple materials. Arch. Ration. Mech. Anal. **48**(1), 243–292 (1972)
10. Scherzer, R., Silbermann, C.B., Ihlemann, J.: FE-simulation of the presta joining process for assembled camshafts — local widening of shafts through rolling. IOP Conf. Ser. Mater. Sci. Eng. **118**, 012039 (2016)
11. Shutov, A.V.: Efficient implicit integration for finite-strain viscoplasticity with a nested multiplicative split. Comput. Methods Appl. Mech. Eng. **306**(1), 151–174 (2016)
12. Shutov, A.V.: Efficient time stepping for the multiplicative Maxwell fluid including the Mooney-Rivlin hyperelasticity. Int. J. Numer. Methods Eng. **113**(12), 1851–1869 (2017)

13. Shutov, A.V., Ihlemann, J.: On the simulation of plastic forming under consideration of thermal effects. Materialwiss. u. Werkstof. **42**(7), 632–638 (2011)
14. Shutov, A.V., Ihlemann, J.: Analysis of some basic approaches to finite strain elasto-plasticity in view of reference change. Int. J. Plast. **63**, 183–197 (2014)
15. Shutov, A.V., Kaygorodtseva, A.A.: Parameter identification in elasto-plasticity: distance between parameters and impact of measurement errors. ZAMM (2019). https://doi.org/10.1002/zamm.201800340
16. Shutov, A.V., Kaygorodtseva, A.A., Dranishnikov, N.S.: Optimal error functional for parameter identification in anisotropic finite strain elasto-plasticity. IOP Conf. Ser. J. Phys. Conf. Ser. **894**(1), 012133 (2017)
17. Shutov, A.V., Kreißig, R.: Finite strain viscoplasticity with nonlinear kinematic hardening: phenomenological modeling and time integration. Comput. Methods Appl. Mech. Eng. **197**, 2015–2029 (2008)
18. Shutov, A.V., Kuprin, C., Ihlemann, J., Wagner, M.F.-X., Silbermann, C.: Experimentelle Untersuchung und numerische Simulation des inkrementellen Umformverhaltens von Stahl 42CrMo4. Materialwiss. und Werkstoff. **41**, 765–775 (2010)
19. Shutov, A.V., Larichkin, A. Yu., Shutov, V.A.: Modelling of cyclic creep in the finite strain range using a nested split of the deformation gradient. ZAMM **97**(9), 1083–1099 (2017)
20. Shutov, A.V., Pfeiffer, S., Ihlemann, J.: On the simulation of multi-stage forming processes: invariance under change of the reference configuration. Mater. Sci. Eng. Tech. **43**(7), 617–625 (2012)
21. Shutov, A.V., Silbermann, C.B., Ihlemann, J.: Ductile damage model for metal forming simulations including refined description of void nucleation. Int. J. Plast. **71**, 195–217 (2015)

Short Term Transversally Isotropic Creep of Plates Under Static and Periodic Loading

Holm Altenbach, Dmitry Breslavsky, Volodymyr Mietielov and Oksana Tatarinova

Abstract The statement and solution method of the two-dimensional problem of orthotropic creep under static and periodic loadings are presented. Experimental investigations of short-term deformation under uni-axial and plane stress states are carried out. Short-term creep curves were obtained for uni-axial specimens and plates with holes. Constitutive equations are developed for steel characterized by the first stage of unsteady creep with orthotropic properties under static and periodic loading. The calculation method in general was verified by comparing numerical and experimental results under the uni-axial and plane stress states.

Keywords Short-term creep · Orthotropic properties · Plane stress state · FEM · Experimental investigations

1 Motivation

Creep in metallic materials can occur at all temperatures and stress levels. As it was pointed out by Lemaitre and Chaboche [1], some alloys exhibit visco-plasticity (creep) at room temperatures (300 K), despite the fact that their melting temperatures can reach 1400 K.

H. Altenbach
Institut für Mechanik, Fakultät für Maschinenbau, Otto-von-Guericke-Universität Magdeburg,
Universitätsplatz 2, 39106 Magdeburg, Germany
e-mail: holm.altenbach@ovgu.de

D. Breslavsky (✉) · V. Mietielov · O. Tatarinova
Department of Computer Modeling of Processes and Systems, National Technical University
'Kharkiv Polytechnic Institute', 2 Kyrpychova str., Kharkiv 61002, Ukraine
e-mail: brdm@kpi.kharkov.ua

V. Mietielov
e-mail: vometel@gmail.com

O. Tatarinova
e-mail: ok.tatarinova@gmail.com

K. Naumenko and M. Krüger (eds.), *Advances in Mechanics of High-Temperature Materials*, Advanced Structured Materials 117,
https://doi.org/10.1007/978-3-030-23869-8_9

With a significant level of stress, which in most cases exceeding the yield limit, and at room temperature, varying in time strains can reach significant values in structural steels. Because of the general rather high level of stresses, creep cannot run too long: either tertiary creep occurs with damage increase, resulting in fracture, or saturation occurs, at which the creep rate drops significantly. In both considered cases, the so-called short-term creep takes place.

Rabotnov and Mileiko [2] define short-term creep as a process of metal creep when a significant deformation, that limits the service function of the structural element and runs over a relatively short period of time. The authors emphasize that under such a significant stress the strain value 5% can be accepted. In the case of short-term creep, the deformation time is from tens to 1000 s. In [2] is noted, that approaches to the solution of short-term creep problems should be applied in the cases where the effect of sufficiently significant loads presents within a short time, and the accumulated creep strains are commensurate with instantaneous elastic-plastic deformations.

Examples of experimental studies of short-term creep as well as methods of its numerical simulation are given in [2–6] among others. As in [2] is emphasized, the models and methods traditionally used in creep calculations can also be used for the description of short-term processes. In this case, in almost all situations, the use of numerical methods of calculation is necessary.

In many cases, short-term creep occurs during cyclic deformation at low and room temperatures. In [7, 8] the results of experimental studies of cyclic creep at room temperatures of titanium alloys are considered. In [9] the similar behavioir of carbon steels was studied. Short-time creep under vibration loading, which leads to processes of dynamic creep in materials [3], was studied for alloys of non-ferrous metals and solders [10, 12, 13] as well as and for heat-resistant alloys [11].

In various technological processes due to the non-uniform mechanical actions, materials with anisotropic mechanical properties, including creep properties, are obtained. When rolling sheet materials, transversal isotropy of the plasticity and creep properties is often realized [14–16]. The models of Hill, Malinin – Khazhinsky and others are used for its description [1, 3, 4, 15, 16].

Also in technological processes sheet materials are subjected to the joint action of static and periodically (i.e. cyclically with the same cycle shape) varying loads. For the case of the same loading cycles for solving the initial-boundary value problem and formulating the governing equations, it is effective to use the multi-scale method with subsequent averaging over the period of stress variation. In [17, 18] this approach was applied to materials with isotropic creep properties, and in [19] a model for describing creep and damage of transversely isotropic materials is presented.

The problem statement describing the creep of transversally isotropic materials under conditions of a plane stress state and periodic loading is presented in this chapter. The formulation of the method for solving initial-boundary value problems based on using the methods of asymptotic expansions and averaging on a time period is given. The govering system of differential equations is solved using the finite element and difference methods in the time domain. The cases of static and combined static and periodically varying loading under uniaxial and two-dimensional plane stress state are considered. The results of an experimental study of the creep of specimens and plates with holes allow verifying the constitutive equations and the calculation method.

2 Problem Statement and Method of Solution

Let us consider the mathematical statement of a two-dimensional creep problem for the area Ω with boundary curve Γ. The Cartesian coordinate system x_i ($i = 1, 2$) is used. We assume that the displacements $u_i|_{\Gamma_1} = \tilde{u}_i$ are specified on the part of the boundary Γ_1. The part of the boundary Γ_2 is loaded by tractions $p_i(x,t)$, and we do not consider the volume forces. The elastic and plastic properties of the material are considered as isotropic as well as the creep properties as transversally isotropic. The case of constant temperature is assumed.

We apply the Lagrange approach and the case of small strains is considered. The following notations are used: $\mathbf{u} = \mathbf{u}(x_i, t)$ is the displacement vector, $\boldsymbol{\varepsilon} = \boldsymbol{\varepsilon}(x_i, t)$, $\boldsymbol{\varepsilon}^{pl} = \boldsymbol{\varepsilon}^{pl}(x_i, t)$, $\boldsymbol{\varepsilon}^{c} = \boldsymbol{\varepsilon}^{c}(x_i, t)$ are the tensors of total strains, plastic and creep strains, respectively; $\boldsymbol{\sigma} = \boldsymbol{\sigma}(x_i, t)$ is the stress tensor, t denotes the time variable. The basic system of equations of the creep theory for the two-dimensional case has the following form [1]

$$\begin{gathered}\sigma_{ij,j} = \gamma \ddot{u}_i;\, \sigma_{ij} n_j = p_i(x);\, x \in \Gamma_2 \\ \varepsilon_{ij} = \tfrac{1}{2}\left(u_{i,j} + u_{j,i}\right), x \in \Omega;\ u_i|_{\Gamma_1} = \tilde{u}_i;\, x \in \Gamma_1;\, i, j = 1, 2 \\ \sigma_{ij} = C_{ijkl}\left(\varepsilon_{ij} - \varepsilon_{ij}^{pl} - \varepsilon_{ij}^{c}\right);\, \mathbf{u}(x_i, 0) = \mathbf{u}_0(x);\ \ \varepsilon_{ij}^{c}(x_i, 0) = 0.\end{gathered} \tag{1}$$

Here, $\mathbf{n}(n_1,n_2)$ is the unit vector of the normal to the contour, γ is the density of the material. The system (1) has to be added by a creep law.

The initial conditions are presented by the vector $\mathbf{u_0}$, determined by the solution of the system (1) in the initial elastic ($\boldsymbol{\varepsilon}^{pl} = \boldsymbol{\varepsilon}^{c} = 0$) or elastic-plastic ($\varepsilon^{c} = 0$) stress-strain states.

As is known [20], the most effective way for solving the problem is the expansion of the time-varying load component acting on the part of the contour Γ_2, in the Fourier series and subsequent representation of $p_i(x,t)$ in the following form

$$p_i(x_i, t) = p_i^0(x_i) + p_i^{\max}(x_i)\Psi^{(1)}(t), i = 1, 2. \tag{2}$$

Here the following notations are used:
$p_i^0(x_i)$ is the time-independent load component; $\Psi^{(1)}(t) = \sum_{k=1}^{\infty} \Psi_k = \sum_{k=1}^{\infty} A_k \sin(\tilde{p}_k t + \beta_k)$ is the component of the load, which varies in time with the period T;

$$\Psi_k(t) = a_k \cos\left(\frac{2\pi k}{T_p} t\right) + b_k \sin\left(\frac{2\pi k}{T_p} t\right);$$

$$A_k = \left(a_k^2 + b_k^2\right)^{1/2};\ \tilde{p}_k = \frac{2\pi k}{T_p};\ \beta_k = \mathrm{arctg}(a_k/b_k);$$

a_k, b_k are coefficients of the Fourier series; p_i^{max} are amplitude values of load components.

Following the approaches proposed in [17–19], the solution of the system (1), taking into account the acting variable load (2), can be found by the application of the method of multi-time scales with subsequent time averaging [21]. According to these approaches, the solution of system (1) can be determined by the solution of such a similar system, in which only unvaried load is taking into account. In this case, the amplitude values of the components of the stress-strain state, which are determined by the action of the variable component $\Psi^{(1)}$, are included into the creep law of special form.

To determine the components of the strain-stress state under creep, which occurs as a result of the action of constant and periodically varying loads, the solution of the following system of equations is necessary:

$$\begin{gathered} \sigma_{ij,j} = 0, \quad x_i \in \Omega;\ i = 1, 2 \\ \sigma_{ij} n_j = p_i^0, \quad x_i \in \Gamma_2; \\ \sigma_{ij} = C_{ijkl}\left(\varepsilon_{ij} - \varepsilon_{ij}^{pl} - \varepsilon_{ij}^{c}\right);\ \varepsilon_{ij} = \tfrac{1}{2}\left(u_{i,j} + u_{j,i}\right), x \in \Omega;\ u_i|_{\Gamma_1} = \tilde{u}_i;\ x \in \Gamma_1; \\ \mathbf{u}(x_i, 0) = \mathbf{u}_0(x); \quad \varepsilon_{ij}^{c}(x_i, 0) = 0. \end{gathered} \tag{3}$$

Now let us consider the creep law of transversally-isotropic material for the case of primary creep. For the case of static load, it is given in [19, 22]:

$$\dot{\boldsymbol{\varepsilon}}^c = \tilde{B}\left(\boldsymbol{\varepsilon}_{vM}^c\right)^{-\alpha} \boldsymbol{\sigma}_v^{n-1}\left[\overline{B}\right]\boldsymbol{\sigma}. \tag{4}$$

The plane stress state is considered, and the following notations are introduced: $\boldsymbol{\varepsilon}^c$ is the vector of creep strain; $\boldsymbol{\sigma}$ is stress vector; $\left[\overline{B}\right]$ is a matrix containing creep constants for transversally isotropic material in the case of two-dimensional stress state. b_{ijkl} are the components of the tensor containg the creep properties of the material; $\varepsilon_{vM}^c = \sqrt{\frac{2}{3}\varepsilon_{ij}^c \varepsilon_{ij}^c}$ is the von Mises creep strain; $\sigma_v = \boldsymbol{\sigma}^T[B]\boldsymbol{\sigma}$ is the equivalent stress, which is a common invariant of the stress tensor and the tensor of material parameters

$$\sigma_{\mathrm{v}} = \left(b_{1111}\sigma_{11}^2 + 2b_{1122}\sigma_{11}\sigma_{22} + b_{2222}\sigma_{22}^2 + 4b_{1212}\sigma_{12}^2\right)^{1/2};$$

$\tilde{B}$, α, n are creep parameters.

Equation (4) is formulated for the case when the main axes of anisotropy (transversal isotropy in this case) coincide with the axes of the Cartesian coordinate system. In the case when they are rotated one to another by the angle θ, the relations (3) can be modified by converting the components of stress tensors and creep strain rates. In this case, the matrix of the coordinate transformation, which is dependent from the angle θ [23], should be added to the right-hand side of (3) as a factor.

Let us present the way of the creep equation deriving for the case of periodic loading [22]. First, we consider the case of uniaxial stress state when a combined cyclic stress $\sigma = \sigma^0 + \sigma^1$ operates on a point (or specimen). Here, the constant stress denotes as σ^0 and stress σ^1 varies with the cyclic frequency $f_1 = 1/T_p$ over the period of the cycle T_p ($f_1 \ll 1$ Hz). In the general case, the stress σ^1 is determined by the parameters of the operating cycle with amplitude, which periodically increases and decreases.

We present the form of the stress σ^1 by expansions in the periodic Fourier series with coefficients a_k and b_k ($k = 1, 2, \ldots$):

$$\sigma^1 = \sigma^{\max}\left(\sum_{k=1}^{\infty}\left(a_k \cos\left(\tfrac{2\pi k}{T_p}t\right) + b_k \sin\left(\tfrac{2\pi k}{T_p}t\right)\right)\right) = \sum_{k=1}^{\infty} \sigma^{ak} \sin\left(\tfrac{2\pi k}{T_p}t + \beta_k\right),$$
$$\sigma^{ak} = \sqrt{\left(\sigma^{\max} a_k\right)^2 + \left(\sigma^{\max} b_k\right)^2},\ \beta_k = \mathrm{arctg}(a_k/b_k), \tag{5}$$

For a combined load, the law of periodic stress varying can be written in such form:

$$\sigma = \sigma^0 + \sigma^1 = \sigma^0\left(1 + \sum_{k=1}^{\infty} M_k \sin\left(\frac{2\pi k}{T_p}t + \beta_k\right)\right), \tag{6}$$

where $M_k = \frac{\sigma^{ak}}{\sigma^0}$ are the stress cycle amplitude coefficients, $\sigma^0 \neq 0$.

Let us rewrite Eq. (4) for a uniaxial stress state:

$$\dot{\varepsilon}^c = \tilde{B}\left(\varepsilon^c\right)^{-\alpha}\sigma^n. \tag{7}$$

We will use the method of multi- (two in the considered problem) scales and asymptotic expansion of the basic unknowns on small parameter $\mu = T_p/t$. We apply this approach to Eq. (7). Let us introduce the process of creep strain growth in two time scales (slow t and fast $\xi = \tau/T_p$, where $\tau = t/\mu$) using the form of asymptotic expansion:

$$\varepsilon^c \cong \varepsilon^{c0}(t) + \mu\varepsilon^{c1}(\xi), \tag{8}$$

where $\varepsilon^{c0}(t),\ \varepsilon^{c1}(\xi)$ are the functions corresponding to the basic process of creep in slow (0) and fast (1) scales of time. We limit us only by the first approximation, assuming in (8) the members with higher degrees of the parameter μ are too small. Further, we can obtain

$$\left(\varepsilon^{c0} + \mu\varepsilon^{c1}\right)^{\alpha} = \varepsilon^{c0}\left(1 + \mu\frac{\varepsilon^{c1}}{\varepsilon^{c0}}\right)^{\alpha} \cong \varepsilon^{c0}. \tag{9}$$

Taking into account the dependence of the creep strain only on the “slow” time [17, 18], after averaging over a period on the “fast” scale, we obtain:

$$\left\langle \varepsilon^{c0}(\xi)\right\rangle = \int\limits_0^1 \varepsilon^{c0}(t)\,d\xi \cong \varepsilon^{c0}(t), \left\langle \varepsilon^{c1}(\xi)\right\rangle = \int\limits_0^1 \varepsilon^{c1}(\xi)d\xi \cong 0. \tag{10}$$

Thus, using the method of asymptotic expansion with a subsequent averaging over the cyclic load period (10), for a uniaxial stress state we obtain the law of creep during periodic loading for materials with transversally isotropic creep properties:

$$\dot{\varepsilon}^c = \tilde{B}\left(\sigma^0\right)^n K\left(M^{(n)}\right)\left(\varepsilon^c\right)^{-\alpha}, \tag{11}$$

where $K(M^{(n)}) = \int_0^1 \left(1 + \sum_{k=1}^{\infty} M_k^{(n)} \sin(2\pi k\xi + \beta_k)\right)^n d\xi$, $M^{(n)} = \frac{\sigma^{ak}}{\sigma^0}$ is the coefficient of asymmetry of the stress cycle.

We generalize Eq. (11) for the case of a complex stress state, proceeding from the traditional postulate of creep theory, which establishes the correspondence between the values of stresses and strain rates at uniaxial and complex stress states [1, 3]. Then Eq. (4), taking into account (11), is rewritten in the following form:

$$\dot{\varepsilon}^{c0} = \tilde{B}\left(\varepsilon^{c0}_{vM}\right)^{-\alpha}\sigma_v^{0n-1} K\left(M^{(n)}\right)\left[\overline{B}\right]\sigma^0 \tag{12}$$

where $\boldsymbol{\varepsilon}^{c0}_{vM} = \sqrt{\frac{2}{3}\varepsilon^{c0}_{ij}\varepsilon^{c0}_{ij}}$ is the von Mises strain and $\boldsymbol{\sigma}^0_v = \boldsymbol{\sigma}^{0T}[B]\boldsymbol{\sigma}^0$ is the equivalent stress, which is a common invariant of the stress tensor and the tensor of material parameters. It is determined by the components of the stress tensor in the “slow” process; $\mathrm{M}^{(n)} = \frac{\sigma_v^{ak}}{\sigma_v^0}$ is the stress cycle asymmetry coefficient; $\sigma_{\mathrm{v}}^{\mathrm{ak}} = \boldsymbol{\sigma}^{akT}[B]\boldsymbol{\sigma}^{ak}$ is an invariant of amplitude stresses. In the widespread case, when the components of the stress tensor are varyied in time by stepped law, the Eq. (5) will take the following form:

$$\begin{aligned}
\boldsymbol{\sigma} &= \boldsymbol{\sigma}^0 + \boldsymbol{\sigma}^1 = \boldsymbol{\sigma}^0\left(1 + \sum_{k=1}^{\infty} M_k \sin\left(\frac{2\pi k}{T_p}t + \beta_k\right)\right), \\
\boldsymbol{\sigma}^{ak} &= \sqrt{\left(\boldsymbol{\sigma}^{\max} a_k\right)^2 + \left(\boldsymbol{\sigma}^{\max} b_k\right)^2}, \beta_k = \mathrm{arctg}(a_k/b_k), \\
a_k &= \frac{1}{\pi k}\sin\left(\frac{2T_s}{T_p}\pi k\right), b_k = \frac{1}{\pi k}\left(1 - \cos\left(\frac{2T_s}{T_p}\pi k\right)\right).
\end{aligned} \tag{13}$$

Here T_s is the value of time of the action of the larger stress $\sigma^0 + \sigma^{max}$; T_p is the value of time of less stress σ^0 action.

As was obtained [17, 18], for the case of a plane stress state, the components of amplitude stress tensors are determined by the solution of the following system ($k = 1, 2, \ldots ..$)

$$\begin{gathered}\sigma_{ij,j}^{ak} = -\gamma(\tilde{p}_k)^2 u_i^{ak},\, x_i \in \Omega; \\ \sigma_{ij}^{ak} n_j = p_i^{\max} A_k,\ x_i \in \Gamma_2; \\ \varepsilon_{ij}^{ak} = \frac{1}{2}\left(u_{i,j}^{ak} + u_{j,i}^{ak}\right) = C_{ijmn}\sigma_{mn}^{ak},\, x_i \in \Omega; \\ u_i^{ak}(0) = 0,\, x_i \in \Gamma_1;\end{gathered} \tag{14}$$

By solution of the system (14), for each kth harmonic, the components of amplitude stresses can be found. This determines the coefficients included in the constitutive Eq. (11).

In the case when the initial von Mises stresses are greater than the yield limit of material, the problem of elastic-plastic deformation is necessary to solve in order to determine the initial conditions for the systems (1) or (3):

$$\begin{gathered}\sigma_{ij,j} = 0_i;\, \sigma_{ij} n_j = p_i(x);\, x \in \Gamma_2 \\ \varepsilon_{ij} = \frac{1}{2}\left(u_{i,j} + u_{j,i}\right),\, x \in \Omega;\ u_i|_{\Gamma_1} = \tilde{u}_i;\, x \in \Gamma_1;\, i = 1, 2 \\ \sigma_{ij} = C_{ijkl}\left(\varepsilon_{ij} - \varepsilon_{ij}^{pl}\right); \\ f\left(\sigma_{ij}\right) = \frac{3}{2} s_{ij} s_{ij} - \Phi\left(\int d\bar{\varepsilon}_i^{pl}\right)^2;\, \varepsilon_i^{pl} = \Phi\left(\int d\bar{\varepsilon}_i^{pl}\right);\, d\varepsilon_{ij}^{pl} = \frac{3}{2}\frac{d\bar{\varepsilon}_i^{pl}}{\sigma_i} s_{ij}.\end{gathered} \tag{15}$$

3 Numerical Solution

As a method of solution of systems (3), (14) and (15), the finite element method (FEM) is used. Applying the main approaches of FEM, we arrive to a system of differential equations [24] for a finite element

$$\left(\int\limits_V [B]^T [C][B] dV\right)\dot{\mathbf{u}}^\gamma = \int\limits_V [B]^T [C]\dot{\varepsilon}^{c\beta} dV + \int\limits_{S_1} [N]^T \dot{\mathbf{p}} dS \tag{16}$$

$$\dot{\boldsymbol{\sigma}}^\beta = [C]\left(\dot{\boldsymbol{\varepsilon}}^\beta - \dot{\boldsymbol{\varepsilon}}^{c\beta}\right), \tag{17}$$

$$\dot{\boldsymbol{\varepsilon}}^\beta = [B]\dot{\mathbf{u}}^\gamma, \tag{18}$$

where $[B]$ is the deformation matrix of the element with number β; $[C]$ is the matrix containing elastic properties of the material (matrix of elasticity); $\mathbf{u}^\gamma$ is the vector of the nodal displacements of the element, $\boldsymbol{\gamma}$ is a number of node; $\boldsymbol{\sigma}^\beta$, $\boldsymbol{\varepsilon}^\beta$ are the vectors of stress and strains in the element; $[N]$ is the matrix of shape functions values; $\boldsymbol{p}$ is a traction vector. The complete system of equations for the whole model is obtained by ensembling the element's stiffness matrices into the global stiffness matrix $[K]$ as well as the vector of nodal forces $\{F\}$ [25]. Finally, for creep problems it has the following form

$$[K]\dot{\mathbf{U}} = \dot{\mathbf{F}} + \dot{\mathbf{F}}^{\mathbf{C}}. \tag{19}$$

Here $\mathbf{U}$ is the global vector of nodal displacements; $\mathbf{F}^c$ is the vector obtained by the values of forces, caused by creep strains. The solution of system (14) is obtained for the values of the nodal displacements in the same way (without creep strains).

The considered finite element formulation was implemented into the software complex *FEM CREEP* [24] and used for calculations. In the calculations, a triangular three-node finite element with a linear approximation of the displacements per element was used. The obtained systems of differential Eq. (19) are solved by the predictor-corrector method of third order or by the Euler method [20]. According to the generally accepted problem statement [26] for integrating the physically nonlinear creep problems, at each time step the vector of creep strain rates $\dot{\boldsymbol{\varepsilon}}^c = \left(\dot{\boldsymbol{\varepsilon}}_{11}^c, \dot{\boldsymbol{\varepsilon}}_{22}^c, 2\dot{\boldsymbol{\varepsilon}}_{12}^c\right)^T$ is calculated using the stress vector $\boldsymbol{\sigma} = (\sigma_{11}, \sigma_{22}, \sigma_{12})^{\mathrm{T}}$, obtained in the previous time step, and the creep law (11):

$$\dot{\boldsymbol{\varepsilon}}^c = \tilde{B}\left(\boldsymbol{\varepsilon}_{vM}^c\right)^{-\alpha} \sigma_v^{n-1} \left[\overline{B}\right] \boldsymbol{\sigma}. \tag{20}$$

We have added for the case of a static load and for the case of a periodic load the expression of the influence function:

$$\dot{\boldsymbol{\varepsilon}}^c = \tilde{B}\left(\varepsilon_{vM}^c\right)^{-\alpha} \sigma_v^{n-1} K\left(\mathrm{M}^{(n)}\right) \left[\overline{B}\right] \boldsymbol{\sigma} \tag{21}$$

At each integration step, the system of linear algebraic equations is solved by the Cholesky decomposition [25].

In many cases, the initial load value is such that the von Mises stress exceeds the yield limit and the strain vector in the finite element consists of elastic and plastic components:

$$\boldsymbol{\varepsilon} = \mathbf{e} + \boldsymbol{\varepsilon}^{pl}. \tag{22}$$

A schematic stress-strain diagram in one-dimensional case is shown at Fig. 1, where 1 corresponds to elastic strains, 2 to yield plateau and 3 to plastic strains with hardening.

To determine the values of the initial plastic strain components, the method known as “increment-initial strain” method [25] was used.

At first, let us consider the algorithm for materials with hardening (linear or power law), when the yield plateau is absent, $\varepsilon^{\Pi} = 0$, and after the first part of the curve the third occurs [4]. We apply the Hencky-von Mises theory [1]. According to this theory, we assume that the increment of the strain vector components $\{\Delta\boldsymbol{\varepsilon}\}^{pl} = \{\Delta\varepsilon_x, \Delta\varepsilon_y, \Delta\gamma_{xy}\}$ is proportional to the effective stress, and the factor depends on the growth of the effective stress σ_{vM}

$$\begin{bmatrix} \Delta\varepsilon_x^{pl} \\ \Delta\varepsilon_x^{pl} \\ \Delta\gamma_{xy}^{pl} \end{bmatrix} = \frac{3}{2}\frac{d\bar{p}_i}{\sigma_{vM}} \begin{bmatrix} 1 & 0 & 0 \\ 0 & 1 & 0 \\ 0 & 0 & 2 \end{bmatrix} \begin{bmatrix} s_x \\ s_y \\ s_{xy} \end{bmatrix}, \tag{23}$$

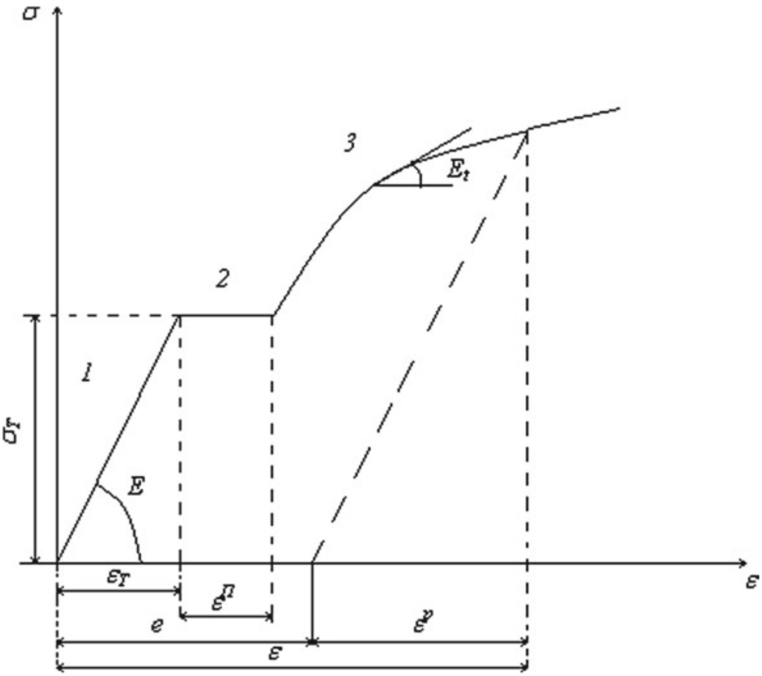

Fig. 1 Schematic stress-strain diagram

where $d\bar{p}_i = \frac{\sqrt{2}}{3}\sqrt{(\Delta\varepsilon_x^{pl} - \Delta\varepsilon_e^{pl})^2 + (\Delta\varepsilon_x^{pl})^2 + (\Delta\varepsilon_y^{pl})^2 + \frac{3}{2}(\Delta\gamma_{xy}^{pl})^2}$. Further we calculate the nodal forces that correspond to the plastic strains considered at the current stage $\Delta\boldsymbol{\varepsilon}^{pl}$, and a system of linear algebraic equations for a finite element is solved

$$\left(\int\limits_V [B]^T[C][B]dV\right)\{\Delta u^\gamma\} = \int\limits_V [B]^T[C]\left\{\Delta\varepsilon^{pl\beta}\right\}dV + \int\limits_{S_1} [N]^T\{\Delta p\}dS \quad (24)$$

$$\left\{\Delta\sigma^\beta\right\} = [C]\left(\boldsymbol{\varepsilon}^\beta - \boldsymbol{\varepsilon}^{pl\beta}\right), \quad (25)$$

$$\boldsymbol{\varepsilon}^\beta = [B]\mathbf{u}^\gamma. \quad (26)$$

At each step the recalculation of the stiffness matrix of the element according to the stress-strain diagram (Fig. 1) with the correspondent tangent module E_t should be performed. It is considered [25, 26] that the load is added in small increment. The relations (24)–(26) are applied from the moment of approaching the von Mises stress σ_i the value of the yield limit σ_T. With each small load step, the required values of the strain components are calculated as

$$\boldsymbol{\varepsilon}_{ij}^{pl\beta} = \boldsymbol{\varepsilon}_{ij}^{pl\beta} + \Delta\boldsymbol{\varepsilon}_{ij}^{pl\beta} \tag{27}$$

The calculations are performed until the "moment" when the external load value is given by the conditions of the considered problem.

This algorithm can be modified for materials, which stress-strain diagram has a so-called "yield plateau". This behavior is classified as an ideal plastic solid [1, 4]. The problem is to determine the accumulated total strain in the solid at the "moment" when the accumulated value of the von Mises strain ε_{vM} is approached and the transition to the zone 3 of the diagram begins (Fig. 1). A direct iterative method is used for calculations [25]. This method is based on the sequence of approximations, which is presented for the uniaxial stress-strain state in this way

$$\begin{aligned} E(\sigma) &= E_0, \sigma < \sigma_T, \\ E(\sigma) &= \frac{E_0\varepsilon_0}{\varepsilon}, \sigma > \sigma_T. \end{aligned} \tag{28}$$

Here the index «0» indicates the current values on the yield plateu.

In the case of a biaxial stress state, the current (tangential) module $E(E_t)$ depends on the invariants of the strain or stress tensor. The algorithm for solving this can be formulated as follows:

1. The problem of "elastic" strains, described by the system (19) is considered. The components of the stress-strain state are determined using the initial values of the elastic modulus E and the Poisson's coefficient ν.
2. For each finite element new values of E and ν are determined, depending on the strain values obtained in the previous step (von Mises strains and stresses are used in Eq. (28)).
3. An "elastic" calculation again is made in which the parameters E and ν defined in the previous step are used.

Steps 2 and 3 are repeated until convergence is achieved, for example, for n and $n+\ 1$ steps the condition $\left|\varepsilon_i^{n+1} - \varepsilon_i^n\right| < \delta$ is used.

For materials in which the stress-strain diagram after the yield plateau is of hardening type (Fig. 1), the algorithms considered are combined: after the calculation of the ideal plastic solid, the distribution of components of the stress-strain state is used as the initial values for calculations based on the hardening model.

4 Short-Term Creep of Uniaxial Specimens

To verify the developed method of calculation and constitutive equations, several experimental investigations were realized. Creep of uniaxial specimens and plates with holes under tension made from steel 3 (its chemical composition in %: 0.58 – 0.67 C, 0.22 – 0.45 Si, 0.5 – 0.9 Mn, max 0.02 S, max 0.03P, 0.08 – 0.15 V, the rest is Fe; closest analogues are A107 or USt 37–2) was considered. This steel is widely used in manufacturing and in construction, for example, in form of complex profiles which was bent from it. This technological operation can run for a rather long time (tens of seconds) with a high level of stress. Steel sheets are produced by rolling, which leads to the transversal isotropy of the creep properties. Therefore, for computer simulation of technological processes it is necessary to have a proven method of calculation and constitutive equation that are implemented in the corresponding software.

The results of the experimental study at room temperature of uniaxial specimens from steel 3 under tension are given in [22]. In experiments with static loading 27 samples were tested at three stress levels: 378.7 MPa, 366.8 MPa and 352.3 MPa. All exceed the yield limit $\sigma_y = 295.8$ MPa. Specimens were cut from the sheets in three directions—along, across the rolling direction and at an angle of 45° to the lat one direction.

The results of the investigations confirmed the hypothesis of transversal isotropy of the creep properties of this material at room temperature. Then the parameter's values for Eq. (4) were determined. Its integrated form was used:

$$\varepsilon_i^c = b_i \sigma^m t^k. \tag{29}$$

where: $b_i = ((\alpha + 1)B_i)^{\frac{1}{\alpha+1}}$, $i = 1, 2, 3$, $m = \frac{n}{\alpha+1}$, $k = \frac{1}{\alpha+1}$. After processing the experimental data, we obtained:

$m = 18.305$, $k = 0.1887$; $\left((\alpha + 1)\tilde{B}\right)^{\frac{1}{\alpha+1}} = b_1 = 3.166.10^{-31}$ $(10\ \mathrm{MPa})^{-\mathrm{m}}/\mathrm{h}$, $b_2 = 0.75b_1$, $b_3 = 0.42b_1$, $n = 96.99$, $\alpha = 4.3$, $b_{1111} = 6.9 \cdot 10^{-4}$, $b_{1122} = -3.45 \cdot 10^{-4}$, $b_{2222} = 6.7 \cdot 10^{-4}$, $b_{1212} = 1.85 \cdot 10^{-4}$, $(10\ \mathrm{MPa})^{-2\mathrm{m/m}+1}/\mathrm{h}^{2/\mathrm{m}+1}$.

As an example, the curves of static short-term creep for specimens which were cut in the rolling direction are presented in Fig. 2. Experimental data are presented by points. Solid lines correspond to calculated data. The curves are built for tensional stress values: curve 1: 378.7 MPa; curve 2: 366.8 MPa; curve 3: 352.3 MPa. In all cases, the difference between the experimental and estimated data did not exceed 15%.

Experiments were also carried out according to the stepped periodic loading program (Fig. 3).

In experiments, it was specified: $T_s = 60$ s. (0.0166 h), $T_p = 240$ s. (0.0066 h). Experiments were done for 10 load cycles (total time 2400 s.). The stress values were $\sigma = 352.3$ MPa, $\sigma^{max} = 26.4$ MPa. During the first 60 s in a cycle, the specimens were loaded with a stress $\sigma = 352.3$ MPa, then 180 s with the stress $\sigma = 378.7$ MPa. These stress values are the minimum and maximum load values used in static experiments.

The derived creep law for the periodic loading Eq. (11) was verified using comparison with the experimental curves. The calculation of the creep curves, which corresponds to the cycle load applied in the experiment, was performed by developed computer program based on C-language. The results of calculations are shown on Fig. 4. Here, curve 1 corresponds to the data for the specimens cutted in the longitudinal direction, curve 2: transversal direction; curve 3 at an angle of 45° to

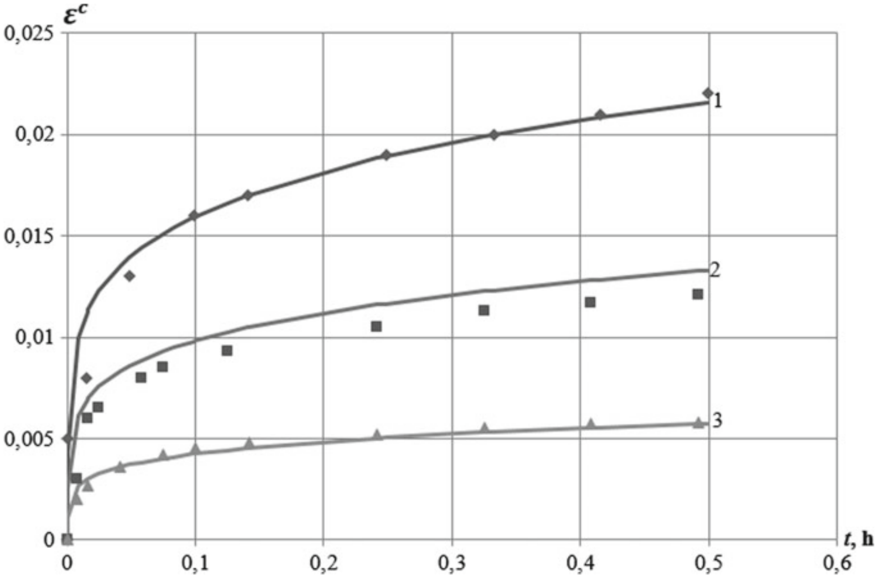

Fig. 2 Static loading. Comparison of numerical and experimental creep curves (specimens cutted in the rolling direction)

Fig. 3 Program of periodic loading

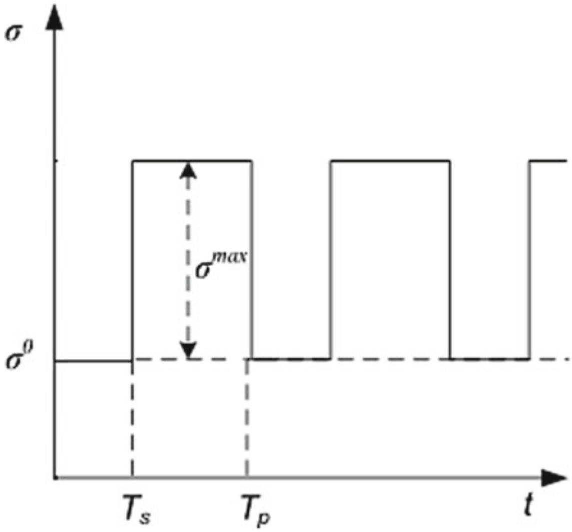

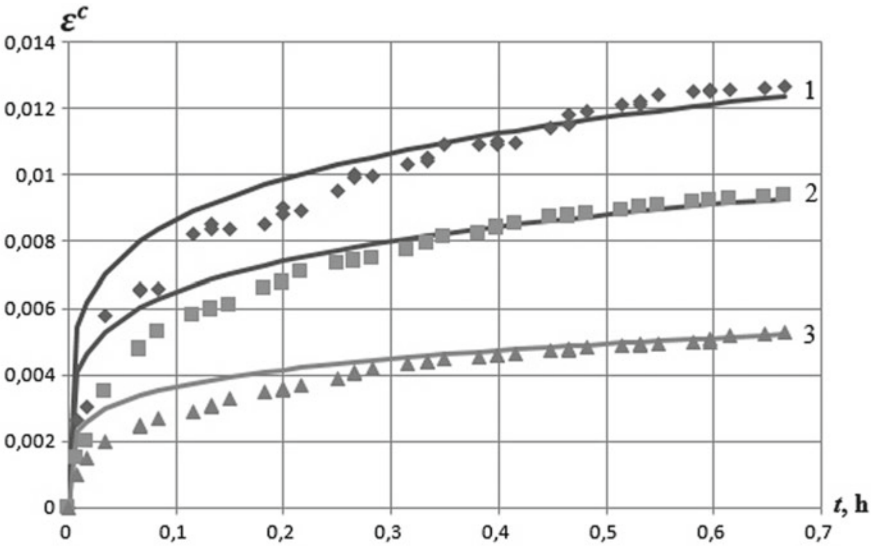

Fig. 4 Periodic loading. Comparison between calculated and experimental data

the rolling direction. Experimental data averaged by three specimens are marked by points, calculated data presented by solid curves.

Figure 4 shows that the proposed creep equations for the case of periodic stress action describe in a satisfactory manner the experimentally obtained curves starting from the 4–5th cycle. The maximum error is obtained in first cycles and is equal to 35%. This takes place because for a small number (1–3) of load cycles, where the value of the parameter μ cannot be considered as small, the averaged equation is not entirely correct. The greater number of load cycles, the less error. Its value in 4–10th cycles does not exceed 10%. It can be seen from the graphs that for the considered creep time the application of the developed averaged equation is acceptable: starting from the fourth load cycle, the difference in experimental and numerical results is insignificant.

The testing of the method's efficiency and the developed software for modeling of transversally isotropic creep under assumption of plane stress state was performed with numerical simulations of plane specimens cutted in different directions. In this case, the specimens are modeled as plane rectangles, loaded with a traction along the axis, which is parallel to their long side. Because the results of experiments were obtained on plane specimens from steel 3, the same typical location of FE models with orientation of 0°, 45° and 90° to the rolling direction was considered. Three FE schemes corresponding to the specified directions are shown in Fig. 5

All three FE models were used for calculations up to 0.5 h, which correspond to the time of the experiments. It was assumed in all calculations, that the models were loaded by tensile traction equal to 378.7 MPa.

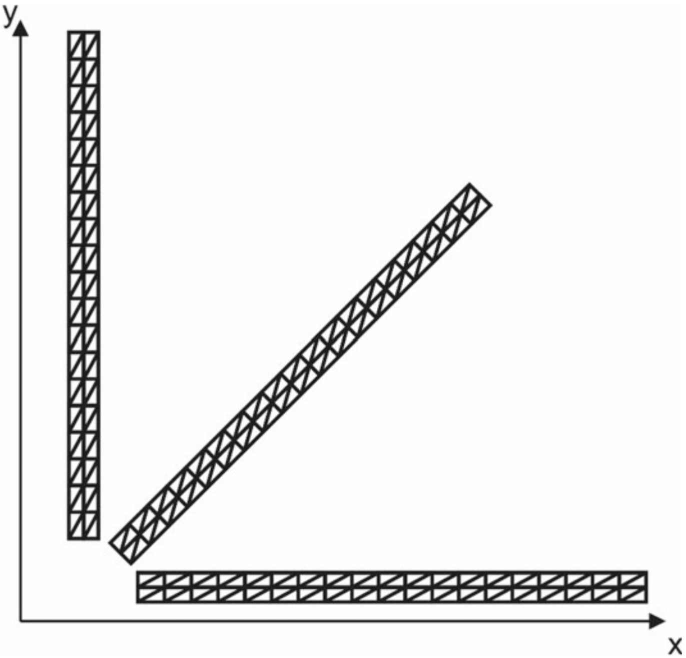

Fig. 5 The location of finite element models of specimens under tension

The results of calculations for the case of static load are presented in Figs. 6, 7 and 8, where the comparison of experimental (points), calculated by Eq. (4) (dotted lines) and FE results (solid lines) are presented. Figure 6 corresponds to the data for the rolling direction, Fig. 7—transverse direction; Fig. 8—at an angle of 45° to rolling direction. The results show that the calculated and FE data coincide with the accuracy of 1–2%, which demonstrates the correctness of all algorithms, including those related to the implementation of the creep law and time integration, and the entire software as a whole. Differences in experimental and FE data are the same as those when comparing them with the calculated ones.

Let us analyze now the results of the experimental data in the case of periodic loading with the results of numerical creep modeling with Eq. (11), which were obtained by asymptotic and averaging methods. We use the same FE models (Fig. 5). The results are presented in Figs. 9, 10 and 11. The numerical results are shown by solid lines and the experimental data by points.

The diagrams show that the developed software tool allows in general a satisfactorying modeling of creep processes at periodic loading in steel 3. The difference between experimental and numerical results does not exceed 10–15% for time domains which are after the first four loading cycles, which is similar to the prevoious static case. At low number of cycles (2–4) the error is 25–30%. For all three directions,

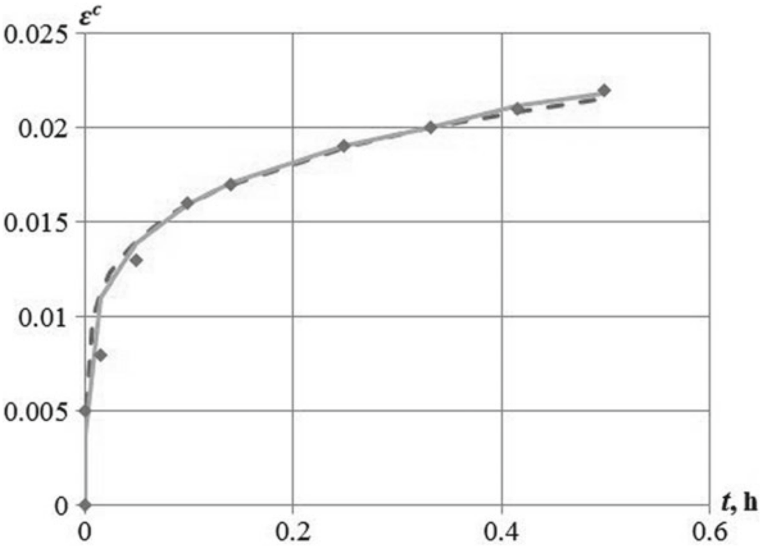

Fig. 6 Comparison of experimental, calculation and finite element data (rolling direction)

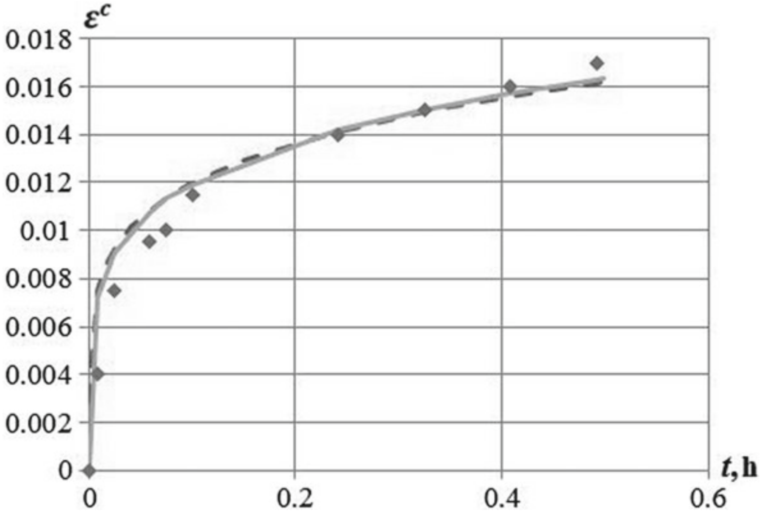

Fig. 7 Comparison of experimental, calculation and finite element data (transverse direction)

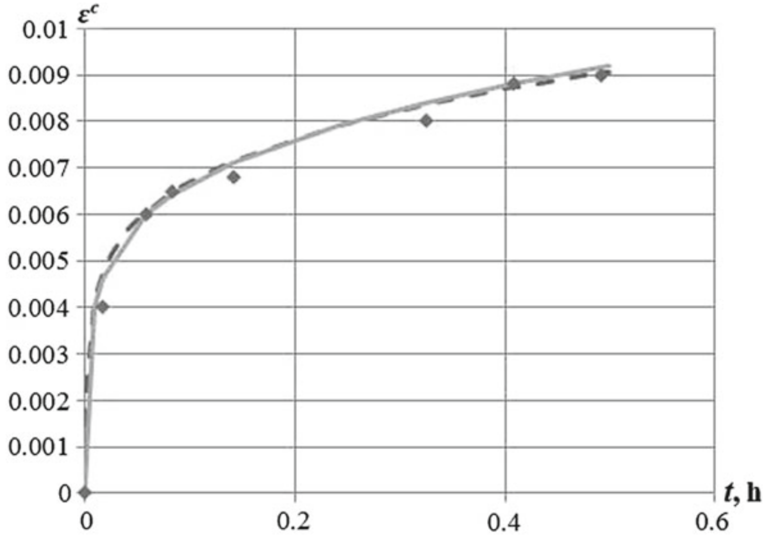

Fig. 8 Comparison of experimental, calculation and finite element data (direction at an angle of 45° to the rolling direction)

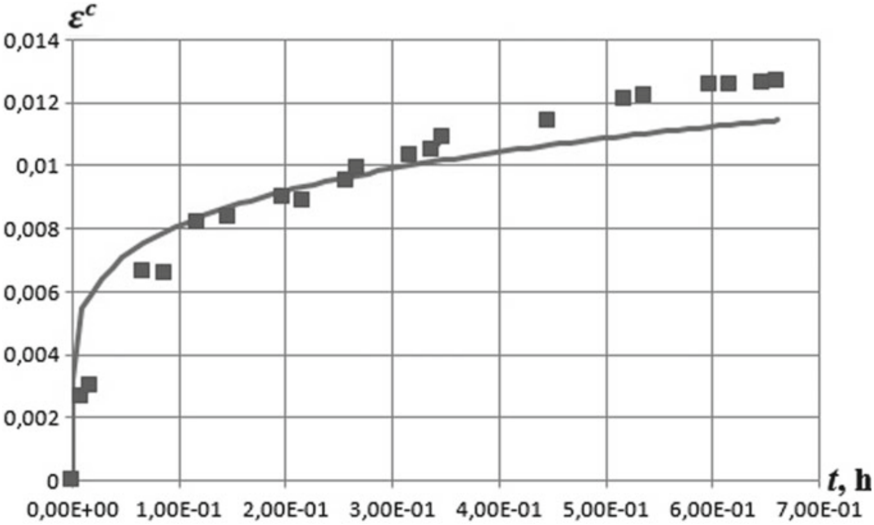

Fig. 9 Comparison of experimental and finite element results (periodic load, rolling direction)

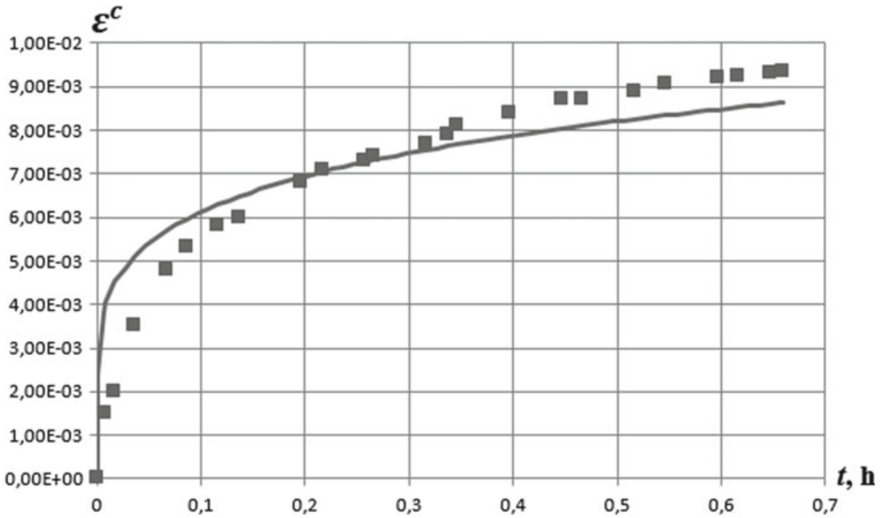

Fig. 10 Comparison of experimental and finite element results (periodic load, transverse direction)

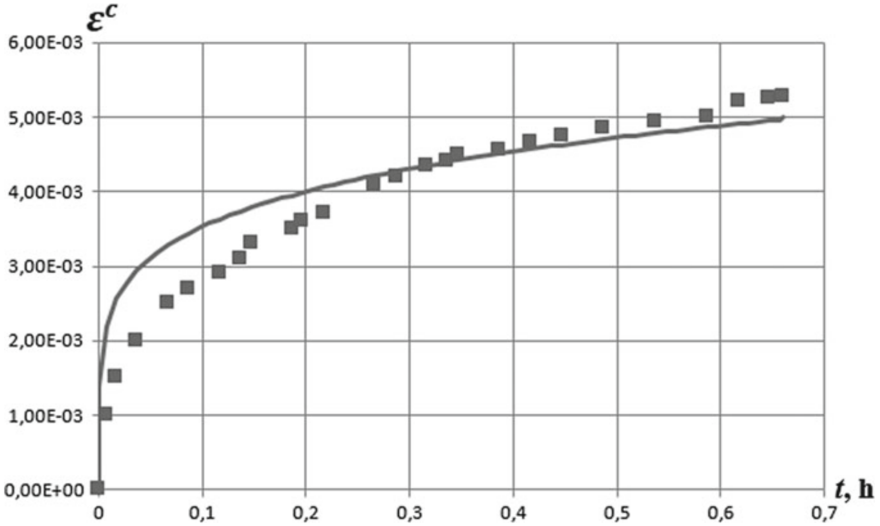

Fig. 11 Comparison of experimental and finite element results (periodic load, direction at an angle of 45° to the rolling direction)

the accuracy of modeling of one-dimensional experiments and two-dimensional calculation schemes can be considered quite satisfactory.

5 Short-Term Creep of Plates with Holes. Experimental Investigations

From the sheets of steel 3 (same material that was used for producing plane specimens) rectangular plates with dimensions 160 × 34 mm were cut out. Each plate was made with 5 holes: one central with diameter 10 mm, and four lateral ones with a diameter 8 mm. Such a scheme was chosen to implement at certain plate's points the stress state, which corresponds to the range of values from creep experiments in specimens. Plates were cut from sheets along the rolling direction. To fix the plates in the AIMA-5-2 test machine, which is designed for tensile testing in creep conditions, the upper and lower technological holes with a diameter of 10 mm were made. The sheme of the plate is shown in Fig. 12. Seven plates were produced. A measuring grid with a step in the longitudinal direction of 1 mm, and with step of 2 mm for transversal one was mechanically added. Video recording was used to obtain data for different moments of time.

The plates with 5 holes were tested at static and periodic tensile loading. In the latter case the program of experiments included partly periodic unloading and loading. Three plates were tested at static loading as well as 4 at periodic. Results of measurements were averaged.

At first let us consider the case of static load. Plates were loaded by weight of 3000 kg (which is equal to tension stress 135 MPa in plate's net section is far from loading hole) during 60 s. Experimental results for different time moments are shown in Fig. 13a–c. From the analysis of photographs it is evident that there is a significant plate's deformation over the time, when circular holes turned into elliptic, and with decreasing the width of the plate in the vicinity of their location. After an instantaneous growth of the strains, their increasing continues in time.

The numerical data of the deformed state were determined by analyzing the resizing of the cells of the dimensional grid. Moment of time $t = 3$ s was considered as the moment of obtaining plastic strains, then the data was analyzed with time steps up to the moment $t = 30$ s. We did not succeed experimentally with a satisfactory accuracy to determine the change in the values of displacement $u\,(x, y)$ in the direction x, which is transverse the direction of tension. Thus, the longitudinal displacements $v(x,\ y)$ were analyzed.

Below, we give the data defined by the measurements in some points of the plates, in which there was the most significant strain increasing (Fig. 14). The data were averaged for three plates. Due to the symmetry of the holes, the data for the left and right halves were also analyzed and added for averaging.

Figure 14 shows the location of the points in which measurements were made for different moments of time. Such points were chosen in the regions on the borders

Fig. 12 Plate with 5 holes

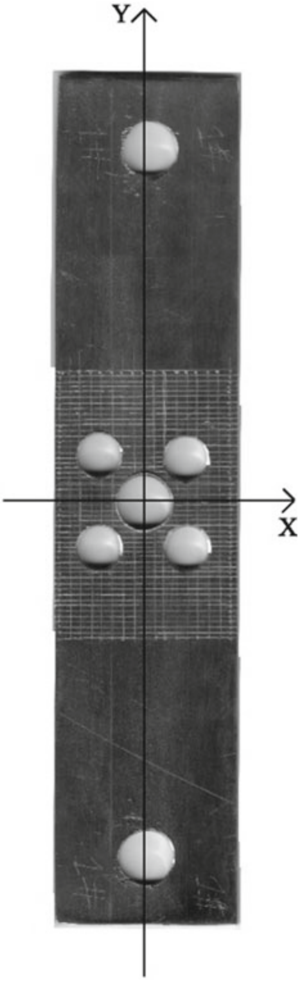

of holes and between them, where the the most significant change in the grid was determined.

Experimental data of varying the displacements in time are shown in Fig. 15, where the points indicate the measured values. The analysis of the obtained results shows the correspondence of character of the curves running in the case of primary creep. Also, let us note their similarity to the curves obtained for specimens in uniaxial tests.

As can be seen from Fig. 15, all the curves for the plate points are qualitatively similar: they have first rapid growth regions at first 20 s, and then their rates decrease. The curve 3 is an exception. It was built for point A, located at the boundary of the

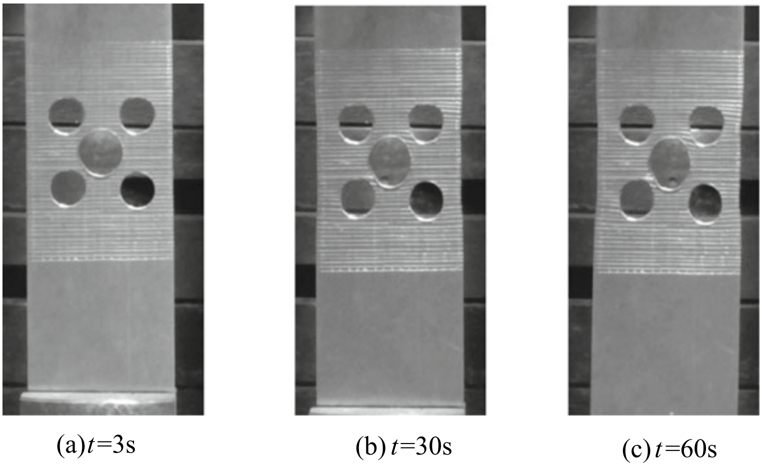
(a) t=3s (b) t=30s (c) t=60s

Fig. 13 Deformed plate at static load at different moments of time

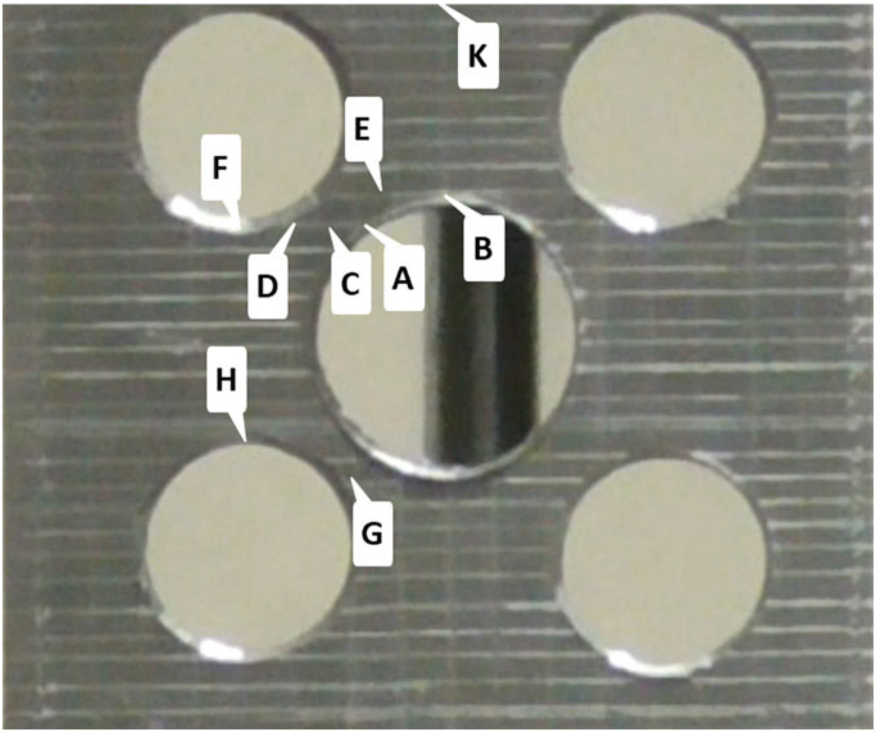

Fig. 14 The location of the plate points in which the measurements of displacements were done (t = 0 s)

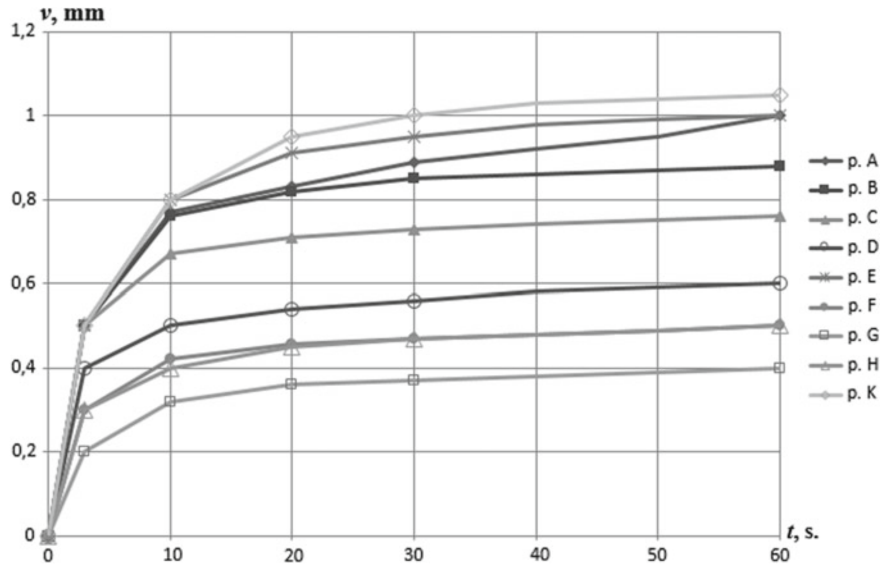

Fig. 15 Varying in time of displacements at the points of the plate, marked by symbols in Fig. 14 (static load)

Fig. 16 Periodic load of plates with holes

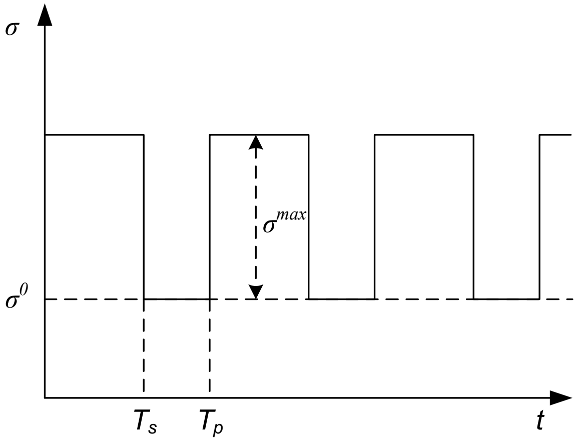

central hole, in which at approximately 50th second, the acceleration of creep begins. According to these data, it is possible to conclude that in this moment the beginning of the third section of the creep curve takes place. It corresponds to accelerated creep, accompanied by a hidden damage. As is well known [3], just in this area, the stress concentration takes place and creep fracture occurs.

Next, we consider the results of an experimental study of the deformation of plates during periodic (cyclic) loading according to the scheme of Fig. 16.

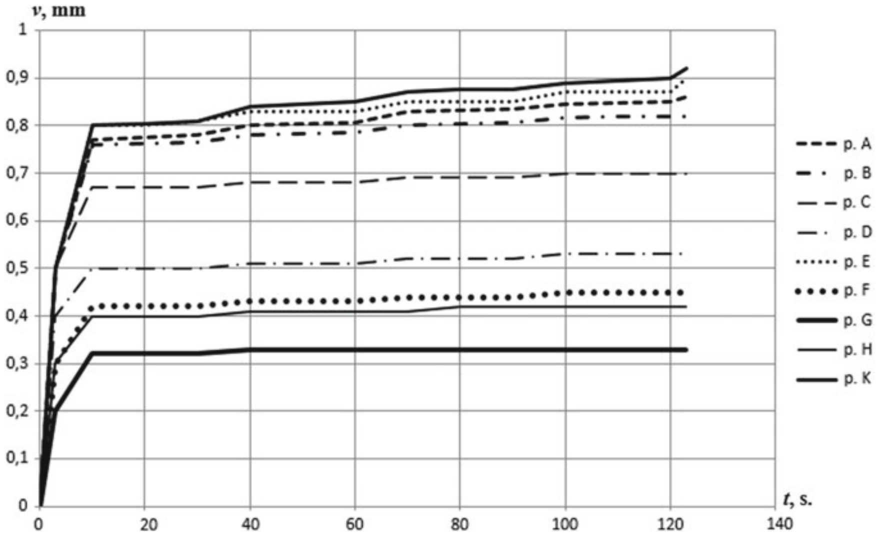

Fig. 17 Varying in time of displacement at the points of the plate, marked by the symbols in Fig. 14 (periodic load)

It was given as follows: for the time $T_s = 10$ s the plate was loaded by stress 135 MPa, as well as next 20 s by stress 121.5 MPa, thus $T_p = 30$ s. During the experiments, it became clear that on the fifth load cycle there was a fracture of the plates in the area of the technological hole designed to organize the load. However, in the areas of transition from the central hole to the small one, as well as from the small hole to the side of the plate, there was a characteristic clouding of the metal, which may indicate a significant damage and close fracture in these places [3, 27]. The analysis of character of deformation showed that there were no fundamental differences in strain running in comparison with experiments at static loading.

Let us consider the results of measurements of longitudinal plate displacements. To obtain this data, a technique similar to that discussed above for static loading was used. Data of measurements obtained by video processing of experiments, for the same points of the Fig. 14 are shown in Fig. 17.

As can be seen from Fig. 17, all obtained curves for plate points are qualitatively similar: with growth in the first 10 s the curves correspond to the curves of purely static load, further due to partial unloading there is a significant deceleration of the growth of displacements.

When plotting the time dependence for longitudinal displacements (Fig. 17), their changes during periods of cycles with lower load values (from 11th to 30th s) were fixed only at points A, B, E, and K, in which maximal displacements took place also in the static experiments. At other points, varying of displacements in the indicated parts of the periods was so small that it could not be determined. It can be explained by the limitations of measurement technique.

As it was already noted, in the places of transition from the central to the lateral holes, characteristic changes of the metal were found, which can be regarded as a evidence of close fracture. This conclusion is also confirmed by the graphs of displacement for those points A and E located in those places. It these points starting from 120th s the accelerated growth of displacement was experimentally obtained.

In general, according to results of experiments with periodic loading of plates it is possible to conclude that there is a significant slowdown in the growth of displacements compared with creep at static loading. The reason is partly unloading. So, for example, at point A for 60 s the value of static displacement is 1 mm, and with a periodic load −0.8 mm; at point E for 60 s. also it is equal 1 mm, and with periodic loading −0.85 mm.

6 Short-Term Creep of Plates with Holes. Numerical Simulation

The results of experimental studies of the deformation of a plate with five holes were compared with numerical data have been obtained by use the developed method and software. As a result of the load's and plate's symmetry, a half-plate model of 17 × 160 mm was used as a calculation scheme, and the plate on the upper side was considered to be loaded with a uniform tension load $p = 135$ MPa (Fig. 18a). The exact loading of the plate through the hole was also simulated numerically. The lower boundary of the plate was considered to be rigidly fixed. The calculation scheme of the plate with the finite element grid, numbering 838 nodes and 1474 elements, is shown in Fig. 18a. This grid was selected after preliminary elastic-plastic calculations that were performed both in the *FEM CREEP* software and in *ANSYS* with the same grids. It was established that the stress state is determined approximately the same, with a difference of 10–15 MPa and qualitatively close zones with the same level of stress. Distribution of von Mises stress is shown in Fig. 18b. The results of the calculations show a significant stress concentration in the zones between the holes and at an angle of approximately 45° to the holes in the directions to the outer sides of the plates, the maximum value of von Mises stress is 394 MPa, which is close to the material strength limit of 395.3 MPa.

Further, the modeling of the plate's creep for 30 s was considered. In the calculations, the values of creep constants of the plate material, obtained by experimental data processing, were used. Numerical simulations are carried out with a variable integration step, from the initial value of 1×10^{-9} to 1×10^{-4} h.

The results of calculations using the *FEM CREEP* software were compared with the data obtained after processing the video of experiments. Let us consider the results of this comparison. The data of the deformation of plates near holes, where a two-dimensional stressed state is realized, are analysed. The measurements were compared for different moments of time up to 30 s. The values of the displacement components v, mm were compared with the values obtained for the corresponding

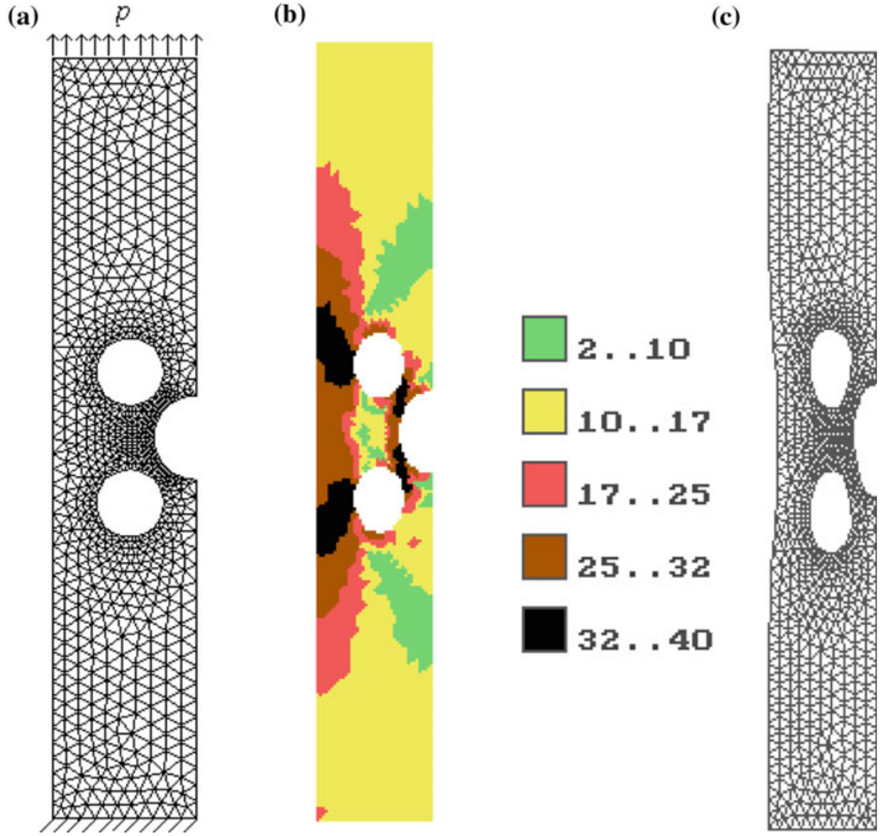

Fig. 18 FE model of the half of a plate (**a**), initial von Mises stress distibution, $\sigma_{vM}\cdot 10^{-1}$MPa (**b**) and deformed FE mesh, t = 30 s, scale 1:60 (**c**)

nodes of the finite element grid. The displacement components *u* with a given deformation pattern have significantly lower values that could not be determined by the used method of grids comparison.

A finite element grid, which is deformed due to calculation data for the time t = 30 s, is presented in Fig. 18c. Comparing it with Fig. 13b, where the photo of the deformed plate is located for the same moment, allows us to draw a conclusion on a qualitatively correct description of deformation under creep.

Let us consider quantitative estimates. Table 1 shows the results of the comparison of experimental and numerically determined values of short-time creep displacement for points located between the three holes in which there is a significant deformation under creep running. The locations of points marked with symbols are presented in Fig. 14. These points in finite element model correspond to the numbers of nodes, shown in Fig. 19. Point K corresponds to the 424th node, which due to the applied scale is not shown in Fig. 19.

Table 1 Comparison of experimental and numerically determined displacements [mm] for t = 30 s

Point/ Node number	A/ 44	B/ 37	C/ 270	D/ 286	E/ 250	F/ 169	G/ 258	H/ 194	K/ 424
Experimental data	0.4	0.35	0.23	0.15	0.45	0.17	0.17	0.17	0.5
Numerical data	0.32	0.34	0.25	0.21	0.3	0.2	0.13	0.19	0.34
Error, %	20	3	9	29	33	15	24	11	32

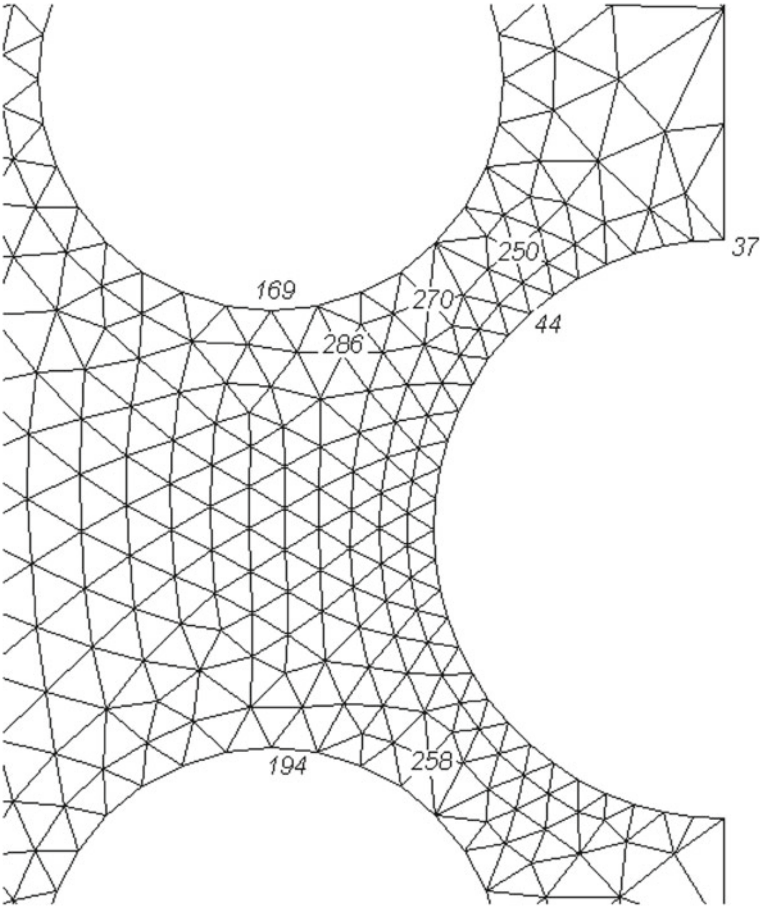

Fig. 19 Location of nodes of a finite element grid near three holes

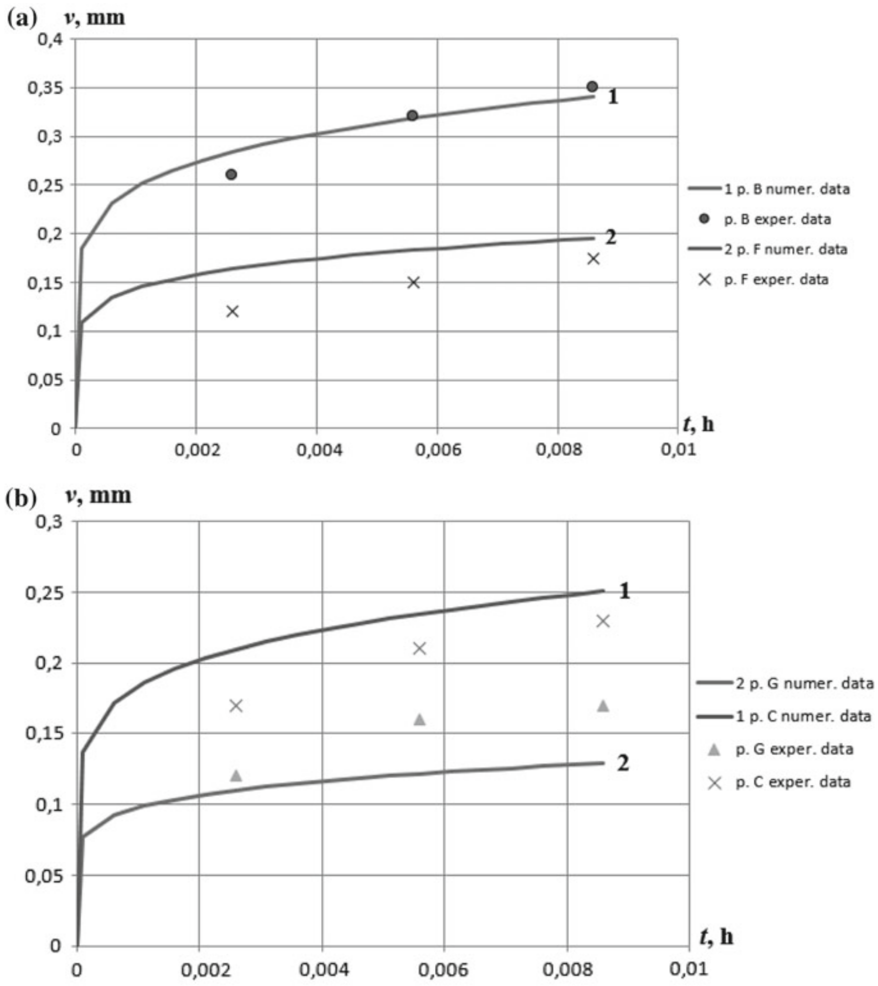

Fig. 20 Displacements versus time in points B, F (**a**) and in points C, G (**b**)

Analysis of the data from Table 1 shows that in the regions with the highest displacement level, the maximum difference between numerical and experimental data is 32–33%, but at other points, the errors are much lower.

Comparison of numerical (solid lines) and experimental data (points) for different moments of time is shown in Fig. 20.

Analyzing the data of Fig. 20, which gives a comparison the displacement's calculation and experimental data at different points of the plate, we conclude that numerical simulation qualitatively reflects the process of deformation in time. Quantitative differences range from 3 to 40% for various plate fragments. The latter value

Table 2 Data on the stress redistribution in the vicinity between two holes, σ_i, MPa

№ el.	1324	1309	1340	1361	1381	1404	1405	1429	1430	1454	1455
$t = 0$ s	254	268	331	332	340	338	349	340	367	358	385
$t = 30$ s	322	301	334	333	348	330	331	317	306	298	313

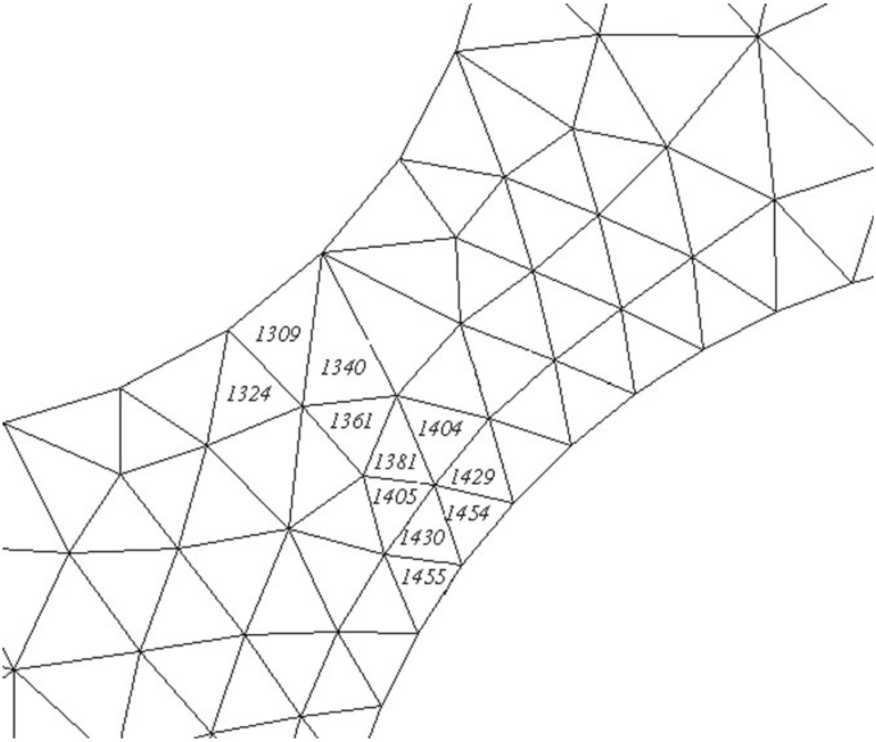

Fig. 21 The location of the elements for Table 2 in the applied finite element grid

is quite large, but it must be taken into account that the experimental data are also determined with a certain error in the measurement.

Numerical simulation of the short-term creep of the plate also provides a qualitatively correct estimate of stress varying: there is a redistribution of stresses in the vicinity between the holes, and between the holes and free side of the plate. The qualitative character of the stress distribution does not change, and the most loaded zones remain the same. As an example, let us consider the data of stress redistribution in the zone between two holes (Table 2). The elements selected for comparison are located between the upper and central holes, their numbers are shown in Fig. 21. In the table, the elements are given starting with numbers at the upper holes and finishing at the lower ones.

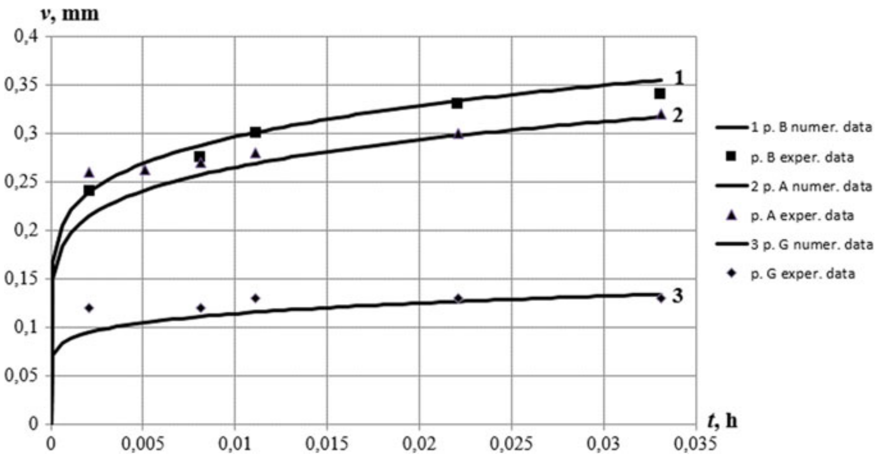

Fig. 22 Comparison of numerical and experimental data (periodic load, points A, B and G)

It is evident from the analysis of Table 2 that for a short period of time (30 s) there is a certain redistribution of von Mises stresses in the area between the holes. Near the central hole there is a relaxation (from 385 to 313 MPa), and near the upper one a certain growth presents.

Next, let us consider the periodic loading of these plates, comparing the experimental and numerical creep results. According to the analysis of experimental data, it can be seen that for comparison it is possible to use the data for four load cycles of 2 min. If you analyze the data shown in Figs. 4, 9, 10 and 11, you can see that 4 is the limiting value of the cycles number, in which in uniaxial case the values with a satisfactory error are obtained. Unfortunately, the peculiarities of the experiment and the creep properties of used steel 3 did not provide the opportunity to increase the number of cycles.

The analysis of the experimental study of creep of the considered plates shows that there is no qualitative difference between the distribution of displacement and the running of the deformation process in the case of static and periodic loading. In this regard, as an example, we give in Fig. 22 only data from the comparison of experimental and numerical results in some characteristic points (Fig. 14), selected for analysis. Point B corresponds to the zone with maximum displacements, point A is a characteristic point for the zone between the upper holes, and point G is located between the lower ones. The calculated data are presented in Fig. 22 by solid lines and the points correspond to experimental results. Experimental data for point A is indicated by triangles, for a point B by squares, and for a point G by diamonds.

As can be seen from the results of the comparison, the varying of displacements in creep process at complex two-dimensional stress state is qualitatively correctly described by the calculated data. Their form, similar to the case of static loading, corresponds to the form of primary creep cyrves. Reducing the creep rate compared

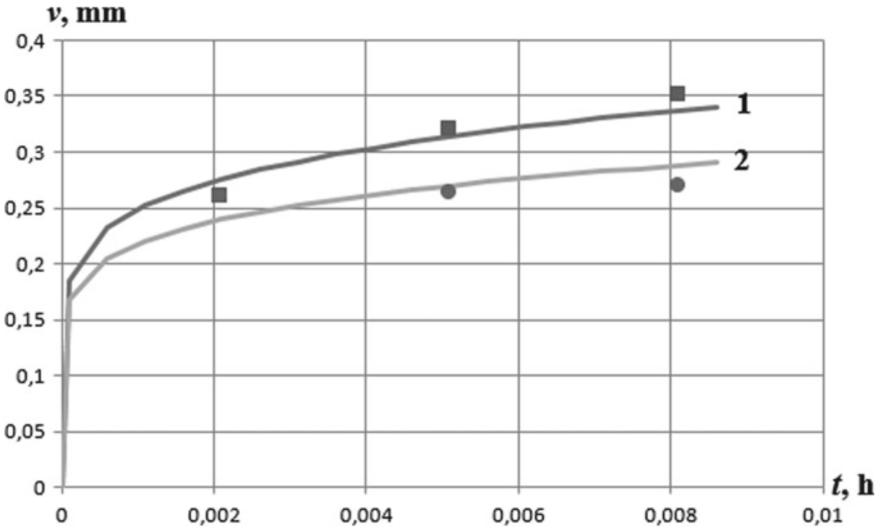

Fig. 23 Comparison of calculated and experimental data for static and periodic loads (point B)

to the static load data, which takes place due to the load decreasing in the second part of the period, is also described qualitatively correct.

Maximum error between numerical and experimental data was determined for the first 10 s at all points, and the largest (at the point G) is 35%. The values for 120 s. (at points C and F) are 25% and 27% respectively. The creep rate, which can be analyzed by the slope of the curves, is evaluated satisfactorily, with an error of 10–15%. As can be seen from the figures, there is an overestimation for numerical data for the first periods. This can be explained by not very exact measurement technique, but also by the insufficient number of load cycles for completely satisfactory experimental conditions, which would require their greater number.

A comparison between calculated displacement curve at point B for cases of static (curve 1) and periodic loading (curve 2) is presented in Fig. 23. As can be seen from the graph, the errors are not very big. For the first ten seconds the experimental points coincide, this occurred because in both cases the loading is the same. Differences of 5–8% between the numerical and experimental data are much smaller than the difference of 30% between the data of static and periodic loading, which can demonstrate the possibility of numerical determination of the influence of periodic loading effect in the complex stress state.

Numerical studies which were done, comparison of their results with experimental data, obtained at the same time with a sufficient error degree, provides the opportunity to use the developed software for solving the practical problems.

7 Conclusions

The chapter provides a description of the method for solving the plane creep problems for structural elements made of materials with transversally isotropic creep properties. The case in which the instantaneous load leads to the appearance of plastic deformations is considered.

The creep law for the case of periodic loading at primary short-term creep for cases of uniaxial and plane stress states is experimentally verified. The values of the constants for the equation describing the transversally isotropic creep are obtained. It is established that:

- the creep curves in all directions (along the width, across and at an angle of 45° to the direction of rolling) of steel sheets are similar;
- the maximum creep rate is realized in the direction along the rolling, and the minimum takes place at the direction determining by an angle of 45° to rolling; the form of the creep curves corresponds to the primary creep;
- the main part of the deformation is obtained in the first minutes of creep, which gives the possibility to classify the curves by the type of short-term creep;
- creep almost stops after 30 min of deformation.

The verification study of the calculated method was carried out by comparing the numerical and experimental results of uniaxial and plane stress conditions that occurs in investigated plates with five holes. The satisfactory for physically nonlinear two-dimensional problems deviation of calculated and experimental data within the limits of 25–30%, with the exception of two points in the case of periodic loading, in which the level of displacement is smaller than more than twice as much as the maximum, is found. The difference may be explained by the measurement technique.

The proposed method for the periodic load case due to its similarity to the standard method for static problems as well as due to decreasing of calculation time can be recommended for the analysis of practical problems with the similar forms of the cycle, which number has not be less than four.

References

1. Lemaitre, J., Chaboche, J.-L.: Mechanics of Solid Materials. Cambridge University Press, Cambridge (1994)
2. Rabotnov, YuN, Mileyko, S.T.: Short-term Creep. Nauka, Moscow (1970). (in Russ.)
3. Rabotnov, YuN: Creep Problems in Structural Members. North-Holland, Amsterdam (1969)
4. Malinin, N.N.: Applied Theory of Plasticity and Creep. Mashinostroenie, Moscow (1975). (in Russ.)
5. Hoff, N.J.: Structures and materials for finite lifetime. Adv. Aeronaut. Sci.: Proc. First Int. Congr. Aeronaut. Sci. **2**, 928–961 (1959)
6. Kassner, M.E.: Fundamentals of Creep in Metals and Alloys. Elsevier Science Technology, London (2015)
7. Nikitenko, A.F., Sosnin, O.V.: Creep and long-term strength under cyclic loading conditions. Strength Mater. **8**, 1395–1398 (1976)

8. Stryzhalo, V.O.: On the applicability of creep theories and methods of estimating durability for case of stepped directed deformation of material in a low-cycle region. Proc. Acad. Sc Ukr. **3**, 14–24 (1978). (in Ukrain.)
9. Lebedev, A.A., Giginyak, F.F., Bashta, V.V.: Cyclic creep of body steels under a complex stress system in the temperatures range 20–400 C. Strength Mater. **10**(10), 1128–1131 (1978)
10. Kennedy, A.J.: Processes of Creep And Fatigue in Metals. Wiley, London (1963)
11. Tsimbalistyi, Ya.I., Troyan, I.A., Marusii, O.I.: Investigation of the vibrocreep of alloy EI437B at normal and high temperatures. Strength Mater. **7**, 1331–1335 (1975)
12. Weinbel, R.C., Schwarzkopf, E.A., Tien, J.K.: Effects of frequency on the cyclic creep and fracture of a lead-rich-lead-tin solder alloy. Scr. Metall. **21**, 1165–1168 (1987)
13. Fakpana, K., Otsukab, Y., Mutohb, Y., Inouec, S., Nagatad, K., Kodani, K.: Creep-fatigue crack growth behavior of Pb-contained and Pb-free solders at room and elevated temperatures. Procedia Eng. **10**, 1238–1243 (2011)
14. Wagoner, R.H., Chenot, J.L.: Metal Forming Analysis. Cambridge University Press, Cambridge (2001)
15. Saanouni, K., Chaboche, J.-L.: Computational damage mechanics: application to metal forming simulation. Compr. Struct. Integr. **3**, 321–376 (2003)
16. Saanouni, K.: Damage Mechanics in Metal Forming: Advanced Modeling and Numerical Simulation. Wiley, London (2012)
17. Breslavskii, D.V., Morachkovskii, O.K.: Nonlinear creep and the collapse of flat bodies. Int. Appl. Mech. **34**(3), 287–292 (1998)
18. Breslavsky, D., Morachkovsky, O., Tatarinova, O.: Creep and damage in shells of revolution under cyclic loading and heating. Int. J. Nonlinear Mech. **66**, 87–95 (2014)
19. Breslavskii, D.V., Metelev, V.A., Morachkovskii, O.K.: Anisotropic creep and damage in structural elements under cyclic loading. Strength Mater. **47**(2), 235–241 (2015)
20. Hamming, R.W.: Numerical Methods for Scients and Engineers. McGraw-Hill, New York (1973)
21. Moiseev, N.N.: Asymptotic Methods of Nonlinear Mechanics. Nauka, Moscow (1969). (in Russ.)
22. Breslavsky, D.V., Konkin, V.M., Mietielov, V.O.: Plasticity and creep of steel 3 at room temperature. Bull. NTU "KhPI". Ser.: Dyn. Strength Mach. **46**(1218), 77–81 (2016)
23. Chaboche, J.-L.: A review of some plasticity and viscoplasticity constitutive equations. Int. J. Plast. **24**, 1642–1693 (2008)
24. Breslavsky, D.V., Korytko, Yu. N., Tatarinova, O.A.: Design and Development of Finite Element Method Software. Kharkiv: Pidruchnyk NTU « KhPI » . (in Ukrain.) (2017)
25. Zienkiewicz, O.C., Taylor, R.L., Wood, D.D.: The Finite Element Method for Solid and Structural Mechanics. Butterworth-Heinemann (2014)
26. Bathe, K.J.: Finite-Elemente Methoden. Springer, Berlin (1990)
27. Walczak, J., Sieniawski, J., Bathe, K.: On the analysis of creep stability and rupture. Comput. Struct. **17**(5–6), 783–792 (1983)